

DRAFT

EIC PDR

September 30, 2024

Electron Ion Collider Preliminary Design Report

Contributors:

E-C. Aschenauer¹, R. Ent², S. Joosten³, M. Żurek³, ADD NAMES AND INSTITUTIONS

¹Brookhaven National Laboratory, USA

²Thomas Jefferson National Accelerator Facility, USA

³Argonne National Laboratory, USA

Contents

0	Style Guide	2
0.1	Chapter Abstract	2
0.2	Wordsmithing	3
0.2.1	Passive voice	3
0.2.2	Verb tenses	3
0.2.3	Apostrophes	3
0.2.4	Capitalization and names	3
0.2.4.1	Pieces of EIC	3
0.2.4.2	Internal phrases	3
0.2.4.3	Discipline-specific approaches or “guiding principles” or buzz phrases	4
0.2.4.4	Formal group names	4
0.2.4.5	Headings	4
0.2.5	Captions	4
0.2.6	Spelling	4
0.2.6.1	Exceptions to U.S. spelling	4
0.2.6.2	Capitalization	4
0.2.7	Commas	5
0.2.7.1	Commas in numbers	5
0.2.8	Plurals and possessives	5
0.2.9	Abbreviations	5
0.2.9.1	Textual treatment of Figures and Tables	5
0.2.9.2	Radio frequency	5
0.2.9.3	etc., et cetera	6
0.2.10	Hyphenation of multi-word adjectival phrases	6
0.2.11	Double letters	10
0.2.12	Mathematical symbols, subscripts and superscripts	10
0.2.13	Quotation marks	10
0.2.14	Citations, references and the bibliography	10
0.2.15	Miscellaneous	11
0.2.15.1	“Calculations show that . . .”	11
0.2.15.2	“Should”, “must”, and reference to future studies	11
0.2.15.3	“Enable”	11
0.2.15.4	Reporting technical results without a clear statement of their import	11
0.2.15.5	Excessive and inconsistent use of lists	11
0.2.15.6	Cross-references	12
0.2.15.7	Isotopes	12
0.2.15.8	*** asterisks in comments	12
0.3	Dimensions and units	12
0.4	Numbering – chapters, sections, and subsections	13

0.4.1	This is the heading of a subsection	13
0.4.1.1	A subsubsection heading like this has no period at the end	13
	This paragraph heading ends with a period.	13
0.4.2	More formatting rules and standards	14
0.4.2.1	Clearpages and Pagebreaks	14
0.5	Equations, Tables, Figures, and plots	14
0.5.1	Equations	14
0.5.2	Tables	14
0.5.3	Converting between LaTeX and Excel table formats	14
0.5.4	Figures	17
0.5.5	Plots	17
0.6	Italics and bold face type	17
0.7	Issues that this Style Guide does not yet address	18
2	Physics Goals and Requirements	19
2.1	EIC Context and History	19
2.2	The Science Goals of the EIC and the Machine Parameters.	19
2.3	Scientific Requirements	19
2.3.1	Systematic Uncertainties	19
2.3.2	Radiative Corrections	19
2.4	The EIC Science (ePIC performance for key observables)	19
2.4.1	Origin of Nucleon Mass	19
2.4.2	Origin of Nucleon Spin	20
2.4.3	Multi-Dimensional Imaging of the Nucleon	20
2.4.3.1	Imaging in Momentum Space	20
2.4.3.2	Imaging in Transverse Position Space	20
2.4.4	Properties of Nuclear Matter	20
2.4.4.1	Gluon Saturation	20
2.4.4.2	Nuclear Modifications of Parton Distribution Functions	20
2.4.4.3	Passage of Color Charge Through Cold QCD Matter	20
8	Experimental Systems	21
8.1	Experimental Equipment Requirements Summary	21
8.2	General Detector Considerations and Operations Challenges	22
8.2.1	General Design Considerations	22
8.2.2	Backgrounds and Rates	22
8.2.3	Radiation Level	22
8.3	The ePIC Detector	22
8.3.1	Introduction	22
	The Context	22
	The Detector	23
	Technological Synergistic Aspects of the Detector Design	27
8.3.2	Magnet	28
	Requirements	28
	Justification	28
	Implementation	29
	Additional Material	29
8.3.3	Tracking	30
8.3.3.1	The silicon trackers	30
	Requirements	30
	Justification	31

	Implementation	37
	Additional Material	48
8.3.3.2	The MPGD trackers	49
	Requirements	49
	49
	Justification	51
	Performance	53
	Implementation	53
	Additional Material	56
8.3.4	Particle identification	56
8.3.4.1	The time-of-flight layers	56
	Requirements and Justifications	56
	Implementation	64
	Additional Material	74
8.3.4.2	The proximity focusing RICH	75
	Requirements	75
	Justification	76
	Implementation	81
	Additional Material	88
8.3.4.3	The high performance DIRC	88
	Requirements	88
	Justification	88
	Performance	91
	Performance Systematic Studies	92
	Simulation tools and validation	92
	Reconstruction methods	92
	Implementation	94
	Additional Material	101
8.3.4.4	The dual radiator RICH	102
	Requirements	102
	Justification	102
	Performance	109
	Implementation	111
	Additional Material	125
8.3.5	Electromagnetic Calorimetry	130
8.3.5.1	The backward endcap electromagnetic calorimeter	130
	Requirements	130
	Justification	130
	Implementation	133
	Additional Material	137
8.3.5.2	The barrel electromagnetic calorimeter	137
	Requirements	137
	Justification	138
	Implementation	147
	Additional Material	152
8.3.5.3	The forward endcap electromagnetic calorimeter	157
	Introduction	157
8.3.6	Hadronic Calorimetry	168
8.3.6.1	The backward endcap hadronic calorimeter	169
	Requirements	169
	Justification	169

	Implementation	172
	Additional Material	174
8.3.6.2	The barrel hadronic calorimeter	175
	Requirements	175
	Justification	176
	Performance	183
	Implementation	185
8.3.6.3	The forward endcap hadronic calorimeter	187
	Requirements	187
	Justification	188
	Implementation	189
	Additional Material	189
8.3.7	Far forward detectors	189
8.3.7.1	The detectors in the B0 bending magnet	190
	Requirements	190
	Justification	191
	Implementation	191
	Additional Material	194
8.3.7.2	The roman pots and the off-momentum detectors	194
	Requirements	194
	Justification	195
	Implementation	196
	Additional Material	199
8.3.7.3	The zero degree calorimeter	199
	Requirements	199
	Justification	199
	Implementation	200
	Additional Material	201
8.3.8	Far backward detectors	201
8.3.8.1	The luminosity system	202
	Beam Size Effect -	202
	High rate of BH radiation and SR background -	204
	Beam Polarisation -	204
	Physical Constraints -	205
	Systematic Uncertainties -	206
	Design and Components	206
	Additional Material	211
8.3.8.2	The low Q^2 taggers	211
	Requirements	211
8.3.8.3	TCS	212
8.3.8.4	Vector Meson production	212
8.3.8.5	Spectroscopy	212
	Justification	213
	Performance	216
	Implementation	216
	Additional Material	218
8.3.9	Polarimeters	218
8.3.9.1	The electron polarimeters	218
	Requirements	218
	Justification	218
	Implementation	218

	Additional Material	219
8.3.9.2	The proton polarimeters	219
	Requirements	219
	Justification	219
	Implementation	220
	Additional Material	220
8.3.10	Readout Electronics and Data Acquisition	220
	Requirements	220
	Device Concept and Technological choice: Streaming Readout	222
	Subsystem Description (components)	223
	Readout Electronics and ASICS	223
	Scope of the Effort	225
	FEB components	225
	RDOs	226
	DAM - Data Aggregation and Manipulation Hardware	227
	GTU - Global Timing Unit	228
	Protocols	228
	DAQ/Online Computing - Echelon 0	230
	Slow Controls	232
	Implementation	233
	Status and remaining design effort:	233
	Environmental, Safety and Health (ES&H) aspects and Quality Assessment (QA planning):	234
	Construction and assembly planning:	234
	Collaborators and their role, resources and workforce:	234
8.3.11	Software and Computing	234
	Requirements	234
	Justification	234
	Implementation	235
	Additional Material	235
8.4	Detector Integration	236
8.4.1	Installation and Maintenance	236
8.5	Detector Commissioning and Pre-Operations	236

List of Figures

1	Example of a non-graphical figure.	17
8.1	Table presenting the Experimental Equipment Requirements Summary in the YR. At present, the table is not updated and it is here as a mere space holder.	21
8.2	A schematic showing how hadrons and the scattered electron for different $x - Q^2$ are distributed over the detector rapidity coverage. THIS FIGURES IS A PLACE HOLDER: IT IS FROM YR AND REQUIRES REVISION.	24
8.3	A schematic showing the ePIC central detector subsystems. THIS FIGURES IS A PLACE HOLDER	25
8.4	Cumulative material budget in radiation lengths (top row) and interaction lengths (bottom row) for the whole CD (left column) and zooming at the CD tracking region (right column). THIS FIGURES IS A PLACE HOLDER BECAUSE IT HAS TO BE COMPLETED WITH SUBSYSTEM CONTOURS AND REQUIRES GRAPHICAL IMPROVEMENTS.	25
8.5	A schematic showing the ePIC far detector subsystems. THIS FIGURES IS A PLACE HOLDER	27
8.6	Maps of simulated fluence (left) and total ionising dose (right) over the ePIC tracking envelope. This is a conservative estimate assuming 10 years of running at top luminosity with 100% efficient accelerator and detector. The black lines indicate the approximate location of the ePIC SVT detector layers.	31
8.7	Schematic layout of the ePIC SVT showing the central region consisting of the inner and outer barrel made of three and two cylindrical layers, respectively, together with the endcap regions made of five annuli each. The figure also shows the surrounding Micro Pattern Gas Detector (MPGD) layers and the envelope of the Time of Flight PID detector.	32
8.8	Sketch of the MOSAIX sensor on a 300 mm wafer showing the size of the RSU, LEC, REC and of the full sensor for the three different widths.	34
8.9	Relative momentum resolution versus total momentum for charged pions (points) together with physics requirements (curves) in different pseudorapidity ranges as indicated. The results are based on full GEANT simulations using the ePIC software stack and ACTS-based track finding and reconstruction using optimized parameters.	36
8.10	Distance of closest approach in the radial direction between reconstructed charged pion trajectories and the event origin versus transverse pion momentum (points) together with physics requirements (curves) in different pseudorapidity ranges as indicated. The results are based on full GEANT simulations using the ePIC software stack and ACTS-based track finding and reconstruction using optimized parameters.	36
8.11	A close-up of a beam telescope constructed from two times three single-RSU sensors from ITS3 Engineering Run 1 with a seventh sensor (DUT) under an angle at the center of the telescope (left) and (right) results from beamtests at FNAL and from simulations for the cluster extent as a function of the beam incident angle onto the DUT.	37

8.12	Schematic overview of data and slow control lines to a group of 4 EIC-LAS.	38
8.13	Top left: CAD representation of the frame supporting the IB. Bottom left: IB half-barrel CAD view with sensors and cable routing. Right: Exploded CAD view of IB from the h-side and the e-side. The orange element is the kapton shield. In blue the air conveyors are shown.	40
8.14	Left: OB staves for L3 and L4. Two staves per layer are shown. Right: Exploded view of an OB stave.	41
8.15	CAD model of the preliminary (half-) disk design. Modules are shown in alternately inward (dark gray) and outward (white) facing orientations. Common bus FPCs are shown in orange. RDOs (green) are arranged on the outside of the disk ring, inside of the interface to the SVT global support structure.	42
8.16	First L4 quarter length stave prototype.	44
8.17	(Left) First test piece of the carbon composite corrugated disc core made in the LBNL composite shop. Heaters with two different heating zones that can mimic the sensor power density are placed on the carbon composite facesheet and are used for thermal measurements. (Right) Observed ΔT for different power dissipations in the LEC heating zone versus coolant air velocity.	44
8.18	An example of a low technology readiness level prototype for the FPC of the outer barrel (layer4). Prototype made by RPE LTU.	45
8.19	ePIC Tracking Subsystems	49
8.20	Nhits	50
8.21	Radiation dose	51
8.22	Geometries of BTOF with insert of sensor and charge sharing distribution (left), and the layout of sensor modules and service hybrids of FTOF on one side (right). . . .	57
8.23	BTOF $1/\beta$ as a function of momentum (p) in the simulation performance with PYTHIA DIS events (left). Upper limits on the 3σ particle separation from BTOF and FTOF as a function of pseudorapidity (right).	58
8.24	Fluence accumulated for 6 months at 100% time, corresponding to one year of data taking, the fluence has to be multiplied by the assumed 10 years of life time of the ePIC detector. Red squares highlight the barrel, end-cap, and B0 trackers detectors.	58
8.25	A schematic design of service hybrids for FTOF, which serves 3 modules or 12 sensors/ASICs.	62
8.26	A schematic design of the module for FTOF, which consists of 2×2 LGADs sensors and ASICs.	63
8.27	Schematic of the AC-LGAD sub-system readout chain. Each component is undergoing design, (pre-)prototyping, testing under various environments, and customization to meet the specific requirements of individual subsystems.	63
8.28	schematic drawings of one BTOF stave (left) and half of the whole FTOF (right) cooling pipes.	64
8.29	Barrel TOF supporting mechanic structure with engagement rings situated and supported by the EPIC global support tube structure (GST). The width of each of the three engagement rings is 5mm.	66
8.30	Left: Picture and beam test results for HPK strip sensor, 1 cm long, $500 \mu m$ pitch, and $50 \mu m$ metal electrode width. Right: Picture and beam test results for HPK pixel sensor, 4×4 , $500 \mu m$ pitch, and $150 \mu m$ metal electrode width. Plots from Ref. [1]. . .	68

8.31	Left: Degradation of the gain layer for AC-LGADs of several wafer (with different N_+ , oxide and active thickness) from HPK latest sensor production, showing no change in gain layer doping up to 10^{13} Neq, which is an order of magnitude over the ePIC TOF radiation requirement. Sensors were irradiated at the TRIGA reactor (Lubjiana) with 1 MeV neutrons. Right: Normalized comparison of response profile of two nearby strips for two HPK 0.5 cm length, 500 μm pitch, 50 μm strip width: one before irradiation and one after 1×10^{14} Neq, even if the total signal is degraded the charge sharing profile is unchanged. Bottom: Current over voltage measurement for irradiated HPK sensors.	69
8.32	Left: FCFD Jitter measurements with 3.5 pf input capacitance and charge injection. Right: EICROC Discriminator jitter versus the injected charge, determined from data on an oscilloscope. Left: FCFD Jitter measurements with 3.5 pf input capacitance and charge injection. Plots from the erd112 and erd109 2024 reports.	70
8.33	Picture of ppRDO connected with CMS ETL module board v0 for testing.	70
8.34	Assembled stave prototype at Purdue.	71
8.35	Assembly process of BTOF stave. Note, the scale is not real.	72
8.36	Assembly process of FTOF modules. RB3 type is shown as an example. Note, the scale is not real.	73
8.37	Collaboration institutions and their responsibilities.	74
8.38	simulation of $1/\beta$ as a function of particle momentum for BTOF and FTOF performance.	75
8.39	The proposed pfRICH detector. See the text for more details.	77
8.40	PLACEHOLDER (Left) The reconstructed Cherenkov angle for electrons, pions, kaons, and protons as a function of momentum. (Middle) N_σ separation between the electron and pion hypotheses as a function of momentum. (Right) Same as the middle panel, for pion and kaon hypotheses.	80
8.41	PLACEHOLDER Yield ratios of π^-/e_{scat} before (open black squares) and after (black full squares) pfRICH veto on π^- in PYTHIA 6 $e+p$ collisions at 18×275 GeV for four η bins, covering full pfRICH η acceptance.	80
8.42	PLACEHOLDER Institutions contributing to the pfRICH effort and their roles, resources, and participating workforce.	87
8.43	ePIC hpDIRC geometry in the Geant4 standalone simulation.	89
8.45	The expected performance of the hpDIRC as a function of the particle's polar angle is illustrated in terms of photon yield (a) for pions and π/K separation power(b). These results are based on a standalone Geant4 simulation for particles with a momentum of 6 GeV/c.	91
8.46	Photographs of the PANDA Barrel DIRC prototype (a), including a close-up of the readout section (b) taken during the CERN test beam. Performance plots illustrate the comparison between simulated and experimental data for photon yield (c) and single photon Cherenkov angle resolution (SPR) (d).	93
8.47	Technical drawings of the ePIC hpDIRC detector, showing the XY cross-section of the bar box (a) and the YZ cross-section of the connection between the bar box and the readout box (b).	94
8.48	ePIC hpDIRC schedule chart alignment with EIC Project schedule	97
8.49	Event displays of a single module of the hpDIRC narrow bar baseline design geometry (a) and the narrow bar with wide plate hybrid geometry (b), illustrating an example of the accumulated hit pattern from charged pions, based on the standalone hpDIRC Geant4 simulation package.	98

8.50	Performance comparison between the hpDIRC narrow bar baseline design geometry (black points) and the narrow bar with wide plate hybrid geometry (red points) in case of photon yield (a) for pions and π/K separation power(b) based on a standalone Geant4 simulation for particles with a momentum of 6 GeV/c.	98
8.51	Photos of available setups developed during the hpDIRC R&D program that will be used for future QA of 3-layer lenses with laser setup at ODU (a), bars and other optics at Jefferson Lab (b) and readout chain including sensors and electronics and other hpDIRC components in hpDIRC prototype at CRT at SBU (c).	100
8.52	(Left) dRICH detector model with highlighted the major components. (Right) dRICH inside ePIC services lines at barrel HCAL end point.	103
8.53	(Left) CAD model of the dRICH photodetector unit (PDU) module with its major components. (Right) dRICH detector box model with 208 PDUs forming a curved active surface.	104
8.54	(Left) dRICH aerogel model. (Right) dRICH mirror model [placeholder].	104
8.55	Transverse map of the expected 1-MeV equivalent neutron fluence per 1 fb ⁻¹ of integrated luminosity in e+p interactions at the maximum EIC center-of-mass energy at the location of the dRICH photodetector (210 < z < 260 cm). The average, maximum and minimum values within the region of the dRICH photodetector (100 < R < 180 cm, indicated by the dashed lines) are reported.	105
8.56	(Left) Dark current measurements on sample SiPM sensors for the studies of repeated irradiation-annealing . (Right) Projected increase of the DCR of SiPM as a function of the integrated luminosity (delivered fluence). The "no annealing" and the "annealing limit" curves show the limits of possible operations. The dashed line indicate the desired maximum DCR threshold.	106
8.57	(Left) Block diagram of ALCOR pixel. (Right) 3D model of the dRICH FEB.	109
8.58	Block diagram of the dRICH gas system [graphically, a preliminary version].	110
8.59	(Left) Contributions to the single-photon angular resolution for aerogel. (Right) Contributions to the single-photon angular resolution for radiator gas.	111
8.60	(Left) Event display. (Center) Reconstructed mass vs momentum. (Right) Pion identification efficiency and pion to kaon mis-identification probability as a function of momentum in three bins of rapidity.	111
8.61	(Left) Service routing around the dRICH. (Center) Installation tool. (Right) Maintenance position.	113
8.62	(Left) Test stand for SiPM characterization. (Center) Performance comparison between different SiPM models. (Right) Prototype version of the SiPM carrier board (top) and FEB (bottom).	114
8.63	(Left) Fraction of residual irradiation damage measured on multiple SiPM candidate samples after "forward-bias annealing" cycles at increasing temperature and integrated annealing time. The measurements are shown for individual sensors (gray points) and as averages (coloured points, uncertainty of the average and RMS are indicated on the plot). (Right) Temperature increase of the SiPM sensor with respect to the temperature of the SiPM carrier board as a function of the "forward-bias annealing" power at different temperature values of the circulating thermostat system.	115
8.64	(Left) C ₂ F ₆ measured transmittance. (Center) Aerogel large tiles assembling as obtained at BELLE-II [2]. (Right) Mirror demonstrator with an optimized dRICH core structure.	116
8.65	(Left) Baseline prototype with reference detector at the SPS-H8 beam line of CERN. (Center) First ePIC-drive detector box under test at the PS-T10 beam line of CERN. (Right) Real-scale prototype model mimicking the basic dRICH construction unit (sector).	117

8.66	(Left) Cherenkov angular resolution obtained for C_2F_6 as a function of the recorded number of photons. The SPE values is consistent with expectations. (Center) SPE angular resolution measured on aerogel as a function of the refractive index. The expected resolution is obtained for an index greater than $n=1.025$. (Right) Comparison in photon yield of sensor with different SPAD size. All the measurements are obtained with the dRICH prototype.	118
8.67	(Left) Prototype PDU and assembled detector plane. (Center) Cumulated ring imaging. (Right) dual-radiator interplay for a mixed hadron beam at 10 GeV/c. After the gas information is used to tag pions, an effective separation between kaon and proton is provided by the aerogel.	119
8.68	Construction plan	122
8.69	Transmission, absorption and scattering length curves as a function of the wavelength for the tile with $n = 1.03$	126
8.70	Transmittance as a function of the wavelength for all the tiles.	128
8.71	Transmission length as a function of the wavelength for all the tiles.	129
8.72	CAD drawing of the EEEMCAL. The small gray shapes are the scintillating crystals. The SiPM photosensor matrices are grouped over four crystals and indicated by the pink area. The green rectangles are part of the backend electronics. The dark gray rectangles and circles on the circumference are part of the cooling system.	131
8.73	Conceptual design of the ePIC electron endcap electromagnetic calorimeter support.	132
8.74	Left: waveform (top) and integrated signal (bottom) showing single photo-electron signals in Hamamatsu 15 μ m pixel SiPMs. Signals are produced with a low-intensity LED. Right: Linearity measurement, showing 2% linearity up to 3500 photo-electrons.	133
8.75	EEEMCal simulated performance using the ePIC detector framework including all materials. Left: energy resolution as a function of the incident particle energy. Right: pion rejection factor as a function of energy and different values of electron efficiency.	134
8.76	EEEMCAL integrated schedule.	134
8.77	EEEMCal installation fixtures that allow for installing the detector safely into the ePIC detector barrel.	136
8.78	Screenshot of the EEEMCal Risk Management Plan and registry.	137
8.79	Structure of Barrel Imaging Calorimeter and its sectors.	139
8.80	Components of Barrel Imaging Calorimeter imaging AstroPix layers.	140
8.81	Simulated energy resolution and sampling fraction for photons in different rapidity ranges of BIC.	142
8.82	Measured energy responses in Baby BCAL to positrons and pions	143
8.83	Simulated angular resolutions for photons at BIC	143
8.84	Simulated performance on particle identification from BIC	145
8.85	Simulated performance on MIP response in BIC	145
8.86	Example performance of AstroPix.v3 chip	146
8.87	Barrel Imaging Calorimeter high-level schedule for design and production phases.	153
8.88	Simulated energy response of photons and electrons in Pb/ScFi and energy response tail in different rapidity range of BIC	154
8.89	Simulated energy resolution and sampling fraction for electrons in different rapidity ranges of BIC.	155
8.90	Barrel Imaging Calorimeter org chart.	156
8.91	The front face of the ePIC hadron end-cap.	159
8.92	Matrix of scintillating fibers prepared to build production fEMCal blocks and SEM image of tungsten powder.	160
8.93	Front and back views of LG plates with installed SiPMs.	162
8.94	Structural and installation tests at BNL.	163

8.95	Response of calorimeter vs position in hodoscope (left panel). Energy resolution for different impact angles (right panel).	164
8.96	Signal (single photon) efficiency and background (merged di-photons) contamination for different cut value of the NN output for 60 GeV (left panel). Probability of misidentifying π^0 as a single photon vs energy (right panel)	164
8.97	fEMCal front end electronics.	166
8.98	Neutron detection efficiency vs. E and thresholds	171
8.99	Position resolution R_{xy} and cluster efficiency vs. E for different tile sizes	171
8.100	Top: Primary, generated particle E distributions in nHCal acceptance $-4.0 < \eta < -1.0$. Bottom: Primary, generated particle p distributions in nHCal acceptance $-4.0 < \eta < -1.0$	172
8.101	Top: Primary, generated particle E distributions in $-2.0 < \eta < -1.0$ range. Bottom: Primary, generated particle p distributions in $-2.0 < \eta < -1.0$ range.	173
8.102	Top: Primary, generated particle E distributions in $-3.0 < \eta < -2.0$ range. Bottom: Primary, generated particle p distributions in $-3.0 < \eta < -2.0$ range.	174
8.103	Top: Primary, generated particle E distributions in $-4.0 < \eta < -3.0$ range. Bottom: Primary, generated particle p distributions in $-4.0 < \eta < -3.0$ range.	175
8.104	Acceptance of photoproduced $J/\psi \rightarrow \mu^+\mu^-$ in $e + p$ collisions at 18 + 275 GeV. Top left: Acceptance vs. μ_1 and μ_2 hitting different HCals. Top Right: Acceptance vs. $-t$ for different number of μ in nHCal. Bottom Left: Acceptance vs. Bjorken x_{bj} for different number of μ in nHCal. Top Right: Acceptance vs. Pomeron x_p for different number of μ in nHCal.	176
8.105	Acceptance of photoproduced $J/\psi \rightarrow \mu^+\mu^-$ in $e + p$ collisions at 20 + 100 GeV. Top left: Acceptance vs. μ_1 and μ_2 hitting different HCals. Top Right: Acceptance vs. $-t$ for different number of μ in nHCal. Bottom Left: Acceptance vs. Bjorken x_{bj} for different number of μ in nHCal. Top Right: Acceptance vs. Pomeron x_p for different number of μ in nHCal.	177
8.106	Acceptance of photoproduced $\Phi \rightarrow K^+K^-$ in $e + p$ collisions at 18 + 275 GeV. Top left: Acceptance vs. K_1 and K_2 hitting different HCals. Top Right: Acceptance vs. $-t$ for different number of K in nHCal. Bottom Left: Acceptance vs. Bjorken x_{bj} for different number of K in nHCal. Top Right: Acceptance vs. Pomeron x_p for different number of K in nHCal.	178
8.107	Acceptance of photoproduced $\Phi \rightarrow K^+K^-$ in $e + p$ collisions at 20 + 100 GeV. Top left: Acceptance vs. μ_1 and μ_2 hitting different HCals. Top Right: Acceptance vs. $-t$ for different number of K in nHCal. Bottom Left: Acceptance vs. Bjorken x_{bj} for different number of K in nHCal. Top Right: Acceptance vs. Pomeron x_p for different number of K in nHCal.	179
8.108	Energy resolution of jets vs. jet energy E compared for inclusive jets(squares) and jets with neutral veto(triangles). Track only jets(blue) are also compared to track and nHCal cluster jets(red).	180
8.109	Jet charged and neutral Fractions in ECCE: The charged (black lines), neutral EM (blue lines), and neutral hadron (red lines) fractions of jets at the truth level in $\eta \in (-3.5, 1.0)$ (upper left panel), $ \eta < 1$ (upper right panel), and $\eta \in (1.0, 3.5)$ (lower left panel). This illustrates that while jets are dominated by charged and neutral EM particles, there are still a distinct population of jets at central rapidity with a substantial neutral hadronic component.	181
8.110	HCal Neutral Hadron Veto	182
8.111	Transverse cutaway view of an sPHENIX Outer HCal module, showing the tilted tapered absorber plates. Light collection and cabling is on the outer radius at the top of the drawing.	183
8.112	Scintillator tiles in a layer of the Outer HCal.	183

8.113 Leakage current in HCal measured once per fill as a function of total number of ZDC coincidence hits	185
8.114 Muon energy deposited on tile: energy deposited on a given scintillator tile (i.e. the sum of G4 hits for a tile) by single GeV/c μ^- with energies between 5 and 10 GeV/c as a function of μ^- pseudorapidity. Distributions were simulated using the 2023.06.1 simulation geometry. A clear MIP peak is observed.	186
8.115 DIS energy deposited on tile: energy deposited on a given scintillator tile (i.e. the sum of G4 hits for a tile) in 18×275 NC DIS events for $Q^2 > 1000$ GeV ² for all particles in the events as a function of their pseudorapidity. Distributions were simulated using the 2023.07.2 simulation geometry.	187
8.116 Resolution of calibrated single pion energies: Resolution of calibrated single π^- energies. Distributions were simulated using the 2023.05.0 simulation geometry. Red markers indicate the output of the calibration using tile-based clusters from the BHCAL, while blue markers indicate the output of the calibration using tower-based clusters from the BHCAL. The closed markers indicate the resolution as obtained by comparing the mean of a gaussian fit to the calibrated energies vs. the particle energies, while the open markers indicate the resolution as obtained by directory comparing the mean of the calibrated energies vs. the particle energies. Calibration is carried out by the LD model.	188
8.117 All four far-forward subsystems in the outgoing hadron beam direction. The green cylinders are accelerator dipole and quadrupole magnets.	190
8.118 Left: The B0 tracker's acceptance of protons (E=110 GeV), as a function of θ_x and θ_y . PLACEHOLDER NEEDS TO BE REMADE W/REAL B FIELD Right: The p_T resolution for protons reconstructed in the B0 tracker. PLACEHOLDER NEEDS TO BE REMADE WITH FINAL LOCATIONS, FINAL TRACKING, PROPER LABELLING ETC	192
8.119 The B0 EM calorimeter's acceptance of photons with a substantial (for now half their energy) deposit in a calorimeter crystal.	192
8.120 The energy reconstructed and associated resolution for the B0 EM calorimeter of photons with $\theta < 13$ mrad in the soft (left) and hard (right) energy reconstruction regimes.	193
8.121 Summary of transverse momentum resolutions for the Roman pots and Off-Momentum Detectors. Contributions are separated by those induced by intrinsic detector choices (e.g. pixel sizes) and those from beam effects (e.g. angular divergence), which have an outsized impact on momentum measurements at very-forward rapidity. Will be replaced with DD4HEP version	196
8.122 Strawman concept for the layout of the RP and OMD sensor staves. A 1x3 configuration is also being consider to reduce the size of the necessary Samtech connector for the staves, but more study is needed to assess impact of either choice, both in terms of construction feasibility and performance.	197
8.123 Strawman concept a readout board concept to communicate with and readout RP and OMD sensor staves. Work needs to be done to solve the issue of power distribution, and to ensure the EICROC ASIC can indeed be readout by the LpGBT. . . .	197
8.124 The layout of the luminosity monitor in the ZEUS experiment [?].	201
8.125 Relative suppression due to the BSE $(d\sigma_{corr}/dy)/(d\sigma_{BH}/dy)$ is shown as a function of $y = E_\gamma/E_e$ for three cases of collider parameters, HERA, EIC 1 & EIC 2. The corresponding beam energies and Gaussian lateral beam sizes at the interaction point are listed [?].	203
8.126 Rate of single and coincidence events for the PS detectors calculated by Dr. Gan-gadharan	205
8.127 The layout of the luminosity monitor in the ePIC experiment of the EIC.	205

8.128 Unpolarised and polarised Bethe-Heitler Cross-Section. [?]	206
8.129 DD4hep implementation of PS Calorimeters.	210
8.130 Left: Low- Q^2 taggers in relation to beamlines and central detector. Right: Tagger module with calorimeter and tracker from recent CAD model.	214
8.131 Hit rates on tracker layers for Quasi Real (Top) and bremsstrahlung (bottom) electrons, incident on Tagger 1 (left) and Tagger 2 (right), This design is based on layers with three carrier boards, each containing twelve Timepix4 hybrid sensors. The dashed lines indicated the centre lines of the Timepix4 ASICs, where the vertical columns terminate.	214
8.132 Maximum and integrated rates for Low- Q^2 trackers	237
8.133 Layout of SciFi calorimeter	237
8.134 Energy resolution for Cherenkov fiber calorimeter	238
8.135 ePIC DAQ component count summary	238
8.136 ePIC DAQ component counts	239
8.137 Expected worse case data rates contributions for the ePIC detector	240
8.138 Maximum data volume per RDO with noise estimates.	240
8.139 Schematic of the ePIC Streaming DAQ	240
8.140 Components of the ePIC Streaming DAQ System	241
8.141 ePIC Electronics and ASICs summary	241
8.142 Discrete block diagram	241
8.143 Discrete Adapter (left) and digitizer FEB PCBs	241
8.144 Discrete key specifications	242
8.145 CALOROC block diagram	242
8.146 CALOROC Key Specifications	242
8.147 EICROC block diagram	243
8.148 EICROC timing performance	244
8.149 EICROC Key Specifications	244
8.150 FCFD block diagram of the frontend	245
8.151 FCFD timing performance	245
8.152 FCFD Key Specifications	245
8.153 ALCOR Si Die (left) and block diagram	246
8.154 ALCOR Key Specifications	246
8.155 Scope of the electronics and ASICs developments	246
8.156 TOF pre-prototype RDO	247
8.157 3D model of dRICH RDO	247
8.158 Schematic layout based for the GTU	248
8.159 Physical concept for the fiber distribution for the GTU	248
8.160 Operation of firmware trigger under assumption that the trigger decision for the dRICH depends upon data from fHCAL	249
8.161 Proposed ePIC slow controls network topology	249
8.162 DAQ/Computing schedule	249
8.163 Electronics and DAQ Resources	250

List of Tables

1	Table illustrating “rules”	15
2	Short top-level parameters caption.	15
3	A parameter table made available for export, using the /Tables subdirectory	15
4	A table with fixed third column width, enabling text filling.	15
5	Two ways to squeeze tables.	16
6	A third way to squeeze tables.	16
8.1	Physics requirements on the relative momentum measurement, dp/p at the event vertex for different ranges in pseudorapidity, η , and on the determination of the radial distance of closest approach, DCA_r , of the particle trajectory to the event vertex with its dependence on tranverse momentum, p_T	30
8.2	Radius, length and material budget of the SVT IB and OB layers.	33
8.3	Position along the beam pipe, outer radius and material budget for the SVT layers in the EE and HE regions.	33
8.5	Summary of power and readout services for the different regions of the sPIC SVT. .	37
8.6	Maximum dose of radiation by different sources at MPGD tracker layers for e+p minimum-bias event at 500 kHz event rate for 10 years EIC running with 6 months run time per year and 100% efficiency [?].	50
8.7	Hit rate per unit area of various MPGD trackers for e+p DIS events at 10×275 GeV with $1.54 \times 10^{34} \text{cm}^2 \text{s}^{-1}$ luminosity scaled from e+p DIS events at 18×275 GeV and $1.54 \times 10^{33} \text{cm}^2 \text{s}^{-1}$ luminosity, 10 GeV electron beam gas and 275 GeV hadron beam gas	51
8.8	Maximum hit rate by a single channel of various MPGD trackers for e+p DIS events at 10×275 GeV with $1.54 \times 10^{34} \text{cm}^2 \text{s}^{-1}$ luminosity scaled from e+p DIS events at 18×275 GeV and $1.54 \times 10^{33} \text{cm}^2 \text{s}^{-1}$ luminosity , 10 GeV electron beam gas and 275 GeV hadron beam gas	52
8.9	Required performance for physics and proposed configurations for the TOF detector system.	57
8.10	RAW and NEQ fluence per system for the lifetime of the ePIC experiment, assuming 10 years of data taking at 50% time.	59
8.11	Summary of BTOF and FTOF low voltage and high voltage powersupply cables to distribution panels and then to the detector FEE (the exact numbers are being checked at the time of writing).	65
8.12	BTOF is designed with a barrel geometry surrounding the beam pipe and interaction point, while FTOF is a disk geometry perpendicular to the beam direction on the hadron side (positive z).	66
8.13	List of the voltage services to the dRICH electronics, indicating the number of primary power-supply channels and boards as well as the cross-section of the cables (AWG). The number of power-supply boards is defined assuming to use commercial 8-channel low-voltage boards.	111

8.14	Planned quality assurance (QA) stations, organized in order to provide redundancy and support specific characterization studies.	121
8.15	Main elements of the dRICH photodetector system with the indication of number of elements per sector and the total.	126
8.16	Baseline specifications of the SiPM sensor devices for the dRICH photodetector. All parameters are defined at room temperature ($T = 25^{\circ}\text{C}$) and at the operating voltage V_{op} , unless otherwise specified.	127
8.17	Tiles list. Tiles from 1 to 17 were produced at the High Energy Accelerator Research Organization (KEK) in Japan and delivered in March 2021 [3], except tiles 6-7 which belongs to a 2000 production manufactured by Matsushita Electric Works (Japan).	128
8.18	EEEMCAL WBS Structure	135
8.19	AstroPix requirements comparison.	139
8.20	Selected BIC Parameters.	141
8.21	Energy resolution parameters for photons in BIC for different η ranges.	141
8.22	Some requirements on performance of fEMCal and its parameters	158
8.23	Requirements and Technical specifications for fEMCal scintillating fibers.	161
8.24	Requirements and Technical specifications for fEMCal SiPMs.	163
8.25	Requirements for the FEB	165
8.26	Control and status registers on the FEB	167
8.27	Maximum expected background rates for backward HCal. The assumed threshold is 170.	170
8.28	Properties of HCal scintillating tiles.	182
8.29	Properties of Kuraray Y-11 (200) wavelength shifting fibers.	184
8.30	Design parameters for the Barrel Hadronic Calorimeter w/o additional absorber, based on the sPHENIX Outer Hadronic Calorimeter.	184
8.31	Summary of systematic uncertainties at ZEUS DPD and PS detector. [?]	206
8.32	Noise Estimates	221
8.33	SALSA specifications.	225
8.34	Types of RDO	226
8.35	DAM/RDO Decoded Synchronous Command Structure. This structure is defined to allow continuous availability of the critical beam related bits and more rare commands. The data in the 40 bits worth of flexible command data encoding remains flexible but must contain enough control bits to select what structure it has. The "type", "type specific" division is an potential holding this flexibility	229
8.36	RDO downlink words	229
8.37	DAQ Computing Resources	230
8.38	Slow Controls data volume and network traffic	233

multi-chapters

Chapter 0

Style Guide

The following is the Style guide as developed for the full design report. This is the guide the accelerator team is following and it will make merging the documents together much easier if everyone uses this guide.

0.1 Chapter Abstract

Summary: Each chapter begins with a stand-alone single “punch line” page that serves as a chapter abstract. Rather than simply duplicating the Table of Contents outline of the subject matter of the chapter, a well-constructed abstract will lay out the key ideas and conclusions that chapter editors wish to convey to readers. The Executive Summary will also describe these key ideas, in a modestly longer form (perhaps $\sim 250 - 1000$ words per chapter). This sample **non-EIC** chapter abstract emphasizes key ideas such as the separation of pre-existing and new subsystems, and the level of technical risk.

The Cryogenic System consists of the cryoplant that provides cooling for cryomodules; the test and instruments cryoplant that provides cooling for test stands and liquid helium for instruments; cryoplant that provides 16 K helium cooling for the target hydrogen moderators, and the distribution system that connects the linac cryoplant to cryomodules. The linac cryoplant and test/instrument cryoplant share common gas management and storage systems. The target cryoplant system is completely separate due to potential for tritium contamination.

The Vacuum System provides vacuum for the linac beam line, target system and instrument lines. It uses well established technology and procedures based on experience at similar facilities, including RHIC, Tevatron, and LHC. It has low technical risk.

Test Stands provide testing and validation of both RF equipment (klystrons and modulators) and cryomodules. Cryogenic connection to cryomodules in the test stands will prototype similar connections in the linac tunnel. The test stand program accommodates the unavoidable uncertainty in EIC construction schedule by allowing for RF equipment testing in a temporary location if necessary. Cryomodule testing will be carried out at the EIC site. All cryomodules will be tested at nominal temperatures and RF power levels before tunnel installation.

29 0.2 Wordsmithing

30 0.2.1 Passive voice

31 Authors should avoid the passive voice as much as possible – as in this sentence. This rule is
 32 sometimes made to be broken – as in this sentence :). The crucial point is that authors should not
 33 use passive voice to avoid identifying the specific individual or group of individuals within the EIC
 34 organization which is/are (or will be) responsible for fulfilling some specific function. It’s not good
 35 enough to say, “Quality management will be implemented”. The purpose of the Design Report is
 36 to explain for EIC itself, and for readers outside of EIC, who will implement quality management,
 37 and how they will do it. Excessive use of passive voice is not just bad writing. It communicates
 38 confusion or uncertainty about the path from aspiration to reality.

39 0.2.2 Verb tenses

40 The simplest way to make everything consistent is to apply a general rule:

41 Use past tense for things that happened in the past, present tense for things that are
 42 happening now, and future tense for things that will happen in the future.

43 If the designs call for something to happen, they call for it in the present tense. But it will happen
 44 in the future tense. Avoid inconsistent usage across chapters, across authors, and even within the
 45 same paragraph by a single author.

46 0.2.3 Apostrophes

47 Decades are written as in the 1960s and 1970s, NOT as in the 1980’s or 1990’s.

48 0.2.4 Capitalization and names

49 0.2.4.1 Pieces of EIC

50 For example, linac, accelerator, target station, test stand. For the sake of consistency these terms
 51 will not be capitalized.

52 0.2.4.2 Internal phrases

53 Correct capitalization for specific “internal” EIC phrases and names will be accumulated here. For
 54 example:

55 Pre-construction Phase NOT Pre-Construction phase
 56 Decommissioning Phase NOT De-commissioning phase
 57 Work Packages NOT Work-packages
 58

59 **0.2.4.3 Discipline-specific approaches or “guiding principles” or buzz phrases**

60 Such as design integration, systems engineering, defense in depth. Recommend capitalizing none
61 of them, but the important thing is to be consistent.

62 **0.2.4.4 Formal group names**

63 When authors identify the parts of the EIC organization who will be responsible for doing some-
64 thing, then capitalize the formal names of that groups from the org chart. Recommend avoiding
65 informal terms such as “test stand personnel”, where possible.

66 **0.2.4.5 Headings**

67 The titles of sections and subsections should have only the first letter capitalized.

68 **0.2.5 Captions**

69 Write Figure and Table captions in a self-contained way, to carry a complete self-contained descrip-
70 tion of the figure. Define symbology in all figures, either in the text or (preferably) in the caption.
71 Captions always end with a period. Use the format:

```
72 \caption[Short caption for List of Tables or Figures.]{Long caption to carry a complete  
73 self-contained description of the figure or table, in the chapter text.}
```

74 **0.2.6 Spelling**

75 The Design Report follows American spelling rules. For example, with “z” not “s”, and “program”
76 not “programme”:

```
77     emphasize not emphasise  
78     meter not metre  
79
```

80 **0.2.6.1 Exceptions to U.S. spelling**

81 1. (None so far).

82 **0.2.6.2 Capitalization**

83 The words “Figure”, “Table”, “Chapter” and “Section” should always be capitalized in the text if
84 they occur with a number. For example, Figure 3.8 occurs in Chapter 3 and Table 5.5 is in Section
85 5.1.3, but there are many other figures and tables in other section, subsections and chapters.

0.2.7 Commas

The incorrect placement of a comma can change the meaning of a sentence. For example, compare “Let’s eat Mom” and “Let’s eat, Mom”. And compare “Scientists, who conduct important research, are well respected in the community” with “Scientists who conduct important research are well respected in the community”.

Commas go where there is a natural pause in a long sentence, where additional information has been added to a sentence and where, if removed, the sentence would still make sense. They are used when listing items – between each item on the list. They are used where two shorter sentences are made into one (usually with the addition of “and”), but still consist of two separate parts. And they are used after “lead” words [however, therefore, consequently, in fact].

0.2.7.1 Commas in numbers

Write 2.4 million and not 2,4 million (as in some parts of Europe).

No commas in numbers below 10,000 – thus, write 1240 and 9999, but 12,400 and 99,999.

0.2.8 Plurals and possessives

For example, use

WPs not WP’s (plural)
EIC’s not EIC’ (possessive)

0.2.9 Abbreviations

0.2.9.1 Textual treatment of Figures and Tables

The words “Figure” and “Table” should always be capitalized in the text. Include a reference or discussion of all Tables and Figures in the main text of the chapter. For example, “Figure 3.8 shows thus-and-such”. The abbreviations Fig. and Tab. should not be used.

0.2.9.2 Radio frequency

The phrase “radio frequency” is always two words and is never hyphenated or capitalized, whether used as an adjective or as a noun. Thus, the two radio frequencies used in the radio frequency system are 352.21 MHz and 704.42 MHz. The upper case abbreviation “RF” is acceptable in many circumstances.

0.2.9.3 etc., et cetera

It is acceptable to use “e.g.” within parentheses, but not outside. For example, Jack and Jill met many animals (e.g. Reynard the Fox) when going down the hill. It is also correct to say that Jack and Jill met many animals, for example Reynard the Fox, but no tortoise. Similar rules apply for “i.e.”.

The periods (i.e. the full stops) should not be dropped, for example “ie” or “eg”.

It is incorrect to use ok, o.k., or okay.

The following are acceptable:

e.g.

etc.

i.e.

RF (in many circumstances)

0.2.10 Hyphenation of multi-word adjectival phrases

In general, hyphenate an adjectival phrase where the second part is a past (-ed) or present (-ing) participle of a verb. Consider the following illustrative (nonsensical) paragraph:

This chapter describes the *beam physics design* of the *neutron-generating* spallation target. Following a brief overview, the chapter presents a detailed description of the *beam physics* of EIC, which drive the accelerator design. The accelerator consists of several sections: the ion source, *normal-conducting* linac, *superconducting* linac and *beam transport* sections. The chapter also describes the *radio frequency* system.

Simplified advice available online includes: “When two or more words are combined to form a modifier immediately preceding a noun, join the words by hyphens if doing so will significantly aid the reader in recognizing the compound adjective.” Not so simple are phrases like “high-power proton beam” where “proton beam” itself is a single idea. Some judgement is involved

For the sake of consistency, the editors have created and are expanding a spreadsheet of words and phrases specifying hyphenation policy for the Design Repoprt. Here are somewhat-arbitrary rules for whether or not to hyphenate some common multi-word phrases, *when they are used as an adjective, a noun, or as a verb*. Alphabetically:

1D, 2D, 3D, 4D

accelerator-driven

back up (verb)

back-flow (noun adj)

backscattering

backup (adj noun)

baseline (adj or noun)

beam dynamics

beam guide

beam instrumentation

153	beam physics
154	beampipe
155	beam port
156	beam time
157	beam transport
158	beamline
159	bispectral
160	bottom-up approach
161	broadband
162	by-product
163	clamshell clamshell-style
164	clean room
165	cold box
166	co-chair (noun)
167	contact-less
168	cool-down (noun or adj)
169	coordinate
170	cost-saving
171	cross reference (noun)
172	cross-reference (verb)
173	cross section
174	cryo-building
175	cryo-pump
176	cryo-system
177	cryomodule
178	cryoplant
179	debunched
180	decision making (noun)
181	decommissioning
182	de-excitation
183	deionised
184	down-mix
185	downtime
186	eigenmode (noun adj)
187	equipartitioning
188	failover
189	failsafe
190	feed box
191	feedthrough
192	follow up (verb)
193	follow-up (adj and noun)
194	hands-on (adj)
195	high level
196	high- β
197	high-current (adj)
198	high-power
199	high-resolution
200	hot cell
201	<i>in situ</i> (italicize)
202	innermost
203	inrush

204	interdependency
205	interlayer
206	intra-layer
207	intra-nuclear
208	Joule-Thomson valve
209	layout (noun)
210	life-cycle (noun)
211	line-of-sight
212	long-pulse
213	lookup
214	Lorentz detuning (noun)
215	Lorentz-detuning (adj)
216	low-resolution
217	magnetoresistance
218	medium- β
219	metadata
220	micropattern
221	microphonics
222	midpoint
223	middleware
224	multi-component
225	multi-layer
226	multi-pacting
227	multi-particle
228	multi-resistant
229	nanoparticle
230	nano-sized
231	nanostucture
232	neutron-generating
233	noninvasive (seen both ways in different dictionaries)
234	normal-conducting
235	on-board
236	ongoing
237	on-site (adj)
238	outermost
239	outgassing
240	overarching
241	phase space (noun)
242	phase-space (adj)
243	pinpoint
244	plug-in
245	post mortem (noun or adj)
246	pre-cools
247	premoderator
248	prequalification
249	radio frequency
250	radionuclide
251	radiotoxic
252	ramp up (verb)
253	ramp-up (noun)
254	read-back

255	ready-made
256	requalification
257	roadmap
258	safety-critical
259	short-pulse
260	short-term
261	shut off (noun verb)
262	shut-off (adj)
263	space charge (noun)
264	space-charge (adj)
265	staff-based
266	start-up
267	state-of-the-art
268	storm water
269	stripline
270	sub-atmospheric
271	subcomponent
272	sub-cool
273	sub-millimeter
274	sub-second
275	superconducting
276	switchyard
277	systemwide
278	thermo-mechanical
279	thermo-plastic
280	thermo-responsive
281	thermosyphon
282	time-frame
283	time scale
284	time-saving
285	time-stamp (noun and verb)
286	timeline
287	timesaving (adj and noun)
288	tool-set
289	top level
290	trade-off
291	tunable
292	tune up (verb)
293	tune-up (adj and noun)
294	twofold
295	uniaxial
296	uninterruptible
297	un-irradiated
298	up-mix
299	uptime
300	von Mises
301	waste water (noun)
302	waveguide
303	work flow (noun)
304	work-flow (adj)
305	workspace

world-leading
 X-ray (upper case X)
 zigzag (noun or adj)

0.2.11 Double letters

In UK spelling, both “focussing” and “focusing” are considered to be correct. In the Design Report we use single “s” spelling in all cases.

Note the ‘double “l” rule for UK English – label becomes labelled, travel becomes travelled, et cetera. Not so with U.S. English in the Design Report.

0.2.12 Mathematical symbols, subscripts and superscripts

Mathematical symbols are written in math-mode, even when they are embedded in text. For example, a longitudinal dimension L is often called a length. Descriptive subscripts and superscripts, as in L_{acc} or $L^{overhead}$, are not written in Roman font. They appear to be italics, no matter how long or short they are.

0.2.13 Quotation marks

L^AT_EX is fussy about some things, like quotation marks. Sooner or later an author, a chapter editor, or a general editor must pay attention. This the correct way to put “a certain piece of text” inside quotation marks. The following “certain piece of text” is incorrect.

0.2.14 Citations, references and the bibliography

Please use inspire hep bibtex entries and notation whenever possible.

Don’t use a “pointer” (for example [4]) in place of naming a reference [4]. That is, use “Joe Blow [4] describes thus and such,” NOT, “[4] describes thus and such”. There should be a space in the text before the citation, so “Joe Blow[4]” is wrong. Multiple citations should be placed with the same square brackets. In the L^AT_EX vernacular, use Joe Blow~\cite{Blow2011} or Joe Blow~\cite{Blow2011,Smith2012}.

We are using bibtex to handle the references, which are gathered into one bib file per chapter, although all references appear in a single bibliography at the end of the Design Report.

During the editing process we are (currently by default) using the L^AT_EX package showkeys, which flags references (to Tables, Figures, sections and subsections) and citations (to references) above the text, or in the margin. This should aid in generating cross-references, for example, even though it is rather ugly. It will be turned off in the final stages of editing, before printing. (Comments and feedback, please!)

0.2.15 Miscellaneous

0.2.15.1 “Calculations show that ...”

This usage, with no indication who carried out the calculations, provides no way for a reader to check the work, or to build upon it in the future. Citations of internal documents, or of individuals to contact to get more information would be helpful for readers, and would also convey a greater sense of credibility. For example, “Relativistic Heavy Ion Collider (2021), unpublished calculations by members of the XYZ working group. Contact Sven Larsson (sven.larsson@bnl.gov) for details.”

0.2.15.2 “Should”, “must”, and reference to future studies

In general, authors should convey the conviction that EIC will do what it should do. In those cases where there is an ongoing internal debate, the Design Report should convey the sense that such debates will be resolved on the basis of a reasoned and careful assessment of the evidence. Only write about future studies in those limited cases where it is needed to show “that we know what we are doing”.

0.2.15.3 “Enable”

Incorrect usage:

“Neutrons pass easily through most materials, enabling the study of large or bulk samples and buried interfaces.”

Correct usage:

“In addition, as the BLM system will be a major tool for beam tune-up, it should also be designed in a way that enables it to pin-point the loss location as precisely as possible.”

The point is that the direct object of enable is made capable of doing something – roughly a synonym for empower. You enable the direct object to do something (enable it to pin-point ...). You could rewrite the first sentence to say, “enabling the study of large or bulk samples ... to take place.” Then it would be correct – although more unwieldy than just saying “making possible the study of ...”

0.2.15.4 Reporting technical results without a clear statement of their import

In general, it is a mistake to assume that “the numbers speak for themselves”. Using words to summarize the meaning of results helps readers to understand them; it also signals that the authors understand the implications of the results they report.

0.2.15.5 Excessive and inconsistent use of lists

Sometimes the use of lists is appropriate, but often there are too many in a draft. Authors should rework most lists into narrative form. For the remaining lists, authors should follow editorial guide-

lines to ensure consistent style across the entire Design Report.

After minimizing the number of lists, Design Report editors will convert most of the remaining lists to enumerated lists. The first letter of each item will be upper case, even when the items in the list are not formulated as complete sentences. Items will generally end with a semi-colon unless the phrases are very short, in which case a comma will be used. The last item in the list will be followed by a period. In those cases in which each item in a list consists of multiple sentences, items will be ended with a period.

0.2.15.6 Cross-references

Should be added throughout the whole Design Report, but only down to \subsection level, so that cross-references can be found and numbered in the Table of Contents. This implies that subsections should be reasonably balanced in length – not too many pages long.

0.2.15.7 Isotopes

Write ^3He , for example, not 3He or He-3.

0.2.15.8 *** asterisks in comments

Sometimes a comment is inserted in a sentence, perhaps indicating that something needs to happen later, such as add a value, a citation, or more text. In this case please include (at least) 3 asterisks in a row *** so that text searches (for example `grep *** *.f`) are made easier. ALSO CONSIDER WRITING IN UPPER CASE***.

0.3 Dimensions and units

Systeme Internationale (SI) units will be used wherever possible. For example, use MPa instead of bar. Some exceptions are inevitable, for example Kilpatrick units. Unusual units should be briefly explained, on their first introduction.

When in doubt, the siunitx package does the Right Thing, for example using:

- `\si{\units}` lower case si
- `\SI{numbers}{\units}` upper case SI

A longitudinal dimension – or length – L should be written in one of these ways:

- $L = 100 \text{ m}$ $\$L = 100\$~\text{m}$
- $L = 100 \text{ }\mu\text{m}$ $\$L = 100\$~\text{\si{\micro\metre}}$
- $L = 100 \text{ km}$ $\$L = \$ \text{\SI{100}{km}}$
- $L = 10^2 \text{ km}$ $\$L = \$ \text{\SI{e2}{km}}$

so that the dimension (“m” or “μm” or “km”) is not in italics, and is separated from the numerical value by a non-breakable space – for example “~” in L^AT_EX vernacular. Do not write $L = 100\text{m}$, $100m$ or $100\ m$. Note that text and mathematical equals signs are different in length (= and =): always use the latter.

Powers of ten are written in one of these ways:

- 3.14×10^{39} `3.14×10^{39}`
- 3.14×10^{39} `\SI{3.14e39}{}`

Complex dimensions may be written in one of these ways:

- $F = 42\text{ J cm}^{-2}\text{ s}^{-1}$ `$F = 42$~J cm$^{-2}$ s$^{-1}$`
- $F = 42\text{ J cm}^{-2}\text{ s}^{-1}$ `$F=$ \SI{42}{J.cm^{-2}.s^{-1}}`

Exceptionally, percentages are written without a space – 42% is correct but 42 % is not. In L^AT_EX vernacular a % sign is the beginning of a comment, so it is necessary to say \% ...

Temperatures are written as 273 K or 100°C or 101°C, without a space between the number and the °C unit symbol.

Angles are preferably written $\theta = 7.5$ degrees, although 7.5° is acceptable.

0.4 Numbering – chapters, sections, and subsections

In the `\documentclass{report}` style, a “section” (such as this, with the numeric label 0.4) has two numbers associated with it.

0.4.1 This is the heading of a subsection

A “subsection” (like this, 0.4.1) is labelled by 3 numbers, namely “chapter_number.section_number.subsection_number”. Sections and subsections begin with a bold face font.

0.4.1.1 A subsubsection heading like this has no period at the end

In bold font, it has no numerical label, and sits separately from the text that immediately follows, even if there is no white space between `\subsubsection{}` and the first word of the text. It does not appear in the Table of Contents.

This paragraph heading ends with a period. Subsequent text remains in the same paragraph. The editors will use their judgement to prevent the excessive use of paragraph headings and boldface text.

0.4.2 More formatting rules and standards

0.4.2.1 Clearpages and Pagebreaks

As a rule there is NO `\clearpage` or `\pagebreak` before a new section (or subsection), and hence no white space.

0.5 Equations, Tables, Figures, and plots

0.5.1 Equations

Start with a simple equation, like Equation 1:

$$H = \frac{\sqrt{3 \langle x^4 \rangle \langle x'^4 \rangle + 9 \langle x^2 x'^2 \rangle^2 - 12 \langle x x'^3 \rangle \langle x^3 x' \rangle}}{2 \langle x^2 \rangle \langle x'^2 \rangle - 2 \langle x x' \rangle^2} \quad (1)$$

Avoid ending a sentence with an equation, in order to avoid deciding whether or not to put a period after the equation.

Here is a simple equation array:

$$\begin{aligned} M_{virg}(\sigma) &= M_{virg0} + k_{virg} \cdot \sigma \\ M_{rel}(\sigma) &= M_{rel0} + k_{rel} \cdot \sigma \end{aligned} \quad (2)$$

0.5.2 Tables

- Table 1 is a relatively complicated multi-column table, while Table 2 is a standard 3-column parameter table.
- Table 3 shows how to make a table exportable, for example to the Parameter Tables appendix.
- The source text for Table 4 shows how to enable text filling in columns.
- Table 5 shows 2 ways to squeeze tables, with the `\scalebox{}` and `` commands.
- Table 6 shows a third way, using `\tabcolsep{}`.

The vertical spacing of Table rows is set in “preamble.tex” by the line `\renewcommand{\arraystretch}{1.0}`.

0.5.3 Converting between LaTeX and Excel table formats

More than one free utility enables table conversion with a drag-and-drop interface. E.g.:

Excel to LaTeX try <https://tableconvert.com/excel-to-latex>

LaTeX to Excel try <https://tableconvert.com/latex-to-excel>

Facility	Location	Status	First oper.	Power [MW]	Instruments	Integrated flux [10^{14}cm^{-2}]	Peak flux [$10^{15}\text{cm}^{-2}\text{s}^{-1}$]
ESS	Lund	Pre-constr.	2019	5	22	–	40
J-PARC	Tokai	Re-furbish	2009			–	

Table 1: A standard Table looks like this, using “toprule”, “midrule” and “bottomrule” separation lines.

Parameter	Unit	Value
Energy	GeV	2.5
Current	mA	50
Pulse length	ms	2.86
Pulse repetition frequency	Hz	14
Average power	MW	5
Peak power	MW	125

Table 2: Long version of caption for top-level parameters.

Parameter	Unit	Value
Energy	GeV	2.5

Table 3: A parameter table made available for export, for example to Appendix E “Parameter Tables”, using input from a /Tables subdirectory file.

System	Subsystem	Test
Target	Shaft and drive	Run at up to 25 Hz.
	Target segments	Leak test at pressure.
	Target Safety System	Demonstrate trip signals generated for all defined cases.
Primary helium loop	Pump, heat exchanger, filter	Pressure and flow tests without target.
	Full loop with target	Full operational test without heat.

Table 4: A table with fixed third column width, enabling text filling.

Nuclide	Decay time [years]						
	0	6	40	100	1000	10 ⁴	10 ⁵
³ H	0.9	83.4	96.4	72	0	0	0
¹⁴ C	0	0	0	0	0.3	0.6	0
³⁶ Cl	0	0	0	0	0	0	0.7
³⁹ Ar	0	0	0	0.1	0.7	0	0
¹⁵⁴ Dy	0	0	0	0	0	0.2	4.3
¹⁶³ Ho	0	0	0	0.7	29.7	53.4	0

Table 5: Two ways to squeeze tables, with the “scalebox” and “phantom” commands.

Nuclide	Decay time [years]						
	0	6	40	100	1000	10 ⁴	10 ⁵
¹³⁷ La	0	0	0	0	1.4	8.7	57.6
¹⁴⁸ Gd	0	0.2	0.9	11.6	0.1	0	0
¹⁵⁰ Gd	0	0	0	0	0	0.3	5.6
¹⁵⁴ Dy	0	0	0	0	0	0.2	4.3
¹⁵⁷ Tb	0	0.1	0.6	9.3	7.2	0	0
¹⁵⁴ Dy	0	0	0	0	0	0.2	4.3
¹⁶³ Ho	0	0	0	0.7	29.7	53.4	0

Table 6: A third way to squeeze tables, with the “tabcolsep”.

0.5.4 Figures

Many figures, like Figure 1, are non-graphical images – perhaps a photograph, drawing or sketch.



Figure 1: This is an example of a non-graphical figure. We need to address the means by which we can give “all” graphs the same look and feel.

0.5.5 Plots

It is clear that for the ePIC detector sections we will mostly be using ROOT and Python, while the accelerator team most likely will be using a different package; so as soon as a figure style is agreed on, we will need to make style packages for ROOT and Python so all figures in the manuscript look stylistically the same.

As teams develop initial plots, please be sure to each the codes available so that they can be remade in a common style.

0.6 Italics and bold face type

In general, restrain the use of *italics* and **bold face**.

Long quotations will be set in italics. Italics will also be used (sparingly) for traditional purposes of emphasis (e.g. “when she was good, she was *very* good.”)

Occasionally, authors wish to draw attention to the subject matter being addressed in a block of text. Usually, this should be done by headings and subheadings. In those limited instances in which use of altered type face is appropriate within the body text, the editors will use bold face, rather than italics. One such situation is for short introductory phrases at the beginning of paragraph-long items in an enumerated list.

0.7 Issues that this Style Guide does not yet address

This Style Guide addresses “consistency of style” issues. Here is a numerical list of issues that could or should be significantly expanded:

1. the use of pronouns
2. specialized terminology
3. acronyms
4. the use of italics
5. the use of digits (e.g. 1) where written numbers are more appropriate
6. the overuse of capital letters (Boron vs. boron, User vs. user, etc.).
7. balancing the length of sections and subsections
8. global glossary
9. Lists
10. Plots (see placeholder 0.5.5)

483 **Chapter 2**

484 **Physics Goals and Requirements**

485 I

486 **2.1 EIC Context and History**

487 Add the EIC context and history here.

488 **2.2 The Science Goals of the EIC and the Machine Parameters.**

489 Add the science goals of the EIC and the machine parameters here.

490 **2.3 Scientific Requirements**

491 **2.3.1 Systematic Uncertainties**

492 Add text here.

493 **2.3.2 Radiative Corrections**

494 Add text here.

495 **2.4 The EIC Science (ePIC performance for key observables)**

496 **2.4.1 Origin of Nucleon Mass**

497 Add text here.

2.4.2 Origin of Nucleon Spin

Add text here.

2.4.3 Multi-Dimensional Imaging of the Nucleon

2.4.3.1 Imaging in Momentum Space

Add text here.

2.4.3.2 Imaging in Transverse Position Space

Add text here.

2.4.4 Properties of Nuclear Matter

2.4.4.1 Gluon Saturation

Add text here.

2.4.4.2 Nuclear Modifications of Parton Distribution Functions

Add text here.

2.4.4.3 Passage of Color Charge Through Cold QCD Matter

Add text here.

Chapter 8

Experimental Systems

8.1 Experimental Equipment Requirements Summary

The YR table (Fig. 8.1) is being reviewed and an updated table with accompanying text will be included in the draft Version1.

Table 10.6: This matrix summarizes the high level requirements for the detector performance. The interactive version of this matrix can be obtained through the Yellow Report Physics Working Group WIKI page (https://wiki.bnl.gov/eicug/index.php/Yellow_Report_Physics_Common).

Positron	Nomenclature	Resolution	Allowed	Tracking	Electrons and Photons	n/p/p	RCAL	Muons				
6.9 to 5.8	low-Q2 tagger	$\sigma_{\theta} < 1.5^\circ$; 10^{-6} $< Q^2 < 10^{-2}$ GeV ²		minimum pT	SI Vertex	Resolution σ_{θ}/E	min E	p-range	Separate	Resolution σ_{θ}/E	Energy	
5.0 to 4.5				300 MeV pions								
4.5 to 4.0		Instrumentation to separate charged particles from photons			300 MeV pions		25% \sqrt{E} (+1-3%)	50 MeV				
4.0 to 3.5	↓ p/A Auxiliary Det						50 MeV			~50% \sqrt{E} + 6%		
3.5 to 3.0							50 MeV					
3.0 to 2.5	Central Detector	opT/pT ~ 0.1% @ 0.5%	~5% or less X	<500 MeV pions, 135 MeV kaons	$\sigma_{xy} \sim 30 \mu\text{m}$ +40 μm	If suppression up to 1:1E 4	50 MeV	≤ 7 GeV/c	≥ 3 σ	~45% \sqrt{E} + 6%	~500 MeV	muons useful for tag, improve resolution
2.5 to 2.0		opT/pT			$\sigma_{xy} \sim 30 \mu\text{m}$ +20 μm		50 MeV					
2.0 to 1.5		opT/pT			$\sigma_{xy} \sim 30 \mu\text{m}$ +20 μm		50 MeV					
1.5 to 1.0		0.05% @ 0.5%			$\sigma_{xy} \sim 20 \mu\text{m}$, $\phi(0) \sim \phi(0)$ ~20 pT @ 0.5% $\mu\text{m} \pm 1 \mu\text{m}$		50 MeV					
1.0 to 0.5		opT/pT			$\sigma_{xy} \sim 30 \mu\text{m}$ +20 μm		50 MeV					
0.5 to 0.0		~0.05% pT + 0.5%					50 MeV					
0.0 to 0.5							50 MeV					
0.5 to 1.0							50 MeV					
1.0 to 1.5							50 MeV					
1.5 to 2.0							50 MeV					
2.0 to 2.5			50 MeV									
2.5 to 3.0		opT/pT ~ 0.1% pT + 2.0%			$\sigma_{xy} \sim 30 \mu\text{m}$ +40 μm	(10-12)% \sqrt{E} (+1-3%)	50 MeV	≤ 30 GeV/c		35% \sqrt{E}		
3.0 to 3.5					$\sigma_{xy} \sim 30 \mu\text{m}$ +60 μm		50 MeV					
3.5 to 4.0	Instrumentation to separate charged particles from photons	Tracking capabilities are desirable for forward tagging					50 MeV					
4.0 to 4.5	↑ e Auxiliary Detectors						50 MeV			30% \sqrt{E} (goal)		
4.5 to 5.0	Neutron Detection			300 MeV pions		4.0% \sqrt{E} for photon energy > 20 GeV	< 3 cm granularity	50 MeV		< 50% \sqrt{E} (acceptable), 30% \sqrt{E} (goal)		
> 6.2	Proton Spectrometer	intrinsic RVE < 1%; Acceptance: $0.2 < p_T < 1.2$ GeV/c										

Figure 8.1: Table presenting the Experimental Equipment Requirements Summary in the YR. At present, the table is not updated and it is here as a mere space holder.

8.2 General Detector Considerations and Operations Challenges

8.2.1 General Design Considerations

This section will discuss the detector challenges with cross-reference to the appropriate sections. The Sec.s to refer to are related to machine parameters (not in chapter 8), 8.1 “Experimental Equipment requirement Summary”, 8.2.2 “Background and Rates” and 8.2.3 “Radiation Level”. At present, all these sections are not available. Therefore, for Version0, a mere list of topics that will be covered is provided.

Discussion of challenges related to:

- Physics requirements (ref. to Sec. 8.1);
- Beams rates, polarization, luminosities (ref. to Sec.s in the machine chapters);
- Integration with the machine and hermeticity (ref. to Sec.s in the machine chapters, ref. to Sec. 8.1);
- Rates and multiplicity (ref. to Sec.c in the machine chapters, to Sec. 8.2.2);
- Radiation hardness (Ref. to Sec. 8.2.3).

8.2.2 Backgrounds and Rates

Add text here.

8.2.3 Radiation Level

Add text here.

8.3 The ePIC Detector

8.3.1 Introduction

The Context The development of the EIC science and the experimental equipment required to successfully implement the science as documented in the NSAC and NAS reports has been driven by an international EIC community, formalized in 2016 in the EIC User Group [5], at present (September 2024) formed by more than 1500 members from almost 300 institutions and 40 countries. Several conceptual general-purpose detectors had been elaborated. A next step effort was required by the EIC project approval with the signature of CD0 in December 2019. The User Group engaged in advancing the state of documented physics studies, which dictate the detector requirements, and consolidate the general-purpose detector concept matching these requirements. This effort resulted in the EIC Yellow Report completed in early 2021 and then published in Nuclear Physics A [6]. This document guided the two proposals for a general-purpose detector elaborated in 2021, which resulted in further progress in the conceptual detector design. In 2022, a merging process of the communities presenting the two proposals and of the two conceptual approaches

resulted in the formation of the ePIC Collaboration [7] (July 2022) and in baselining of the ePIC detector as EIC project detector. At present (September 2024), ePIC has more than 850 members from 177 Institutions and 25 countries, confirming the international vocation of the community pursuing the EIC science and detector.

The Detector THIS DETECTOR DESCRIPTION IS AN INTRODUCTION TO THE WHOLE SECTION 8.3. IT WILL BE REVISED WHEN THE SUBSYSTEM MATERIAL IS UPLOADED TO ENSURE A BETTER CONSISTENCY OF THE SECTION 8.3.

The detector challenges and the technologies matching these challenges are discussed in Sec. 8.2.1. The resulting design of the ePIC detector consists in a Central Detector (CD) surrounding the Interaction Point 6 (IP6) making optimal use of the space available at the Interaction Region (IR) complemented by equipment situated along the outgoing beam lines, the Far Detectors (FD), which complete the phase-space coverage.

Figure 8.2 illustrates the CD kinematic coverage; Fig. 8.3 presents a schematic overview of the CD structure. The overall CD length is imposed by the constrain of the IR design. The asymmetric beam energies reflect in an asymmetric design of the detector and, together with the requirements from physics, imposes the choice of the different detector technologies that have been adopted. The setup is designed around the solenoid providing the magnetic field for the momentum analysis. The adoption of a solenoid shapes the CD in a barrel region where the subsystem have pseudo-cylindrical layouts and two endcap regions, the forward one equipping the region around the outgoing ion beam and the backward endcap around the outgoing electron beam. The barrel subsystems cover, approximately, the pseudorapidity η region $(-1.5, 1.5)$, while the endcaps equip the regions up to pseudorapidity $|3.5 - 4.0|$, the upper bound being dictated by the beampipe layout. The separation in barrel and endcap region is not rigid with exceptions where the optimization of the detector design suggests it. For instance, the most inner layers of the tracking system have acceptance well beyond $\eta < |1.5|$, the barrel Cherenkov PID counter and the barrel electromagnetic calorimeter extends in the backward endcap.

The CD subsystems have a layered structure, from inside to outside: tracking subsystems, particle identification devices, electromagnetic calorimeters, solenoid coils in the barrel, and hadronic calorimeters.

The reference operation condition of the new **MARCO magnet** (Sec. 8.3.2), specifically designed for ePIC, is with 1.7 T field intensity and it can provide up to 2 T. It has good homogeneity in the central region and provides projective field lines in the forward endcap to match the requirements posed by the usage of a gaseous radiator in the forward RICH. The solenoid axis coincides with the electron beam line in the IR to limit the synchrotron radiation from the beam electrons. This results in helicoidal trajectories of the beam ions, due to the crossing angle of the two beams.

The **tracking system** (Sec. 8.3.3) is the most inner subsystem in order to ensure the minimum distortion of the trajectories by the material crossed by the particles. It consists of pseudo cylindrical layers completed by discs in the endcaps. The low material budget (Fig. 8.4) is guaranteed by the selected tracker technologies, with the thin ITS3 MAPS, even in support-less arrangement in the most inner layers, and MPGDs for the most external layers. The two tracker technologies support each other thanks to key complementary characteristics. MAPS sensors offer extremely fine space resolution, but poor timing information in the order of a few microsecond range. In-time hits can be selected combining MAPS information with the measurements in the MPGDs, which have time resolution of 10-20 ns. Further space and time information will be provided by the time-of-flight layers in the barrel and the forward endcap and by the first layer of the barrel imaging electromagnetic calorimeter equipped with AstroPix MAPS sensors. The minimization of the material budget

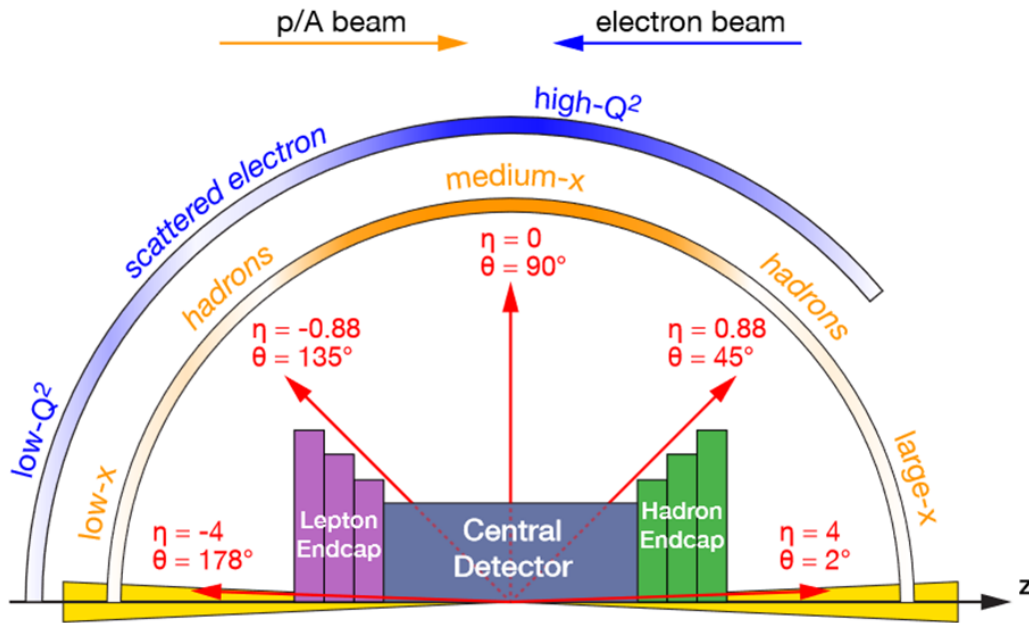


Figure 8.2: A schematic showing how hadrons and the scattered electron for different $x - Q^2$ are distributed over the detector rapidity coverage. THIS FIGURES IS A PLACE HOLDER: IT IS FROM YR AND REQUIRES REVISION.

is one of the ingredients allowing fine resolution for momentum determination and vertex reconstruction. To this end, fine intrinsic resolution is requested for the trackers and it is provided by the ITS3 MAPS. The momentum resolution is affected by the available lever arm and the solenoidal configuration of the magnetic field, the latter having its largest impact on the very forward and backward trajectories.

The tracking information is also a key ingredient for the performance of the Cherenkov imaging devices; in particular, very fine resolution of the particle direction is needed for the barrel DIRC. The most external tracker layers in the barrel, positioned in front of the DIRC, further support this requirement.

The **particle identification subsystems** (Sec. 8.3.4) surround the tracking systems. Their mission is twofold: (i) supporting the electromagnetic calorimeters by complementing the pion/electron separation to ensure the high purity of the electron sample; (ii) identifying hadrons, as needed by a large fraction of the physics program. The coverage of the wide kinematic domain imposes the adoption of a variety of technologies with time-of-flight measurements complementing Cherenkov imaging devices. Time-of-flight dedicated layers by AC-LGADs are present in the barrel and in the forward endcap, the barrel layer being by strip sensor elements to reduce the material budget, while the forward endcap layer is by pixelized AC-LGADs. In the backward endcap, the fine time-resolution provided by the photosensors of the Cherenov counter, which are sitting in the endcap acceptance, provide timing information via the Cherenkov light generated in the sensor window. The Cherenkov imaging counter in the backward endcap is a proximity focusing RICH with aerogel radiator and extended proximity gap to increase the resolution and, correspondingly, enlarging the momentum range for particle identification. As already underlined, the use of fine-time resolution HRPPDs by MCP technology as photosensors also provides timing information.

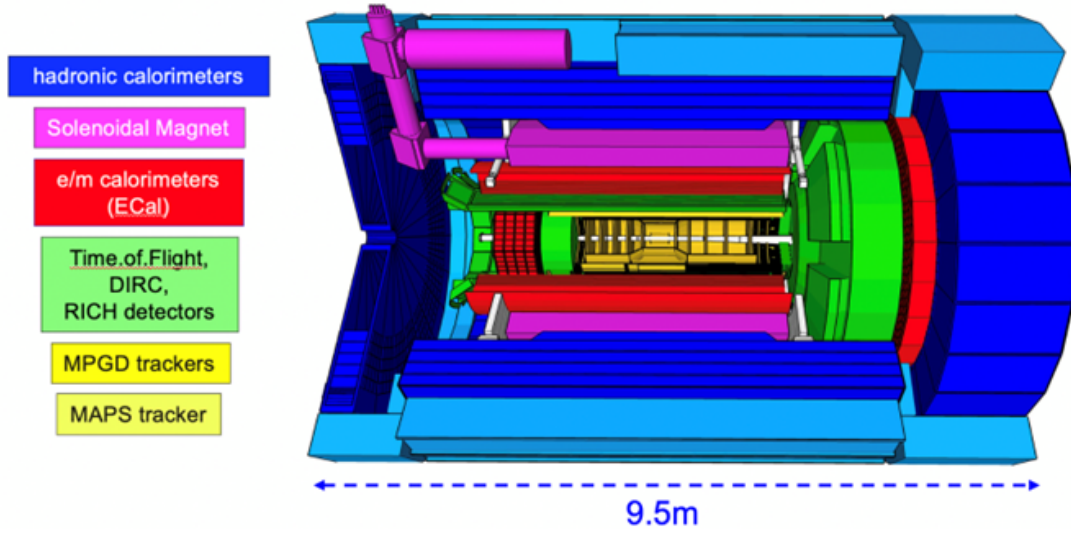


Figure 8.3: A schematic showing the ePIC central detector subsystems. THIS FIGURES IS A PLACE HOLDER

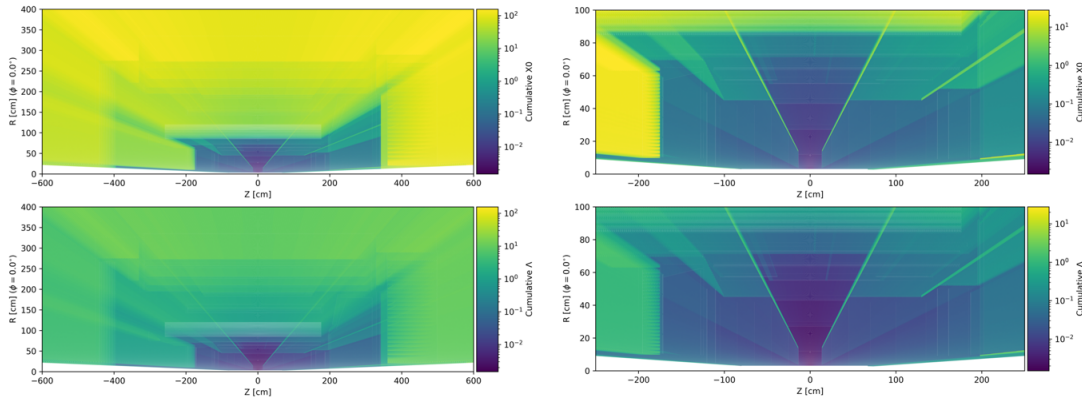


Figure 8.4: Cumulative material budget in radiation lengths (top row) and interaction lengths (bottom row) for the whole CD (left column) and zooming at the CD tracking region (right column). THIS FIGURES IS A PLACE HOLDER BECAUSE IT HAS TO BE COMPLETED WITH SUBSYSTEM CONTOURS AND REQUIRES GRAPHICAL IMPROVEMENTS.

618 The whole detector components are positioned in the acceptance, in front of the electromagnetic
 619 calorimeter. This layout is compatible with the overall detector design; in fact, the bulky elements,
 620 namely the sensors with readout electronics and services are just in front of the calorimeter acting as
 621 a pre-shower element. In the barrel, a high performance DIRC is used, this choice being dictated by
 622 the reduced space. The DIRC fused silica bars, acting as radiator and as photon lightguides, make
 623 possible positioning the image expansion elements and the read-out electronics with its services
 624 in the backward region, outside the acceptance cone. The dual radiator RICH (Sec) in the forward
 625 endcap is equipped with two radiators, aerogel and gas, therefore acting as a couple of Cherenkov
 626 imaging counters dedicated to particle identification in two different momentum ranges, while
 627 economizing in space and single photon sensors. It is a focusing RICH with spherical mirrors as

focusing elements. The photosensors and related services are placed outside the acceptance thank to appropriate mirror orientation.

The electromagnetic calorimeters (Sec. 8.3.5) are external to the particle identification devices and, once more, the different technologies are imposed by the physics requirements, the kinematic ranges and the overall constraints. The budget of the material in front of the calorimeters is low and mainly concentrated near to the calorimeter front face. The backward endcap electromagnetic calorimeter is by fine granularity lead tungstate crystal offering very fine energy resolution. In the barrel, the electromagnetic calorimeter has a hybrid architecture combining imaging layers by AstroPix MAPS and sampling calorimetry by lead and scintillating fibers with sampling layer between the imaging layers and in the most external calorimeter portion. The layout is pseudo cylindrical with the read-out equipment at the cylinder edges minimizing the space requirement in the crowded barrel area. The electromagnetic calorimetry in the forward region is by sampling calorimetry with scintillating fibers inserted in matrices of tungsten powder embedded in epoxy. This calorimeter offer a near to 1 ratio of the signal amplitude response for electrons and hadrons and, therefore, it is design to operate in duet with the hadronic calorimeter place immediately behind.

All the **hadron calorimeters** (Sec. 8.3.6) are by iron as converter and scintillating active elements, even if with very different implementations. The forward endcap calorimeter is by SiPM-on-tile technology, with finer granularity in the central zone, near to the beam pipe, to cope with the higher rates. The barrel calorimeter, placed behind the solenoid coils, acts as a tail catcher. The backward endcap calorimeter ... (to be completed: layout in evolution).

All the calorimeter subsystem in the ePIC detector make use of SiPMs as photosensors, even if of different size and pixelization, with common approach for the readout chain.

The global layout of the FDs (Sec.s 8.3.7 and 8.3.8) is illustrated in a artistic view in Fig. 8.5.

The **forward FDs** include tracking and electromagnetic calorimetry inserted in the first dipole of the ion beam line B0, off-momentum detector trackers and roman-pot trackers and a zero-degree-calorimeter. The technology for the trackers is by AC-LGADs, which have good radiation hardness. The B0 electromagnetic calorimeter is by lead tungstate crystals. The zero-degree-calorimeter is formed by a long SiPM-on-tile module with fine granularity adequate for photon and neutron detection. A crystal layer can be inserted in front of it for those studies that require the detection of low energy photons.

The **luminosity system** is part of the backward FD. Based on the measurement of the photons from the Beta-Heitler process at IP, it consists of a high-rate calorimeter for direct photon detection and a couple of pair spectrometers to detect the electrons and positrons generated by the Beta-Heitler photons in the exit window. The high-rate calorimeter and the calorimeters in the pair spectrometers are by tungstate and scintillating fibers. Tracking in the pair spectrometer is by AC-LGADs. The **low- Q^2** taggers consist in tracking stations followed by an electromagnetic calorimeter. The selected technologies must cope with extremely high rate in this kinematic region. Therefore, tracking is by TimePix4 and calorimetry by tungstate and scintillating fibers.

Integral elements of the detector are the **electronic read-out chain**, the data acquisition system (Sec. 8.3.10) and the **software implementation and computing model** (Sec. 8.3.11). The overall underlining model that has guided the selection of the components and the design of the read-out/DAQ/software/computing architecture is the streaming readout concept. Streaming readout has been selected to simplify the readout scheme as no triggers are required and to increase the information selection flexibility, to improve the event building from the holistic detector information, to improve, via continuous dataflow, the knowledge of backgrounds and, therefore, enhances the control over systematics. In this approach, already at the front-end level, the ASICs, which

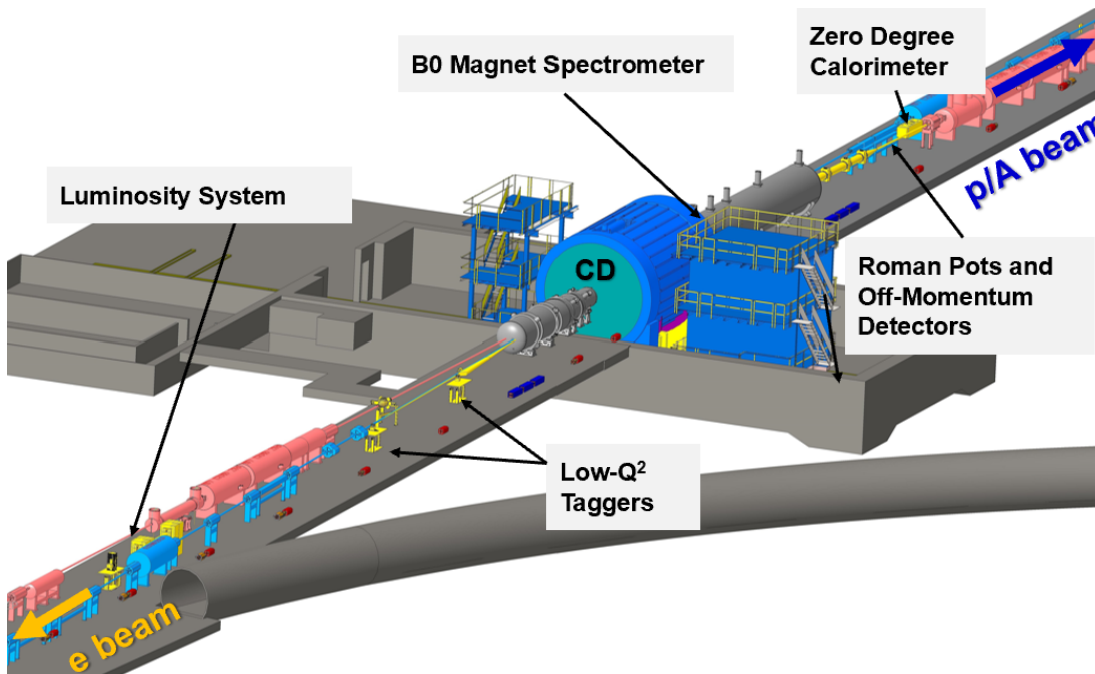


Figure 8.5: A schematic showing the ePIC far detector subsystems. THIS FIGURES IS A PLACE HOLDER

are intimate related to the sensors and their performance, have been selected with architectures compatible with their usage in streaming readout mode.

Independent setups are designed to measure and monitor the **beam polarization** (Sec. 8.3.9). Rapid, precise beam polarization measurements will be crucial for meeting the goals of the EIC physics program as the uncertainty in the polarization propagates directly into the uncertainty for relevant observables as asymmetries. The basic requirements for beam polarimetry are non-destructive with minimal impact on the beam lifetime, uncertainty at the 1% level, the capacity of measuring the beam polarization for each bunch in the ring with rapid, quasi-online analysis in order to provide timely feedback for accelerator setting up. The electron beam polarimetry will be based on the well established Compton polarimeter techniques, where the polarized electrons scatter from 100% circularly polarized laser photons. This approach offers the advantage that both longitudinal and transversal polarizations are measured. Hadron polarimetry has been successfully performed on RHIC polarized proton beams for nearly two decades. Through continual development a relative systematic uncertainty $\pm 1.5\%$ was achieved for the most recent RHIC polarized proton run. As the only hadron polarimeter system at a high energy collider it is the natural starting point for hadron polarimetry at the EIC. Hadron polarization will be measured via a transverse single spin left right asymmetry in the pp interaction on targets by plastic material (H-C composition), where the experimental challenge is the control of the background events.

Technological Synergistic Aspects of the Detector Design The synergistic aspects of the ePIC detector have been carefully maximized in view of the optimal usage of the workforce and the financial resources. This is illustrated by the following examples.

SiPM sensors, recently introduced in calorimetry applications, are adopted for all the electromag-

netic and hadronic calorimeters in ePIC. They offer a cost-effective technology that can operate in magnetic field, can provide wide dynamic range when the sensor type is properly chosen to tune the response parameters, and present low noise level by applying appropriate thresholding. The use of a common technology makes possible to access the effect of the radiation by a single effort and the use of the same front-end ASIC CALOROC.

Also the calorimetry reconstruction software is synergistic for the overall set of subsystems.

In electromagnetic calorimetry, the sampling approach with tungsten and scintillating fiber is adopted for the forward endcap calorimeter and in FDs: calorimetry in B0, luminosity system and low- Q^2 taggers.

In hadron calorimetry, the SiPM-on-tile technology is used for the forward endcap calorimeter and its insert in the central area, as well as for the zero-degree calorimeter.

In particle identification by Cherenkov imaging counters, MCP-based photosensors are used for the backward endcap RICH and the barrel DIRC, that can be read by the same read-out ASIC HGCROC (information to be crosschecked). The backward endcap RICH and the forward endcap RICH use aerogel as radiator and the quality assessment station will be used for both batches. The reconstruction software in both RICHes has large communalities and it is based on the same ray-tracing algorithm.

AC-LGADs form the time-of-flight layers and are used for tracking in the forward FD in B0, off momentum detectors and roman pots, and selected for the pair spectrometers of the luminosity system.

In tracking by MAPS, the different sensors of the inner layers, the outer layers and the forward and backward disks are all evolutions of the ITS3 sensor, therefore all based on stitching the same readout chip element.

The same hybrid MPGD architecture with a preamplifying GEM layer followed by a μ RWELL is used in the most outer tracker in the barrel and the most external discs in the endcaps. All MPGDs, namely the hybrid MPGDs and the cylindrical Micromegas in the barrel are coupled to the same front-end ASIC: SALSA.

A single integrated effort is at the basis of the tracking reconstruction with the use of the software package AC.

8.3.2 Magnet

Requirements

Requirements from physics: Add text here.

Requirements from Radiation Hardness: Add text here.

Requirements from Data Rates: Add text here.

Justification

732 **Device concept and technological choice:** Add text here.

733 **Subsystem description:**

734 General device description: Add text here.

735 Sensors: Add text here.

736 FEE: Add text here.

737 Other components: Add text here.

738 **Requirements from Data Rates:** Add text here.

739 **Implementation**

740 **Services:** Add text here.

741 **Subsystem mechanics and integration:** Add text here.

742 **Calibration, alignment and monitoring:** Add text here.

743 **Status and remaining design effort:**

744 R&D effort: Add text here.

745 E&D status and outlook: Add text here.

746 Other activity needed for the design completion: Add text here.

747 Status of maturity of the subsystem: Add text here.

748 **Environmental, Safety and Health (ES&H) aspects and Quality Assessment (QA plan-**
749 **ning:** Add text here.

750 **Construction and assembly planning:** Add text here.

751 **Collaborators and their role, resources and workforce:** Add text here.

752 **Risks and mitigation strategy:** Add text here.

753 **Additional Material** Add text here.

8.3.3 Tracking

Add text here.

8.3.3.1 The silicon trackers

Requirements

Requirements from physics: The Silicon Vertex Tracker (SVT) needs to meet stringent performance requirements, set by the EIC science program, on acceptance and resolutions for charged-particle trajectories. At a high level, the SVT needs to precisely measure the scattered electron and charged hadrons produced in the electron-ion beam collisions. The scattered ion, if it remains intact, is outside of the SVT acceptance. The SVT also needs to measure charged decay-particles from hadrons containing heavy quarks and from vector meson decays. It is to aid in particle-identification a) through determination of the displacement of the geometrical origin of the decay particles (secondary vertex) from the collision point (event vertex) via precision reconstruction of both vertices and b) by providing directional and impact information on charged-particle trajectories through the outer gaseous tracking subsystems and into the outer particle-identification subsystems.

Table 8.1 contains the resolution requirements on the particle momentum measurement at the event vertex for different ranges in pseudorapidity and on the determination of the radial distance of closest approach of the particle trajectory to the event vertex with its dependence on transverse momentum. The SVT is the innermost subsystem of the ePIC central detector. Constraints from the

η range	dp/p [%]	DCA_r [μm]
$(-3.5, -2.5)$	$0.10 \times p \oplus 2.0$	$30/p_T \pm 40$
$(-2.5, -1.0)$	$0.05 \times p \oplus 1.0$	$30/p_T \pm 20$
$(-1.0, 1.0)$	$0.05 \times p \oplus 0.5$	$20/p_T \pm 5$
$(1.0, 2.5)$	$0.05 \times p \oplus 1.0$	$30/p_T \pm 20$
$(2.5, 3.5)$	$0.10 \times p \oplus 2.0$	$30/p_T \pm 40$

Table 8.1: Physics requirements on the relative momentum measurement, dp/p at the event vertex for different ranges in pseudorapidity, η , and on the determination of the radial distance of closest approach, DCA_r , of the particle trajectory to the event vertex with its dependence on transverse momentum, p_T .

overall detector size and the outer subsystems limit the active volume of the SVT to $-105 < z < 135$ cm and a radius of approximately 42 cm. In combination with the 1.7 T solenoidal field, this leads to a requirement on the point resolution of better than 10 μm as well as the need to minimize traversed material by limiting the number of detection surfaces and minimizing their radiation lengths.

Requirements from Radiation Hardness: We have evaluated the radiation levels in the SVT using the current knowledge of the beam configuration and beam backgrounds from beam gas interactions and synchrotron radiation. Figure 8.6 shows the current estimates for fluence (in 1

MeV $n_{eq} \text{ cm}^{-2}$) and dose (in rad). The black lines indicate the approximate locations of the SVT detection surfaces. These radiation maps have been estimated for the beam configuration with the highest luminosity and include contributions from hadron and electron beam gas interactions. The results assume that the machine and detector run at 100% efficiency for 6 months per year over a period of 10 years. This is to obtain a conservative estimate. Even under these assumptions, the radiation levels in the SVT will be low to moderate. The majority of the SVT will see fluence levels well below $10^{11} n_{eq} \text{ cm}^{-2}$. Innermost central layers and layers in the hadron going direction will experience slightly higher fluence between 10^{11} and $10^{12} n_{eq} \text{ cm}^{-2}$, with some small regions reaching above $10^{12} n_{eq} \text{ cm}^{-2}$. The dose rate map indicates that areas close to the beam pipe will experience a total ionising dose between ten and a few hundred krad, while the rest of the SVT remains below 10 krad.

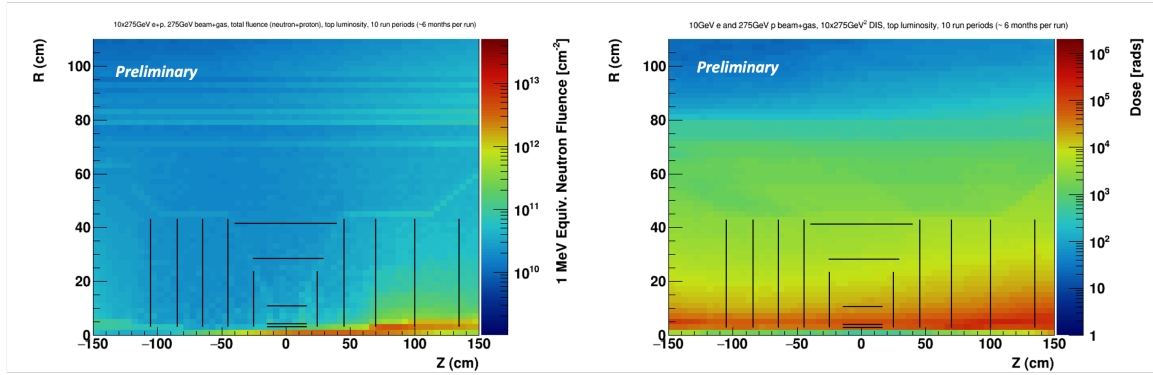


Figure 8.6: Maps of simulated fluence (left) and total ionising dose (right) over the ePIC tracking envelope. This is a conservative estimate assuming 10 years of running at top luminosity with 100% efficient accelerator and detector. The black lines indicate the approximate location of the ePIC SVT detector layers.

Requirements from Data Rates: EIC physics rates are expected to be below 0.5 MHz. That is, only a small fraction of the EIC beam crossings produces a physics event and physics event pileup from within a single beam crossing is negligible. The dominant fraction of these events originate from a region, $|z| < 80 - 100 \text{ mm}$, surrounding the nominal interaction point. We thus estimate that event pileup within the SVT is determined by its readout frame or integration window of $2 \mu\text{s}$ or a small multiple thereof. Within this window, SVT will also accumulate hits from noise and beam backgrounds. We estimate that the associated hit load and data volume will exceed that from physics events. Hit occupancies will be low in view of the high SVT granularity. We estimate a hit probability per pixel per readout frame of $\mathcal{O}(10^{-7})$ and a typical total data rate at the level of 15 Gbps. The sensor and readout chain need to be efficient under these conditions.

Justification

Device concept and technological choice: To meet the stringent requirements on charged-particle tracking and vertexing, we have designed the SVT to provide a well-integrated, large acceptance, high granularity, and low-mass tracking and vertexing subsystem. The SVT has four regions covering a total active area of approximately 8.5 m^2 . An Inner Barrel (IB) and Outer Barrel (OB), made of three and two detecting layers respectively, cover the mid-central pseudorapidity

range and have an active volume that extends radially to approximately 42 cm. Endcaps, each with five detecting annuli surrounding the beampipe, are placed on either side of the nominal interaction point with their active area constrained to $-105 < z < 135$ cm and an outer radius equal to that of the OB. The Electron Endcap (EE) is positioned in the direction of the electron beam and has acceptance for a large fraction of the scattered electrons, while the Hadron Endcap (HE) provides acceptance for many of the hadrons produced in physics collisions. Figure 8.7 shows The SVT regions and geometrical layout.

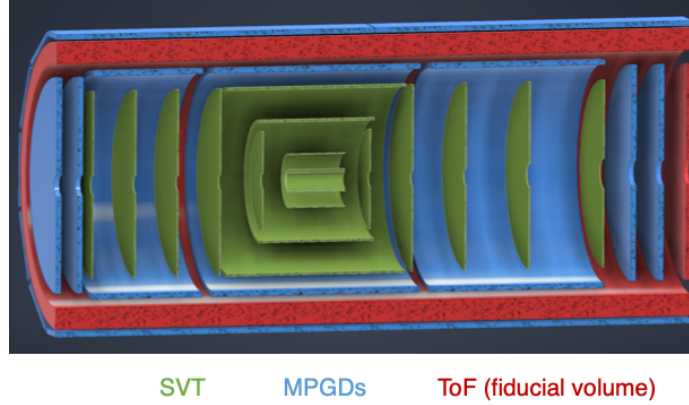


Figure 8.7: Schematic layout of the ePIC SVT showing the central region consisting of the inner and outer barrel made of three and two cylindrical layers, respectively, together with the endcap regions made of five annuli each. The figure also shows the surrounding Micro Pattern Gas Detector (MPGD) layers and the envelope of the Time of Flight PID detector.

We designed the SVT to cover the required pseudorapidity range and to reach spatial resolutions as low as $\leq 5 \mu\text{m}$ through a combination of high granularity ($\sim 20 \mu\text{m}$ pixel pitch), low power sensor design ($\leq 40 \text{ mW cm}^{-2}$), and lightweight support structures, cooling, and electrical services. Our development aims at achieving 0.05% X/X_0 in the IB, 0.25% X/X_0 in the innermost OB layer and in the disks, and 0.55% X/X_0 in the outermost OB layer. We selected a sensor technology based of the ALICE-ITS3 development [8] to meet our requirements. This is a new generation, large area Monolithic Active Pixel Sensor (MAPS) in a commercial 65 nm CMOS imaging process.

Subsystem description:

General device description: Tables 8.2 and 8.3 show the positioning and size of the SVT detecting layers, together with their material budget target. We designed the IB to provide precise vertex reconstruction, while also contributing to momentum measurement. This is achieved with a combination of very thin layers at optimised radii. The IB will use the ALICE ITS3 wafer scale sensor [8] with a suitable adaptation of the ITS3 ultra-thin detector concept to the large EIC beam pipe diameter. The IB design has three layers of silicon sensors thinned below $50 \mu\text{m}$ and bent around the beam pipe, with minimal mechanical support, air cooling, and no electrical services in the active area, to reach the very low material budget target of $X/X_0 = 0.05\%$. The innermost layer is positioned as close as possible to the beam pipe, taking into account the constraints coming from the large beam pipe radius and the requirements from beam pipe bake-out, which will be performed with the IB installed. The position of the second layer is chosen to maximise vertex resolution. The outermost layer of the IB aims at maintaining the very low material budget at a radius of 120 mm and serves both vertexing and sagitta measurements. The OB, EE and HE will be equipped with the EIC

Large Area Sensor (LAS), a modified version of the ITS3 sensor, optimized for high yield, low cost, large area coverage. These sensors will be mounted on lightweight support structures, in the form of staves for the OB and disks for the endcaps, with integrated cooling and electrical interfaces for power, data and slow control. The OB layers and the endcap disks are positioned to provide high precision measurements over a large level arm to improve momentum resolution and optimize acceptance at large pseudorapidity. The inner openings of the disks will accommodate beam pipe bake-out constraints as well as beam pipe divergence. These translate into six different inner opening geometries over ten disks.

Region	Layer	radius [mm]	length [mm]	X/X_0
IB	L0	36	270	0.05%
	L1	48	270	0.05%
	L2	120	270	0.05%
OB	L3	270	540	0.25%
	L4	420	840	0.55%

Table 8.2: Radius, length and material budget of the SVT IB and OB layers.

Region	Disk	z [mm]	r_{out} [mm]	X/X_0	Region	Disk	z [mm]	r_{out}	X/X_0
EE	ED0	-250	240	0.25%	HE	HD0	250	240	0.25%
	ED1	-450	415	0.25%		HD1	450	415	0.25%
	ED2	-650	421	0.25%		HD1	700	421	0.25%
	ED3	-850	421	0.25%		HD3	1000	421	0.25%
	ED4	-1050	421	0.25%		HD4	1350	421	0.25%

Table 8.3: Position along the beam pipe, outer radius and material budget for the SVT layers in the EE and HE regions.

Sensors: The SVT will be constructed with MAPS sensors, that integrate sensing and front-end electronics functionalities in one device. The ePIC SVT will use MAPS sensors developed in a 65 nm CMOS imaging process based-off the ALICE ITS3 development [8]. This technology enables a high granularity and low power consumption design, and offers stitching on 300 mm wafers for the development of large area sensors. These characteristics are key to delivering a high precision detector through high spatial resolution and minimized material budget.

The SVT IB will use the ALICE ITS3 sensor, called MOSAIX. A sketch of MOSAIX on a wafer is shown in figure 8.8. MOSAIX is composed of an active matrix of Repeated Sensor Units (RSUs). Twelve RSUs are stitched along the length of the sensor. The sensor will be three, four, and five RSUs wide for L0, L1 and L2 respectively. Each RSU is further divided into 12 tiles that can be switch off independently in case of faults to improve yield over such large area device. A row of twelve RSUs, together with the left and right endcap (LEC, REC) is called a segment. The LEC contains circuits for power, slow control and data. The REC is used for power only to ensure a uniform power distribution over the full sensor length.

Data links for each segment can be configured with 3 links, plus one spare, at 10.24 Gb/s or 6 links, plus 2 spares, at 5.12 Gbps. For each segment, seven electrical links provide clock, synchronisation and control signals, referred to here as slow control signals. The clock runs at 40 MHz, while the other control signals will run at 5 Mbps. MOSAIX has different power domains for analogue and digital circuitry at 1.2 V, plus two more domains for specific blocks, one at 1.2 V and one at 1.8 V [8]. The sensor's bias voltage will be in a range between -1.2 and -4.8 V.

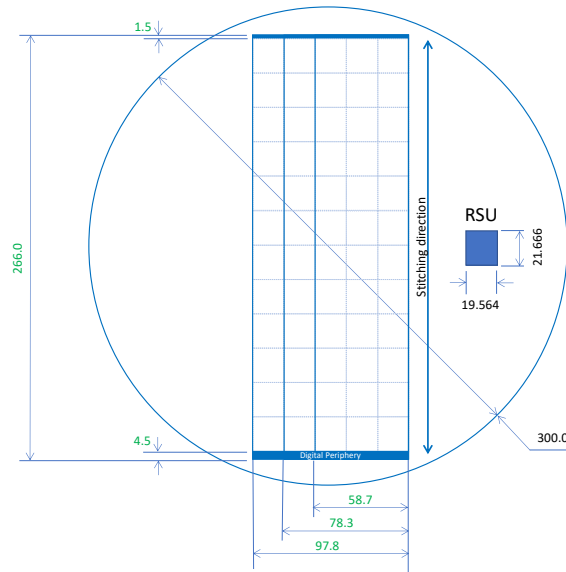


Figure 8.8: Sketch of the MOSAIX sensor on a 300 mm wafer showing the size of the RSU, LEC, REC and of the full sensor for the three different widths.

The SVT OB and endcaps cover an area of approximately 8 m². Considerations based on yield, cost, integration, and coverage require the use of a sensor with a smaller size. These regions will use the MOSAIX sensor with modifications to reduce the size. This sensor would still be large in traditional terms and is therefore referred to as the EIC Large Area Sensor (EIC-LAS). The EIC-LAS will be one RSU wide and either 5 or 6 RSUs long. In addition to reducing the size of the sensor, the EIC-LAS will see a reduction of the number of data links to match the lower SVT data rate, reducing material and easing integration aspects. To further ease the integration of the EIC-LAS in the OB and endcaps, EIC-LAS sensors will be powered in series by a constant current and a dedicated communication protocol will be used to reduce the number of slow control links from the counting room to the sensor. These features will be provided by a supporting ASIC, referred to as the Ancillary ASIC (AncASIC).

FEE: One AncASIC will be used per EIC-LAS. This chip includes three main features. It integrates the SLDO regulator for serial powering. This regulator will generate the voltages needed by the EIC-LAS from the input current. This design is adapted from the original SLDO design for the upgrades of the ATLAS and CMS pixel detectors at the HL-LHC. One AncASIC will integrate four SLDO regulators. The AncASIC will also contain a Negative Voltage Generator (NVG) block. The NVG is a diode-based charge-pump circuit (Dickson-type charge pump voltage multiplier). It will generate the sensor's negative bias voltage from one of the regulated power supply at 1.2 V generated by the SLDO. The third block is the Slow Control (SC). Slow control signals from the counting room will be transmitted over I2C for multiple EIC-LAS sensors over one link. The SC block will decode them into

the MOSAIX format (i.e. into seven links). The AncASIC will be produced in a 110 nm SOI process offering multiple MPW per year and the required transistors' ratings for the SLDO and NVG.

Other components: All components of the SVT detector are designed with the goal of achieving the low material budget target, while providing a robust, high precision system. Traditionally the bulk of the material in silicon detectors is contributed by the powering system. The SVT will adopt a current based power distribution scheme, so called serial powering, for the OB and disks. Groups of up to four EIC-LAS sensors are powered in series by a constant current, with the electronics low voltage generated close to the sensors by the SLDO regulators in the AncASIC. This scheme reduces cabling material and provides the only viable powering solution to fit within the available space for services in the ePIC detector. For the smaller IB system, a traditional voltage based, direct powering scheme is foreseen. Data, slow control signals and power are routed over aluminium-based flexible printed circuits (FPC) between the SVT active elements (MOSAIX, EIC-LAS, AncASIC) and the readout (RDO) boards. Four different RDO boards are used in the SVT. The interface board receives data from the sensors for transmission to the counting room. The control board receives slow control signals from the counting room to be transmitted to the AncASIC. Lightweight communication between these RDO boards and the counting room is achieved by use of optical fibers. An aggregator board achieves a reduction of the optical fiber lines through multiplexing via FPGA to match the number of fibers to the available channels of the FELIX data acquisition board in the counting room. The electro-optical interface components used on the interface and control boards are the lpGBT [9] and VTRx+ [10] devices developed by CERN. The power board provides interface for power distribution for sensors and Anc-ASIC as well as RDO boards. Whilst the functionality of the RDO boards and FPC remains the same, different designs will be needed for IB, OB and disks to accommodate the different powering schemes, number of data links, and sensors grouping. The preferred cooling solution for the SVT detector is air cooling, baselined for the two innermost layers of the IB and under study elsewhere. The OB, EE and HE are designed to allow air flow through the low mass staves and disks, made of carbon composite material, that support the sensors.

Performance We have simulated track finding and reconstruction within the ePIC software framework to quantify momentum and vertexing resolutions. Figure 8.9 shows the simulated relative momentum resolution for single charged pions versus their total momentum for different pseudorapidity regions, together with the requirements. The simulations show that the momentum resolutions are substantially met over most of the SVT acceptance. The performance in the range of smallest pseudorapidity, $-3.5 < \eta - 2.5$, is limited by constraints on the SVT lever arm from ePIC's outer subsystems in this region and overall detector size. Figure 8.10 shows the simulated radial distance of closest approach, DCA_r , for the reconstructed trajectories of simulated charged pions to the event origin versus pion transverse momentum in different pseudorapidity regions, together with the requirements. The simulations show that the requirements on DCA_r are substantially met over the SVT acceptance.

We have performed beamtests at FNAL with a single-RSU sensor, called babyMOSS, from ITS3 Engineering Run 1. In these tests, two times three sensors were arranged in a telescope and exposed to the test beam. A seventh sensor, the Device Under Test (DUT), was placed at the center of the telescope and its angle with respect to the incident beam was varied in the horizontal plane of the telescope. Figure 8.11 shows a close-up of the telescope and results for the cluster extent as a function of the incident beam angle onto the DUT from data and simulations. The results demonstrate that the geometrical effect from the angle dominates over diffusion and otherwise confirm the expected point resolution.

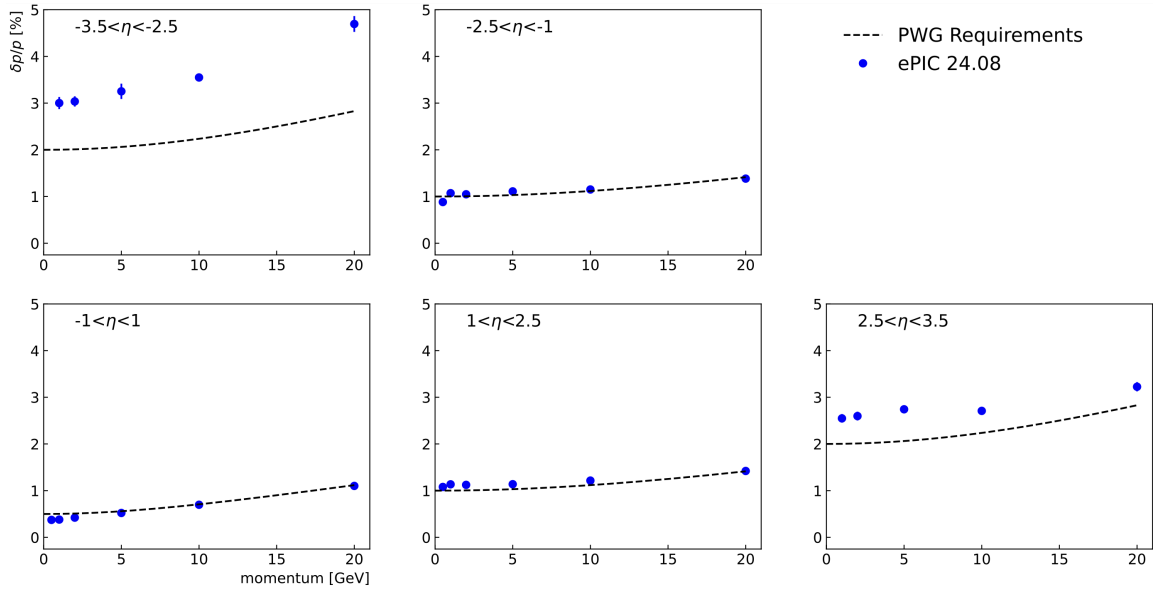


Figure 8.9: Relative momentum resolution versus total momentum for charged pions (points) together with physics requirements (curves) in different pseudorapidity ranges as indicated. The results are based on full GEANT simulations using the ePIC software stack and ACTS-based track finding and reconstruction using optimized parameters.

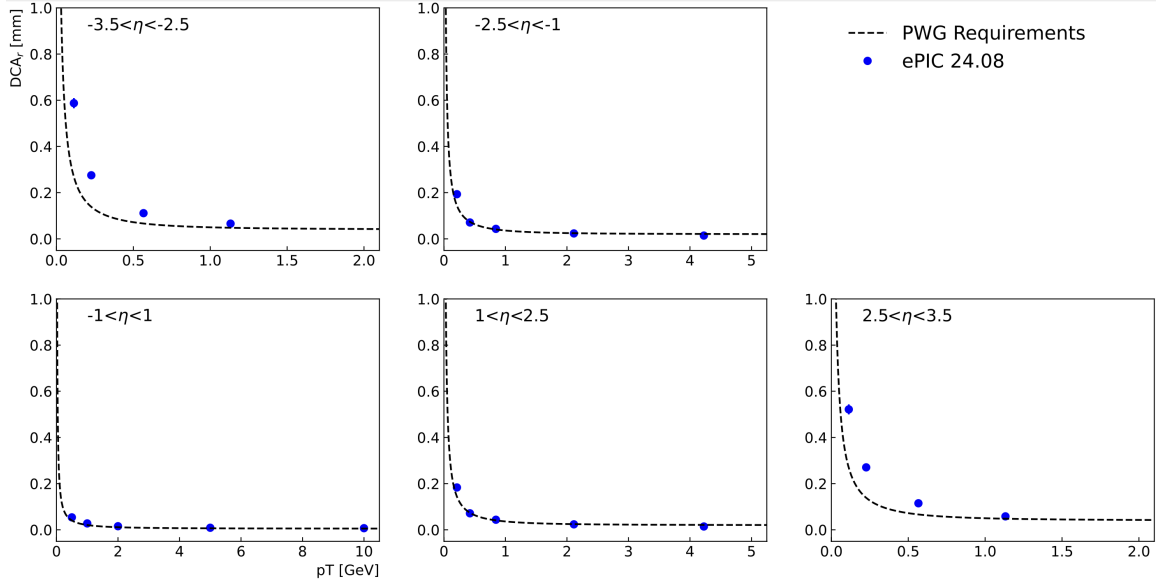


Figure 8.10: Distance of closest approach in the radial direction between reconstructed charged pion trajectories and the event origin versus transverse pion momentum (points) together with physics requirements (curves) in different pseudorapidity ranges as indicated. The results are based on full GEANT simulations using the ePIC software stack and ACTS-based track finding and reconstruction using optimized parameters.

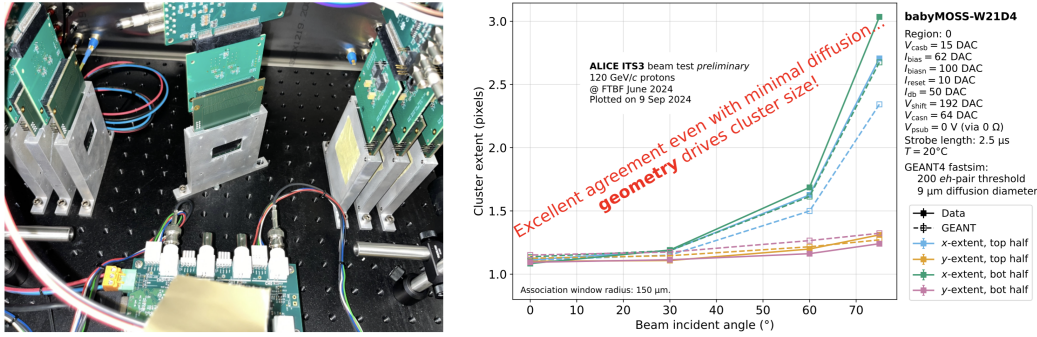


Figure 8.11: A close-up of a beam telescope constructed from two times three single-RSU sensors from ITS3 Engineering Run 1 with a seventh sensor (DUT) under an angle at the center of the telescope (left) and (right) results from beamtests at FNAL and from simulations for the cluster extent as a function of the beam incident angle onto the DUT.

Region	Sensor	Electrical services group	# power lines/group	# slow control lines/group	# data lines/group
IB	MOSAIX	MOSAIX segment	10	7	8
OB	EIC-LAS	Up to 4 EIC-LAS)	2	3	4
ED	EIC-LAS	Up to 4 EIC-LAS	2	3	4

Table 8.5: Summary of power and readout services for the different regions of the sPIC SVT.

936 Implementation

937 **Services:** Services to the SVT are of two types: electrical/fiber-optical services and cooling.
 938 Electrical/fiber-optical services to the SVT comprise power, data and slow control. For the IB
 939 (MOSAIX sensor and direct powering), electrical services will be by MOSAIX segment. For the
 940 OB and endcaps (EIC-LAS and serial powering), they will be by group of up to four EIC-LAS. A
 941 summary of the data, slow control and power lines needed in the different regions of the SVT is
 942 given in Table 8.5. The table illustrates the reduction in power lines using serial powering versus
 943 direct powering. In the IB each MOSAIX segments will need ten lines (including the return line)
 944 to serve the four power domains of the electronics plus the sensor bias. For each segment, the full
 945 MOSAIX current will be transmitted. In the OB and endcaps two lines (including the return line)
 946 will be needed to deliver the same power to up four EIC-LAS (i.e. four segments). The current
 947 flowing on these lines will be the current needed by only one EIC-LAS, reducing the current being
 948 transmitted to the detector of up to a factor four, and correspondingly reducing cables cross section
 949 and material budget.

950 Figure 8.12 shows the data and slow control distribution for a group of 4 EIC-LAS. Each data line
 951 connects to one input of a VTRx+ on the interface board. Given the high speed of the data trans-
 952 mission, this board will be placed at the end of each stave and disk for signal integrity. The VTRx+
 953 transmits the data of a group of up to 4 EIC-LAS over one optical fiber to the counting room. Slow
 954 control signals are transmitted over optical fibers to the control board, placed along the support
 955 structure. Once converted into electrical signals, one lpGBT elink provides the slow control signals
 956 to up to four AncASICs. Each lpGBT has 16 elinks, meaning that each control board will serve mul-
 957 tiple groups of EIC-LAS. The slow control signals are transmitted between the control board and
 958 the AncASIC either in a daisy-chain architecture (as shown in the figure) or via multi-drop. The
 959 exact configuration is still being evaluated. The AncASIC converts the incoming I2C protocol to the
 960 MOSAIX protocol expected by the EIC-LAS. As the OB and endcaps are powered in series, each

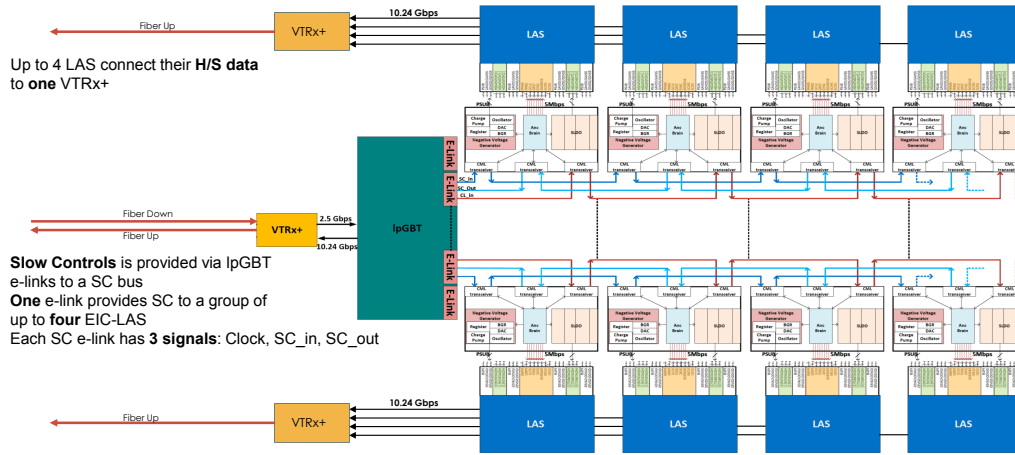


Figure 8.12: Schematic overview of data and slow control lines to a group of 4 EIC-LAS.

to select conductive tracks made of aluminium ($X_0 = 8.9$ cm) instead of traditional copper ($X_0 = 1.4$ cm). Dielectrics like polyimide ($X_0 = 28.57$ cm) are the default solution for the manufacturing technologies of aluminium-based FPCs deployed in scientific experiments. The selection of the dielectric material is dependent on its loss-tangent properties versus the frequency of the signals to be transmitted. Typically the most stringent requirements to signal attenuation are set by the high-speed data transmission lines. In case of the ePIC SVT, it is envisaged that data links can transmit signals as fast as 10.24 Gb/s for a length of ~ 50 cm. The baseline configuration for the FPCs assumes a stack-up made of two aluminium conductive layers (each ~ 15 μm thick) separated by a polyimide dielectric substrate (~ 35 μm), and then additional polyimide cover layers (~ 35 μm combined thickness) to insulate the conductive tracks from external electrical shorts. This cross section (~ 100 μm in total) would equate to a combined material budget of $\sim 0.06\%$ X_0 . The combination of serial powering, slow control daisy-chained/multi-drop configuration and impedance matching at $100\ \Omega$ for clock, control lines and data, enables a reduction of the number of signals to be propagated. This is particularly important for staves and disks where the FPCs overlap the sensitive area of the MAPS. By combining these power and signal distribution techniques, it is estimated that the minimum width for the FPC can as narrow as 6 mm. This is $\sim 1/3$ of the width of the LAS (~ 19 mm).

The transmission of the signals to the counting room will see a further stage of processing. The data fiber-optic lines will be aggregated in the aggregator board which has multiple fiber inputs, an FPGA for extracting the payload from these fibers, and one fiber output towards the FELIX board, thus reducing the number of fiber inputs at the Data Acquisition FELIX boards. It is estimated that approximately 5000 data fiber links run from the sensors to the aggregator board. Assuming an aggregation factor of 10, there will be approximately 500 fibers towards the DAQ FELIX boards, which can be accommodated by 11 FELIX boards (assuming each FELIX board will have 48 fiber inputs).

Cooling adds to the service load, including the target radiation lengths in the SVT active areas. The preferred cooling solution for the SVT detector is air cooling, baselined for the two innermost layers of the IB and under study elsewhere, with liquid cooling in strategic places as necessary. We will operate the sensors at or near room temperature ($\sim 25^\circ\text{C}$), which requires a lower coolant temperature. Thermal performance of the cooling is measured with $\Delta T = T_{\text{sensor}} - T_{\text{inletairorcoolant}}$. Our target for thermal tests and simulations is ΔT of 10°C , although this is not a strict requirement.

For the inner layers of the IB, the baseline is air cooling with thermally conductive foam near the LEC. Measurements from ALICE ITS3 show this is reasonable to cool the MOSAIX sensor. Air will be forced between L0 and L1. To cool L2, options for natural convection with liquid cooling near the LEC if necessary. The air inlet and outlet are under design, with the bulk of the material to be placed on the hadron-going side of the detector.

In addition to cooling during operation, the IB will need to be kept cool during beam-pipe bake-out. The aim is for no additions to the operational cooling, i.e. no additional material (e.g. insulators) or changes (i.e. liquid instead of air). ANSYS studies at Jlab and LBNL have shown that there is a path forward to keep the detector cool. Climate chamber studies at LBNL and CERN have shown no failures up to 50 °C.

The target for both the OB staves and the EE and HE disks is air cooling. We are targeting a maximum air velocity of 12 m/s within the structures of the staves and disks. Current estimates are approximately 1700 m³h⁻¹ total air split between the staves and disks. This will require compressed air to mitigate the otherwise excessive size of the air tubes coming into the detector and pressure regulation inside the detector. Studies are ongoing to reduce these numbers, including the use of thermally conductive materials (e.g. carbon foam) to help with heat dissipation. The SVT will be interlocked to turn off in the case of failure of its cooling system, including conditions so as to prevent pressurising the system beyond its design values.

Subsystem mechanics and integration: The inner barrel (IB) layers will be made of two symmetric half-layers, which will be the basic assembly elements of the detector. The two innermost layers (L0 and L1) will be based on four MOSAIX sensors (two for each half-layer), while the outermost layer (L2) will contain eight MOSAIX sensors (four for each half-layer). All the sensors equipping a given half-layer will be placed one next to the other to fully cover the half-layer surface and bent on a cylindrical shape at the corresponding radius (c.f. table 8.2).

Each IB half-layer will consist of the following components: the MOSAIX sensors, a local support structure mainly made in carbon foam shaped as a frame along the edges of the sensors, two sets of FPCs wire-bonded to the sensor peripheries for powering and data/control transmission. The sensor cooling will be air-flow based and delivered through appropriate ducts that will be part of the local support structure and matched to the global mechanics described below.

The IB global support will be the main structure supporting the MOSAIX sensors already assembled in half-barrels. The current design foresees a cylindrical frame structure for each layer, supported by two conical endcaps, one for L0-L1 and a second for L2, the last including a flange for connection to the other half-cone and to the OB. The material is currently fixed in a carbon fiber composite, whose thickness will be approximately 0.5 mm. FPC and cables from the e-side are routed along the inner surface of the conical support. A half-cylindrical shell made of polyamide is placed outside and close to L2 for general protection of the barrel and to constrain the airflow on the surface of L2. Air is distributed through conveyors in the volumes between L0 and L1 and between L2 and the outer shell. The current design of the cables (power lines) which run from e-side to h-side need that the longerons of the local mechanics have also the role of cable trays, the requirement of rigidity and the U-shape for cables routing suggesting carbon fiber composite as a preferred material choice, while alternatives are being considered. Figure 8.13 shows CAD representations of the IB support.

For the OB, EE, and HE, we introduced a modular approach in the SVT design to simplify the assembly process of these complex detector elements. A modular approach reduces complexity by breaking down the system into sub-units (i.e. detector modules) that we will pre-assemble and pre-test and then mount/interlink in the final staves or disks. The advantage is that defects in sub-units

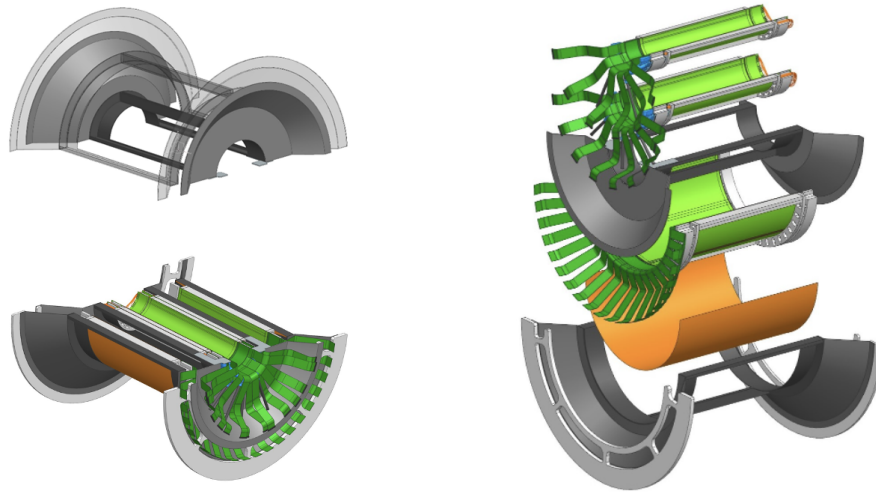


Figure 8.13: Top left: CAD representation of the frame supporting the IB. Bottom left: IB half-barrel CAD view with sensors and cable routing. Right: Exploded CAD view of IB from the h-side and the e-side. The orange element is the kapton shield. In blue the air conveyors are shown.

like detector modules are detected earlier in the production flow. This makes it easier to re-work problems and/or discard faulty components earlier in the production flow. A modular approach also reduces debugging complexity of the final product like a stave or disk. Overall introducing a modular approach in the design of the OBs and Disks increases the predictability of the production rate of the SVT in the production phase. It mitigates risks of delays by design and it increases confidence in planning for the production phase.

The goal in the definition of a detector module is to identify a coherent sub-unit from a functional prospective, and to shape it into a design-for-manufacturing unit. Electrical and mechanical constraints shape the implementation of the module.

The first point to consider is that the deployment of Large Areas Sensors (LASes) in the ePIC SVT represents an unprecedented technological evolution in the field of particle trackers, without any previous, directly applicable example. The concept of a LAS is an evolution of the concept of previous detector modules where individual dies were combined into a module. The LAS combines directly via stitching multiple repeated sensor units into a single large area silicon die. A LAS is itself an evolution of the traditionally assembled detector modules with many single dies. Despite this, the LAS operation depends on the ancillary ASIC (AncASIC). Therefore an electrically coherent unit is represented by a LAS and its AncASIC.

The two components (i.e. LAS and AncASIC) of this electrically coherent unit need to be electrically connected via flexible printed circuits boards and micro-electronics interconnection techniques. This electrically coherent unit needs to be supported by a mechanical frame to be interfaced with cooling systems and to meet handling requirements.

The design of a module for the outer barrel envisions two LAS with their respective two AncASIC, once for each LAS. The mechanical frame is made of a thin film of polyimide that holds together all the module components.

The design of a module for the disks envisages one LAS and one AncASIC and a mechanical frame

1071 made of a carbon fibre plate.

1072 We will test modules standalone after their assembly and before their assembly into staves or disks.

1073 The outer barrel (OB) layers will be segmented in staves. The staves are composite structures using
 1074 carbon fibre (CF) skins, a central CF I-beam spar and cross-ribs made of K9 foam. The side walls will
 1075 be formed by the FPCs. The structure has openings where modules will be placed. During module
 1076 mounting the modules are glued on top of these openings, forming a closed hollow structure with
 1077 large second moment of area, and thus high stiffness. The closed structure provides a contained
 1078 channel for the forced flow of air through the stave, that will remove the heat from the sensors and
 1079 ancillary ASICs. In addition to their structural function, the cross-ribs made of highly thermally-
 1080 conductive K9 foam are placed underneath high-power density components (the left endcap of the
 1081 EIC-LAS and the AncASIC) to improve the transfer of the heat into the air coolant flow.

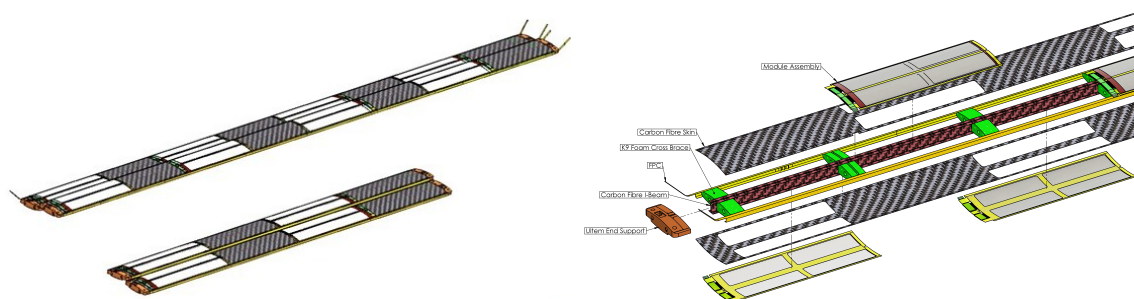


Figure 8.14: Left: OB staves for L3 and L4. Two staves per layer are shown. Right: Exploded view of an OB stave.

1082 Each stave is one OB module (two EIC-LAS) wide, and has modules on both facings, staggered in
 1083 z so that the active areas of the modules provide overlap for tracks from the vertex. L4 staves will
 1084 hold 4 modules on each facing, or 8 modules in total, while L3 staves will have half that number.
 1085 The dimensions of the staves are dictated by the layout of the SVT and we achieve the required
 1086 coverage with LAS made up of 6 RSUs in L3 and 5 RSUs in L4, respectively. L3 will consist of two
 1087 halves with 44 staves in total in a castellated layout to cover the full azimuth. L4 will consist of two
 1088 halves and have 70 staves. Our initial FEA analysis of the modal frequencies finds $f_1 = 91.6$ Hz.

1089 The staves will connect mechanically at their ends to segmented half-cones that are part of the SVT
 1090 support structure. This interface still needs to be detailed, but will constrain stave rotations at the
 1091 support, while allowing for limited misalignment of the support cones and thermal expansion of
 1092 components. The interface will also contain the couplings of the air channel inputs to the supply
 1093 distribution. The cones interface at their outer radius with a support tube surrounding the entire
 1094 SVT, including its services, and also connect to the the global support structure of the IB and the
 1095 innermost disks.

1096 The EE and HE disks are a two-sided design with a corrugated carbon composite core. The purpose
 1097 of the corrugation is to add strength without adding too much mass. The corrugated channels can
 1098 be used for air flow to cool the disks. It also gives options for sensor layout to maximize overlaps
 1099 of inactive area. Modules with one EIC-LAS will be tiled over the valleys of the corrugation on
 1100 either side of the disk, creating overlap along the long axis of the sensor. Modules will be placed in
 1101 an alternating inward and outward facing orientation along the corrugation which ensures that an
 1102 active area of the neighboring sensor covers the insensitive LEC.

1103 Each disk will have a ring at the outer radius that will sandwich the corrugated core to provide
 1104 mechanical support, a mounting point for the RDOs, and an inlet for air cooling. Those rings

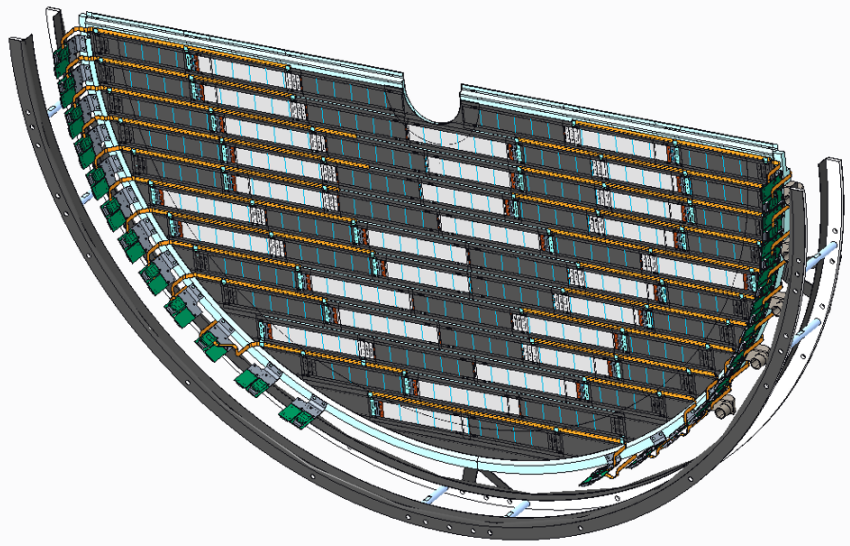


Figure 8.15: CAD model of the preliminary (half-) disk design. Modules are shown in alternatingly inward (dark gray) and outward (white) facing orientations. Common bus FPCs are shown in orange. RDOs (green) are arranged on the outside of the disk ring, inside of the interface to the SVT global support structure.

will then connect mechanically to either the SVT support cone (ED0-1, HD0-1) or support cylinder (ED2-4, HD2-4). This design is currently being optimized in conjunction with the global mechanics. A CAD model of the disk design is shown in Figure 8.15.

Calibration, alignment and monitoring: Calibration procedures are needed to optimize the settings for the pixels in the ITS3 and EIC-LAS sensors. We anticipate these to be similar to those used for the existing ITS2, MLR1, and ER1 sensors, and consist in data-taking scans where one injects a charge into groups of pixels and varies their settings. We have made initial estimates of the time required to perform such scans and anticipate that such scans can be done in a parallel fashion in approximately half an hour with the final readout system.

Alignment procedures are needed to achieve the required resolutions. We will survey the IB (half-) layers, staves, and disks with precision coordinate measuring machines during their construction and will pursue a global survey during installation. Final alignment will be track-based.

Monitoring will include sensor settings and other slow-control data, including temperatures, as well as analysis in near-realtime of residuals in alignment and other observables.

Status and remaining design effort:

R&D effort: The development of the MOSAIX sensor is well underway. Two submissions have already taken place in 2020 and 2022. The former, so called MLR1, included numerous test structures for technology exploration and to develop prototype circuit blocks for future sensors. The latter, ER1, contained exploratory designs to study stitching principles, methodology and yield. The submission of the MOSAIX sensors (ER2) aiming to satisfy ITS3 requirements is planned for beginning of 2025. ePIC designers are integrated in the MOSAIX

design team and contributing to the development of logic libraries, and circuitry for data transmission over the full sensor length between RSUs. The final submission (ER3) will be the MOSAIX production version for the ITS3 detector and the ePIC SVT IB.

Work on the EIC-LAS has started in terms of defining the required modifications. Design work will start once the design database is available upon signature of the necessary CERN-EIC agreement.

The AncASIC is in development with good progress on all functional blocks. Multi-Project Wafer (MPW) runs are foreseen until the full chip will be ready for production in 2026.

E&D status and outlook – IB: We have developed a preliminary design for the two innermost (L0 and L1) half-layers of the IB and its global support mechanics. Different solutions have been explored for bending and assembly of each half-layer: connecting two sensors in a single object and following a “half-layer” based procedure has been considered largely preferable mainly due to advantages from overlaps with the ITS3 building concept. Once the two half-layers have been individually built, they are assembled in a L0-L1 half-barrel. Blank silicon pieces with dimensions corresponding to the final MOSAIX sensors have been used to finalize the conceptual design of the L0-L1 assembly and build the first half-barrel prototypes. In parallel, a preliminary design of the whole SVT IB mechanics, including an external shell to L2, has been also developed and a first mock-up has been produced.

We will evolve the conceptual designs for the half-barrel assembly and for the global mechanics, towards properly engineered realistic ones. The next half-barrel assembly to be built has to integrate as much as possible all the basic components of the final detector (although in a prototyping shape) and allow for thermo-mechanical studies to finalize the cooling design. Test campaigns in a climate chamber and in a wind tunnel facility for ageing and cooling studies are planned. Building of a first L2 half-layer prototype, based on the guidance from the L0-L1 assembly experience, is also scheduled to happen in parallel.

For the SVT IB global mechanics, we will use carbon fiber composites as the main material for the support, given the low mass and excellent mechanical properties. In the coming months an engineered version is planned, with the goal of both verifying possible space conflicts within the global mechanics and matching with the SVT IB assembly procedures.

E&D status and outlook – OB: We are currently prototyping the curved surface stave design for L4 to evaluate tooling and assembly procedures, as well as the performance of the design. These prototypes will be equipped with mechanical dummy sensors (40 μm unpatterned silicon) for mechanical studies, and thermo-mechanical dummy sensors (40 μm silicon encapsulated in xxx μm thick Kapton with xxx μm thick Cu traces). In particular, we will verify/measure

- Manufacturability (co-cure), mechanical integrity and good compaction of carbon fibre,
- Mechanical response spectrum up to 500 Hz and associated Q values,
- Deformations with air flow up to 20 m/s,
- Surface temperatures with thermo-mechanical dummy sensors powered up to xxx W per stave,
- Thermo-mechanical deformations with thermo-mechanical dummy sensors powered up to xxx W per stave.

The results from these studies will guide us in the finalisation of the stave design. In the first phase we are prototyping the stave design with the curved facings, as this is the more challenging to construct.

Interfaces to the support cones will be designed in parallel with the design work on these structures.

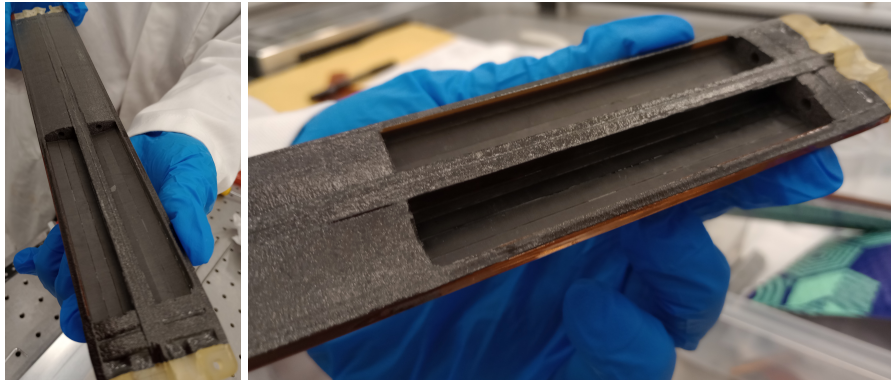


Figure 8.16: First L4 quarter length stave prototype.

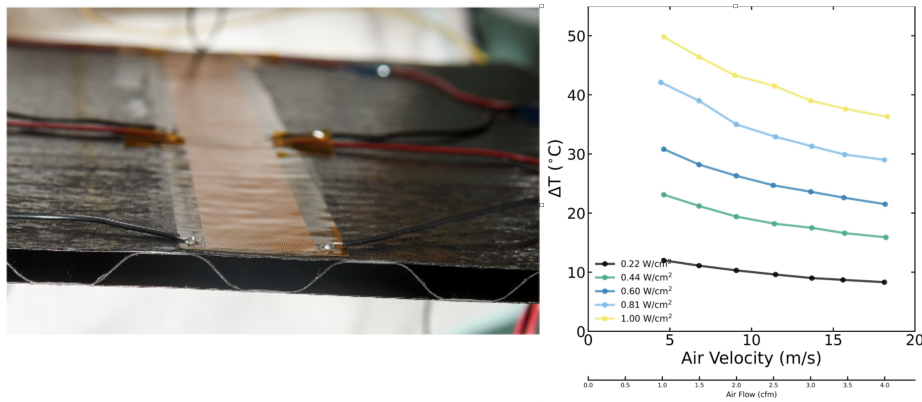


Figure 8.17: (Left) First test piece of the carbon composite corrugated disc core made in the LBNL composite shop. Heaters with two different heating zones that can mimic the sensor power density are placed on the carbon composite facesheet and are used for thermal measurements. (Right) Observed ΔT for different power dissipations in the LEC heating zone versus coolant air velocity.

E&D status and outlook – Disks: Work continues on the design and layout of the disks. We are finalizing the carbon fiber layouts for both the corrugated core and the flat module sheets. An initial test piece has been constructed and tested for thermal performance using copper trace heaters. The prototype is shown in Figure 8.17. The measured ΔT is well within 10°C for the EIC-LAS RSUs, but is high for the LEC, though trending in the right direction with increased air flow, and depends on the design dissipation. The thus far high values of ΔT for the LEC region can be due to many factors, including the low thermal conductivity of the carbon fiber and the overall thinness of the contact surface. We are studying mitigation possibilities with materials that have large thermal conductivity (e.g. carbon foam).

We are currently developing prototypes focused on the development of assembly tooling, module handling, and thermal and mechanical tests. Prototypes will undergo vibration tests to understand mechanical stability. Dummy silicon is in hand to construct a quarter disk mechanical prototype. We expect thermo-mechanical dummies at the end of the calendar year to create a thermo-mechanical prototype.

The bench tests will be paired with ANSYS structural and fluent simulations to understand the performance under air flow and the structural integrity of the disk. This will also need

to be accompanied by bench tests and simulations that include the disc support ring and the outer ring.

E&D status and outlook – FPCs: The development of the flexible printed circuits (FPCs) for the ePIC SVT adopts an iterative approach where a sequence of prototypes will inform the evolutionary development of the final design. The activity on the FPC started in September 2023 and it is progressing as part of Work Package 3 “Electrical Interfaces”. The first iteration of prototypes is underway. This started with targeting an initial design for OB L4. A definition stage captured the design requirements for powering, data transmission and geometrical factors until March 2024. This was followed by a design stage and then by an order submission to RPE LTU (Ukraine). The first set of prototypes are currently being manufactured. The prototypes from RPE LTU will be tested at Daresbury Laboratory and at the University of Oxford. They will also be distributed to other interested sites. In parallel, the community of institutes interested in FPCs started to grow. Since 09/05/2024, the WP3 community started to have monthly meetings with representatives from BNL, Daresbury Laboratory, LANL, LBNL and the University of Oxford. LBNL started to evaluate prototypes from Omni Circuit Board (Canada). LANL also approached a third supplier called Q-Flex Inc. (USA) to procure low level prototypes. The aim is to evaluate the capabilities of three different supplier to manufacture FPCs with aluminium conductors. Signal and power integrity of the FPCs will be tested and the performance over samples of different suppliers compared. A key requirement is signal attenuation for the high speed differential transmission lines (10 Gb/s). Wire bonding and single point Tape Automated Bonding (spTAB) are being evaluated as potential interconnection techniques in ongoing and future prototypes.

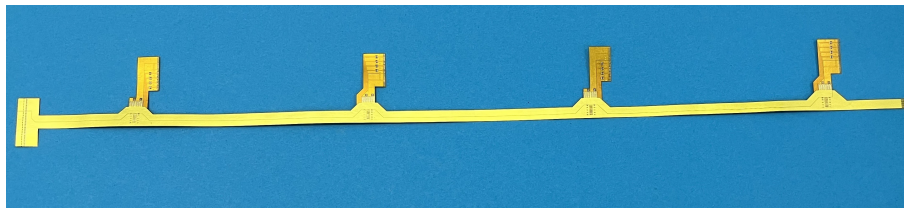


Figure 8.18: An example of a low technology readiness level prototype for the FPC of the outer barrel (layer4). Prototype made by RPE LTU.

E&D status and outlook – Powering: The need to regulate voltages for the MOSAIX sensors as close to the IB (to minimise losses) dictates the need for a(t least one) powering board. Considerations for the design and development of these boards are ongoing; this includes deciding how many regulation stages give the best balance between power losses (fewer stages is likely to mean longer lengths of the most lossy cables, when delivering low voltage and high current), versus additional material in the detector volume (more stages equals more high material powering board, and the final voltage regulation is likely closer to the active area of the IB).

Conceptual powering schemes were developed and used to define specifications for the AncASIC and FPC designs for the OB and Disks. Requirements are being iterated based on limitations introduced by these designs so that they can be iteratively improved. Testing and confirmation of requirements will occur as prototypes become available; this includes:

- Verifying output voltages and current capacity of the individual SLDOs.
- Verifying output voltages of NVGs.
- Daisy-chaining AncASICs to verify serial powering chain performance.

- Quantifying performance of the FPCs in terms of current carrying capacity and voltage-drop along the conductor lengths.
- Combining the above elements to test full serial powering chain prototypes (1 FPC feeding current to 4 AncASICs, each loaded with an EIC-LAS-like structure).

E&D status and outlook – Powering: Work on readout electronics has mainly concentrated on testing evaluation boards of the various components being considered for SVT readout: lpGBT, VTRx+, radiation tolerant FPGA PolarFire, optical FireFly. As part of the ITS3 work-package responsible for readout (WP6) we follow closely the developments in ITS3, since a lot of the electronics for SVT is modeled after ITS3 designs. An initial prototype for the Fiber Aggregator Board was discussed and is now under development using a commercial FPGA board (ZCU102) mated with the optical FireFly FMC card to provide up to 8 fiber inputs and multiple fiber outputs. The VLDB+ board from CERN (containing both lpGBT and VTRx+ was used setup a full chain starting from a Skyworks clock generator board as a stand-in for the Global Timing Unit (GTU), a Xilinx ZCU102 board running lpGBT-FPGA firmware as a stand-in for the FELIX board, and the VLDB+ board as the RDO. A measurement of the jitter of the clock recovered by the lpGBT showed demonstrated adequate performance of this chain to provide a low-jitter clock to the sensors.

Together with Nikhef and Utrecht University, we are currently developing a test system for the serializer chiplet of the ER1 prototype submission. This serializer is a prototype for the 10Gbps serializer to be deployed in the Left End Cap of the final ITS3 sensor. The test system consists of an FMC card which contains the bonding pads for the serializer chiplet, as well as various drivers and connectors including the possibility to drive the high-speed signal onto a Flex-PCB to test the signal integrity over those traces. The FMC card itself will connect to a commercial Xilinx FPGA board for pattern generation and checking.

Another prototype development is the “MOSAIX Mock-up” board currently being designed at ORNL consisting of an FMC daughter card which contains the various Readout components (2 data VTRx+ and an lpGBT / VTRx+ combination for the slow controls interfaces. It will interface to a ZCU102 board where firmware will simulate the responses to slow controls commands, while also allowing to simulate data packets to be sent over the up to 8 fiber optic lines of the 2 VTRx+ interfaces in order to develop both data acquisition protocols and slow controls interfaces of the Readout Electronics to the MOSAIX sensor without the need of an actual MOSAIX sensor.

E&D status and outlook – Cooling: Our prior work has shown that foam can be an important factor in the cooling and thermal performance of staves and disks. This is an integral part of the OB stave design and is being pursued as an option for under the LEC in the disk design. Both will be tested using thermal and thermo-mechanical dummies with upcoming prototypes.

The final air cooling system will be designed based on the overall air volume of the SVT. Current estimates put the total air volume around 1000 cfm total, which would require a pressurized system. The air will be pressurized before entering the ePIC detector volume and then regulated down to various pressures as required by the different parts of the SVT (e.g. OB design requires air above 1 atm).

Simulations from LBNL and Jlab have shown that during beam-pipe bake-out a 5 mm distance from the beam-pipe can keep the silicon below 30 °C with air flow below 10 m/s. However, air flow between the beam-pipe and L0 brings down the temperature of the beam-pipe and can affect ability to reach the 100 °C required inside. Studies are ongoing to determine what hot gas temperature is needed to bring the beam-pipe to temperature and what effect that has on the silicon. We also plan to study if airflow only between L0 and L1 is sufficient to keep the detector below the current 30 °C requirement as this will help mitigate the effect of

1275 the air cooling on the beam-pipe itself. Simulations will be paired with thermo-elastic studies
1276 in a climate chamber that will study cycling, longevity, and assess the point of failure.

1277 Other activity needed for the design completion: We are continuing our testing characteriza-
1278 tion of the products from the ITS3 sensor development sequence. We are currently preparing
1279 for the first tests on MOSAIX at CERN, in collaboration with ITS3, using a high-frequency
1280 wafer probe setup that we are jointly developing. Laboratory tests of thinned and diced
1281 wafers are also being planned, as well as beamtests and irradiation efforts.

1282 The AncASIC will be manufactured in a different process than the MOSAIX and EIC-LAS
1283 sensors. We are readying an initial MPW submission in this 110 nm process and are planning
1284 for its testing and validation. Test structures and the main functional modules of AncASIC,
1285 the SLDO, NVG and Slow Control, will undergo irradiation to verify their correct functioning
1286 in the expected radiation environment.

1287 Status of maturity of the subsystem:

1288 **Environmental, Safety and Health (ES&H) aspects and Quality Assessment (QA plan-**
1289 **ning:** We will follow and adhere to all applicable ES&H standards during the development, con-
1290 struction, installation, and ultimately commissioning and operation of the SVT. Hazards include
1291 those associated with adhesives, carbon composites, flammables, wafer-probing and wire-bonding,
1292 use of radioactive sources, testbeams, and irradiation facilities, and electrical safety. Where possi-
1293 ble, we will work across institutions to implement standardized controls and mitigations, as well
1294 as documented safety procedures.

1295 System tests in the development phase of the SVT are integral to our Quality Assessment. Quality
1296 Control forms an integral part of WBS and schedule during construction and assembly.

1297 **Construction and assembly planning:** The L0-L1 half-barrels will be manufactured in Italy
1298 by INFN: the current plan is to have a main assembly site in Bari and a backup one in Padova
1299 currently being equipped. The L2 production half-layers will be built in the US. Both construction
1300 activities will include a final QC step of the corresponding complete assembly: this will include
1301 operation with air-cooling to verify thermal performance and testing of readout and control lines.
1302 After a successful pass of the QC step, L0-L1 half-barrels and L2 half-layer will be shipped to BNL.
1303 The global IB mechanics will be produced by INFN in Padova, undergo a QC step based on a
1304 metrological survey and finally shipped to BNL. At BNL the L0-L1 half-barrels and L2 half-layers
1305 will be assembled to the global mechanics to form complete IB half-barrels. All the connections to
1306 services (powering, cooling and readout) will be put in place to allow a final QC step.

1307 Modules and staves for the OB layers will be manufactured in the UK. Currently we plan to manu-
1308 facture modules at two sites, Birmingham and Daresbury Lab. This production includes electrical
1309 bonding of the sensors and ancillary ASICs to the bridge FPC. Module construction concludes with
1310 a QC on the completed module before shipping to the stave loading sites. Stave production, which
1311 comprises manufacture of the stave composite structures, and gluing of modules onto the struc-
1312 tures and electrical bonding of the bridge FPCs to the main FPCs. These production steps will be
1313 performed at Oxford and RAL. Again, the final step of the stave construction will be a QC of the
1314 completed stave. This will comprise operation with internal air cooling to verify thermal perfor-
1315 mance, operation of control lines and readout of modules. After successful pass of these QC steps,
1316 staves will be shipped individually to BNL. At BNL staves will be mounted on the support half-
1317 cones from the inside, starting with the outermost layer L4. This involves mechanical connection,
1318 connection of the air supply, and dressing of the FPCs and mounting of the RDOs on the outside of

the support cones. After the mounting of the L4 staves they will be tested, and after that the same procedures will be repeated for the inner OB layer, L3.

Disks and their modules will be produced and assembled in the US. LBNL, Purdue, and LANL are expected to be disk assembly sites, with LBNL and Purdue also serving as module assembly sites. Assembly of modules includes gluing of sensors to carbon composite structures, as well as electrical connection (wire or tab bonding) to a bridge FPC and the AncASIC. Modules will undergo QC before being assembled onto disk structures. The corrugated carbon composite disk structures and module flat sheets will be produced at LBNL and shipped to LANL and Purdue. Disc support rings will be produced by an outside vendor, validated at LBNL, then shipped to disk assembly sites. Disks will be assembled in halves, first on one side and then the other. Disk assembly includes gluing modules and common bus FPCs onto the front and rear sides of the discs and making electrical connections. QC is planned for each corrugated row assembly and then again after completion of the front and rear sides of each disk. Disks will be shipped in halves to BNL, where they will be installed into the larger SVT assembly. Disks are the last piece to be installed, after the IB and OB. Assembly will occur from the inner disks outward. ED0 and HD0 will be mounted to the SVT support cones. ED2–4 and HD2–4 will be mounted to the support cylinder. ED1 and HD1 could be mounted to either and will be iterated with global mechanics. Installation must include the dressing of the services, connecting of the air supply, and mounting of the RDOs. Each half disk will be tested after installation.

We plan to produce the outer global support structures at Purdue and/or LBNL. Readout will be led by ORNL with testing at multiple sites.

Collaborators and their role, resources and workforce: (Placeholder:) The SVT currently has collaborators at 20 institutions with the main institutional roles and resources outlined above.

Risks and mitigation strategy: The SVT depends crucially on its sensors, the ITS3 sensor used in the IB and the ITS3-based EIC-LAS used in the OB, EE, and HE, since they form the only known way to meet the full performance requirements within ePIC. Their development is ongoing and presents a risk. Together with the project we have identified two branchpoints, which are both based on schedule delays:

1. the ITS3 schedule remains compatible with the EIC project schedule, but EIC-LAS development is delayed,
2. the ITS3 schedule is delayed and becomes incompatible with the EIC project schedule.

If the first branchpoint were triggered, the SVT OB will be replaced with two MPGD barrel layers derived from the outer MPGD tracker, specifically its innermost (micromegas) layer. The SVT EE and HE will in this case each be replaced with in total up to seven near-identical MPGD disks, specifically based on the existing uRWELL disks. If, in addition, the second branchpoint were triggered, the SVT IB will be replaced by two or three layers based on the existing ITS2 sensor, as used in the ALICE and sPHENIX experiments, without EIC-specific modifications.

Additional Material

8.3.3.2 The MPGD trackers

Requirements

Requirements from physics: Micro-Pattern Gas Detector (MPGD) technologies have been chosen to complement the Si based tracking layers. MPGDs are relatively fast detectors able to provide precision space point measurements with good timing resolution, while also maintaining the overall conservative material budget that is required of the ePIC detector [?]. MPGDs will play a role in pattern recognition, ensure the central tracking system covers the required full pseudorapidity range $-3.5 \leq \eta \leq 3.5$, and aide in PID reconstruction.

The EIC collider is expected to deliver collisions with bunch lengths lasting about 10ns [?], which will require the MPGD detectors to provide timing resolutions $\mathcal{O}(10 \text{ ns})$ to separate events from adjacent bunches. For ep collisions of $10 \times 275 \text{ GeV}$, the DIS physics rate is expected to be around 500 kHz, while hadron and electron beam gas backgrounds rates are estimated to be 32.6 kHz and 3177.25 kHz, respectively [?]. Combining the timing information from the MPGDs with information from the Si detectors should allow pattern recognition algorithms to discriminate between physics and background signals. In addition to providing hit information with good timing resolu-

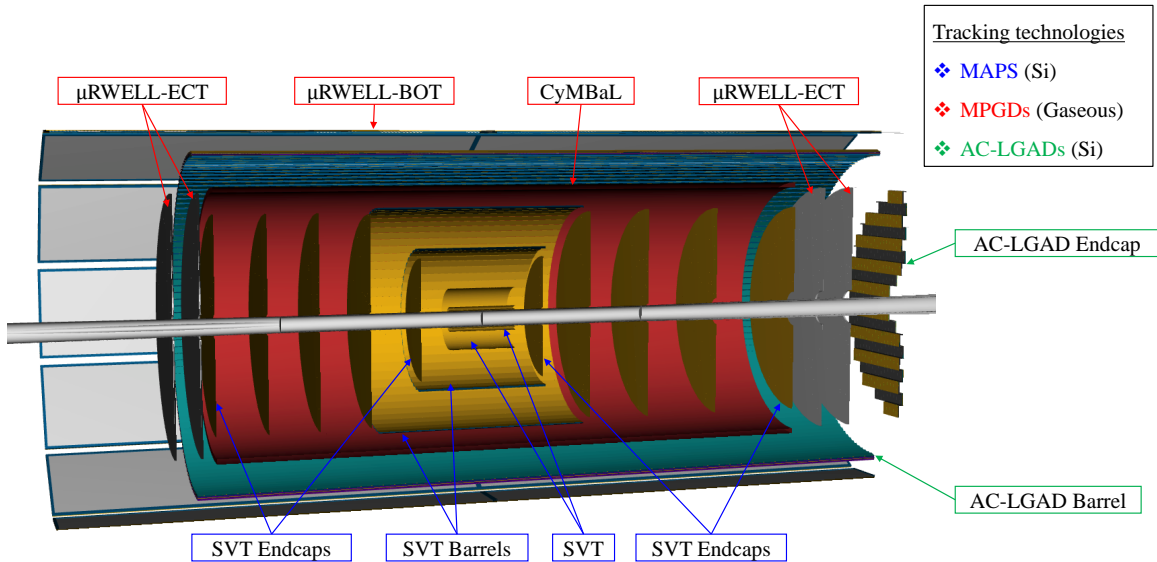


Figure 8.19: ePIC Tracking Subsystems

tions, the MPGDs will provide additional hit points needed for robust track reconstruction. Early simulations showed that the number of hit points used in the track reconstruction reduced from around 6 hits near $\eta = 0$, to only 3 hits at $|\eta| > 3$, due to tracks moving out of the acceptance of some of the Si layers. ePIC endcap gaseous trackers, (μ RWELL-ECT) were implemented to recover additional hits at larger η values. Figure 8.20 shows the hit number distribution in the current ePIC tracking detector as a function of η for different momentum ranges. In this configuration the ePIC tracker measures at least 5 hits per track over the region ($|\eta| < 3.5$).

Finally, as detailed in the Yellow Report [?], the hpDIRC requires the track entering the PID volume

to have good angular resolution (0.5 mrad at $p = 6$ GeV) in order to meet its performance requirements. Given the relatively low particle momenta of ePIC compared to high energy physics, mitigating multiple scattering effects will be crucial to meeting the hpDIRC requirements. This will be accomplished by providing the hpDIRC with precision hit points just before a particle enters its volume via [ePIC barrel outer gaseous tracker, \(\$\mu\$ RWELL-BOT\)](#) and after the particle exits the PID volume via the BIC.

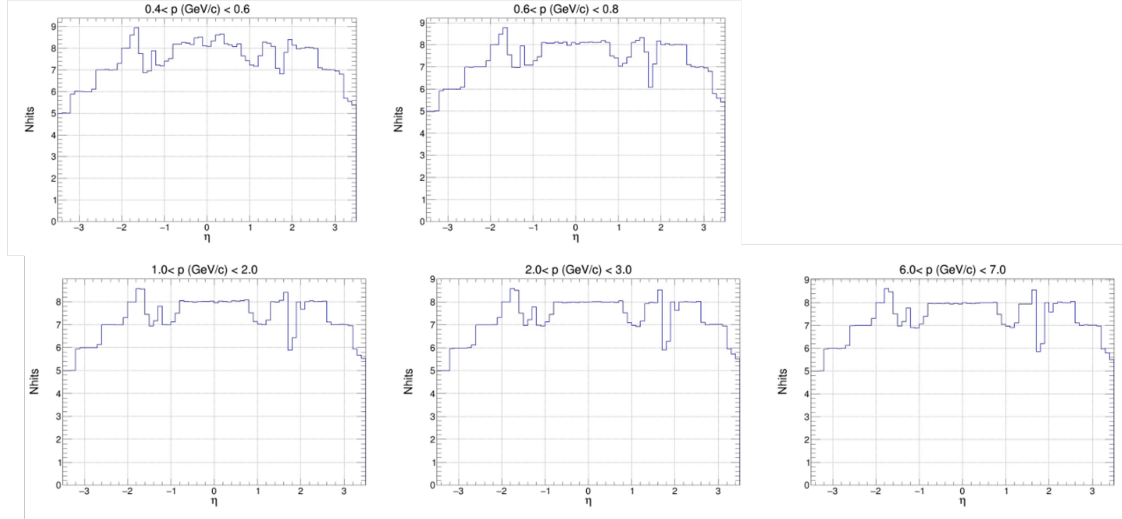


Figure 8.20: Total tracker hits vs. η for various momentum ranges.

Requirements from Radiation Hardness: Detailed simulation on radiation dose in ePIC has been performed. Fig. 8.21 shows the estimate of hadron and EM radiation doses in ePIC simulation along with location of MPGD layers [?]. Table 8.6 shows the maximum estimated radiation dose from various sources for MPGD trackers at various locations with 10 years of running at top machine luminosity and 100% detector and accelerator luminosity based on e+p PYTHIA simulation.

MPGD tracker	EM Radiation dose [krads]	Hadron Radiation dose [krads]	1 MeV neutrons equivalent fluence [cm^{-2}]	1 MeV protons equivalent fluence [cm^{-2}]
CyMBaL	0.22	0.15	2.7×10^{10}	2.0×10^{10}
μ RWELL-BOT	0.3	0.1	2.8×10^{10}	4.2×10^9
electron ECT	0.064	0.03	1.1×10^{10}	1.7×10^9
hadron ECT	0.87	0.23	3.0×10^{10}	8.5×10^9

Table 8.6: Maximum dose of radiation by different sources at MPGD tracker layers for e+p minimum-bias event at 500 kHz event rate for 10 years EIC running with 6 months run time per year and 100% efficiency [?].

Based on past experience with MPGD trackers in various experiments [ref] the MPGD trackers in ePIC will experience low radiation dose and hence will not pose aging problem. The electronics

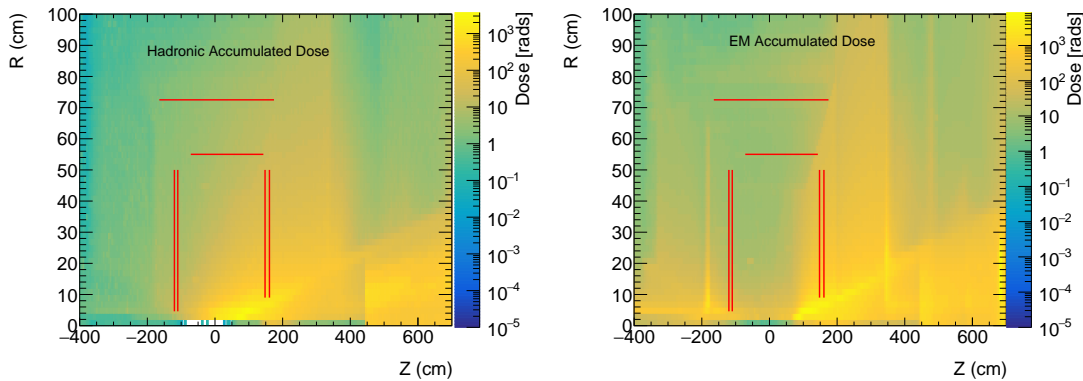


Figure 8.21: (left) EM radiation and (right) Hadron radiation dose estimate for minimum bias PYTHIA e+p events at 10x275 GeV at top machine luminosity for 6 months of running at 100% machine and detector efficiency [?]. The locations of MPGD trackers are shown by red lines [?].

1394 based on SALSA and also DC-DC converter, which will be mounted on the detector back end, are
1395 radiation hard as is shown by electronics group for ePIC (ref of electronic pTDR).

1396 **Requirements from Data Rates:** Table 8.7 shows hit rate per unit area for each MPGD sub-
1397 system in ePIC which is far lower than rate capability of MPGD detectors[add some old reference
1398 here]. Table 8.8 shows the maximum hit rate experienced by a channel for various MPGD trackers
1399 in ePIC [?]. The rates are low enough for ASIC developed for MPGD which can handle rate of 100
1400 kHz/channel.

MPGD tracker	DIS e+p rate [Hz/cm ²]	Hadron beam gas rate [Hz/cm ²]	Electron beam gas rate [Hz/cm ²]
CyMBaL	26.37	14.33	5.5
μ RWELL-BOT	9.82	5.33	1.7
electron ECT	144.68	78.63	437
hadron ECT	1326.36	720	201

Table 8.7: Hit rate per unit area of various MPGD trackers for e+p DIS events at 10x275 GeV with $1.54 \times 10^{34} cm^2 s^{-1}$ luminosity scaled from e+p DIS events at 18x275 GeV and $1.54 \times 10^{33} cm^2 s^{-1}$ luminosity, 10 GeV electron beam gas and 275 GeV hadron beam gas

1401 **Justification**

1402 **Device concept and technological choice:** Add text here.

1403 **Subsystem description:**

MPGD tracker	DIS e+p events [Hz]	Hadron beam gas [Hz]	Electron beam gas [Hz]
CyMBaL	3.68	0.05	4.78
μ RWELL-BOT	2.76	0.04	4.78
electron ECT	9.2	3.56	102
hadron ECT	101.2	4.39	39.88

Table 8.8: Maximum hit rate by a single channel of various MPGD trackers for e+p DIS events at 10×275 GeV with $1.54 \times 10^{34} \text{ cm}^2 \text{ s}^{-1}$ luminosity scaled from e+p DIS events at 18×275 GeV and $1.54 \times 10^{33} \text{ cm}^2 \text{ s}^{-1}$ luminosity, 10 GeV electron beam gas and 275 GeV hadron beam gas

CyMBaL: the inner cylindrical Micromegas barrel layer, i.e. CyMBaL, sits at a radius of 55 cm and covers, in the longitudinal direction, from $z=-105$ cm to $z=143$ cm. CyMBaL consists of 32 identical Micromegas tiles, bent at two different radii of 55 cm and 57.5 cm, that overlaps in the azimuthal (8 modules) and in the longitudinal directions (4 modules) to provide full acceptance coverage. A module is $67 \times 48 \text{ cm}^2$, with an active area of about $61 \times 46 \text{ cm}^2$. The base technology chosen for the CyMBaL modules is the cylindrical resistive Micromegas developed for the CLAS12 Barrel Micromegas Tracker (BMT) at JLab [?]. This technology meets the requirements in material budget ($\sim 0.5\% X/X_0$) and it has been designed to work in high magnetic field (5 T) and high charged particle fluxes. The CyMBaL's layout is presented in Appendix ?? . With the goal of limiting the material budget in the active area, the front-end electronics boards (FEBs) will be placed at the periphery of the system. The signals from the inner modules will be brought to the FEBs using micro-coaxial flat cables.

μ RWELL-BOT: The layout of the MPGD barrel outer tracker is presented in in ?? . For the large μ RWELL-BOT detector modules, thin-gap GEM- μ RWELL hybrid detector technology has been chosen to satisfy the detector requirement in term of position and timing resolution as well as detector efficiency and operation stability. The concept of thin-gap GEM- μ RWELL hybrid detector is presented in ?? . Proof of concept and preliminary performance results on small size prototypes tested in beam at Fermilab in 2023 are also reported in ?? . The design of the full size μ RWELL-BOT module prototype based on the thin-gap GEM- μ RWELL technology is presented in ?? as part of the Project Engineering Design (PED) effort to develop the engineering test article μ RWELL-BOT module based on thin-gap GEM- μ RWELL technology.

μ RWELL-ECT: Two MPGD disks are located both in the hadronic and the leptonic sectors, to cover the $|\eta| > 2$ pseudorapidity tracking regions. The disks geometrical envelope are detailed in Appendix ?? : the two

FEE: To meet the requirement of streaming readout new front-end chips for MPGD trackers in ePIC are being developed by Sao Paulo Universities and CEA Saclay IRFU . The chip , known as SALSA , has the following characteristics.

- 64 channels with large input capacitance range, optimized for 50-200 pF, reasonable gain up to 1nF
- Large range of peaking times: 50-500 ns.
- Large gain ranges: 0-50 to 0-5000 fC.
- Large range of input rates, up to 100 kHz/ch.
- Reversible polarity.

Other components: Add text here.

Performance

CyMBaL: The CyMBaL design aims at providing complete azimuth coverage. Along the longitudinal direction where the two halves of the system meet, only ~ 3 cm will not be covered. CyMBaL modules are expected to provide a hit spatial resolution around $150 \mu\text{m}$ with a time resolution of $10 - 20$ ns.

μ RWELL-BOT: The barrel outer tracker will provide hit space point resolution better than $150 \mu\text{m}$ on average in the eta range of $-1 \leq \eta \leq 1$ and $100 \mu\text{m}$ in the azimuthal direction φ and a timing resolution of ~ 10 ns. The tracker has an acceptance gap of 15% along because of space constraints imposed by the limited space in the ePIC detector. The tracker will operate at a nominal efficiency of $\sim 95\%$. The anticipated particle rate is low and does not pose any challenge in term of safety operation and long term stability of the μ RWELL-BOT trackers during the lifetime of the ePIC detector.

μ RWELL-ECT:

Implementation

Services:

CyMBaL: Each module will require:

- Two gas supply lines (in and out). Two modules might be connected in series for the gas distribution to limit the number of piping.
- Two high voltage lines (one negative line for the cathode and one positive line for the resistive layer. The mesh will be grounded.

Each module will be readout by four FEBs. Each FEB will required:

- Four connection lines for the low voltage distribution (LV): one pair for the **1.8 V and one for the 3.3 V**.
- Cooling in and out lines. Studies on the type of cooling and possible implementation in a serialize distribution will be done in synergy with the other subsystem of ePIC.
- One 4-line optical fiber connection to the RDO.

Subsystem mechanics and integration:

CyMBaL: CyMBaL integration and mechanics rely on the central tracker global support structures. CyMBaL modules will be connected to the support structure.

Calibration, alignment and monitoring:

CyMBaL: Two main calibration tasks are identified:

- Determination of the working point by efficiency scans. This calibration should be performed before the data taking campaigns and if there are important changes of the running conditions (as examples: gas composition and the temperature inside the ePIC barrel.

- Special runs for determining the pedestal value and the common noise to be subtracted from the ADC samples. Monitoring of the pedestal and the common noise during the data taking is under discussion in the DAQ working group.

CyMBaL module positions will be surveyed before integration. This database will be used as the starting point for the software alignment, that will be based on track reconstruction with and without magnetic field, and will involve all the tracking detectors.

It will be essential to continuously monitoring key parameters to assure uniform performance of CyMBaL.

- The gas delivering system must be continuously monitored. Any change in gas composition will dramatically affect CyMBaL performance.
- The environmental temperature, pressure and humidity close to the CyMBaL modules must be monitored: feedback loop to adjust the detector gains with changes in environmental parameters will be considered.
- The currents drawn by each high voltage channel must be monitored and logged with a frequency of about 1 Hz.
- The LV currents and the temperatures of each FEB must be monitored. Automatic safety actions should be in place if the readings show abnormal values.
- During data taking, hit occupancy maps, 2D efficiency, signal amplitude and timing distributions will be constantly monitored.

Status and remaining design effort:

CyMBaL: The resistive Micromegas technology has been extensively used in nuclear and particle physics experiments. In particular, 1D-readout cylindrical Micromegas tiles are in used at JLab in the BMT of the CLAS12 experiment since 2017, in experimental conditions well more challenging than those expected at the EIC. The main focus of the ongoing R&D is to upgrade the BMT technology to 2D readout. In order to limit the number of readout channels, the R&D also focus on exploiting the charge sharing thorough the resistive layer and using ~ 1 mm pitch readout strips. Several combinations of strip readout patterns together with layers of different resistivity have been tested in a beam test in MAMI in 2023. Further studies are ongoing with the cosmic rays test bench in Saclay and an additional beam test at CERN is planned for 2025. The production of cylindrical tiles is being refurbished using the BMT PCBs and a first completed detector is expected to be tested in Fall 2024. In parallel, the design of a CyMBaL module prototype has begun and its production is expected to be completed by Summer 2025.

μ RWELL-BOT: The R&D phase for the development of the μ RWELL-based trackers for EIC detector was completed in summer 2023 and the effort transitioned into project engineering design (PED) effort to develop the full size thin-gap GEM- μ RWELL engineering test article as a beta version of pre-production module 0 of μ RWELL-BOT tracker in ePIC detector. The design effort including the CAD drawings of all mechanical parts i.e. frames and support structures as well as the sensitive devices such as the GEM foil, the μ RWELL and the U-V strip readout PCB is in advanced stage and expected to be completed by end 2024. The fabrication of the full size engineering test article and the initial tests in a cosmic setup will take place during the first half of 2025. The second half of the year 2025 will be dedicated to a full characterization of the prototype in beam at CERN or Fermilab including stability and performance in magnetic field with strength similar to the one expected from the ePIC magnet. The 1.5 T GOLIATH magnet of the CERN NA H4 beam test area available to the

MPGD-focused DRD1 collaboration is one of option under consideration for the magnetic field test of the thin-gap GEM- μ RWELL engineering test article. The PED effort to develop the μ RWELL-BOT module including a detailed review of the design choices and options, the timeline and outlook for the completion of the engineering test article effort in anticipation of the module production phase is described in detail in ??

Environmental, Safety and Health (ES&H) aspects and Quality Assessment (QA planning): Considering MPPD consortium is composed of international collaboration so each factory responsible for assembling modules will follow guidelines of their local government to be in compliance with ES&H requirements. This include minimizing wastes during assembly procedure and disposal of harmful wastes in safe manner as directed by local government. During final integration of the detector subsystem at BNL , scientists and technicians will follow DOE guidelines as directed by BNL management.

The Quality Assessment protocol will cover the entire production lane of MPPD detectors. The readout PCBs will be assessed for mechanical precision and electrical continuity. The resistive layers will be checked for uniformity, During each step of the assembling, electrical continuity and high voltage capability of the different electrodes will be tested. Once the assembly of the module is finished, the module is checked for gas leakage and HV stability before bringing it outside of the clean rooms. Each finished detector will be then tested with cosmic rays in dedicated test benches. In these tests, the main parameters that will be studied for each module are the noise levels and the number of dead channels, efficiency and and gain and their uniformity over the surface. A database will be used to log all the information and results for each produced module.

Construction and assembly planning:

CyMBaL: CEA-Saclay will be the main production site for CyMBaL modules. The readout PCBs will be produced by industry partners. In Saclay, all the remaining part of the production process will be realized. The resistive layer will be added using serigraphy and the low-tension micromesh will be added using the bulk process (cite?) will be performed in the Saclay MPPD Lab. The curving and mechanical integration of the final detector will be done in a dedicated clean room. For quality assurance, each module will be tested using the available cosmic rays test bench.

μ RWELL-BOT: The construction and assembly plan and timeline for the μ RWELL-BOT is described in detail in appendix ??

Collaborators and their role, resources and workforce:

CyMBaL: CyMBaL design, production and tests will be lead by CEA Saclay. The details of the workforce will be added in appendix before the next draft.

μ RWELL-BOT: Three institutes — Jefferson Lab, Florida Institute of Technology, and the University of Virginia will participate in the construction, assembly, and characterization of μ RWELL-BOT ϕ -modules to ensure timely mass production. They will collaborate to develop a set of technical documents, ensuring that all modules are produced under consistent conditions, using appropriate infrastructure, and following standardized procedures for construction and quality control testing. All components of a μ RWELL-BOT -module will be designed by Jefferson Lab, however, each production site will procure and inspect the

components separately. It is crucial that all three production sites are equipped with suitable clean room infrastructure for the construction and assembly of μ RWELL-BOT -modules, as well as identical instrumentation for a standardized component inspection and module characterization. Each of the three institutes will be responsible for the construction and characterization of eight μ RWELL-BOT -modules (+ spares). The essential equipment needed for each institute are listed in Tab. ?? of appendix ?. Each institution will leverage on its existing MPGD infrastructure (clean room and detector lab and existing equipment) to minimize instrumentation costs but will upgrade wherever possible to meet the more demanding requirement of μ RWELL technology assembly. The personnel effort, expressed as a percentage of research time over the duration of the project, at each institute is provided in tables ?, ?, ? of appendix ?.

Risks and mitigation strategy: Add text here.

Additional Material Add text here.

8.3.4 Particle identification

Add text here.

8.3.4.1 The time-of-flight layers

Requirements and Justifications

Requirements from physics: With single hit timing resolution of 35 ps from the Barrel TOF (BTOF) and 25 ps from the Forward TOF (FTOF), the AC-LGAD TOF detector system can provide particle identification for low momentum charged particles, e.g., π -K separation at the 3σ level for $p_T < 1.2$ GeV/c for $-1.2 < \eta < 1.6$, and $p < 2.5$ GeV/c for $1.9 < \eta < 3.6$, respectively. By combining the PID information for low momentum particles from the TOF detectors and high momentum particles from Cherenkov detectors, ePIC will have excellent PID capability over a wide momentum range in a nearly 4π acceptance, which is crucial to achieve the goals of the EIC physics program. Besides precise timing resolution, AC-LGAD sensors can also provide precise spatial resolution, and thus aid track reconstruction and momentum determination. The requirements on the timing and spatial resolutions, as well as the material budgets are being evaluated in ePIC MC simulation to find the optimal configuration without over-designing these detectors. Table 8.9 summarizes the current specifications of the timing and spatial resolutions, material budgets, the covered area, channel counts and dimensions. Figure 8.22 shows the BTOF and FTOF layouts with an insert showing charge sharing on a sensor. Figure 8.23 shows the performance of the TOF detector in the form of $1/\beta$ as a function of particle momentum p for ep DIS events from PYTHIA+GEANT4 simulation. Together with the other PID detectors, we are able to demonstrate that the ePIC PID performance which includes the TOF detectors as one of the integral components meets the requirements.

Requirements from Radiation Hardness: The radiation fluence and dose at ePIC are significantly less than in the LHC experiments. It is safe to assume that the maximum foreseen fluence

Subsystem	Area (m^2)	dimension (mm^2)	channel count	timing σ_t (ps)	spatial σ_x (μm)	material budget (X_0)
Barrel TOF	12	0.5*10	2.4M	35	30 ($r \cdot \phi$)	0.015
Forward TOF	1.1	0.5*0.5	3.2M	25	30 (x, y)	0.05

Table 8.9: Required performance for physics and proposed configurations for the TOF detector system.

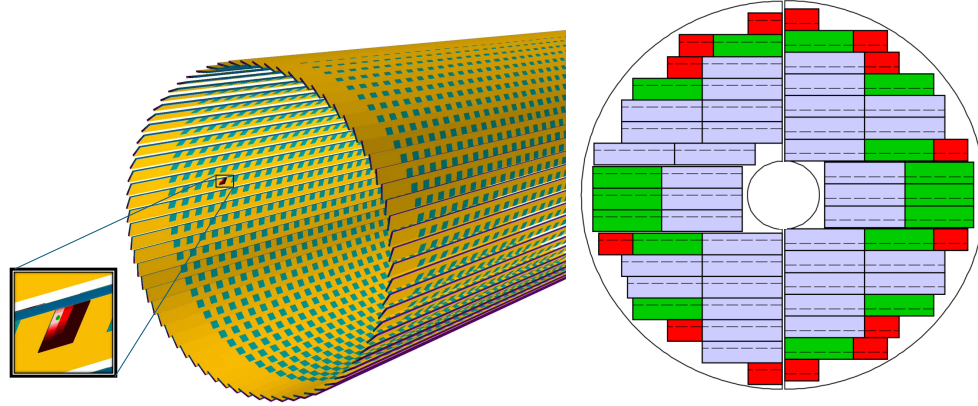


Figure 8.22: Geometries of BTOF with insert of sensor and charge sharing distribution (left), and the layout of sensor modules and service hybrids of FTOF on one side (right).

for the lifetime of the TOF detectors will be $< 5 \times 10^{12} n_{eq}/cm^2$, as seen in Fig. 8.24 and Tab. 8.10. Here the highest fluence between raw and 1MeV n_{eq}/cm^2 fluence was considered, as the standard NIEL correction is not applicable for some aspects of LGAD radiation damage.

Much work has been done to characterize and improve the radiation resistance of LGAD gain layers to meet the requirements at the LHC [11] (up to 2.5×10^{15} 1MeV n_{eq}/cm^2). Because of the sensitivity of the sensor performance to the value of the N+ sheet resistance (a feature absent from the conventional LGADs made use of for the LHC), it is possible that AC-LGADs may be significantly less radiation tolerant than their conventional cousins. Indeed, N-type doping is known to be particularly sensitive to hadronic irradiation, with N-bulk sensors inverting to P-bulk before exposure of even 1×10^{14} is accumulated. Furthermore, LHC LGAD detectors are designed to run at -30C to reduce the post-radiation leakage current, while in ePIC, the sensors will be operated at room or slightly lower temperatures for the experiment's lifetime. The leakage current increase due to radiation damage for the fluence in ePIC has to be low enough not to trigger a thermal runaway combined with the power dissipation from the readout chip, especially for the forward and end-cap region where the chips are bump bonded on top of the sensors.

Therefore, a radiation exposure run was performed before the ePIC LGAD design was finalized. Several sensors from HPK and BNL were irradiated at FNAL ITA facility (400 MeV protons) and at the TRIGA reactor in Ljubljana (MeV-scale neutrons) to probe radiation effect from ionizing and non-ionizing particles. The radiation exposure would be done in steps, allowing potential charge-collection pathologies, should they exist, to be mapped out for the development of models and corrections. By studying the sensor performance before and after irradiation, the change in N+ resistivity can be characterized, and this particular risk can be addressed. Sensors irradiated with

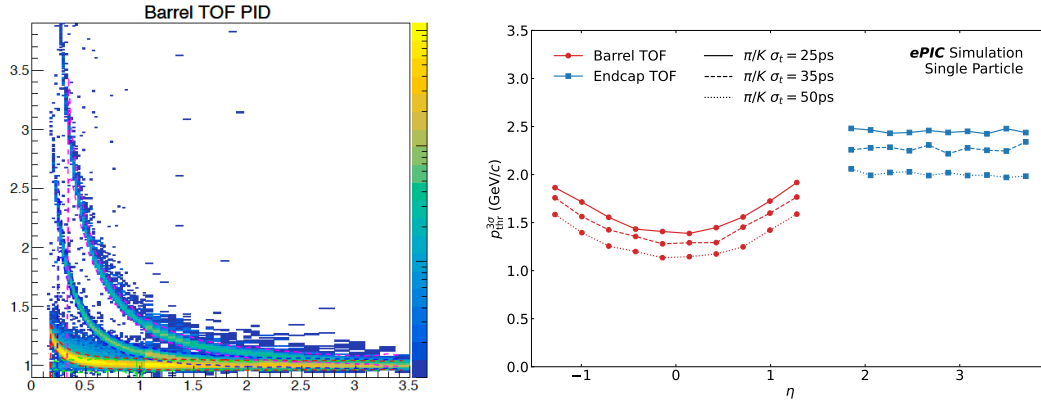


Figure 8.23: BTOF $1/\beta$ as a function of momentum (p) in the simulation performance with PYTHIA DIS events (left). Upper limits on the 3σ particle separation from BTOF and FTOF as a function of pseudorapidity (right).

1619 1 MeV neutrons were received in the Summer of 2024 and tested; the results are encouraging, as
 1620 seen in the following sections. Sensors were irradiated at the FNAL ITA facility but are still cooling
 1621 down from the activation; they will likely be available for testing in early 2025.

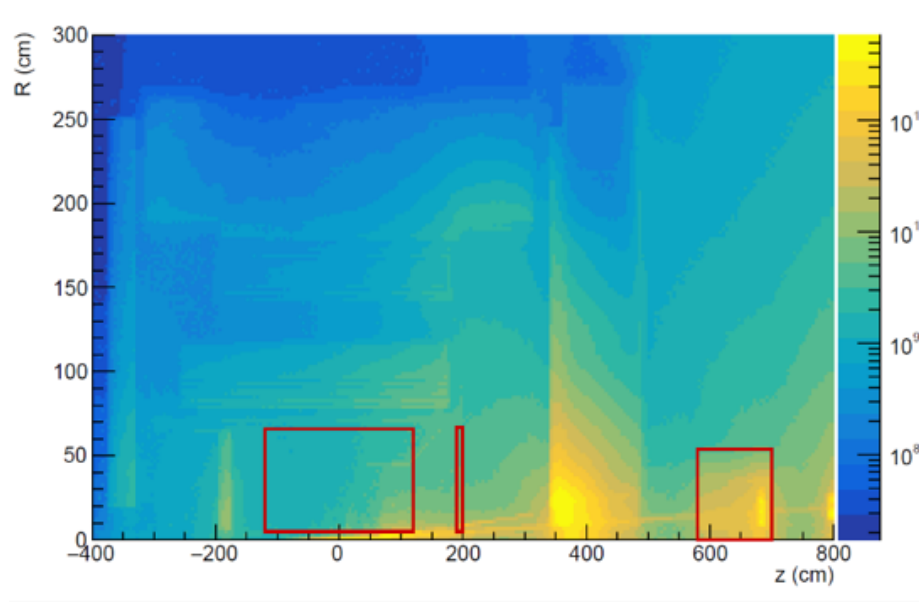


Figure 8.24: Fluence accumulated for 6 months at 100% time, corresponding to one year of data taking, the fluence has to be multiplied by the assumed 10 years of life time of the ePIC detector. Red squares highlight the barrel, end-cap, and B0 trackers detectors.

1622 **Requirements from Data Rates:** As the sensors and ASICs differ between the BTOF and FTOF,
 1623 the rate requirements are presented separately for both of these sub-components. On top of that,

RAW fluence			
System	Average	Min	Max
Barrel	5.4×10^{10}	3.4×10^{10}	5.9×10^{11}
End-cap	1.3×10^{11}	5.1×10^{10}	1.6×10^{12}
B0 trackers	3.9×10^{11}	3.3×10^{10}	1.8×10^{12}
NEQ fluence			
System	Average	Min	Max
Barrel	3.6×10^{10}	1.1×10^{10}	1.3×10^{12}
End-cap	1.2×10^{11}	3.2×10^{10}	8.4×10^{11}
B0 trackers	4.5×10^{11}	2.7×10^{10}	4.2×10^{12}

Table 8.10: RAW and NEQ fluence per system for the lifetime of the ePIC experiment, assuming 10 years of data taking at 50% time.

the phase space coverage is different (mid-rapidity vs forward rapidity) which mandates different particle rate and background calculations.

BTOF: The BTOF simulations show an average of 5 charged particles per ep collision at the highest center of mass energy. At the 500 kHz collision rate this amounts to a 2.5 MHz particle rate on the surface of the BTOF barrel. BTOF contains 2.4 million channels which give an average hit frequency per channel of 1 Hz. Due to charge sharing of the AC-LGAD strips we expect a particle to generate signals on maximum 3 strips/channels of the readout ASIC.

FTOF: The FTOF simulation shows an average of 2 charged particles per ep collision at the highest center of mass energy. At the 500 kHz collision rate this amounts to a 1 MHz particle rate on the surface of FTOF disk. Since FTOF is expected to contain 5.8 million channels the average hit frequency per channel is 0.2 Hz. Due to charge sharing of the AC-LGAD pixels we expect a particle hit to generate signals on maximum 3x3 pixels/channels of the readout ASIC.

Electronics Noise: Noise measurements have consistently shown a rate of 30 Hz per channel. Such a noise rate is achieved with a 5-sigma cut and is deemed to be even somewhat pessimistic but this is the number we plan to use during these calculations.

Data Rates: We will assume a typical CERN-developed ASIC's zero-suppressed data format which is: 32 bits header, Nx32 bits of channel data (ADC, TDC, ch Id) and 32 bits trailer. Such data formats are used in e.g. HGCROC which is a precursor to our expected ASICs.

For BTOF the expected signal rate of bits per second per ASIC is 1 Hz (particle rate) \times 5 \times 32 (bits for 3 hits) \times 64 (channels) = 10 kbps, while the noise rate is 30 Hz (noise) \times 3 \times 32 (bits for a single hit) \times 64 (channels) = 185 kbps. Summing up these 2 contributions we reach the total data rate per-ASIC of 195 kbs. Since an RDO reads out 128 ASICs per half stave we expect a rate per RDO (or fiber) of 24 Mbps. For the entire BTOF which contains 288 half staves we reach a total rate requirement of 7 Gbps.

For FTOF the expected signal rate of bits per second per ASIC is 0.2 Hz (particle rate) \times 11 \times 32 (bits for 9 hits) \times 1024 (channels) = 72 kbps, while the noise rate is 30 Hz (noise rate) \times 3 \times 32 (bits for a single hit) \times 1024 (channels) = 3000 kbps. Summing up these 2 contributions we arrive at the per-ASIC data rate of 3.1 Mbps. For the worst case of 28 ASICs per RDO (or fiber) = 87 Mbs per fiber link to DAQ. For the total FTOF sub-detector of 212 RDOs we reach 18 Gbps.

We note that these rates are very small and well within the reach of ASICs, interconnects as well as

fiber interfaces of our electronics and DAQ. We also note that the data rates are dominated by the electronics noise which we can control by raising or lowering the various ADC or TDC thresholds of the ASIC thus adjusting the system performance even ASIC-to-ASIC if required.

Device concept and technological choice: AC-coupled Low-Gain Avalanche Diode (AC-LGAD) is a new silicon sensor technology. Signals produced by charged particles in the sensor active volume are amplified via an internal p+ gain layer near the sensor surface. Signals induced on a continuous resistive n+ layer on top of the p+ gain layer, are AC coupled to patterned metal readout electrodes, which are on the sensor surface and separated by a dielectric layer from the n+ layer. The internal signal amplification and thin active volume enables precise timing measurement, while charge sharing among neighboring electrodes can provide precise position measurement. The AC-LGAD technology has been chosen to use for particle identification, tracking, and far-forward detectors at EIC where precision timing and spatial measurements are needed.

Subsystem description:

General device description: The BTOF consists of 144 tilted staves, each of which is made of two half staves with a total length of around 270 cm sitting at a radial position around 65 cm. AC-LGAD strip sensors are mounted on low mass Kapton flexible printed circuit boards (FPCs), and are wire-bonded with front-end ASICs. The FPCs are glued onto mechanical structures made from low density Carbon-Fiber (CF) materials, and bring power and input/output signals to the sensors and ASICs. The heat generated by the frontend ASICs are removed by an embedded Aluminium cooling tube in the CF structure. The FTOF consists of detector modules made from AC-LGAD pixel sensors bump-bonded with front-end ASICs. These detector modules are mounted from both sides onto a thermal-conductive supporting disk with embedded liquid cooling lines located around 190 cm away from the center of the experiment. Since the irradiation flux at the EIC is much smaller than that at the LHC, it is assumed that the radiation damage will not be a concern and the AC-LGAD sensors can be operated at room temperature.

Sensors: The sensors identified for the TOF timing layer are AC-LGADs that can provide both exceptional position resolution and timing resolution [1, 12–14] while maintaining low channel density. The BTOF will employ strip sensors 1 cm long with a pitch of 500 μm and a metal electrode width of 50 μm (large pitch up to 1000 μm is also under investigation). The sensor thickness will likely be 50 μm to reduce the input capacitance to the pre-amplifiers but 30 μm thick strip sensors are also under investigation. The full sensor size will be $3.2 \times 2 \text{ cm}^2$ with 1 cm segments. The FTOF will employ pixel AC-LGADs with a pitch of 500 μm and metal electrode size of 50 μm (large pitch up to 1000 μm and electrode size of 150 μm are also under investigation). The thickness of the pixel sensors will likely be 20 μm to maximize the time resolution reach, as the input capacitance is not a concern for small pixels. Nevertheless, 30 μm thick pixel sensors are also under investigation. The full-size sensor will be $1.6 \times 1.6 \text{ cm}^2$ with $0.5 \times 0.5 \text{ mm}^2$ pixels. Studies on smaller-scale devices are presented in [1, 12] and in the following. The full-size strip sensor prototypes have been produced for the first time in the most recent HPK fabrication and received at the time of writing. Procurement of the full-size pixel sensor prototypes is still in progress. A complete evaluation of the full size prototype sensors is expected in the middle/end of 2025.

Front-End Electronics (FEE): The FEE for AC-LGAD based detectors is focused on the development of an ASIC and service hybrids. An ASIC featuring a Constant Fraction Discriminator (CFD) chip is being developed at Fermilab for the BTOF. The efforts have been focused

on optimizing the analog frontend design to read out AC-LGAD strip sensors. Two versions of the ASICs, FCFDv0 and FCFDv1, featuring single- and multi-channel preamplifier and CFD, respectively, have been fabricated and tested. The new versions, FCFDv1.1 with further improvement to the frontend design tailored to 1 cm AC-LGAD strip sensors, FCFDv2 with digital readout, are under development with an expected deliver date in early 2025 and 2026, respectively. The EICROC project by the French group is focused on designing an ASIC for reading fine-pixelated AC-LGAD sensors, optimized pixel-based AC-LGADs detectors at ePIC such as B0, OMD, Roman Pots, and FTOF. The first version, EICROC0, is a 4x4 channel ASIC with $0.5 \times 0.5 \text{ mm}^2$ pixel size, featuring components like a transimpedance pre-amplifier, 10-bit TDC for timing, 8-bit ADC for amplitude measurement, and an I2C slow control interface. It is designed for low capacitance and sensitivity to low charges (2 fC), operating with 1 mW per channel, and targeting 30 ps timing and $30 \mu\text{m}$ spatial resolution. The prototype is currently under testing, with noise issues being addressed for future iterations. The next version, EICROC1 (expected in 2025), will feature a 16x8 channel configuration, followed by the final 32x32 channel version for full-scale implementation.

The service hybrids (SH) consists of a readout board (RB) and power board (PB). A schematic design of service hybrids, which serves 3 modules or 12 sensors/ASICs, for FTOF is shown in Fig. 8.25. The readout board will aggregate data from multiple ASICs to a lpGBT (from CERN) transceiver chip via e-links, and then convert to optical signals via a VTRx+ chip (from CERN) to be transmitted to the backend data acquisition system. lpGBT and VTRx+ are designed for HL-LHC so have been proven to be sufficiently radiation hard for the EIC environment. The VTRx+ has one uplink up to 10 Gbs (for receiving clock and control signals), and four downlinks (for data transmission), each up to 2.56 Gbs, so it can transmit data up to four lpGBTs. The readout board also hosts interface connectors to the module board (as described later) and power board, as well as to input LV and BV cables. The power board provide low voltages for ASICs (1.2V), as well for lpGBT (1.2V) and VTRx+ (2.5V and 1.2V) on the readout board via DC-DC converters. The CERN bPOL48V module is chosen as the main converter, which takes an input of 15V and converts it into 1.2V and 2.5V. As illustrated in Fig. 8.25, the RB is situated on top of the PB and sensor module. The PB is directly contacting the cooling structure to facilitate efficient cooling of heat dissipation from DC-DC converters. The SH will have three different types with different lengths, serving 3 (12), 6 (24) and 7 (28) modules (sensor/ASICs). This will provide the most efficient coverage of a circular shaped disk while minimizing number of cables and fibers. The example shown in Fig. 8.25 is the shortest version (about 100mm long) which serves 3 modules. The latest layout design for FTOF disk is shown in Fig. 8.22 (right), where different colored boxes indicate different types of SHs. Prototyping of the SH is in an advanced stage. A pre-prototype readout board (ppRDO) has been developed and under testing, based on an Xilinx FPGA chip and a commercial SFP+ optical transceiver. The first prototype RB and PB based on CERN chips will be soon developed, especially based on similar existing design of the CMS endcap timing layer (ETL) detector.

Flexible Printed Circuit boards: The Flexible Printed Circuit (FPC) is used to read out data and distribute power to the sensors and ASICs. In the acceptance region, a material budget of $1\% X/X_0$ is required, meaning the FPC material should be as minimal as possible. Additionally, the FPC must be 135 cm in length. To meet these stringent requirements, careful consideration of the FPC material is necessary, as signal loss is expected with such a long FPC, especially if using polyimide, a standard material in FPCs. The sPHENIX experiment encountered a similar challenge with their Inner Tracker (INTT), a silicon sensor tracker, and successfully addressed it by using Liquid Crystal Polymer (LCP) instead of polyimide as the dielectric material. This technology will be adopted for our detector as well.

BTOF stave design: Barrel staves are divided into two half-staves, with services and con-

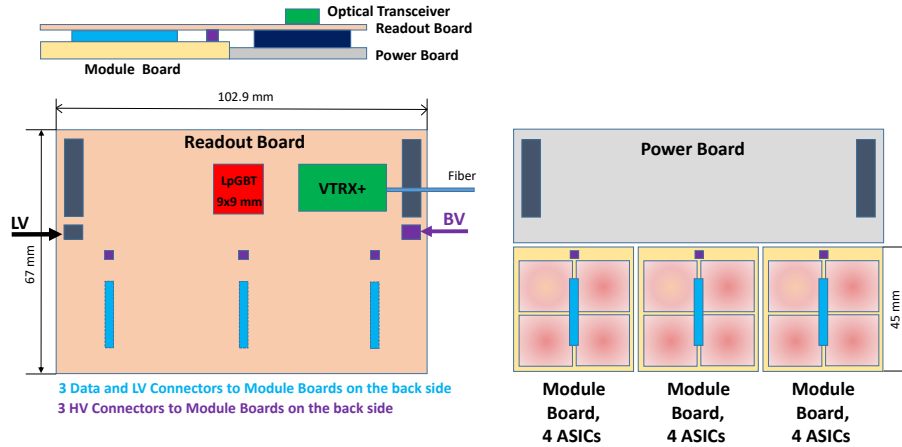


Figure 8.25: A schematic design of service hybrids for FTOF, which serves 3 modules or 12 sensors/ASICs.

nections coming from the outer side. The half-staves consist of a support structure with an integrated cooling pipe, flexible printed circuit (FPC), sensors, and ASICs. Sensors and ASICs are mounted on both the front and back sides of the half-stave, making it double-sided, with enough overlap to achieve 100% coverage in the stave direction. The lateral overlap and tilting ensure 100% coverage in the direction parallel to the staves. In total, there are 64 sensors and 128 ASICs on each side of the half-staves.

FTOF module design: A schematic design of the module for FTOF is shown in Fig. 8.26. Each module consists of 2×2 LGADs sensors and ASICs. It is covered by a module PCB board (MB), which will provide LV power (1.2V) and transmit the data of ASICs via a board-to-board connector to the RB. In addition, the MB also has a BV connector to the RB for providing the BV to LGADs sensors. ASIC readout will be wire-bonded to a metal pad near the edge of the module on the side facing the baseplate and cooling structure, as illustrated in Fig. 8.26 (right). LGADs sensor and ASIC will be connected via bump bonding. Dimensions shown are preliminary and will be adjusted as the prototyping progress. In the current design, the LGADs sensor is placed underneath the ASIC. The motivation is to have the sensor as close as possible to the cooling structure to ensure lower and stable temperature, which has been proven to be essential for achieving optimal time resolution. An alternative option would be to swap the ASIC and sensor layer, which has the advantage of more efficiently dissipating heat primarily generated by the ASIC. A final choice will be made as the prototype progress, especially after realistic thermal performance studies have been carried out.

Performance The AC-LGAD systems, including the BTOF, FTOF, and far-forward systems (Roman Pots, OMD, and B0 tracker), share a common readout chain currently under development. Performance evaluations are being conducted in various laboratory environments as part of the ongoing R&D efforts. A schematic of the full readout chain is shown in Fig. 8.27. The effort can be divided into two parts: 1) integrating the sensors with ASIC, 2) development of the readout-board and power board.

The Fermilab team has been developing an ASIC targeting the AC-LGAD strip sensors for BTOF.

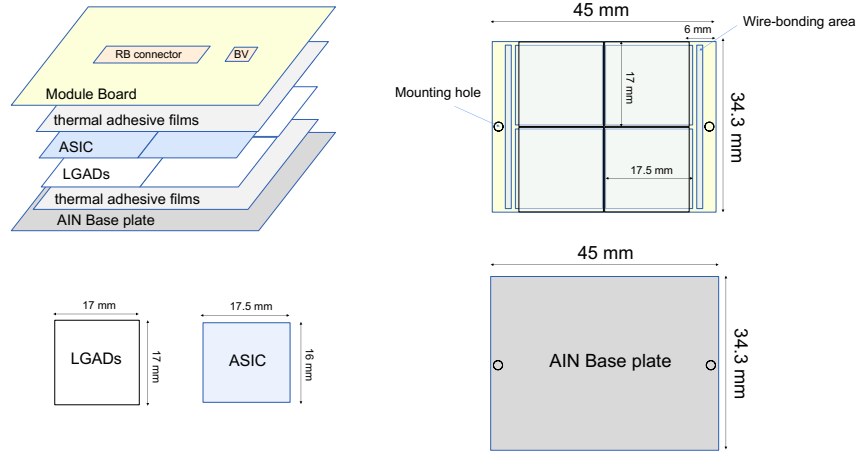


Figure 8.26: A schematic design of the module for FTOF, which consists of 2×2 LGADs sensors and ASICs.

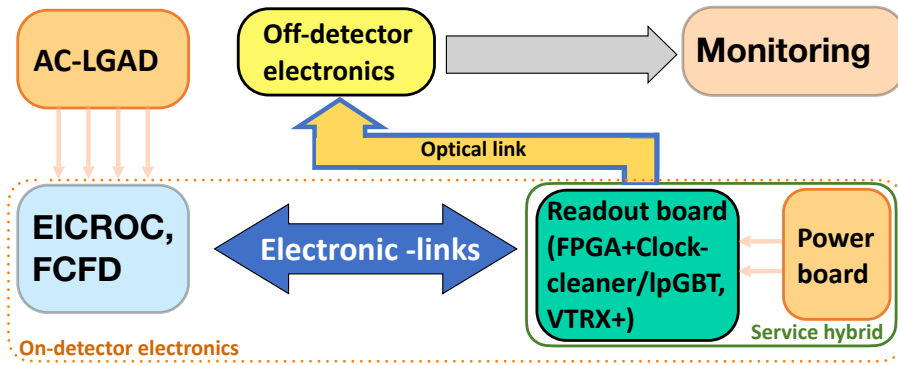


Figure 8.27: Schematic of the AC-LGAD sub-system readout chain. Each component is undergoing design, (pre-)prototyping, testing under various environments, and customization to meet the specific requirements of individual subsystems.

1777 Studies showed that Constant Fraction Discriminator (CFD) could provide a better timing reso-
 1778 lution with small signal amplitude from LGAD than leading edge discriminator [15]. The first
 1779 single-channel CFD-based ASIC (FCFDv0) wire-bonded to a DC-LGAD sensor achieved 35 ps
 1780 timing precision with beam, where the dominant contribution is expected from the intrinsic resolu-
 1781 tion of the LGAD sensor. A 6-channel prototype (FCFDv1) was developed for AC-LGAD sensors,
 1782 demonstrating 11 ps jitter in charge injection and 50 ps time resolution with 0.5 cm AC-LGAD
 1783 strip sensor in test beam. Ongoing efforts are focused on optimizing the frontend design for 1 cm
 1784 AC-LGAD strip sensors for the BTOF.

1785 Assemblies of 4×4 AC-LGAD pixel sensors with $500 \times 500 \mu m^2$ pixelation and $30 \mu m$ thickness,
 1786 and 4×4 EICROC0 ASICs, were completed by the BNL, IJCLab, OMEGA, and Hiroshima groups
 1787 on test-boards developed by IJCLab/OMEGA. Testing included scans of the analog and digital
 1788 components using charge injection and beta particles from a Sr-90 source, resulting in a measured
 1789 jitter of 8-9 ps for charges above 20 fC. Both wire-bonded and flip-chip assemblies were developed

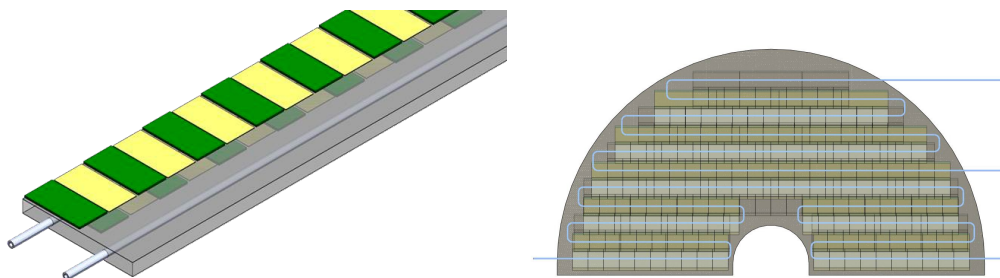


Figure 8.28: schematic drawings of one BTOF stave (left) and half of the whole FTOF (right) cooling pipes.

for various characterizations. Additional tests using Transient Current Technique (TCT) laser scans were conducted to map out charge distribution, and various tests are still ongoing.

ORNL is developing flexible Kapton PCBs for TOF applications, where sensors and mockup ASICs will be glued, wire-bonded, and co-cured onto a composite structure at Purdue for evaluation. Flip-chip options will be available soon, aiming to support low-cost sensor-ASIC hybridization techniques.

In FY24, BNL, LBNL, and Rice developed a prototype board (ppRDO) for precise clock distribution and ASIC integration for AC-LGAD systems. Key milestones, including schematic designs, part orders, PCB layout, and initial testing, were completed ahead of schedule. Firmware development and performance tests on clock-cleaning, jitter, and power distribution are ongoing. The collaboration aims to continue in FY25, focusing on the development of a readout board (RBv1) and power board (PBv0) for AC-LGAD systems, supporting TOF applications and ensuring DAQ compatibility. The ppRDO includes three components: 1) FPGA, 2) clock cleaner, and 3) SFP+ module. Future versions will adopt IpGBT to replace the FPGA and clock cleaner, and VTRx+ to replace the SFP+ module, improving performance, radiation hardness, and integration.

Implementation

Services: Electric power is distributed to the detector components via the Power Board (PB), which is part of the Service Hybrid (SH). The SH also includes the functionality of the Readout Board (RDO). In the case of BTOF, one SH supports 64 sensors and 128 ASICs, with SHs placed on both sides of the stave. For FTOF, several types of SHs are used, covering 12, 24, or 28 sets of sensors and ASICs. The SH is distributed on the mechanical and support disk, together with sensor modules.

Low Voltage (LV) and High Voltage (HV) cables are connected to the PB, where multiple DC-DC converters step down or adjust the voltages as needed. HV is applied to groups of multiple sensors, rather than distributed individually to each sensor. The size of each sensor group is determined by the design of the sensors and the electronics. Table 8.11 summarizes the service (cables and tubes) necessary for TOF detectors.

A liquid cooling system is employed to control the temperature of the detector. For the BTOF stave, one or two cooling pipes are integrated into the stave sandwich structure, with liquid flowing in one direction along the length of the stave. In FTOF, a winding liquid pipe is integrated into the support sandwich structure. The flow rate and pipe diameter are determined by the amount of heat

subsystem	item	quantity	diameter (mm)	lengths (m)	description
BTOF	FEE LV	24	20	15–25	Rack to Panel, 8AWG (24 AWG sense pairs)
BTOF	FEE LV	72	6.3	8	panel to detector, Alpha PN: 2424C SL005
BTOF	FEE HV	18	14	15–25	Rack to Dist. Panel
BTOF	FEE HV	144x2	1.5	8	panel to sensor
BTOF	cooling tubes	144x2	5	> 2.6	supply/return from panel to stave (Aluminum)
BTOF	cooling tubes	4x2			supply/return to panel
FTOF	FEE LV	212	9.04	25	supply/return LV from FEE to Rack
FTOF	FEE HV	14	14	25	rack to dist. panel
FTOF	FEE HV	212	2.42	10	panel to sensor
FTOF	cooling tubes	2x2	5		supply/return from panel to detector (Aluminum)
FTOF	cooling tubes	2			supply/return to panel

Table 8.11: Summary of BTOF and FTOF low voltage and high voltage powersupply cables to distribution panels and then to the detector FEE (the exact numbers are being checked at the time of writing).

1821 generated and the detector's performance requirements, thermal finite element analysis determines
 1822 the design. The pressure must remain below the surrounding air pressure to ensure safe operation.
 1823 Fig. 8.28 shows a single BTOF stave with cooling pipe (left) and half of the FTOF structure with
 1824 cooling pipes (right).

1825 **Subsystem mechanics and integration:** Both the BTOF and FTOF detector systems are sup-
 1826 ported by their own support structure, which is integrated and supported by the global support
 1827 tube (GST). The BTOF is a barrel geometry time-of-flight detector system located at a radius of
 1828 63cm from $z = -117.5\text{cm}$ to $z = +171.5\text{cm}$ along the beam direction as shown in Fig. 8.29. Both
 1829 detector subsystems have 7.5cm space in radial direction for BTOF and in the beam direction for
 1830 FTOF. The three engagement rings (each of 5mm width) are made from composite materials as a
 1831 sandwich and support the BTOF detector - they are itself supported by the GST. A first concept

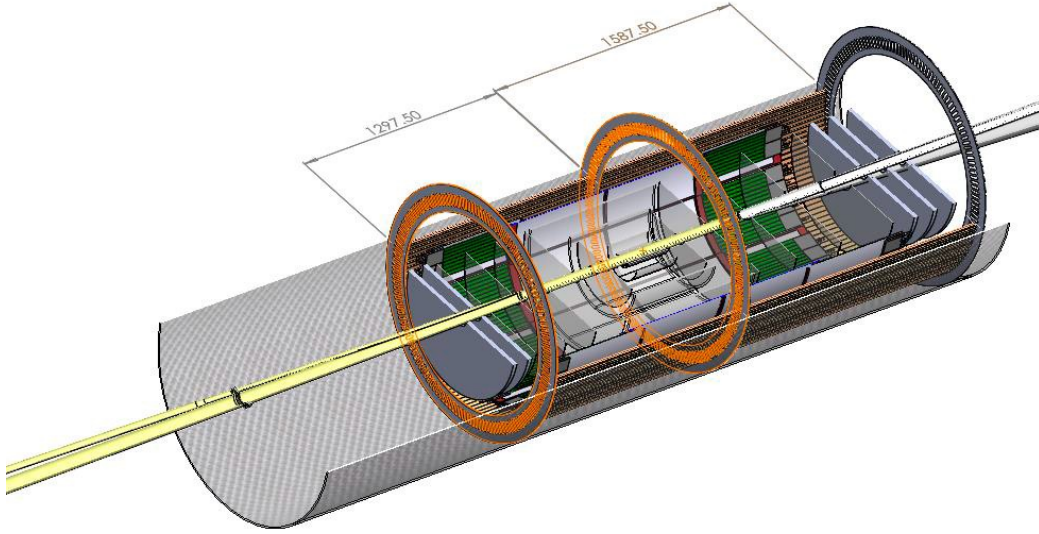


Figure 8.29: Barrel TOF supporting mechanic structure with engagement rings situated and supported by the EPIC global support tube structure (GST). The width of each of the three engagement rings is 5mm.

1832 was developed for a BTOF stave mounting mechanism employing the engagement rings by clips
 1833 with staves at an 18 degree angle. Staves are removable individually to ease maintenance. The
 1834 FTOF detector is designed in two half disc structures, or dee's, that are kinematically mounted to
 1835 the GST. Services (readout, power, cooling) of the BTOF and FTOF are routed either way and sup-
 1836 ported itself by the GST. Table 8.12 lists the positions of BTOF and FTOF relative to the global ePIC
 1837 geometry.

subsystem	z_{min} (cm)	z_{max} (cm)	inner radius (cm)	outer radius (cm)	stave angle
Barrel TOF	-117.5	171.5	62	69.5	18°
Forward TOF	185	192.5	10.5	60	0

Table 8.12: BTOF is designed with a barrel geometry surrounding the beam pipe and interaction point, while FTOF is a disk geometry perpendicular to the beam direction on the hadron side (positive z).

1838 **Calibration, alignment and monitoring:** **Calibration and alignment:** For spacial calibration
 1839 and alignment, the TOF layer is essentially treated as a layer of the overall tracking system. There-
 1840 fore, spacial alignment will be carried out as part of the entire tracker. This is typically based on the
 1841 match between tracks reconstructed in other layers of the tracking, then extrapolated to the TOF
 1842 and the hits in the TOF. By combining the information from many tracks, high precision can be
 1843 achieved.

1844 To exploit timing in the reconstruction of the charged tracks, the different TOF channels will have

to be synchronised to a precision of a few picoseconds. The absolute time calibration (or phase shifts relative to the beam clock) is not a particular concern, as all the event reconstruction relies on the relative time between tracks within the same collision event. The time offsets of the TOF channels can be inter-calibrated using all the tracks collected online through a fast reconstruction stream. The distribution of the reconstructed time at the vertex of these tracks – assuming they are pions – should have an rms spread of approximately 50 ps, including the time spread of the luminous region and detector resolution. The mean time of this distribution over many tracks provides the reference calibration points. Non-pion particles will contribute to the tail of the distribution, which can be cleaned up using an iterative procedure but not necessary. These calibrations can be made available for the prompt reconstruction of the events and updated frequently.

Monitoring: In the readout scheme of the TOF, a common clock is distributed to the individual channels belonging to the same service hybrid. The time stability of the clock distribution can be monitored with a precision of a few ps every second.

Status and remaining design effort: eRD112 and eRD109

eRD112: Sensor R&D effort A brief summary of eRD112 activities is reported in this section, for a more detailed review of the sensor development effort consult the 2024 erd112 report document. HPK sensors from the latest production have been tested at the Fermilab test beam facility; the results are summarized in Ref. [1]. The summary best results are reported in Fig. 8.30. The same HPK production was tested in laboratory with focused laser TCT and showed similar results as reported in Ref. [13]. The presented strip sensors (Fig. 8.30, Left) show a constant time resolution of around 35 ps, which is within the requirements for the ePIC TOF. The strip reconstructed position resolution is between 10-20 μm , which is also within the ePIC TOF requirement of 30 μm . The best result for pixel sensors (Fig. 8.30, Right) shows an homogeneous time resolution of 20-25 ps, well within ePIC TOF requirements. The position resolution instead is 20-70 μm across the device; the charge-sharing mechanism allows for precision reconstruction in between metal electrodes, but the resolution is significantly worse for hits directly on the metal electrodes.

The position resolution requirement for the FTOF is 30 μm . Therefore, pixel technology needs to be refined to meet the requirements. The new HPK production (expected by the end of the year) includes smaller electrode sizes and larger gaps between electrodes that could provide good reconstruction across the sensor. However, it was observed that a larger gap decreases the total S/N between electrodes, which might degrade the overall performance of the sensors. Results from a BNL production provide a promising alternative to square metal pixels. The S/N is better across the sensor for a cross-shape electrode given the same central metal shape, allowing for better reconstruction using charge sharing. HPK did not include cross-shape geometry in the latest production, but it might be included in the next one. Another producer of cross-shaped AC-LGADs is Fondazione Bruno Kessler (FBK). The FBK prototypes were investigated with a laser TCT, and a similar behavior was observed for cross-shaped devices [14].

The sensors irradiated at the Triga Reactor with 1 MeV neutrons were received in Spring 2024 and characterized both for electrical properties (capacitance and current over voltage) and with the laser TCT station. Gain degradation can be probed with measurements of capacitance over voltage by identifying the gain layer depletion point (V_{GL}). Fig. 8.31, Left, shows the change in the gain layer for the irradiated HPK AC-LGADs from several wafers, with different N+, oxide and active thickness, up to 1×10^{15} Neq; in the region of interest for ePIC $< 10^{13}$ Neq the gain layer is unchanged. The charge-sharing properties after irradiation were tested using a focused IR laser in the laboratory. As seen in Fig. 8.31, Right, the spatial response of the sensor is unchanged after irradiation up to 5×10^{14} Neq. The current increase in the irradiated HPK sensors is also negligible until $< 10^{13}$ Neq, as shown in Fig. 8.31, Bottom. The measurements were done at room temper-

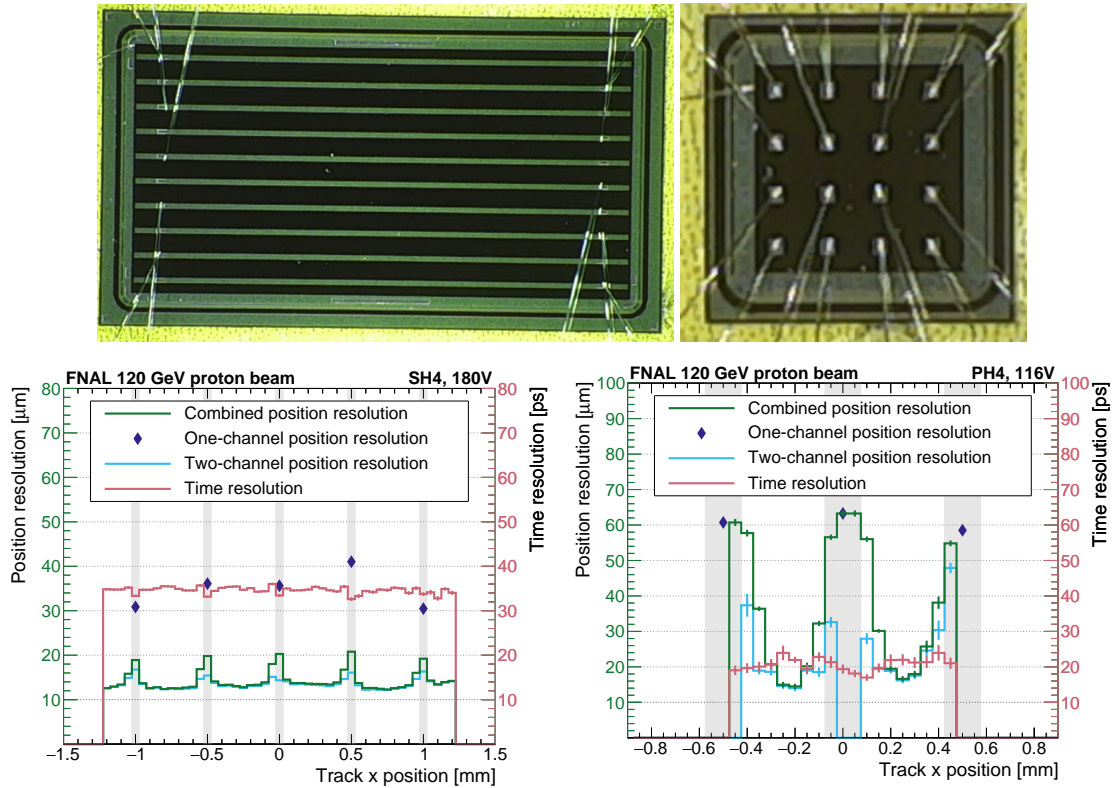


Figure 8.30: Left: Picture and beam test results for HPK strip sensor, 1 cm long, 500 μm pitch, and 50 μm metal electrode width. Right: Picture and beam test results for HPK pixel sensor, 4x4, 500 μm pitch, and 150 μm metal electrode width. Plots from Ref. [1].

1892 ature; therefore, no cooling will be necessary to reduce the dark current, which would increase
 1893 the sensor power dissipation in ePIC. In conclusion, no change in the behavior of the sensors is
 1894 expected during the lifetime of the ePIC detector due to radiation damage.

1895 **eRD109: readout R&D effort** A more detailed review of the electronics development effort can
 1896 be found in the 2024 eRD109 report document. In the following section, a brief summary will be
 1897 provided.

1898 The Fermilab team has continued the development of the FCFD ASIC prototype and, in FY23, has
 1899 designed the first multi-channel prototype with this approach, labeled as FCFDv1. Numerous tech-
 1900 nical improvements were implemented based on the experience with FCFDv0, aimed at addressing
 1901 the stability and performance of the system. The FCFDv1 ASIC was submitted for production in
 1902 September 2023, and received in January 2024. A specialized readout board was designed to ac-
 1903 commodate the FCFDv1 connected to a 0.5 cm HPK AC-LGAD strip sensor. Initial measurements
 1904 of the performance were done using internal charge injections performed with an LGAD-like sig-
 1905 nal. With input capacitance ~ 3.5 pF a jitter of around 11 ps was achieved, as shown in Fig. 8.32,
 1906 left. Test beam campaigns have been performed to study the performance of the FCFDv1 in June
 1907 2024. The newly introduced amplitude readout was found to function well, and results show 100%
 1908 efficiency when combining neighboring strips. The time resolution measured from the beam test
 1909 was around 50 ps. A further design improvement is foreseen in FCFDv1.1 to accommodate 1 cm
 1910 AC-LGAD strip sensor and improve the timing resolution.

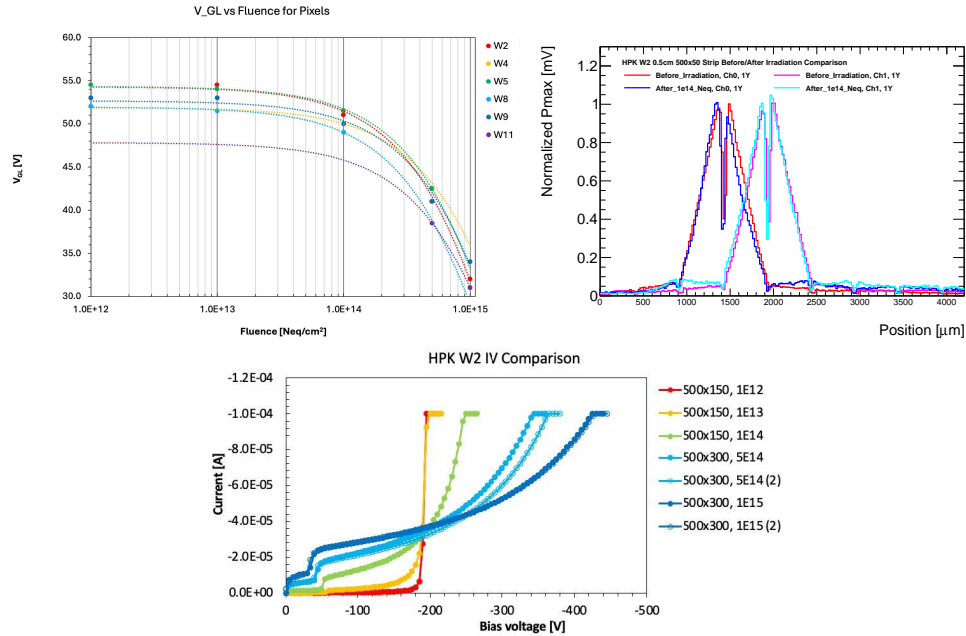


Figure 8.31: Left: Degradation of the gain layer for AC-LGADs of several wafer (with different N^+ , oxide and active thickness) from HPK latest sensor production, showing no change in gain layer doping up to 10^{13} Neq, which is an order of magnitude over the ePIC TOF radiation requirement. Sensors were irradiated at the TRIGA reactor (Ljubljana) with 1 MeV neutrons. Right: Normalized comparison of response profile of two nearby strips for two HPK 0.5 cm length, 500 μm pitch, 50 μm strip width: one before irradiation and one after 1×10^{14} Neq, even if the total signal is degraded the charge sharing profile is unchanged. Bottom: Current over voltage measurement for irradiated HPK sensors.

The development of the EICROC0 chip is proceeding as planned. In 2024, an updated PCB (“2024” PCB), has been designed by OMEGA. This updated PCB features improved testability and grounding, as well as the removal of supplementary PLLs. The chip shows good homogeneity between channels and Jitter < 35 ps for an injected charge of > 4 fC, both for the pre-amplifier and for the discriminator output, as seen in Fig. 8.32, Left. A large correlated noise still remains with the updated “2024” PCBs (already observed in the “2023” PCB), which leads to large TDC jitters, over 50 ps, when by design, the TDC jitter is expected to be of the order of 10 ps. Nevertheless, the intrinsic performance of the preamplifier, the TDC, and the ADC, taken individually, is confirmed to be in agreement with the design and within the ePIC detector specifications.

The development of pre-prototype readout board (RDO) with high precision clock distribution has been completed. Figure 8.33 shows a picture of the ppRDO. It is connected with the CMS ETL module board v0, which consists of the full-sized ETROC2 chip for testing purpose. The ppRDO will be evolved into the prototype RB for FTOF next that consists of lpGBT and VTRx+ chips, instead of FPGA and SFP+. Those efforts will be carried out under engineer designs as described later.

E&D status and outlook: E&D activities

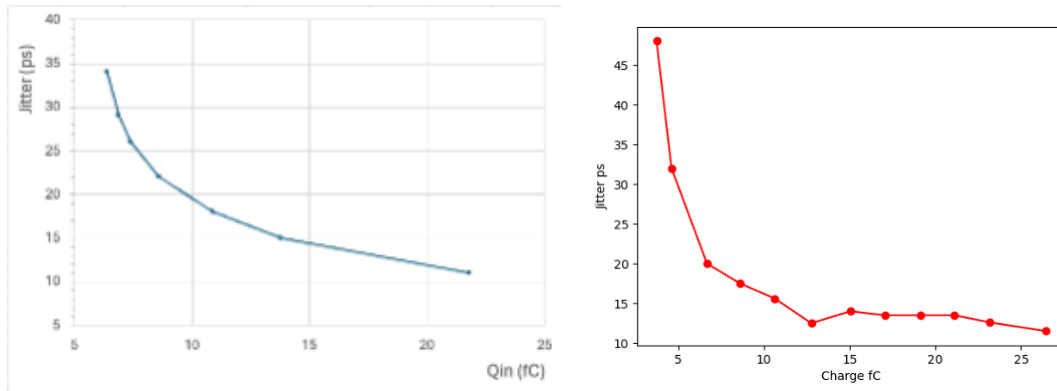


Figure 8.32: Left: FCFD Jitter measurements with 3.5 pf input capacitance and charge injection. Right: EICROC Discriminator jitter versus the injected charge, determined from data on an oscilloscope. Left: FCFD Jitter measurements with 3.5 pf input capacitance and charge injection. Plots from the erd112 and erd109 2024 reports.

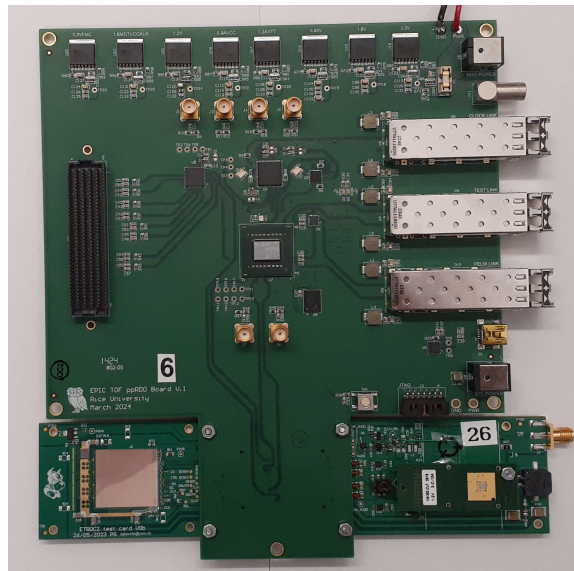


Figure 8.33: Picture of ppRDO connected with CMS ETL module board v0 for testing.

1927 **Thermo-Mechanical demonstrator:** The fabrication of a demonstrator stave following the double-
 1928 sided design, as seen in Fig. 8.35, is ongoing. The demonstrator will be a thermal/mechanical
 1929 demonstrator of the assembly procedure and chip/sensor power dissipation. A mock-up stave,
 1930 example in Fig. 8.34, will be co-cured with a readout flex with a cooling pipe in the center, and a
 1931 series of Si heaters and full-size HPK sensors from the latest production will be glued to the stave, then
 1932 wire-bonded together and to the readout flex. The demonstrator will be used to probe the power
 1933 dissipation, the temperature gradient across the stave, and the mechanical assembly procedure.
 1934 Demonstrator results are expected by Q1 2025.



Figure 8.34: Assembled stave prototype at Purdue.

Environmental, Safety and Health (ES&H) aspects and Quality Assessment (QA planning): We also carried out QA long-term and stress-test reliability studies of LGADs as a stepping-stone towards studies on AC-LGADs. The tests were conducted in an ambient chamber at various environmental conditions. We kept the sensors under bias voltage over periods of weeks, at different temperatures, ranging from -60 to +80 degrees Celsius and under different humidity conditions. Under these extreme conditions we carried out I-V scans. At intervals of time between temperature cycles, we also collected signals from beta particles from a Sr-90 source at room temperatures to study any deterioration in noise or charge collection. The results were presented at IEEE conference: While we saw an impact of humidity and temperature on current and breakdown voltage, the sensors recovered their original performance in subsequent cycles. In addition, we also studied the impact of passivation on sensors to minimize charge build-up and early mortality. We confirmed that passivation is critical to minimise the impact of humidity on sensors and prevent early mortality. Such tests were critical after issues have been observed in silicon sensors used for tracking detectors in other experiments, such as those at the HL-LHC. As part of our QA strategy, we also sent to colleagues of UNM BNL-made AC-LGADs to have them irradiated at various fluences in a proton beam at ITA, in a gamma beam at SANDIA and with neutrons at the TRIGA reactor. The first results are shown in the previous sections.

For both sensors and readout chips, it is imperative to evaluate the yield of the test productions to adjust the final production orders. The QA plans to evaluate the yield of the sensor productions are as follows: each produced sensor will be tested in the laboratory in a probe station with simple current over voltage (IV) and capacitance over voltage (CV) tests. AC-LGADs have a single point of DC connection on the N+, so only 1 or 2 needles are necessary for the test; a probe card is not necessary for QA. The IV test will allow us to check the current level and the breakdown voltage for each produced device; the current level has to be $< 1\mu A$ to not introduce power dissipation issues. The breakdown voltage of all devices has to be within 10% to avoid issues in the HV distribution. The CV test will allow to probe the gain layer depletion voltage and demonstrate that all devices have homogeneous gain; for LHC prototypes [11], the gain homogeneity was within 1%. A selection of devices from the full production will be characterized by mounting them on analog front-end boards with laser TCT and at test beam facilities to ensure the homogeneity of the charge-sharing response.

To evaluate the yield of the chip (EICROC, FCFD) productions, a sample of chips from each batch will be tested and probed for homogeneity in all the channels using a calibration input. All channels have to be within 10% of homogeneity. A selection of chips will be coupled (wire bonded or bump bonded) with a matching working sensor and mounted on a prototype PCB to probe correct and homogeneous operation in a realistic configuration. Then the boards will be tested with a laser TCT or at test beam facilities.

Once the state of sensors, readout chips, and flex is advanced, a fully loaded demonstrator stave is envisioned. The mounting procedure will already be tested during the assembly of the thermo-mechanical demonstrator. The full demonstrator will then be tested with radioactive sources in laboratory or at test beams.

Construction and assembly planning: The BTOF detector has a cylindrical shape, consisting of 144 tilted staves. These staves are assembled at designated sites within class-7 or higher clean rooms before being transported to BNL for final construction. Each staff is approximately 270 cm long and is divided into two half-staves of 135 cm. A half-staff includes a support structure with an integrated cooling pipe, a flexible printed circuit (FPC), sensors, and ASICs. The sensors and ASICs are mounted on both sides of the half-staff, with 64 sensors and 128 ASICs on each side. Wire-bonding is used to connect the ASICs to the sensors and electronics. Only components that pass various quality inspections—such as visual checks, metrology, and electrical tests—proceed to the assembly stage. During the half-staff assembly, one FPC is glued onto the support structure (Fig.8.35 (a)). To ensure precise alignment, a specialized tool is used, featuring pins and holes that guide the placement of the FPC and the correct application of glue. After assembly, the staves undergo both electrical and mechanical tests. Subsequently, sensors and ASICs are installed on the FPC surface using alignment tools similar to those used during the FPC mounting process (Fig.8.35 (b)). These tools help position the components and apply adhesive. Electrical connections are verified, and the ASICs are bonded to the sensors using wire-bonding, followed by wire encapsulation (Fig.8.35 (c)). 2 support structure with wire-bonded sensor, ASIC, FPC which is corresponding to front and back side, are attached to each other (Fig.8.35 (d)). Upon completing the installation on both sides (Fig.8.35 (e)), the final round of testing is conducted. Fully tested staves are then shipped to BNL for integration into the global support structure of the ePIC detector, which contains 144 slots for precise alignment of the staves within the global coordinate system.

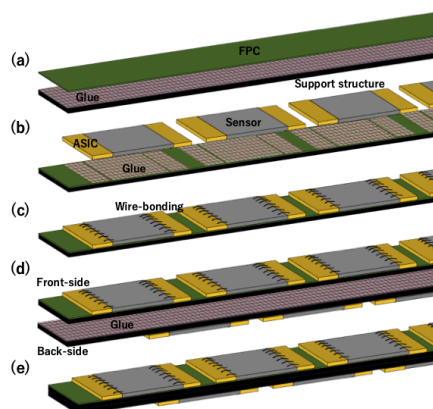


Figure 8.35: Assembly process of BTOF staff. Note, the scale is not real.

1994

The FTOF is constructed in a double-sided disk shape by populating modules with dimensions indicated in Fig. 8.26. Each module includes 4 sensors, 4 ASICs, a module board, and an Aluminum Nitride (AlN) base plate, which acts as a thermal conduit to the cooling system. The modules are connected to a service hybrid (SH) that consists of a power board (PB) and a readout board (RB). As mentioned earlier, three different configurations of SH are used, depending on the number of modules being supported: 3 modules (RB3), 6 modules (RB6), and 7 modules (RB7). There are about 780 modules in total to patch the disk shape. Sensor and ASIC are connected by bump-bonding. The module board is connected to the ASICs through wire bonding and has a connector to interface with the RDO. Assembly of the modules occurs in class-7 (or higher) clean rooms, while the PB and RB can be assembled under standard conditions. The assembly of each module begins with the connection of one sensor to one ASIC using bump-bonding technology (Fig.8.36 (a)). Automated machines are used for sensor and ASIC placement, alignment, and bonding. After bonding, the electrical performance of the sensor-ASIC hybrids is tested. Following this, 4 sensor-ASIC hybrids are mounted on the module board, using a dedicated tool to ensure precise alignment

(Fig.8.36 (b)). Thermal adhesive films are placed between the hybrids and the module board to ensure efficient heat dissipation. Once mounted, the ASICs are wire-bonded to the module board, and the wires are encapsulated for protection. After the bonding process, the AlN base plate is attached to the opposite side of the hybrid (Fig.8.36 (b)), with thermal adhesive films again used between them to aid heat transfer. The thermal adhesive films are also put between them. The modules undergo thorough quality checks before moving on to SH assembly. The RBs and PBs are manufactured using standard circuit board techniques and come with dedicated connectors for integration. SHs are available in configurations supporting 3, 6, or 7 modules, with the RB and PB connected via dedicated interfaces (Fig.8.36 (c)). Once assembled (Fig.8.36 (d)), the modules and SHs are tested for connectivity and performance. After passing all tests, the modules and SHs are shipped to BNL, where they are attached to the disk-shaped support structure. Specialized tools ensure the accurate placement of the components. Modules and SHs are mounted on both sides of the support structure to eliminate acceptance gaps between sensors. When installing the modules and SHs on the opposite side, a fixture is used to maintain the required clearance between components. Finally, the fully assembled disk is installed into the ePIC detector.

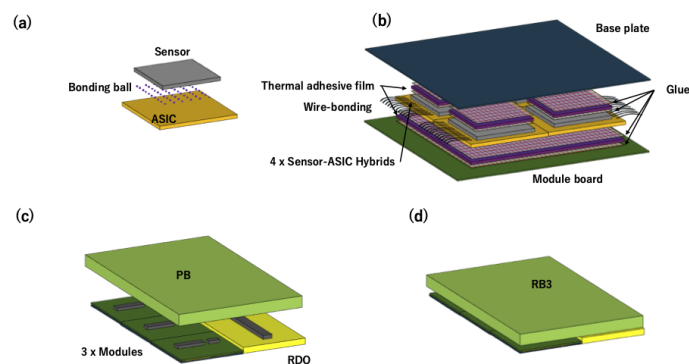


Figure 8.36: Assembly process of FTOF modules. RB3 type is shown as an example. Note, the scale is not real.

2023

Collaborators and their role, resources and workforce: Table 8.37 shows the participating institutes with their role, the contact person and potential commitments. This shows substantial participation by the international collaborators outside of the U.S.. We also anticipate substantial funding support from the international collaborators for the BTOF detector as well.

Risks and mitigation strategy: Our R&D results (eRD112) show that the performance of the sensors would meet physics requirements for TOF subsystems. Those studies were done with smaller chip dimension. The production for R&D study with full-size sensor chip is underway. There is a potential risk that the performance of sensors with larger size would be worse. The mitigation is to reduce the sensor size.

The HPK sensors for R&D (eRD112) is of small quantity. A mass production would be a risk in terms of chip yield and schedule delay. The mitigation is to explore other possible production sites (Taiwan/FBK).

FCFD ASIC design (eRD109) currently only has analog signal readout. The design and test of the digitization component is underway and expected to have first pass early next year. Addi-

2037

Institute	Contact Person	NOW (TDR->Project)
Brookhaven National Laboratory	Prithwish Tribedy tribedy@bnl.gov	DAQ readout chain readout, sensor-ASIC integration, sensor with FF AC-LGAD; EICROC testing
Fermi National Accelerator		FCFD ASIC (no ePIC)
Los Alamos National Laboratory	Xuan Li xuanli@lanl.gov	
Rice University	Wei Li wl33@rice.edu	B/FTOF FEE?, Backend electronics (postdoc), simulation and reconstruction
Oak Ridge National Laboratory	Oskar Hartburch hartbricho@ornl.gov	sensor-ASIC integration, frontend electronics (waffle probing), module assembly
Ohio State University	Daniel Brandenburg Brandenburg.89@osu.edu	BTOF/FTOF: module assembly; backend electronics
Purdue University	Andreas Jung anjung@purdue.edu	Module assembly
Univ. of California, Santa Cruz	Simone Mazza simazza@ucsc.edu	Sensor, sensor-ASIC integration, module assembly (no in-kind)
University of Illinois at Chicago	Olga Evdokimov mailto:evdolga@uic.edu	
Hiroshima University	Kenta Shigaki shigaki@hiroshima-u.ac.jp	FTOF EICROC testing, sensor testing (30%), simulation
RIKEN	Yuji Goto goto@bnl.gov	BTOF: module assembly
Shinshu University	Kentaro Kawaide kawade@shinshu-u.ac.jp	Sensor testing, simulations
University of Tokyo	Taku Gunji gunji@cns.s.u-tokyo.ac.jp	DAQ streaming readout
South China Normal University	Shuai Yang syang@scnu.edu.cn	
Univ of Sci. and Tech. of China	Yanwen Liu	
Indian Institute of Tech., Mandi	Prabhakar Palni prabhakar.palni@unigoa.ac.in	FTOF Module Assembly/QA, sensor testing
National Inst. of Sci. Edu. Res.	Ganesh Tambave ganesh.tambave@niser.ac.in	Module Assembly
National Central University		FF AC-LGAD (sensor QA)
National Cheng-Kung University	Yi Yang yiyang@ncku.edu.tw	Mechanics and cooling systems
National Taiwan University	Rong-Shyan Lu rslu@phys.ntu.edu.tw	FF AC-LGAD; module assembly
Univ. Técnica Federico Santa María		Simulations
LBNL	Zhenyu Ye yezhenyu2003@gmail.com	BTOF ASIC testing; SH
Kent State University	Zhangbu Xu zxu22@kent.edu	Simulation, readout test, machine shop (in-kind)
Nara	Takashi Hachiya hachiya@cc.nara-wu.ac.jp	BTOF module assembly/validation/FPCB

Figure 8.37: Collaboration institutions and their responsibilities.

tional resource may be need to mitigate potential schedule delay and cost increase. In addition to the baseline chips EICROC and FCFD, third-party ASICs are also taken into consideration: FAST (INFN Torino), AS-ROC (Anadyne Inc. + UCSC), and HPSoC (Nalu + UCSC). The most advanced one is the High-Performance System-on-Chip (HPSoC) ASIC, designed by Nalu Scientific [16], in close collaboration with SCIPP, and fabricated in 65 nm CMOS by TSMC. HPSoC comprehends a fast analog front end and, unique to all other current LGAD readout ASICs, will capture the full signal waveform at a sampling rate of 10-20 GS/s. Together, these are expected to address the EIC goal of 25 ps timing resolution or better per measured space point. V2b of the chip has a working digital back-end and is currently under review.

We have performed heat conductivity and cooling simulations, and R&D test on cooling capacity (currently with PED funding). Those show promising outcome for meeting the cooling needs. The potential risk is that the cooling capacity is not sufficient to maintain a stable and relatively uniform temperature. A possible mitigation strategy is to use different material for cooling pipe with better heat conductivity and higher flow rate.

Additional Material

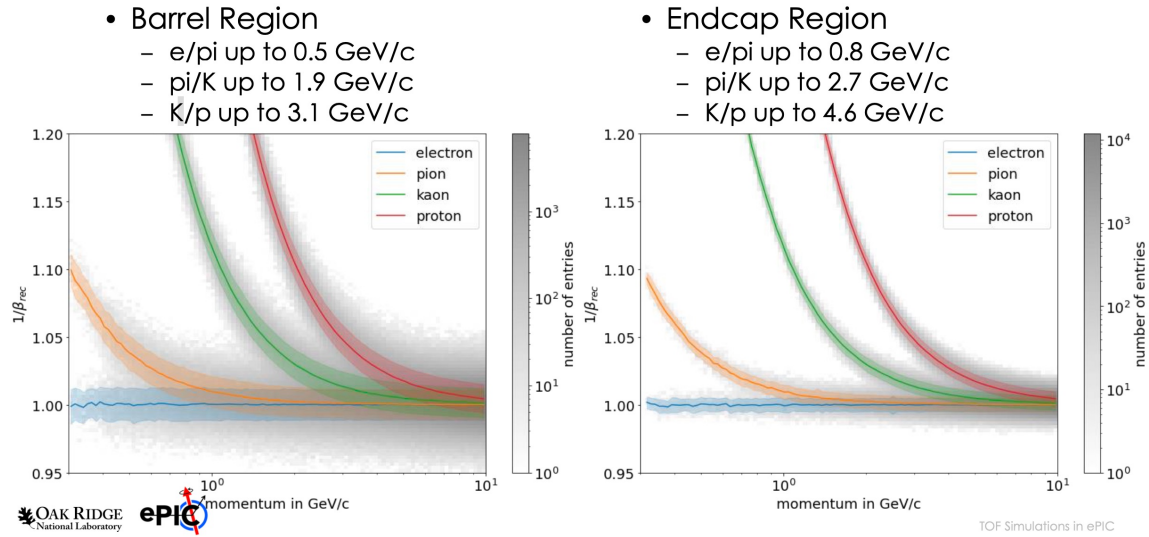


Figure 8.38: simulation of $1/\beta$ as a function of particle momentum for BTOF and FTOF performance.

8.3.4.2 The proximity focusing RICH

Requirements

Requirements from physics: The ability to identify different species of hadronic particles (pions, kaons, and protons) and to separate these from electrons will be essential for realizing much of the EIC physics program. Particle identification capabilities in the electron going endcap region of the ePIC detector ($-3.5 \leq \eta \leq -1.5$) will be provided by a proximity focusing ring imaging Cherenkov detector (pFRICH). Hadrons in this region generally originate from collisions probing low x at a given Q^2 , which is a phase space of great interest for studies in both $e+p$ and $e+A$ configurations. In $e+A$ collisions this is the kinematic region where the onset of gluon saturation is expected. Saturation generally describes novel QCD phenomena originating from the overlap of the gluon wavefunctions, which is thought to happen at low x where gluon densities are high. This is also a region that has never been explored by polarized $e+p$ experiments before and measurements of identified kaons in the backward region, for example, will provide information on the polarized strange quark distributions.

Studies of physics requirements in the EIC Yellow Report define the particle identification (PID) requirements in the backwards region. Driven mostly by SIDIS measurements, the requirements in the pseudorapidity range $-3.5 \leq \eta \leq -1.5$ demand 3σ separation or better of $\pi/K/p$ for momenta $p < 7$ GeV/c. Evaluations of particle yields and coverage of the relevant SIDIS phase space have shown that the lack of hadron PID capability for $p > 7$ GeV/c in the pFRICH acceptance will have little effect on the EIC physics program.

The Yellow Report enumerated overall requirements on the e/h ratio and identified the need for hadron suppression on the order of 10^4 in the backward region. At high momenta, this suppression will be predominantly provided by the electromagnetic (EM) calorimeter but it is clear that at lower momenta the electron ID capabilities of the backward EM calorimeter will not be sufficient to achieve the overall required electron purity. The extra suppression power can only be met by

additional PID capabilities from the RICH detector, especially in the region below $3 \text{ GeV}/c$ where the hadron distributions are at their maximum. To access low Q^2 , it is essential to provide PID in this region which includes $Q^2 = 1$ up to $\eta = -2$ and lower Q^2 up to the quasi-real photoproduction regime further backward. As low- Q^2 is correlated with low- x (at high inelasticity), e/h separation is essential to access the lowest x for the reasons outlined above.

The original baseline design of the ePIC detector included ToF detectors based on AC-LGAD technology in the forward, backward, and barrel regions. Their purpose was to provide PID in the momentum region below the aerogel threshold ($\lesssim 1 \text{ GeV}/c$). While physics measurements exist that require PID at low momenta in the forward and barrel region, there are no such arguments for the backward range. The main argument for the presence of a ToF detector for $\eta < -1$ was to aid in providing the start time, t_0 , for all ToF measurements in ePIC, mainly by utilizing the scattered electron. It was determined that the pFRICH, utilizing HRPPD sensors with a single photon timing resolution performance of $\sim 30\text{-}40 \text{ ps}$, could provide the same t_0 performance as a dedicated ToF system by using the copious amounts of Cherenkov photons produced as charged particles traverse the sensor fused silica windows. Thus, the dedicated backward ToF detector was removed from the ePIC baseline design meaning the pFRICH will need to provide the necessary t_0 with a resolution of $\sigma_t < 25 \text{ ps}$. This, in conjunction with vertex-time correlations, will provide a high quality t_0 for events where the scattered electron is detected in the backward region. It will also provide input in cases where the t_0 has to be derived from a bootstrap method using all timing detectors in the full ePIC coverage.

Requirements from Radiation Hardness: Studies of min-bias and background rates on sensors are being finalized. We will add appropriate text when they are complete.

Requirements from Data Rates: Previous data rate estimates need to be compared to rate studies above. Will add text when complete.

Justification

Device concept and technological choice: The operation of a generic proximity focusing RICH detector is based on a very simple set of principles. A charged particle passing through a thin layer of radiator (often aerogel with an appropriate refractive index) with a velocity higher than the speed of light in that medium emits Cherenkov light (photons) at an angle which is solely determined by the particle mass, momentum, and refractive index of the radiator. The 3D momentum of the particle is typically provided by a tracking system. If the average refractive index of the radiator is also known, measurements of the Cherenkov light emission angle can determine the particle mass, thus allowing identification of different particle species, e.g. distinguishing electrons, pions, kaons, and protons.

The ePIC pFRICH was designed as a conceptually simple detector, based on proven principles, providing a high degree of performance that is practically uniform over the whole available angular acceptance in η and ϕ . In order to reach the performance requirement of 3σ separation or better of $\pi/K/p$ for momenta $p < 7 \text{ GeV}/c$, the pFRICH design was optimized in the following ways: (1) the proximity gap length was maximized as much as possible within the volume available in ePIC; (2) the radiator thickness was taken to be small enough to reduce the contribution to the single photon angular resolution to below $\sim 5 \text{ mrad}$, yet produce enough photons per track to robustly reconstruct the Cherenkov angle; (3) the HRPPD pixellation was chosen such that it contributes at

most ~ 2 mrad to the angular resolution; and (4) the acrylic filter cuts off all UV light produced in the aerogel below ~ 300 nm, where the $dn/d\lambda$ dependency is strongest. In addition to satisfying the PID requirements in the backward direction, the small material budget of the pFRICH design minimizes the impact on the the resolution of the endcap electromagnetic calorimeter which sits directly downstream.

Subsystem description:

General device description: The layout of the proposed ePIC pFRICH detector is shown in Fig. 8.39. It consists of a 1.3 m diameter and ~ 49 cm long cylindrical vessel with the outer and inner walls made from a lightweight honeycomb carbon fiber sandwich and front and rear plates made of a carbon fiber reinforced plastic (CFRP). The vessel sits 123.6 cm from the nominal interaction point. Forty-two 2.5 cm thick aerogel tiles of a trapezoidal shape are installed in individual opaque compartments in a container mounted on the upstream side of the vessel. A thin acrylic filter is installed immediately after the aerogel container. The vessel is continually flushed with dry purified nitrogen. Sixty eight HRPPD photosensors are installed in individual slots in the rear CFRP mounting plate with their fused silica windows facing the aerogel. Inner and outer conical mirrors cover the cylindrical sides of the vessel in order to increase the η acceptance of the Cherenkov photons produced in the aerogel radiator. Readout boards equipped with four 256-channel EICROC ASICs are mounted on the rear ceramic anode plates of each of the HRPPDs.

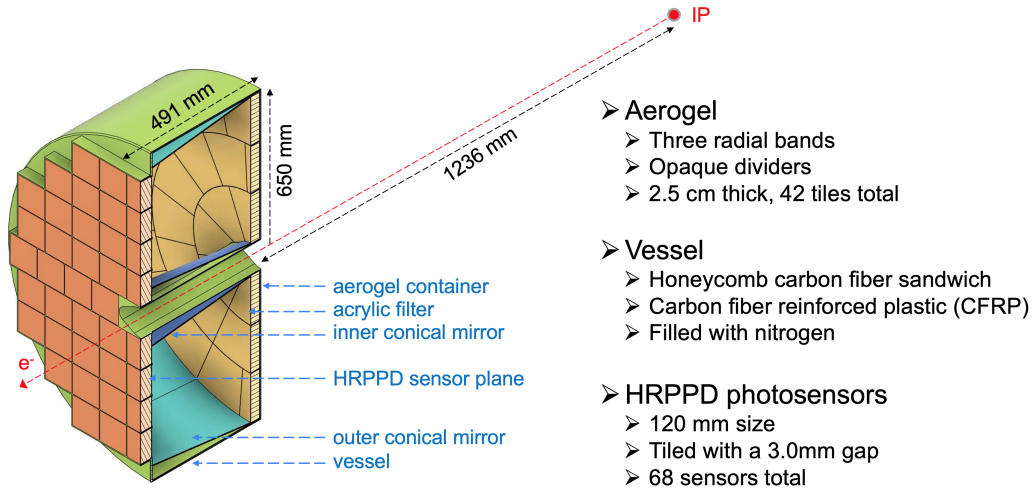


Figure 8.39: The proposed pFRICH detector. See the text for more details.

Sensors: An improved version of the Micro-Channel Plate Photomultiplier Tubes (MCP-PMTs) manufactured by Incom Inc. [17], the so-called High Rate Picosecond Photon Detectors (HRPPDs), will be used as the photosensor solution. The sensor dimensions will be 120 mm x 120 mm, with a 104 mm x 104 mm fully efficient active area in the center (75% geometric efficiency) and will have slightly tapered 5 mm thick UV-grade fused silica windows, and 3 mm thick multi-layer ceramic anode base plates. A DC-coupled variety of these sensors will be used, with the inner side of the anode base plate patterned into 32 x 32 square pixels, corresponding to 1024 channels per sensor, and a pitch of 3.25 mm. The sensors will be equipped with a UV-enhanced high quantum efficiency (QE) bialkali photocathode, with

peak values exceeding 30% at 350 nm [18]. The HRPPDs will be fitted with a pair of 600 μm thick MCPs with a pore diameter of 10 μm , open area ratio in excess of 70%, and bias angle of 13 degrees in a conventional chevron configuration. These will be operated at an amplification voltage of up to ~ 700 V to comfortably achieve an overall detector gain above 10^6 if needed. HRPPDs will have a single photon Transit Time Spread (TTS) of ~ 30 -40 ps. The anode base plates will be manufactured from multi-layer High Temperature Co-fired Ceramic (HTCC) by Kyocera (Japan). They will have a custom design, matching the uniform 32 x 32 pixellation on the inner (vacuum) side of the sensor, short shielded traces inside of the ceramic stack, and a pattern of square pads with a smaller pitch on the outer side, matching the readout PCB design.

FEE: Each sensor will be equipped with four 256-channel EICROC ASICs [19], designed by the OMEGA group [20], each serving one quadrant of the sensor. EICROC ASICs will be built via a 130 nm technology process, with an expected power consumption of 1-3 mW/channel [19]. They will provide a Time of Arrival (TOA) and an ADC measurement with a dynamic range of 1 pC for each pixel, which should be sufficient for both single photon hits (both imaging and timing) and multi-photon hits (timing only) at a moderate HRPPD gain of a few times 10^5 . The ASICs will be able to measure the TOA with a resolution better than 20 ps per pixel assuming detector capacitance on the order of ~ 10 pF, leading edge length of the HRPPD signal below 500 ps, and collected charge of a few dozens fC achieved by tuning the MCP gain [20]. These ballpark parameters seem to be easily within reach for pFRICH HRPPD sensors.

The ASICs will be bump bonded to the readout PCB in a “flip-chip” fashion to minimize the parasitic capacitance of the traces inside of the PCB stack. Preliminary estimates show that in such a scheme, where four 16 x 16 primary pixel arrays with a pitch of 3.25 mm are first “compressed” to a 2.0 mm pitch inside the HRPPD ceramic base plate and then further reduced to a 500 μm pad size in the readout PCB stack in order to ultimately match the EICROC ASIC pitch, the combined pad and trace capacitance should not exceed 10 pF. This is well within the expected operating range of the ASICs.

Each ASIC will be connected via a dedicated copper link to its respective readout unit (RDO), located on the outer circumference of the rear side of the pFRICH vessel. Each RDO will serve 16 EICROC ASICs, for a total of 17 RDOs. The RDOs will then be connected to a single Data Aggregation Module (DAM). The DAM board is envisioned to be a FrontEnd Link eXchange (FELIX) board [21] installed in the DAQ. The RDO will be connected to the DAM via a high speed optical link capable of at least 5Gb/s throughput. The RDOs will follow the same design used by the ePIC pixelated AC-LGAD detectors. These boards will utilize lpGBT for aggregation of ASIC data and VTRX+ to provide the fiber interfaces. The RDO should deliver timing signals synchronized to the beam crossings with jitter < 5 ps.

Other components: In addition to the vessel structure and sensors described above, two other components will be critical to the pFRICH: the aerogel radiators and mirrors. The pFRICH will be equipped with aerogel tiles produced by Chiba Aerogel Factory Co., Ltd. [22] with a nominal refractive index, $n \sim 1.040$ and a thickness of 2.5 cm. The aerogel will be cut using a water jet technique into trapezoidal tiles providing a required radial and azimuthal segmentation with minimal dead area. This type of aerogel will replicate the performance of the material used in the Belle II experiment [23], and in particular, will be very transparent in the near UV range, with an absorption length and Rayleigh scattering length in excess of 5 mm down to ~ 275 -300 nm. The aerogel tiles will be installed in segmented containers (slots) with ~ 500 μm thick walls and held in place with a thin filament. The container walls will be opaque to suppress stray photons leaking out of the aerogel tile side facets, which are not expected to be of a high optical quality after water jetting.

The pFRICH will also utilize three types of mirrors to increase the active acceptance of the detector. The outer mirror cone consists of 12 segments approximately 40 cm in length which sit just inside the outer wall of the pFRICH vessel. These mirrors will recover Cherenkov photons from charged particles with large polar angles which pass through the aerogel but would exit the vessel before reaching the sensor plane. Similarly, a set of inner mirrors which wrap around the beam pipe and surrounding support structures will reflect photons emitted by small angle charged particles (close to $\eta \approx -3.5$) back onto the sensor plane. Finally, small pyramidal mirrors will be placed on top of the HRPPD side walls to reflect (funnel) photons hitting this area back into the sensor acceptance. The mirrors themselves will have a reflectivity of approximately 90% for wavelengths between 300 and 600 nm and will be produced at Stony Brook University using an evaporator with the CFRP substrate material provided by Purdue University.

Performance

Monte-Carlo simulations: The performance of the pFRICH design was studied using a custom simulation and reconstruction software suite. The geometry of the detector, along with other relevant characteristics such as the ePIC magnetic field map, aerogel optical properties, mirror reflectivity, and HRPPD quantum efficiency were modeled in GEANT4 v10.05.p01 [24]. The reconstruction made use of the Inverse Ray Tracing (IRT) library, which is part of the ePIC software stack [25], and a ROOT [26] based data structure providing access to all photo-electron, track, and event level quantities.

Parameters relevant to the performance of the pFRICH were determined by simulating single particles thrown at a variety of energies and angles. On average, roughly 11 Cherenkov photons were detected from particles at the saturation momentum, which is in agreement with first principles estimates taking into account a realistic sensor quantum efficiency. The working acceptance of the detector, defined as the region in which the ratio of tracks producing at least one detected photon over the total number of tracks is greater than 80%, was found to cover $-3.5 < \eta < -1.5$. Single photo-electron (SPE) and track level resolutions in the working acceptance were also determined, with the SPE resolution being roughly 5 mrad and independent of momentum, while the track level resolution improved with the number of detected photons and reached a value of 1.7 mrad.

The algorithm for event based reconstruction of the Cherenkov angles was validated using multi-particle simulations. The reconstructed Cherenkov angle (in units of mrad) as a function of particle momentum (in units of GeV/c) is shown in the left panel of Fig. 8.40 and compared to the theoretical expectations for a given mass hypothesis. It is seen that the reconstructed angles and theoretical expectations are in good agreement, confirming that the event based reconstruction is performing well. This plot also shows that the Cherenkov saturation angle is approximately 295 mrad. The N_σ separation count between the electron-pion and pion-kaon hypotheses as a function of momentum are shown in the middle and right panels of Fig. 8.40, respectively. It is seen that 3σ separation is possible up to roughly 2.5 GeV/c for electron-pion and 9 GeV/c for pion-kaon hypotheses. Performance was found to be relatively uniform across the whole acceptance of the detector.

One of the main purposes of the pFRICH detector is to identify low momentum scattered electrons in the backward direction. Specifically, it will help with separating the electrons from π^- mesons, which are expected to dominate in the pFRICH acceptance. Using PYTHIA-6 $e+p$ collisions at 18×275 GeV, it was shown that the pFRICH will provide good π^- -electron separation for $p < 2$ GeV/c and decreasing separation power for momenta up to ~ 5 GeV/c as seen in Fig. 8.41. The pFRICH detector therefore plays an important role in the ePIC detector,

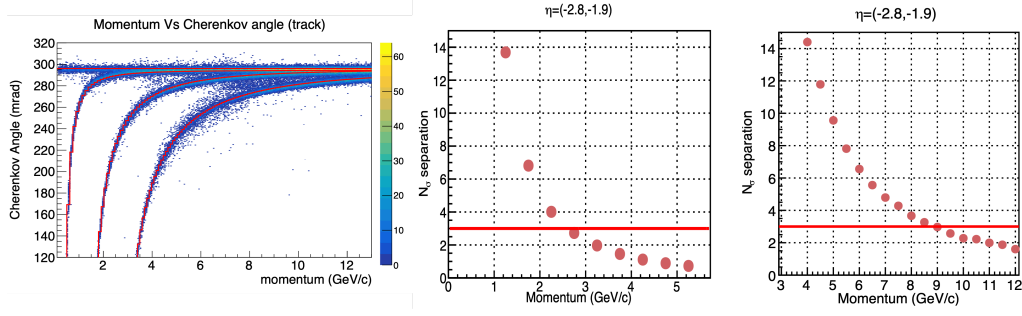


Figure 8.40: PLACEHOLDER (Left) The reconstructed Cherenkov angle for electrons, pions, kaons, and protons as a function of momentum. (Middle) N_σ separation between the electron and pion hypotheses as a function of momentum. (Right) Same as the middle panel, for pion and kaon hypotheses.

2244

allowing identification of the scattered electrons in kinematic region not accessible by other detectors.

2245

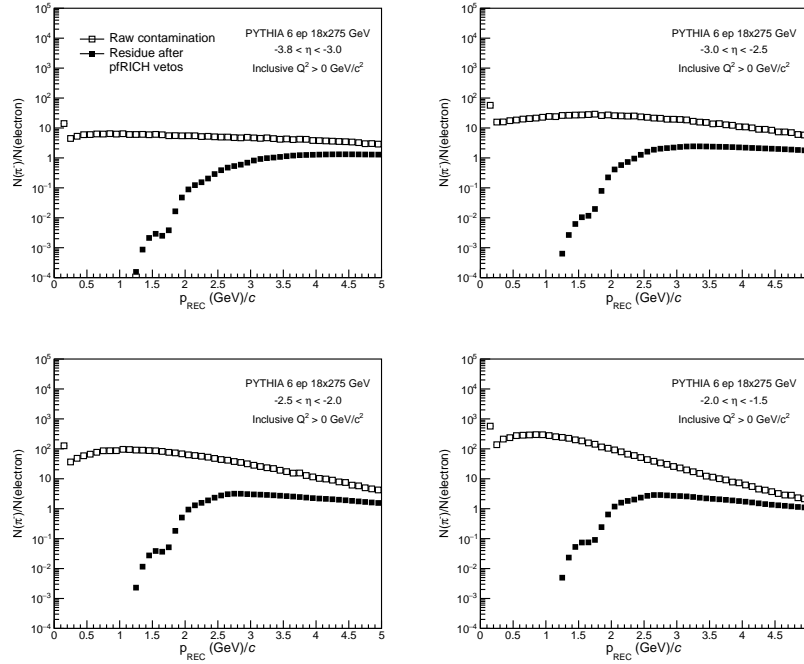


Figure 8.41: PLACEHOLDER Yield ratios of π^-/e_{scat} before (open black squares) and after (black full squares) pFRICH veto on π^- in PYTHIA 6 $e+p$ collisions at 18×275 GeV for four η bins, covering full pFRICH η acceptance.

2246

2247

2248

2249

2250

Another important utilization of the pFRICH is hadron identification in the backward region in SIDIS studies. For that reason, the ability to separate π , K , and p hadrons was studied using simulation of $e+p$ collisions at 18×275 GeV in PYTHIA-8. Specifically, the expected purity of leading K^- mesons was evaluated and was shown to be close to 100% up to hadron momenta of $p < 6$ GeV/c. This means that pFRICH will play an important role in SIDIS

studies as it can efficiently distinguish various hadron species in a wide momentum range.

Hardware component evaluation: Hydrophobic silica aerogel manufactured by the Aerogel Factory [22] will be used for the radiator in the pFRICH detector. Three hydrophobic aerogel tiles, with nominal dimensions of $11\text{ cm} \times 11\text{ cm} \times 2.5\text{ cm}$, density of 0.14 g/cm^3 , and refractive index of 1.04, were ordered from the Aerogel Factory to verify and assess their refractive index and transparency, two aerogel properties which are critical to the detector's performance. The refractive index was determined at Temple University by measuring the deflection of the refracted light exiting the corners of the aerogel (see QA section). The refractive index measured by Temple University (n_{TU}) and the Aerogel Factory (n_{AF}) were found to be in agreement, with a typical value of $(n_{TU} - n_{AF}) / (n_{AF} - 1) \sim 2\%$. The optical transparency was evaluated by measuring the transmittance as a function of wavelength. Transmittance curves for each tile were measured by the Aerogel Factory using a monochromator and spectrometer (Hitachi U-4100) [27], at BNL using a monochromator and spectrometer (Hitachi U-3210), and at Temple University using a LED and spectrometer setup which provides measurements at four discrete wavelengths. These three sets of measurements were found to be consistent with each other within the quoted errors. A sufficiently high transmittance of about 68.5% at 432 nm was found when averaging the results from three different measurements over the three produced aerogel tiles at Temple. The wavelength dependent transmittance measurements were used to extract additional information such as clarity, transmission length, and scattering length.

The mirrors will be produced by the pFRICH subsystem collaboration members, with substrates fabricated at Purdue University and coating performed at Stony Brook University. Optimization of the substrate and coating procedures is ongoing with a number of mirror samples being produced with different substrate manufacturing techniques, coating chamber settings, and coating material thickness. The reflectivity of the various mirror samples was evaluated at BNL using a dedicated test stand. The best performing mirror sample, manufactured using a ~ 12 kilo-angstrom thickness aluminium coating, showed a measured average reflectivity of 0.89 for wavelengths between 300 and 600 nm.

Implementation

Services: Services relevant for the pFRICH include High Voltage (HV) and Low Voltage (LV) systems to operate the photosensors and power the front-end electronics, respectively, a cooling system to regulate the temperature of the electronics and sensors, and a gas system to maintain the proper environment inside the pFRICH vessel.

The HV and LV modules will be located on the electronics platform, about 15 meters away from the pFRICH detector, in a low Total Ionizing Dose (TID) environment. Therefore, standard off-the-shelf units can be used. The high-voltage system will consist of 340 individual stackable negative HV channels. Twenty three CAEN A1515BV 16-channel 1.4kV/1mA floating ground modules [28] will be used. The HV modules will be housed in a pair of CAEN SY4527 mainframes [29], equipped with additional 1200 W power module boosters. Each of the twenty three modules will be connected to an enclosed box distribution PCB installed on the rear side of the pFRICH vessel. The box is fed from individual 15 m long multi-conductor high voltage cables. For the HV interconnect, CERN-approved 52-pin Radiall cable connectors and receptacles will be used throughout the system. The distribution PCB will arrange five of the isolated channels of the A1515BV in a manner to provide five individual stacked voltage levels and a common ground referenced return to each HRPPD. The respective five bias levels and ground will be connected to the pads on the rear side

of the HRPPDs via narrow profile Teledyne Reynolds shielded 26 AWG coaxial cables, conductive vias in the Front End Board (FEB) stackup with a matching pad pattern, and custom Samtec compression interposers.

The EICROC ASICs will require 1.2 V low-voltage power. Under the assumption of up to 3 mW/channel power dissipation this corresponds to 3 W power (or up to 2.5A current) per photosensor FEB. Accounting for other electronics components present on such a FEB, and providing a 20% safety margin, we estimate the total power consumption to be less than 300 W for the whole system. This number is used as input for designing the cooling system discussed below. We will be using a single Wiener MPOD Mini LX crate with a MPOD-C controller and four MPV4008I1 4-channel LV modules [30]. One Low Voltage channel will serve four FEBs. 15 m long tray rated 10 AWG jacketed cables with 20AWG (sense wires) will run between the electronics platform and a LV distribution panel on the rear side of the pfRICH vessel. From there, 18 AWG multi-conductor cables will distribute power to the individual FEB cards.

The pfRICH cooling system will consist of several off-detector components and a few on-detector thermal interfaces and assemblies. The primary heat dissipating components will be the ASICs, which are anticipated to produce just over 1 W each (4 W per module), or about 300 W for the 68 total modules. In addition to the ASICs, the sensors are anticipated to dissipate just under 1.5 W each or 100 W total. Conservatively, the total power output will be roughly 400 W. Following the geometry, each row of sensors will have its own pair of titanium cooling tubes directly over the ASICs. The pair of tubes that contact the same row of sensors will be in series, and all rows will be in parallel with each other. The tubes will be attached to aluminum plates with thermal epoxy, and a gap pad between the plate and ASIC will maximize thermal contact. Using a stock tube of 0.25" OD and 0.218" ID and maintaining a minimal temperature gradient in the water allows the mass flow rate to be calculated. From there the Reynolds number and pressure drop can be determined, confirming the viability of the system. Additionally, a finite element analysis (FEA) was performed to confirm the water temperature difference and determine the thermal gradient across the various components. With the described configuration, the sensors reach a maximum temperature of about 32 C in the analysis.

The three primary off-detector elements of the cooling system are a Polyscience chiller, Chilldyne circulator, and a distribution panel. The Polyscience chiller will allow the water to be slightly colder than room temperature, or about 15 C, which is the lowest recommended temperature without nearing the dewpoint in the interaction region. The unit is also capable of flowing about 10 liters per minute (lpm), dissipating about 800 W at that temperature and maintaining the temperature within +/-0.1 C. The Polyscience chiller would be paired with a Chilldyne negative pressure system capable of circulating water at about 8 lpm and ~10psi. It offers a significant advantage over a positive pressure solution, as if there is a leak in the system, it will draw air into the tube instead of letting water out and potentially damaging electrical components.

The gas system for the pfRICH detector is designed to circulate dry nitrogen at precise pressure and flow rates to remove moisture from within the pfRICH chamber. High-purity nitrogen ($\text{H}_2\text{O} < 3 \text{ ppm}$) will be supplied from cryogenic sources. To provide secondary protection, moisture traps such as silica gel dryers will be installed near the nitrogen source. The system will maintain both the required moisture levels and gas purity by ensuring that it is sufficiently gas tight and that the chamber is kept at a slight overpressure (4 mbar) above atmospheric pressure, preventing any infiltration of ambient air. A 0.5 μm filter will be added near the source to capture dust particles. A standby nitrogen source will be available to ensure continuous operation in the event of a primary source failure. To manage fluctuations in the source pressure, a digital pressure outlet controller will be used. Additionally, nitrogen flow will be regulated by a non-pressure-limiting digital mass flow controller. The nitrogen flow rate is expected to allow several complete volume exchanges per

hour, with the precise rate to be finalized later.

Pressure inside the chamber will be controlled using a tank blanketing pressure regulator, which maintains a positive internal pressure relative to varying atmospheric conditions. An overpressure protection bubbler will serve as a safeguard against excessive pressure within the chamber. To ensure uniform nitrogen distribution and prevent localized air pockets, nitrogen will be introduced into the chamber at two locations near the top side of the pFRICH vessel, closer to the aerogel plane, and exhausted through two openings near the sensor plane at the bottom. All exhausted gases will be vented outside the experimental area. The entire gas system will undergo pressure testing at 1.5 times the operating pressure to ensure integrity. For monitoring and troubleshooting, pressure gauges and transmitters will be installed, with critical data such as chamber pressure and flow archived for reference.

Subsystem mechanics and integration: The shell that creates the volume of the detector will be made primarily of carbon fiber to optimize the radiation length in ePIC. Specifically, the sensor plane is intended to be made from a bulk carbon fiber layup at approximately 14.7mm thick at its thickest point. The bulk carbon fiber will be molded and CNC-cut to allow for individual sensor frames and staves to be bonded in-place to create 68 sensor pockets along this plane of the detector. Each individual HRPPD sensor will be added into the sensor plane from the outside of the vessel and sealed in each of the sensor pockets with a face seal. The overall plane will be sealed to the cylinder at the outer and inner walls using a tightly spaced bolt-pattern and an o-ring groove on the upstream end of the sensor plane to accommodate another face seal.

On the upstream end of the vessel, the aerogel plane will be made from a carbon fiber honeycomb layup around 1/4" thick. The outer and inner circumferences of the aerogel plane will house a sealing ring made from bulk carbon fiber and an o-ring groove to create a face seal. Attached to this aerogel plane will be a web of carbon fiber that creates radial rows of pockets for the aerogel to be placed in. These tiles will be held into the pockets using a thin transparent line strung across the opening in order to contain them in place.

The cylindrical portion of the vessel is comprised of identical end rings on the upstream and downstream end that house the threaded bolt holes and sealing surfaces for the sensor plane and aerogel plane face seals. These end rings are approximately 3/4" (on the bolting surface) and 1" in thickness (in the z-direction). They are made from bulk carbon fiber and contain threaded inserts that are placed by CNC-machining the insert locations and bonding and threading them into place. The rest of the cylinder is made from single sheets of carbon fiber on the inside and outside of the vessel, as well as a 3/4" nomex honeycomb layer in between.

The inner wall of the cylinder is created in a similar manner to the outer wall, namely a honeycomb construction with the end rings embedded into both ends for bolting and sealing to the aerogel and sensor planes. However, the shape of the inner wall is made such that there is 5 mm of clearance (radially) from the beam pipe flange that the pFRICH will need to pass by to be installed in ePIC. This makes the shape of this inner wall similar to an egg or an avocado.

Lastly, the conical mirrors are designed such that they are attached solely to the sensor plane. This is being done to ensure that the mirrors can be controlled in relation to the sensors and will be unaffected by manufacturing misalignments and tolerance stack-up issues throughout the rest of the vessel. As such, they will hang cantilevered perpendicular the sensor plane for both the inner and outer mirrors. The outer mirrors will be concave and the inner mirrors will be convex. The construction will be a combination of a molded, bulk carbon fiber base with a bonded lexan sheet on top of it (which will have been deposited with a mirror film).

Once the pFRICH has been fully assembled and ready to be placed in the overall ePIC detector, it will be moved around the assembly hall on a cart. The cart will integrate lifting eyelets for the installation of the pFRICH into ePIC, rails identical to its final location, and wheels to transport, store and work on the detector when it is out of the barrel. This tooling will allow us to lift the cart with the pFRICH secured in place with the crane in the detector hall, position it against the barrel, align the rails, and transfer the pFRICH into its final position by translating it along the z-axis.

Calibration, alignment and monitoring: A laser-based system will be used to monitor the pFRICH performance throughout its operational life. The purpose is to monitor, on a pixel-to-pixel basis the single photon timing resolution, the single photon pulse height amplitude (HRPPD gain), HRPPD QE, and the relative delays between channels on a few ps level. The system will also monitor the reflectivity of the conical and pyramidal mirrors. To measure the timing resolution, an array of six fibers is introduced inside the detector volume from the aerogel side which casts a broad profile of low-intensity light onto the sensor plane such that each HRPPD pixel accumulates some number of single photon hits after a given number of laser pulses. The distance between a given fiber tip and an HRPPD pixel (minimum of 40 cm) defines the flight time for photons emitted from this fiber, hence the distribution of reconstructed flight times will reveal the timing resolution for this single pixel. Similarly, a separate array of six fibers is arranged such that emitted photons reflect off of the outer mirror surface before impinging on the HRPPDs. In this case, the single photon counting rate is monitored for any degradation over time, which would indicate the deterioration of either the photocathode quantum efficiency or mirror reflectivity, or both.

The pFRICH monitoring system deploys a picosecond PiLas laser which produces a 405 nm laser beam with a nominal ~ 45 ps pulse width. The beam is coupled to a custom 1-to-14 optical fiber splitter by Thorlabs, that evenly distributes the light into arrays of fibers routed into the detector vessel. Two additional fibers are connected to silicon photodiodes to provide laser signal quality verification and an initial timestamp (t_0). A custom-sized 5 mm \times 5 mm engineered diffuser is used to generate a uniform 50° square pattern to optimize the intensity profile emitted from each fiber. Additionally, a fiber delay line is added to each fiber branch to provide the ability to easily separate out in time photons originating from a given fiber. In all, there are three sets (segments) of fibers downstream of the splitter that deliver photons from the laser to the detector vessel: delay fibers, long extension fibers, and fibers mounted permanently inside the detector vessel. Finally, multiple fast photodiode sensors are used to sample the laser light before and after the splitter to monitor the light output intensity and the timing performance.

A relative alignment of the conical mirror segments inside of the vessel, and surface mapping will be performed on a fully assembled detector (up to the front wall removed) prior to the installation in ePIC, by using a 3D scanning system which is being built now for the purposes of first article mirrors QA assessment. The vessel as a whole will be aligned in ePIC after the installation, following a generic procedure developed by EIC engineers for all detector subsystems. Appropriate survey targets will be mounted on the rear and barrel sides of the vessel if required.

Status and remaining design effort: As shown in the previous text, the present pFRICH design fully meets the EIC Yellow Report requirements and subsequent amendments (see performance section):

- Pseudorapidity coverage from -3.5 to -1.5 in the electron-going endcap
- π/K separation on a 3σ level up to 7 GeV/c in this whole acceptance
- ~ 20 ps timing reference for ePIC ToF subsystems in the barrel and the forward endcap

by combining single photon signals from aerogel and signals from multi-photon flashes of Cherenkov photons produced by charged particles in HRPPD fused silica windows

R&D effort: The pFRICH design is based mostly on proven technologies, therefore, the remaining R&D effort is fairly small. FY25 R&D activities (partly funded through eRD110 consortium) will be limited to HRPPD aging studies, which will be performed at JLab and INFN Trieste.

E&D status and outlook: Several engineering design activities and first article productions described earlier in the text in more detail have been performed in FY24, and will continue into FY25:

- Full size mirror production and quality assessment
- First article pFRICH vessel outer shell production
- Adjustments of the production process of CFRP-based parts, mirror substrates and HRPPD pockets in the sensor plane in particular
- Fine tuning of the aerogel refractive index and bulk uniformity measurement procedure
- HRPPD sensor design modifications required after the first batch was produced
- HRPPD performance confirmation in the ~ 1.7 T magnetic field typical for a pFRICH location in ePIC

Other activity needed for the design completion: The readout backplane design cannot be fully completed at this stage because of the unavailability of a final design iteration of the anticipated ASIC chip (EICROC) in either of its low channel count configurations (64, 128 or 256 channels).

The performance of the pFRICH in its anticipated configuration needs to be confirmed in a beam test for both Cherenkov photon imaging and timing in the whole momentum range required for e/π , π/K and K/p separation. Such a beam test will be performed with electron and hadron beams at Fermilab in Spring 2025, with an extensive use of first article components (outer vessel shell, aerogel, mirrors, HRPPDs).

Status of maturity of the subsystem: The design of the pFRICH subsystem is in a fairly mature state. As described in previous sections, the pFRICH consists of a cylindrical vessel with two endcap plates, an aerogel tile plane, an HRPPD sensor plane with onboard electronics, mirrors and a number of subsystems (HV and LV, cooling, gas, light monitoring). Engineering design of all of these components (except for the HRPPD ASIC backplane for reasons explained in section 3.4.3) is by now sufficiently advanced to be more than 60% ready by the CD-2 EIC Project phase at the end of 2025.

Environmental, Safety and Health (ES&H) aspects and Quality Assessment (QA) planning: The environmental, safety, and health impacts of the pFRICH subsystem are expected to be minimal. When installing and integrating the pFRICH into the overall detector, all applicable safety standards (i.e. OSHA, Critical Lift procedures, etc.) will be followed and adhered to. Furthermore, the composition of the vessel itself consists mainly of carbon fiber, epoxy, and plastic and any (small) excess can be retained for future use or disposed of via standard waste streams. The operation of the detector will require a modest 400 watts of cooling power and the working gas is pure nitrogen which does not pose any greenhouse concerns.

The individual HRPPDs, mirrors, and aerogel tiles used in the pFRICH will all undergo rigorous quality assessment (QA) checks to ensure that their operation and/or properties are within acceptable limits. Beyond the testing done by the manufacturer, the performance of individual HRPPDs

will be evaluated using test stands located at BNL, JLab, and possibly Yale University. While the details of the test stands differ, they all consist of a light-tight enclosure to house the HRPPD, a fiber-coupled light source (either a pulsed laser or a monochromator), an optical assembly to focus the light onto the sensor, power supplies, and readout electronics. The gain uniformity, quantum efficiency, photon detection efficiency, and dark count rates will be determined over the entire active photosensor area. In addition, the use of a Menlo Systems Elmo 780 femtosecond laser at BNL will allow precision determination of the timing characteristics of the sensors.

The reflectivity of the mirror samples produced at SBU is determined using a dedicated test stand at BNL. The setup consists of a monochromator light source, dark box, optical assembly, and motorized sample and sensor mount. Light from the monochromator is fed via fiber to the optical assembly where a beam splitter directs a fraction of the light to a reference photodiode and passes the remaining beam to focusing elements and then on to the mirror and measurement photodiode. The mirror sample and measurement photodiode sit on independently rotating platforms allowing measurements at a variety of angles. The mirror reflectivity is determined by taking the ratio of the photodiode current with and without the mirror present. Variations in the monochromator light source intensity are corrected using the reference photodiode. This stand is designed to evaluate mirror test samples with a maximum size of several square centimeters. Detailed QA and mapping of the detector mirrors will be performed *in situ* before the pfRICH vessel is sealed during final assembly. A dedicated 3-D scanner will be constructed for this purpose utilizing the techniques developed with the sample test stand.

The aerogel quality assessment will be performed at Temple University and include assessments of the refractive index, transparency, uniformity and mechanical specifications. So far, the refractive index has been determined from the Fraunhofer method by measuring the deflection of the light passing through the corner of the aerogel tile. Work is currently underway to develop a setup and approach that is based on measuring changes in the polarization between the light incident on the aerogel and the light that is reflected from its surface. This would allow for localized refractive index measurements to ensure not only the aerogel has the proper mean refractive index, but also its uniformity across the whole tile. Transparency QA will make use of wavelength dependent transmittance measurements carried out using a newly commissioned and validated UV/VIS LED-spectrometer system. The transmittance data will be fitted with the Hunt Formula to extract aerogel properties such as the scattering surface coefficient and clarity, as well as the wavelength dependent properties which include the transmittance, transmission length, and scattering length. The density will be calculated by measuring the aerogel mass using a precision scale (100 μ g) and volume via caliper and touch probe. Reference jigs can be made to ensure that the aerogel mechanical specifications such as the side-to-side length, tile height, and surface planarity variations are within acceptable ranges.

Construction and assembly planning: The pfRICH has been designed such that it can be fully assembled and inserted into ePIC in one piece. Individual components such as vessel walls, sensor and aerogel planes, mirrors, HRPPDs, and aerogel tiles will be manufactured and tested at various locations and then shipped to BNL for final assembly. It is envisioned that final subsystem assembly will take place in a cleanroom or dedicated lab space within the physics building at BNL. Once assembled, the pfRICH will be transported by truck roughly 1.3 miles to the experimental hall where it will be integrated with the other ePIC subsystems.

The assembly of the pfRICH itself will proceed via the following general steps: (1) assemble the aerogel plane by fastening it to the outer and inner walls, (2) place the sub-assembly such that the upstream end is facing down, (3) add aerogel tiles and aerogel retaining system into the aerogel plane, (4) pre-assemble most of the sensor plane by affixing the inner and outer mirrors and any

vessel services (i.e. inner gas tubing, laser monitoring system, etc.) to the sensor plane, (5) lift the sensor plane over the rest of the vessel and lower the sensor plane and mirrors into place, (6) fasten the sensor plane to the subassembly at the inner and outer walls, completing the cylindrical vessel, (7) systematically insert and secure the individual HRPPD modules into the back of the sensor plane, (8) lift the completed pFRICH, rotate it into its operating position, and install it onto the transportation/storage cart.

Collaborators and their role, resources and workforce: The pFRICH Detector Subsystem Collaboration (DSC) member institutions, as well as other affiliated groups are listed in the table below, along with their anticipated commitments.

Institution	Role	Workforce	Resources
Brookhaven National Lab	Project lead HRPPD and mirror testing Gas, cooling, HV & LV systems, DAQ Detector and physics simulation	5 Staff	HRPPD test stands (pico/femto-second laser, dark box with a motion control, high performance scope, waveform digitizers) Mirror test stand (monochromator) Sample temperature control chamber
Chiba University*	Connection to aerogel factory	N/A	Aerogel production equipment
Duke University	Detector modeling	1 Staff	
INFN Genova*	HRPPD B-field studies	1 Staff	
INFN Trieste*	Detector modeling HRPPD aging and B-field studies	1 Staff	HRPPD test stand (laser, dark box, waveform digitizers)
Jefferson Lab*	Mechanical design EIC Project Support HRPPD testing	2 Staff	HRPPD test stand (laser, dark box, motion control, digitizers)
Ljubljana University & JSI*	Expert input on detector design	N/A	
Mississippi State University	Laser monitoring system	1 Staff, Students	
Purdue University	Vessel and mirror fabrication	2 Staff, Students	Machine shop / fabrication lab
Stony Brook University	Vessel fabrication Mirror coating	1 Post-Doc, Students	Mirror coating chamber Vessel form
Temple University	Aerogel testing and QA	1 Staff	Aerogel test stand
University of Debrecen	HRPPD backplane design & fabrication	1 Staff	
University of Glasgow	MCP-PMT evaluation	1 Staff, Students	MCP-PMT test stand (laser, dark box, cosmic ray stand, electronics)
Yale University	Software support HRPPD QA	1 Staff, Students	HRPPD test stand (dark box with motion control, digitizers)

* No institutional commitment

Figure 8.42: PLACEHOLDER Institutions contributing to the pFRICH effort and their roles, resources, and participating workforce.

Risks and mitigation strategy: A number of risks has been identified in the past, and mitigation strategies developed.

A reliable large area highly pixellated photosensor with a high quantum efficiency and single photon timing resolution better than ~ 50 ps is a core component of the pFRICH design. The pFRICH team, together with the EIC eRD110 consortium (Photosensors) has been routinely working with one of the two manufacturers remaining on the market (Incom Inc.) for several years to help the company re-design their HRPPD sensors so they fully meet EIC specifications. The ongoing evaluation of the first seven EIC HRPPDs produced in 2024 shows that overall quality, as well as reproducibility of parameters verified so far (quantum efficiency in particular) meet the requirements. As a fallback photosensor solution, we consider Photek Auratek MCP-PMTs. Such a PMT has been ordered already, and its performance will be evaluated against the pFRICH detector needs in FY25.

Aerogel tiles of required quality can be produced in a very few places worldwide. The pFRICH team, together with the EIC Project, has been routinely working with the Aerogel Factory in Japan

over the last two years, to make sure the quality and production capacity meet our requirements. A technical lead of the Chiba Aerogel Factory in Japan is also a member of the pFRICH DSC, see Fig. 8.42. Our simulations show, that in case Aerogel Factory cannot produce sufficiently large tiles to cover the whole front wall of the vessel in a configuration with three radial bands as shown in Fig. 8.39, one can resort to using tiles of a readily available size up to 145 mm in a four-band configuration, with an acceptable loss of performance caused by additional dead area introduced by an extra row of radial spacers between the tiles.

Additional Material Add text here.

8.3.4.3 The high performance DIRC

Requirements

Requirements from physics: The PID system in the central section of the ePIC detector has to provide 3 standard deviations or more separation of π/K up to 6 GeV/ c and contribute to low momentum e/π identification.

Requirements from Radiation Hardness: The anticipated radiation doses in the areas of the hpDIRC optics and the potentially sensitive readout section of the hpDIRC are predicted to be modest. These estimates are based on minimum-bias PYTHIA e+p events at 10×275 GeV, assuming maximum machine luminosity over a six-month period of annual operation at 100% machine and detector efficiency for 10 years. Under these conditions, we expect a total dose from electromagnetic and hadronic radiation of less than 100 rad and a 1-MeV-neutron equivalent fluence of up to 10^{10} neutrons per cm^2 .

Requirements from Data Rates: Add text here.

Justification

Device concept and technological choice: A radially compact detector based on the DIRC (Detection of Internally Reflected Cherenkov light) principle is a specialized type of RICH counter. It employs solid, rectangular-shaped radiators made of synthetic fused silica, which also serve to guide Cherenkov photons to the readout section located outside the crowded area of the detector. This design keeps the active radiator section of the DIRC detector radially compact, minimizing its impact on the performance of subsequent systems and simplifying integration into the ePIC. The photons are recorded by an array of pixelated photon sensors mounted at the back of the expansion volume. Thanks to the excellent optical finish of the optics the emission angle of Cherenkov photons, with respect to the particle track, is maintained during the photon transport via the total internal reflection and can be reconstructed from the measured position of the photon on the detector surface and the arrival time of each photon. The general concept of a barrel DIRC detector was first successfully demonstrated by the BaBar DIRC and followed by several experiments worldwide. The ePIC high-performance DIRC (hpDIRC) is inspired by the lens-based focusing concept of the PANDA Barrel DIRC, with several advancements to meet the performance requirements of the Electron-Ion Collider (EIC). The hpDIRC concept was developed as part of the EIC generic R&D

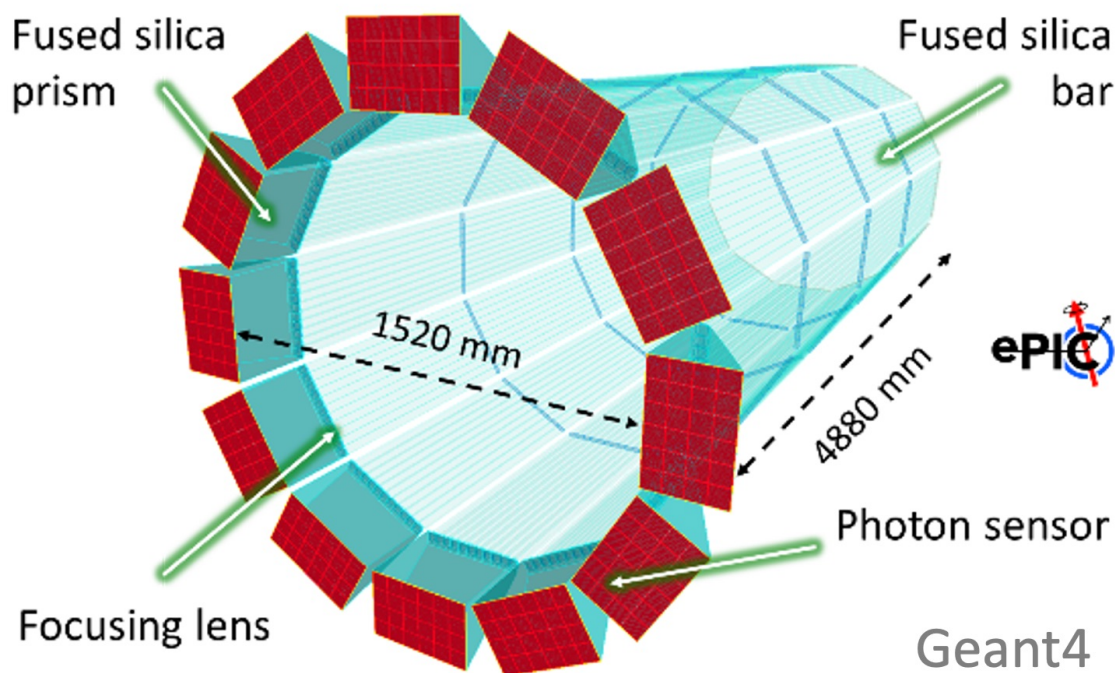


Figure 8.43: ePIC hpDIRC geometry in the Geant4 standalone simulation.

2583 program performed by the EIC PID collaboration (eRD14) and direct EIC Project R&D eRD103 with
 2584 the focus on extending the momentum coverage well beyond the DIRC counter state-of-the-art.

2585 Subsystem description:

2586 General device description:

2587 The baseline design of the ePIC hpDIRC detector, implemented in a detailed Geant4 simula-
 2588 tion, is shown in Fig. 8.43. It is divided into twelve optically isolated sectors that comprise
 2589 a bar box and a readout box, surrounding the beamline in a 12-sided polygonal barrel with
 2590 an inner radius of about 760 cm. Each bar box includes a set of ten radiator bars, made of
 2591 synthetic fused silica, each 4880 mm long, with a cross-section of 17 mm × 35 mm. The bars
 2592 are placed side-by-side, separated by small air gaps, in a light-tight container, called a bar
 2593 box. Mirrors are attached to one end of each bar to reflect Cherenkov photons towards the
 2594 readout end, where they exit the bar and are focused by a 3-layer spherical lens on the back
 2595 surface of the prism that serves as an expansion volume.

2596 Bars:

2597 The baseline ePIC hpDIRC design envisions each of the 120 long bars comprising three legacy
 2598 BaBar DIRC bars and one shorter new bar manufactured by industry. The number of bar
 2599 boxes and bars per box has been optimized to align with the width of the BaBar DIRC bars
 2600 while maximizing the azimuthal acceptance of the hpDIRC. This approach assumes that the
 2601 BaBar bars can be extracted from their bar boxes without compromising their optical and me-
 2602 chanical integrity. The disassembly and evaluation of the BaBar bars are currently underway,
 2603 with a decision expected by Spring 2025.

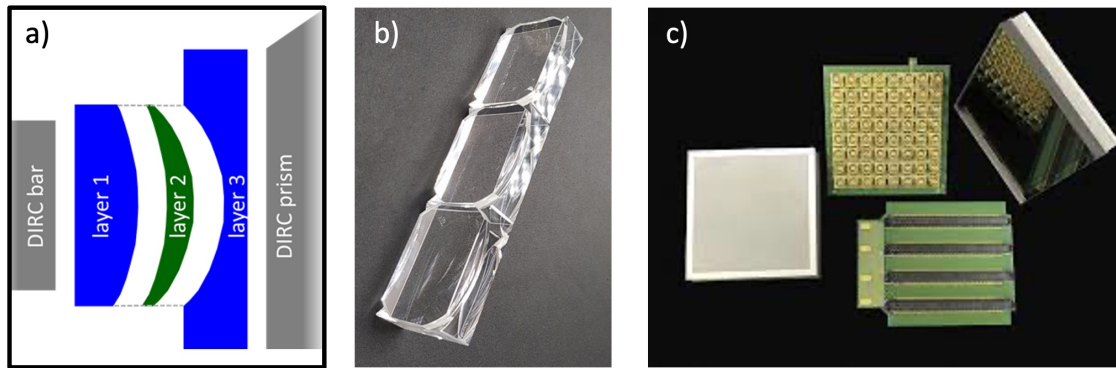


Figure 8.44: a) Schematic of the side view of one hpDIRC section and an exploded view of the 3-layer lens. b) Photo of prototypes of the 3-layer spherical lenses. c) Photec AuraTek MAPMT253.

Lenses:

The 3-layer spherical focusing lens is a novel component of the hpDIRC and is essential for achieving the required PID performance. The lens design, shown in Fig.8.3.4.3a, dramatically reduces photon loss caused by air gap transitions in standard lens systems. It does this by focusing Cherenkov light through refraction at the interface between synthetic fused silica and a high-refractive-index material, such as sapphire or lanthanum crown glass. A thin layer of the high-refractive-index material is sandwiched between two layers of synthetic fused silica, with carefully optimized radii of curvature on all spherical surfaces. This design combines defocusing and focusing transitions to form a flat detector plane that accommodates a wide range of photon angles, matching the layout of the sensor array on the expansion volume prism. Several prototypes using different materials for the middle layer have been produced by the optical industry, and examples of these three prototypes are shown in Fig.8.3.4.3b.

Prisms:

The prism expansion volume is made of synthetic fused silica, has a 32° opening angle, and dimensions of $237 \text{ mm} \times 350 \text{ mm} \times 300 \text{ mm}$. The detector plane of each prism is covered by an array of 24 sensors shown in red in Fig. 8.43.

Sensors:

In the baseline design of the hpDIRC, commercial microchannel plate photomultiplier tubes (MCP-PMTs) with a pore size of $10 \text{ }\mu\text{m}$ or smaller are employed as photosensors to capture the position and arrival time of Cherenkov photons. A pixel size of 3.2 mm was chosen based on Geant4 simulations as a balance between cost, performance, and feasible sensor technology for the hpDIRC. Lifetime-enhanced 2" MCP-PMT tubes are commercially available from Photonis and Photek with suitable DC-coupled anode configurations. The simulation utilizes Photonis Planacon XP85122 MCP-PMTs, incorporating realistic sensor characteristics, including photon timing, collection efficiency, and quantum efficiency. With the stop of production of Photonis tubes, Photek MAPMT 253 sensors, shown in Fig. 8.3.4.3, are the primary candidates for hpDIRC. They share the same footprint and are expected to exhibit similar properties to the Photonis tubes.

FEE: Fast ASIC-based readout systems are being developed by the EIC project to meet the demands of various ePIC detector systems. For the hpDIRC, the readout electronics must be capable of detecting small signals (on the order of a few millivolts) from MCP-PMTs while maintaining excellent single-photon timing precision. Additionally, the electronics need to

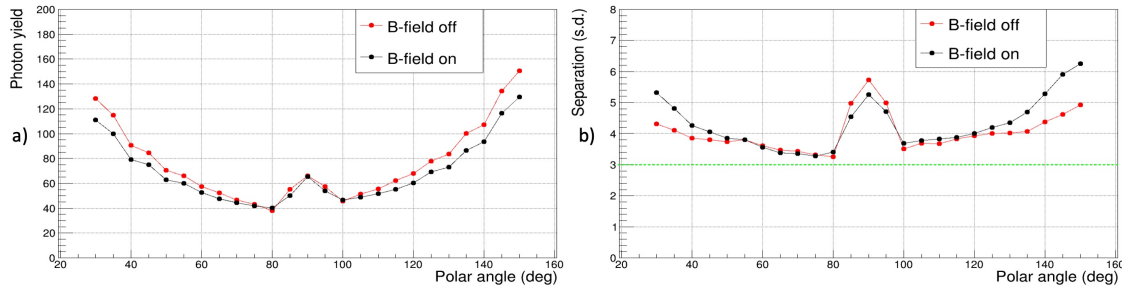


Figure 8.45: The expected performance of the hpDIRC as a function of the particle's polar angle is illustrated in terms of photon yield (a) for pions and π/K separation power (b). These results are based on a standalone Geant4 simulation for particles with a momentum of 6 GeV/c.

match the channel density and sensor footprint, as they will be directly coupled to the back of the sensor to minimize distance and achieve optimal timing precision. The two leading candidates for hpDIRC readout are EICROC and FCFD, which are discussed in detail in Section XXX.

Performance Figure 8.45 presents the expected performance based on standalone Geant4 simulation studies using a particle gun. The plots illustrate a scenario where particles are fired at a whole range of polar angles but with an azimuthal angle fixed at zero degrees so perpendicular to one of the middle bars. The black points represent the photon yield and separation power for charged pions and kaons as a function of polar angle at a momentum of 6 GeV/c with the magnetic field enabled, while the red points display the same data with the magnetic field disabled.

The number of detected Cherenkov photons per particle (plot a) ranges from 40 to 150, depending on the polar angle. The sharp increase in photon yield at steeper forward and backward angles is due to the longer track length in the fused silica bar, with an asymmetry in forward/backward yields resulting from photon loss along longer propagation paths at smaller polar angles. The peak in photon yield near a polar angle of 90° occurs because a larger fraction of emitted photons satisfies the total internal reflection criterion near perpendicular incidence, compared to slightly larger or smaller angles.

The separation power for both particle hypotheses (plot b) is obtained from Gaussian fits to the log-likelihood differences between pairs of particle hypotheses. It is calculated as the difference between the means of the two Gaussians divided by their average width. The slightly improved performance for polar angles above 100° is due to shorter photon paths, resulting in higher photon yields and reduced chromatic dispersion in the bar material.

Similar studies were conducted for electron-pion (e/π) separation, which is primarily the responsibility of the Electromagnetic Calorimeter. However, the hpDIRC can also contribute to this task at lower momenta. At these lower momenta, multiple scattering presents a challenge, but assuming the tracking resolution outlined in the Yellow Report, the hpDIRC can maintain a 3-standard-deviation separation power up to 1.2 GeV/c.

The expected particle identification (PID) performance of the hpDIRC surpasses the ePIC PID goal, achieving more than 3 standard deviations of separation power for e/π identification up to 1.2 GeV/c and π/K separation up to 6 GeV/c across the entire polar angle range.

Performance Systematic Studies Most of the hpDIRC performance studies were conducted using a particle gun, providing precise control over the parameters under investigation while covering the entire required angular and momentum ranges. Detailed studies examined a range of azimuthal angles, ensuring particle interactions across the full width of the bar box, including bars outside the central region. While a moderate performance deterioration was observed in some of the non-central bars, the system maintained the required 3-standard-deviation separation power.

The effect of the magnetic field on hpDIRC performance was found to be negligible, as confirmed through simulations that incorporated a realistic ePIC magnetic field map.

Additionally, studies using Pythia-generated physics events were performed to assess the frequency and effect of multiple tracks per event within a single bar and hpDIRC module. Even in the extremely rare cases where two or more particles are very close in momentum, polar, and azimuthal angles within a single event, the impact on performance was found to be moderate, demonstrating the robustness of the hpDIRC system.

Most studies were based on an assumed angular tracking resolution of 0.5 mrad at 6 GeV/c. However, the simulation software is prepared to import and integrate a more detailed tracking parametrization when it becomes available.

To enhance the efficiency of physics studies in ePIC, detailed hpDIRC PID Look-Up-Tables (LUTs), including the threshold mode, were generated using Geant4 simulations. These LUTs are now employed to streamline physics analyses without the need for full reconstruction.

Simulation tools and validation A detailed standalone Geant4 simulation, featuring realistic geometry and material properties, was developed in collaboration with the PANDA Barrel DIRC group and validated through modular prototype tests using particle beams at CERN. The simulation incorporates measured values for MCP-PMT quantum efficiency, collection efficiency, and timing resolution. It also accounts for the coefficient of total internal reflection of the DIRC radiator bars as a function of photon energy, the bulk transmission of the bars, glue, and lenses, as well as the wavelength-dependent refractive indices of the materials used, the photocathode, and the reflectivity of the mirrors. Background contributions from hadronic interactions and delta electrons in the bar, along with effects from MCP-PMT dark noise and charge sharing between anode pads, are also simulated. All relevant resolution factors for hpDIRC performance are modeled using Gaussian smearing with conservative resolution assumptions. The total timing precision per photon, including sensor and readout electronics, is set to 100 ps, and the angular resolution of the ePIC tracking system at the hpDIRC radius is assumed to be 0.5 mrad for particles with a momentum of 6 GeV/c.

Figure 8.46 presents photos of the modular PANDA Barrel DIRC prototype along with results obtained during the 2018 test beam campaign at CERN. Although the PANDA prototype differs significantly from the ePIC hpDIRC in terms of geometry (single bar), slower readout electronics, and lower-quality sensors with larger pixels, the studies and results are highly valuable for hpDIRC development. The same software used for all ePIC hpDIRC performance studies was employed to simulate the PANDA prototype. As shown in Fig. 8.46c and d, the agreement between the simulation and experimental data is excellent

Reconstruction methods The hpDIRC utilizes two primary reconstruction methods for identifying particles based on Cherenkov photon detection: geometric reconstruction and time-based imaging reconstruction. These methods are essential for translating the detected photon patterns into meaningful physical information, particularly the Cherenkov angle, which is crucial for parti-

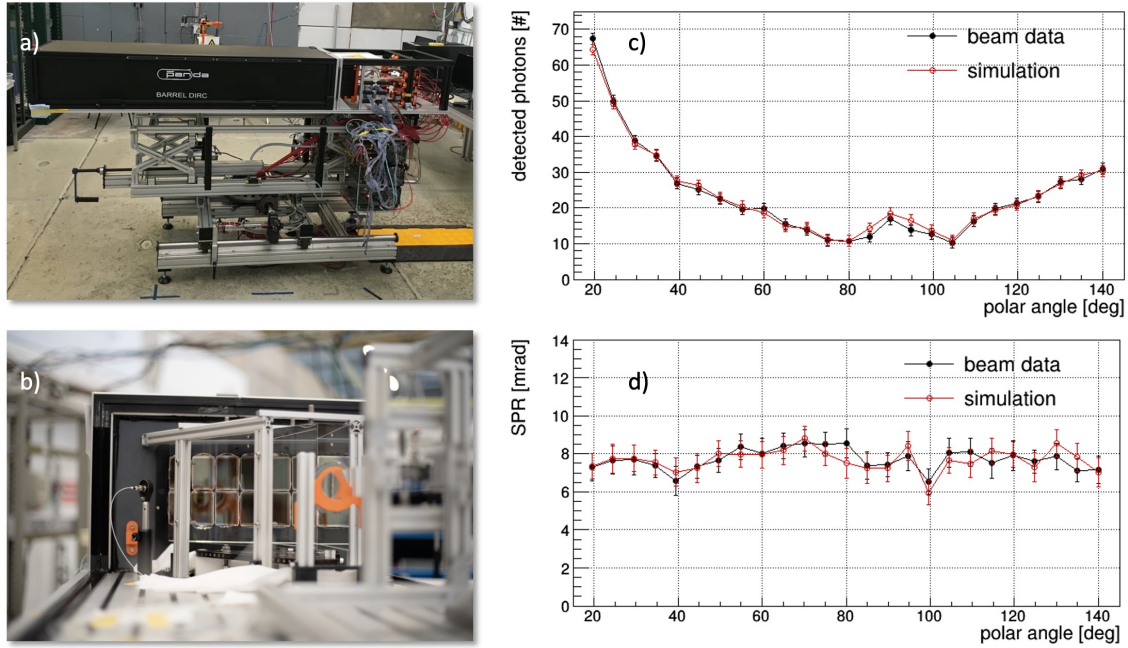


Figure 8.46: Photographs of the PANDA Barrel DIRC prototype (a), including a close-up of the readout section (b) taken during the CERN test beam. Performance plots illustrate the comparison between simulated and experimental data for photon yield (c) and single photon Cherenkov angle resolution (SPR) (d).

cle identification.

Geometric reconstruction in DIRC detectors is based on determining the Cherenkov photon direction from the mutual location of the radiator's readout end and the pixel hit by the photon. This method allows direct reconstruction of the Cherenkov angle for each detected photon by utilizing both the photon's direction and the beam particle's direction. Photon directions are pre-calculated using full simulations, taking into account the optical materials, and stored in look-up tables (LUT). Discrete ambiguities arise due to photon reflections within the optical system, but these can be reduced by applying a cut on the difference between the expected and measured photon arrival times. The geometric method primarily relies on the photon position, using timing information to suppress background noise, and provides key performance variables such as the single-photon Cherenkov angle resolution and the yield of signal and background photons.

The time-based imaging reconstruction method enhances particle identification (PID) by fully utilizing both the timing and position information of the detected photons. This method compares the measured photon arrival times against expected distributions for each particle hypothesis, stored as probability density functions (PDFs) derived from experimental data. For each photon, a time-based likelihood is calculated, which is then combined with the Poissonian PDF of the number of detected photons to yield the full PID likelihood. Unlike geometric reconstruction, the time-imaging method is suitable for both narrow-bar and wide-plate radiators, offering better separation power between particle hypotheses. This method can achieve the best resolution and allows for the most effective corrections of distortions, improving the overall performance and precision of the hpDIRC in particle identification.

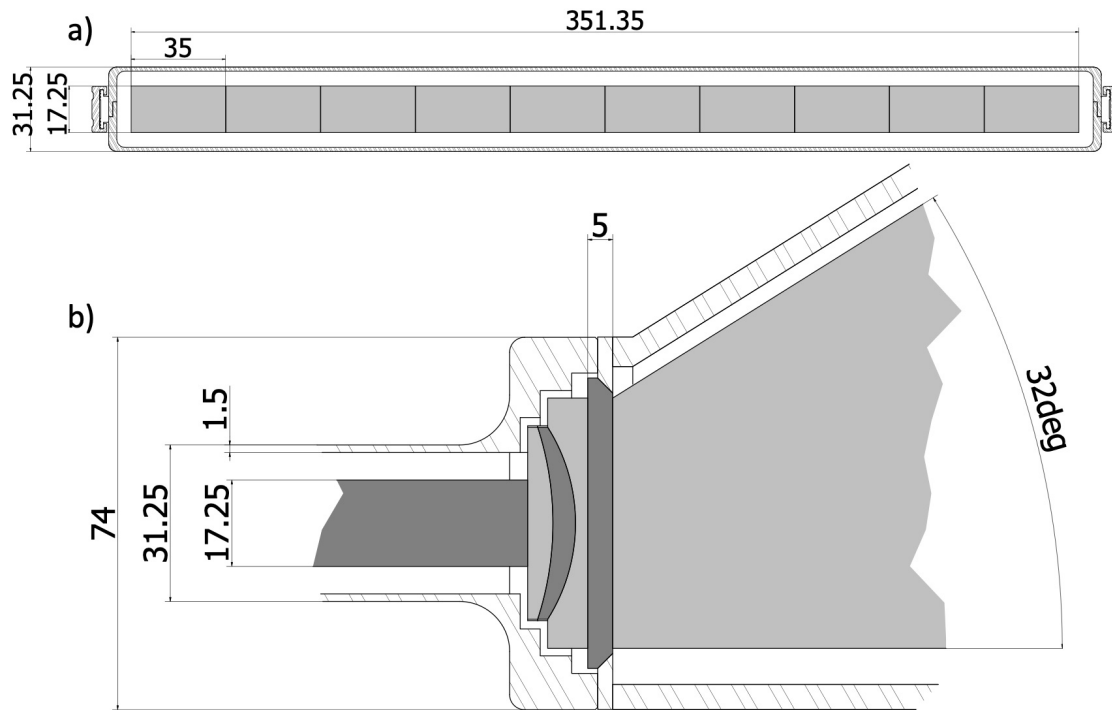


Figure 8.47: Technical drawings of the ePIC hpDIRC detector, showing the XY cross-section of the bar box (a) and the YZ cross-section of the connection between the bar box and the readout box (b).

Implementation

Subsystem mechanics and integration: The hpDIRC consists of two primary sub-assemblies: the readout section and the bar section. Both sections are composed of 12 boxes made of carbon fiber reinforced polymer (CFRP), with varying thickness depending on the stress conditions in different regions.

The readout section houses the fused silica expansion prism, readout sensors, and front-end electronics. The expansion prism has an angle of 32° and maximum dimensions of 300 mm in length, 352 mm in width, and 237.5 mm in thickness. MCP-PMTs are coupled to the 352 mm x 237.5 mm backplane of the expansion prism using an optical interface. Sensors and associated readout electronics are mounted on a 3D-printed frame. The rear of the readout box is sealed with a light-tight plate that has ports for sensor and electronics cables, fibers for calibration lasers, and monitoring cameras. Dry nitrogen gas flows through the readout box to keep the prism's surface clean and free from dust, condensation, or residue. To maintain stable temperatures and cool the electronics, water circulates through tubing.

The bar section is composed of a top and bottom shell with overall dimensions of 4627 mm in length, 368 mm in width, and 31.25 mm in height. Figure 8.47a shows the XY cross-section of the hpDIRC bar box with indicated key dimensions. The thicker part of the carbon fiber shell on the sides will be used during installation to slide in the bar box and hold it in place. The carbon fiber thickness is 1.5 mm across the width and 3 mm across the height. Each bar box contains 10 long radiator bars, lenses, and mirrors. The radiator bars are 35 mm wide, 17.25 mm thick, and 4580

mm long, spaced 0.15 mm apart using shims to ensure optical isolation. Each long radiator bar is made up of four shorter bars bonded together with an optically transparent adhesive, similar to the BaBar DIRC construction. Three of the shorter bars, each 1225 mm long, are repurposed from the BaBar experiment, while the fourth is newly manufactured to meet the total length requirement of 905 mm.

At one end of each bar, a 3 mm-thick flat mirror reflects photons back toward the readout end. At the opposite end, a three-layer lens is attached to the bar using the same adhesive used to join the short bars. The lens-mirror-bar joints are kept in compression by adjustable spring plungers located behind the mirrors, which reduce stress on the joints and prevent movement during installation or operation. The spring system also compensates for differential thermal expansion and contraction between the bars and the bar box. Each short bar is supported by two pairs of fixed nylon buttons along its length, which minimize stress on the glue joints and prevent photon loss by reducing contact with the radiator surface. Eight support pairs are evenly distributed along each long bar's length, with adjustable spring buttons pressing the bars against the fixed buttons to maintain secure positioning while preserving optical isolation. Similar support mechanisms are used for the 17.25 mm-thick end of the bars, where all 10 bars are pressed against a single set of fixed buttons. To handle the additional stress at the button locations and accommodate holes for the spring buttons, the CFRP is locally thickened at these points. Like the readout boxes, the bar boxes are also flushed with dry nitrogen to protect the radiator bars' surfaces, with nitrogen introduced at the mirror end and vented near the lenses.

The hpDIRC consists of 12 paired bars and readout boxes. The lenses at the bar box end are coupled to a thin window that seals the box, while this window is in turn connected to the prism in the readout box using an optical interface during installation. The readout box, equipped with the prism, is compressed against the bar box window to form a tight optical seal. Figure 8.47b illustrates the XZ cross-section of the connection between the bar box and the readout box, with key dimensions highlighted. The 5 mm thick window between the 3-layer lens and the prism represents an initial design, which may be adjusted following further studies of strains and forces acting on the system.

The hpDIRC is positioned radially just inside the Barrel Electromagnetic Calorimeter (EM Calorimeter) and just outside the outer Micro-Pattern Gas Detector (MPGD) within the ePIC detector. Both the bar boxes and the MPGD are supported by the EM Calorimeter through high-precision rails mounted on triangular brackets extending radially inward from the calorimeter's inner diameter.

Installation: During installation, the bar boxes are placed on a specialized lifting fixture, allowing them to be rotated into their final orientation before being transferred along the rails to their designated positions. The readout boxes are supported by an external ring attached to the Hadron Calorimeter via a series of legs. Each readout box is aligned with its corresponding bar box using specialized brackets and rails, which allow the readout box to be slid into position, compressing the optical interface and forming the connection. This rail system also enables the readout boxes to be removed without disturbing the bar boxes if necessary.

Services: Gas and Moisture Control: To maintain a low-moisture environment for the bars, dry nitrogen gas from liquid nitrogen boil-off will flow through each box. The nitrogen gas will be monitored for humidity and filtered through a molecular sieve and mechanical filters to remove particulates. Some of the input N₂ gas will leak from the bar boxes, also helping to keep the bar box slots in the mechanical support structure free of condensation.

Power Supply and Monitoring: Both high and low-voltage supplies will be provided for each MCP-

2796 PMT sensor. A control and monitoring system will be implemented for the readout and bar box
2797 sections. The high voltage required for each MCP-PMT can be supplied by commercially available
2800 multichannel power supply modules, housed in crates located outside the beam area.

2799 The low-voltage power supplies, which regulate power to the front-end electronics (FEE), need to
2800 be placed as close as possible to the detector, in racks dedicated to the hpDIRC system. A modular,
2801 multichannel approach—similar to the high-voltage system—is planned for the control and moni-
2802 toring of voltages, currents, and onboard temperatures for all FEE boards. The low voltage levels
2803 will range from 1 to 48 V, with currents reaching several amperes.

2804 **Cooling System:** The highly integrated FEE design generates a significant amount of heat in the
2805 compact readout unit. This heat will be extracted by a water cooling system, and the necessary
2806 supply lines are included in the mechanical design of the readout boxes, although further opti-
2807 mization is required.

2808 **Environmental Monitoring:** Standard commercial devices will monitor environmental parameters
2809 such as temperature and humidity at various locations inside the hpDIRC volume to ensure opti-
2810 mal performance and safety.

2811 **Calibration, alignment and monitoring:** Time Calibration: To achieve the time resolution
2812 required for the hpDIRC, it is essential to eliminate time offsets between pixels, which may arise
2813 from differences in cable lengths and pixel-to-pixel variations within the photon sensors. A laser
2814 monitoring system will be employed to provide channel-by-channel time-zero information, which
2815 will be stored in a database. This data will be used to accurately calibrate the photon arrival times
2816 for all pixels.

2817 **Optical Calibration and Alignment:** The exact positioning of the optical components will be deter-
2818 mined during the hpDIRC DIRC installation, using a laser and precise survey marks. The recon-
2819 struction of the Cherenkov angle, based on the hit pattern on the MCP-PMT array, depends on the
2820 accurate relative positions and orientations of all optical elements, including the photon sensors
2821 and their individual pixels.

2822 **In-Beam Calibration and Alignment:** After installation in the ePIC detector, the alignment of the
2823 hpDIRC will be verified using beam data. Samples of muons, pions, kaons, and protons—identified
2824 by other ePIC sub-detectors or through kinematic fitting—will be used to calibrate the hpDIRC
2825 DIRC's measurement of the Cherenkov angle. Clean samples of pions, kaons, and protons will be
2826 selected based on specific decay channels.

2827 Geometric reconstruction will then be used to calculate the Cherenkov angle per photon for each
2828 track and sensor pixel. Any deviation between the measured and expected Cherenkov angles in the
2829 calibration samples will be utilized to develop a correction function or multi-dimensional lookup
2830 table. This information will be stored in the configuration database to correct for residual mis-
2831 alignment and optimize the performance of the hpDIRC. A similar procedure was successfully em-
2832 ployed in the BaBar DIRC, where a 10% improvement in Cherenkov angle resolution was achieved
2833 by applying per-photon corrections based on a dedicated particle calibration sample.

2834 **Status and remaining design effort:** Preparations for the hpDIRC are progressing in line with
2835 the overall project schedule. In the chart shown in Figure 8.48, the top few lines highlight the
2836 major milestones of the project from the present day through to the start of the experiment and
2837 CD-4 approval. Below these milestones is a detailed breakdown of key work packages, including
2838 the optical components, readout system, and mechanical design. The hpDIRC is expected to be

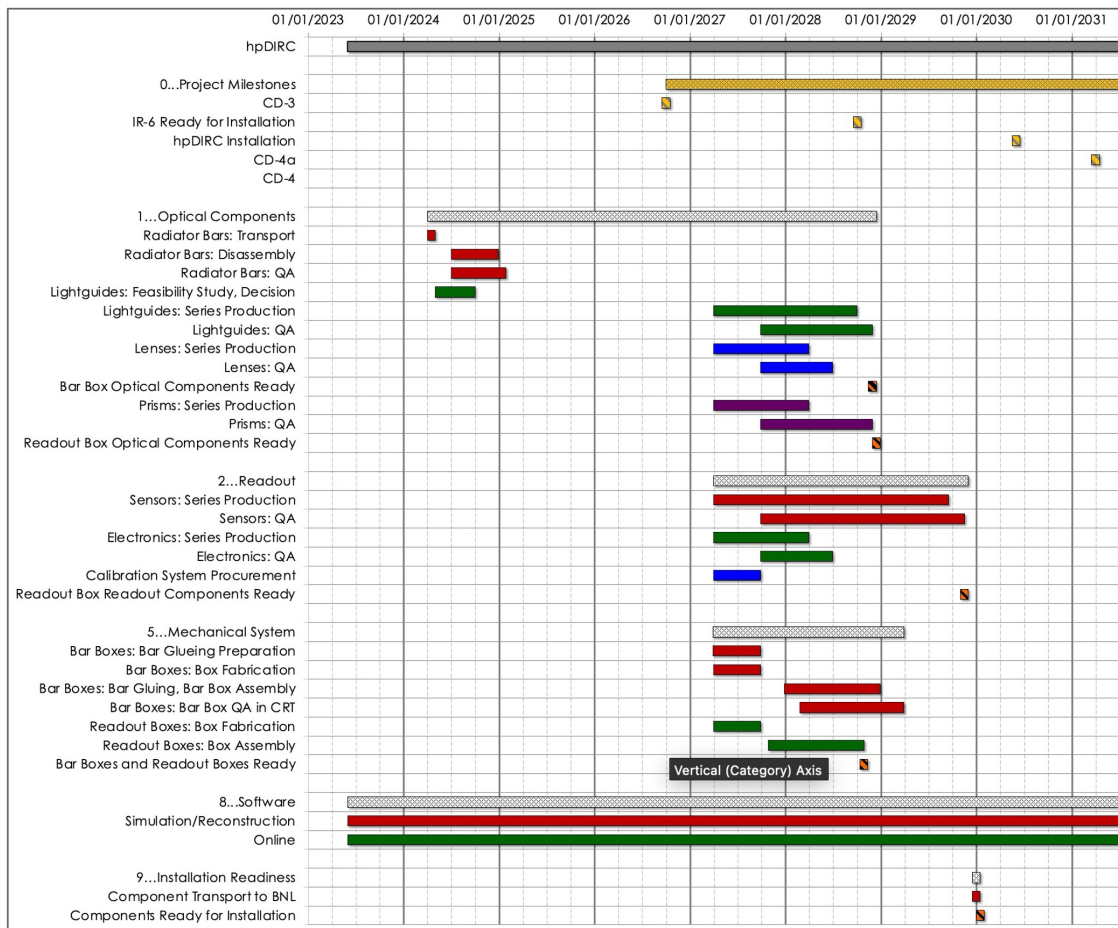


Figure 8.48: ePIC hpDIRC schedule chart alignment with EIC Project schedule

2839 fully ready well in advance of the installation deadline, with a substantial time buffer built into the
 2840 schedule.

2841 The length of the ePIC barrel necessitates a "light guide section" to direct photons from the active
 2842 part of the hpDIRC bars to the expansion volume prism, where they are imaged. In the baseline
 2843 hpDIRC design, shorter bars with the same cross-section as the narrow bars are used, as shown in
 2844 Figure 8.49a for one module.

2845 Figure 8.49b illustrates an alternative hybrid design, featuring a single wide plate in the light guide
 2846 section that replaces the narrow bars. The primary motivation for this geometry was potential cost
 2847 savings, but it also introduced additional opportunities. For instance, the choice of lens type be-
 2848 came a question: should it be a set of spherical lenses matching each narrow bar or a single large
 2849 cylindrical lens? Furthermore, where should the lens be positioned—after the light guide section as
 2850 in the baseline design, or perhaps before the prism expansion volume, or even earlier, between the
 2851 narrow bars and the plate to initiate the expansion sooner? Detailed simulation studies of several
 2852 configurations led to the selection of a geometry featuring a set of spherical 3-layer lenses with an
 2853 optimized shape, placed before the light-guide plate, as the leading candidate for the alternative
 2854 design. Figure 8.50 compares the performance of this alternative design (red points) with the base-
 2855 line design (black points). The wide plate alternative shows significant performance improvement

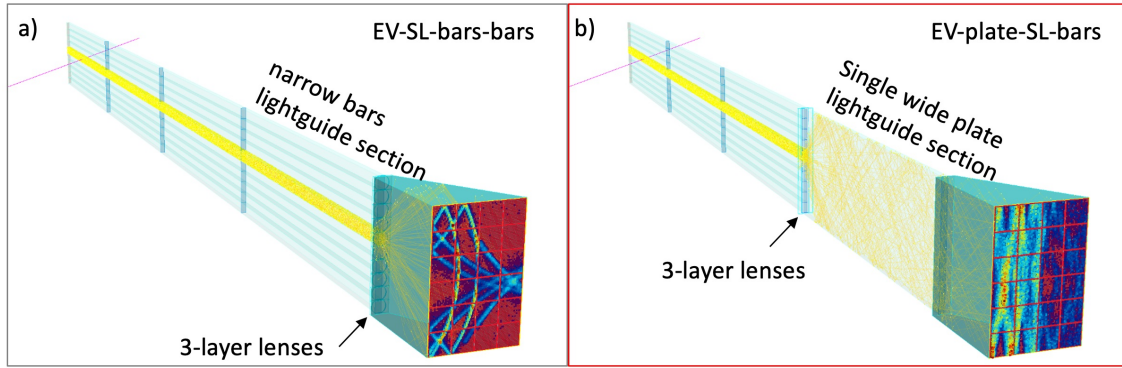


Figure 8.49: Event displays of a single module of the hpDIRC narrow bar baseline design geometry (a) and the narrow bar with wide plate hybrid geometry (b), illustrating an example of the accumulated hit pattern from charged pions, based on the standalone hpDIRC Geant4 simulation package.

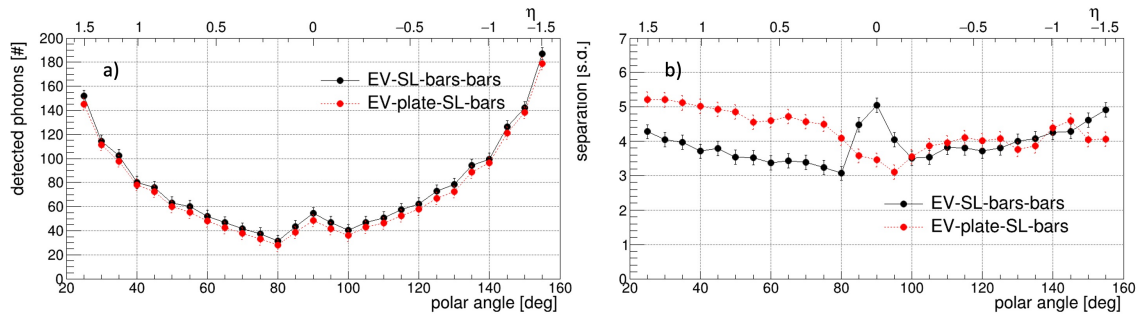


Figure 8.50: Performance comparison between the hpDIRC narrow bar baseline design geometry (black points) and the narrow bar with wide plate hybrid geometry (red points) in case of photon yield (a) for pions and π/K separation power(b) based on a standalone Geant4 simulation for particles with a momentum of 6 GeV/c.

for particle tracks with polar angles below 80° , comparable performance for polar angles above 100° , and a slight reduction in performance for tracks around 90° and above 145° . Despite these reductions, the separation power in the lower-performance regions remains above the required 3 standard deviations, making this hybrid design a promising alternative. However, this geometry has not yet been experimentally validated and would require further investigation before it could replace the current baseline design.

Remaining R&D effort: The primary objectives of the remaining hpDIRC R&D are to validate new, untested components, ensure their successful integration into the hpDIRC system, and optimize the final design. Ultimately, the goal is to achieve a validated, cost-efficient hpDIRC design for the ePIC detector, which will be demonstrated through a vertical-slice prototype in a Cosmic Ray Telescope (CRT) setup. Several critical aspects of the hpDIRC design still require thorough study and verification to guarantee the necessary performance, mitigate risks, and explore new opportunities.

Additional RD projects with a direct impact on the hpDIRC include eRD109 (focused on readout and ASIC designs) and eRD110 (focused on photosensors). The development of compact readout

2871 electronics for fast single-photon detection, using high-density sensors, must be completed and
2872 integrated into the hpDIRC prototype to validate the performance of a cost-optimized design for
2873 particle identification (PID).

2874 The final hpDIRC prototype will assess the optimized sensor arrangement and explore a potential
2875 new focusing approach within a hybrid design, as shown in Fig. ??, which combines a narrow bar
2876 with a wide plate. This configuration offers significant cost-reduction potential, but it has not yet
2877 undergone experimental testing, necessitating experimental validation to inform the final hpDIRC
2878 design decisions. Additionally, the reuse of BaBar DIRC bars—another key cost-saving measure—is
2879 currently being explored with support from Jefferson Lab and the EIC Project, as discussed above.

2880 **Environmental, Safety and Health (ES&H) aspects** The hpDIRC system is designed to op-
2881 erate without the use of any flammable gases or cryogenic liquids, which eliminates the risks asso-
2882 ciated with these hazardous substances. Both the bar boxes and readout boxes will be purged using
2883 boil-off dry nitrogen, which will flow at a rate of a few liters per hour per box. This method ensures
2884 that the environment inside the boxes remains dry and free from contaminants, contributing to the
2885 system’s safety and reliability.

2886 In terms of electrical hazards, the sensors employed in the hpDIRC require high voltages, reaching
2887 up to 2.5 kV. To prevent the risk of electrical shock, the high-voltage (HV) connections will be
2888 completely inaccessible during normal operation. Furthermore, the HV module will be keyed off,
2889 ensuring that only trained personnel will be allowed to operate it, providing an additional layer of
2890 safety in the system’s design.

2891 The hpDIRC will also utilize a class 3B Helium-Cadmium (HeCd) laser pulser for the calibration of
2892 sensors and electronics. Since lasers pose a radiation hazard, special precautions will be taken: the
2893 laser will be fully enclosed within optical fibers to prevent exposure, and only trained personnel
2894 will be authorized to operate the laser, ensuring that the risk of accidental radiation exposure is
2895 minimized.

2896 For the cooling of the readout electronics, a chilled liquid will be used, though the specific details
2897 of the liquid have yet to be determined. To avoid the risk of a chemical leak, the cooling liquid will
2898 circulate at sub-atmospheric pressure, which helps prevent potential leaks and ensures the safe
2899 operation of the cooling system.

2900 The entire hpDIRC system will comply with all applicable Environment, Safety, and Data (ES&D)
2901 standards and Occupational Safety and Health Administration (OSHA) regulations. This commit-
2902 ment to compliance ensures that the system adheres to the highest safety protocols, protecting both
2903 the equipment and the personnel involved in its operation.

2904 **Quality Assessment (QA planning:** The quality assurance (QA) plans for the hpDIRC com-
2905 ponents and modules prior to construction are centered around a combination of process control
2906 at the vendor sites and extensive laboratory measurements. The radiator bars and light guides
2907 will undergo vendor-provided QA to assess their mechanical properties. Following this, a laser
2908 scanning system at JLab will be used to monitor the internal photon transport efficiency of either
2909 disassembled BaBar DIRC bars or newly produced DIRC bars. This ensures that the optical perfor-
2910 mance of the bars meets the necessary standards for the ePIC hpDIRC.

2911 For sensors and electronics, laser pulser systems will be deployed at CUA, JLab, or USC (to be de-
2912 termined) to perform comprehensive measurements, including gain, quantum efficiency, collection
2913 efficiency, and dark count rate. These tests will verify the operational integrity and performance of
2914 the sensors, which are critical for the overall functionality of the detector.



Figure 8.51: Photos of available setups developed during the hpDIRC R&D program that will be used for future QA of 3-layer lenses with laser setup at ODU (a), bars and other optics at Jefferson Lab (b) and readout chain including sensors and electronics and other hpDIRC components in hpDIRC prototype at CRT at SBU (c).

The lenses will be evaluated at the laser laboratory at ODU, where the shape of the focal plane will be carefully analyzed to ensure proper optical alignment and focusing. Prisms will be subjected to vendor-provided QA, followed by further checks at WSU to confirm their specifications. Similarly, the bar boxes and prism boxes will undergo QA at the vendor sites, with additional testing and validation at SBU.

Once the DIRC modules are fully assembled, including the coupling of the bar box to the readout box (a vertical slice), the Cosmic Ray Telescope at SBU will be used for testing. This will ensure that the assembled DIRC modules function as intended before final integration.

After installation of the DIRC module in ePIC, a picosecond laser pulser calibration system will be employed to fine-tune the system. Cameras will also be used to continuously monitor the optical coupling between the sensors, prisms, and lenses, ensuring that the entire optical system is correctly aligned and operational throughout the experiment. These comprehensive QA measures are critical to ensuring the high-performance operation of the hpDIRC system in the ePIC experiment.

Construction and assembly planning: In the current plan for the ePIC hpDIRC construction, the assembly will take place at three different locations. The bar boxes will be assembled at Jefferson Lab, utilizing the existing infrastructure developed for the disassembly of the BaBar bar boxes and the quality assurance of the bars. Short bars will be glued together to form ten long bars per bar box, with 3-layer lenses attached, and will then be mounted inside carbon fiber, light-tight shells. The readout boxes will be assembled at Wayne State University, incorporating newly acquired expansion volume prisms, as well as readout sensors and electronics previously validated at USC. Once both the bar boxes and readout boxes are assembled, they will be transported to BNL for initial alignment and matching before their final installation into the ePIC detector.

2937 **Collaborators and their role, resources, and workforce:** The hpDIRC system collaboration
2938 (DSC) consists of a core group of institutions that have long-standing experience with DIRC coun-
2939 ters, having contributed to the BaBar, GlueX, PANDA projects, and the EIC DIRC R&D program.
2940 Many of these groups have been involved in these efforts since 2011, bringing a wealth of exper-
2941 tise to the development of the hpDIRC system for the ePIC detector. This collaborative network
2942 is expected to expand, with few expressions of interest (EoIs) from various institutions interested
2943 in contributing to different aspects of the project closer towards constriction. The process of align-
2944 ing expertise and interest with system priorities is already underway, ensuring that the work is
2945 distributed efficiently.

2946 Among the key collaborators, Jefferson Lab together with CUA have been handling the transport
2947 and disassembly of BaBar DIRC bar boxes and validating the quality of the disassembled bars.
2948 They continue this effort with the optional quality assurance (QA) of new bars or plates for the
2949 light guide section. Jefferson lab expressed interest in continuing this support with extension to the
2950 gluing of bars and lenses and finally assembling the bar boxes

2951 Stony Brook University (SBU) is preparing an important QA tool with their Cosmic Ray Telescope.
2952 The initial plan is to use it for incremental integration of new components into the hpDIRC pro-
2953 totype like disassembled BaBar bars, sensors, and electronics, but eventually, it will be used for
2954 validation of full bar box modules.

2955 Old Dominion University (ODU) will contribute by evaluating the focal plane of the lenses and
2956 conducting QA procedures, ensuring the optical components meet the required standards.

2957 On the sensor side, USC will handle QA and tests related to the readout chain, ensuring the sen-
2958 sors operate within specified parameters. Wane State University (WSU) will oversee the assembly
2959 and QA of the readout boxes, another critical component of the system. Finally, institutions like
2960 CUA, GSI, William & Mary, and WSU are heavily involved in simulation and reconstruction ef-
2961 forts, which are essential for optimizing the performance and integration of the hpDIRC system
2962 into the overall ePIC detector framework.

2963 This broad collaboration, with specific responsibilities assigned to various expert groups, ensures
2964 that all components of the hpDIRC system are developed and tested by specialists, assuming more
2965 junior workforce like graduate students and postdoctoral researchers can be added through exter-
2966 nal grants.

2967 **Risks and mitigation strategy:** The disassembly of the BaBar bar boxes is in an advanced stage
2968 of preparation, with the process set to begin soon. Immediately after disassembly, the quality of
2969 the legacy BaBar bars will be evaluated to determine their suitability for use in the ePIC hpDIRC.
2970 A decision on their usability is expected by early summer 2025. If new radiator bars are required, a
2971 vendor will need to be identified, and the procurement and production process initiated. Based on
2972 the current production timeline for PANDA Barrel DIRC radiator bars, the production of new bars
2973 for ePIC should still align with the project schedule.

2974 Both the baseline commercial MCP-PMTs and HRPPDs require testing and evaluation, which are
2975 being prepared by different groups. These tests will be conducted in parallel to ensure the necessary
2976 sensors are available within the required timeframe before installation. The development of ASIC-
2977 based readout electronics is being coordinated by the EIC project, with two parallel solutions under
2978 consideration.

2979 **Additional Material** Add text here.

8.3.4.4 The dual radiator RICH

Requirements The dual radiator Ring Imaging Cherenkov (dRICH) detector is part of the particle identification system in the forward (ion-side) end-cap of the ePIC detector and complements the forward time-of-flight system and calorimetry, see Fig. ?? . The dRICH has to provide acceptance in the pseudo-rapidity range defined by the ePIC beam pipe and the barrel detector and to operate within the limited envelope allowed by the rest of the compact and hermetic ePIC detector. Distinctive features of the detector are: use of aerogel and gas radiators to extend the covered momentum range, usage of solid-state photomultiplier (SiPM) to ensure single photon detection capability in high and not-uniform magnetic field, non-conventional optics with curved active surfaces and compact readout electronics to fit into ePIC.

Requirements from physics: The dRICH is required to provide continuous hadron identification from ~ 3 GeV/c to ~ 50 GeV/c, and to supplement electron and positron identification from a few hundred MeV/c up to about 15 GeV/c. Such an extended momentum range imposes the use of two radiators, gas and aerogel, with a common imaging system to ensure compactness and cost-effectiveness. The radiator gas must ensure π/K separation at $3\text{-}\sigma$ level up to 50 GeV/c in the most forward region, namely for $\eta > 2$. The aerogel radiator must cover the intermediate momentum interval, bridging the upper limit of the time-of-flight (≈ 2.5 GeV/c) to the Cherenkov threshold of the dRICH gas (≈ 12 GeV/c). These requirements dictate the prescriptions on the refractive index and the radiator chromaticity in the sensitivity region of the photosensors. The dRICH has to provide open acceptance in the ePIC forward pseudo-rapidity range $1.5 < \eta < 3.5$. To provide proper light focalization within the due volume, the dRICH active area is located behind the shadow of the barrel detector and its support ring, close to the MARCO solenoid coils. In this region, see Fig. ?? , the $\approx 1T$ strong and not-uniform ePIC magnetic field imposes the use of unprecedented detectors (SiPM).

Requirements from Radiation Hardness: The radiation sensitive components (sensor and front-end electronics) of the dRICH detector are concentrated in a region of moderate radiation level, below $O(10^{11})\text{ cm}^{-2} n_{eq}$ of maximum integrated fluence where n_{eq} is a 1-MeV neutron equivalent particle, see Fig. ?? . Close to the beam line, where the integrated dose can reach a value of 15 krad, only radiation tolerant materials reside like silica aerogel [31].

Requirements from Data Rates: The SiPM sensor features an intrinsic significant dark count rate, currently of the order of 50 kHz/mm² at room temperature, that indefinitely increases with the radiation damage. To mitigate this effect, the dRICH sensors are operated at low temperature (less than -30 C) and regularly annealed at high temperature (up to 150 C), in order to never exceed a maximum 300 kHz dark rate per channel. The latter value corresponds to a conservative limit taken to preserve the detector performance requirements for Physics and it is supported by present simulation studies that confirm the particle-identification capabilities of dRICH are unaffected.

Justification The specifications outlined above largely define the main technological choices: the momentum range dictates radiator refractive indexes that can be reliably met only by aerogel and gas, the ePIC environment, space and magnetic field, imposes sensor characteristics that can only be met by SiPM.

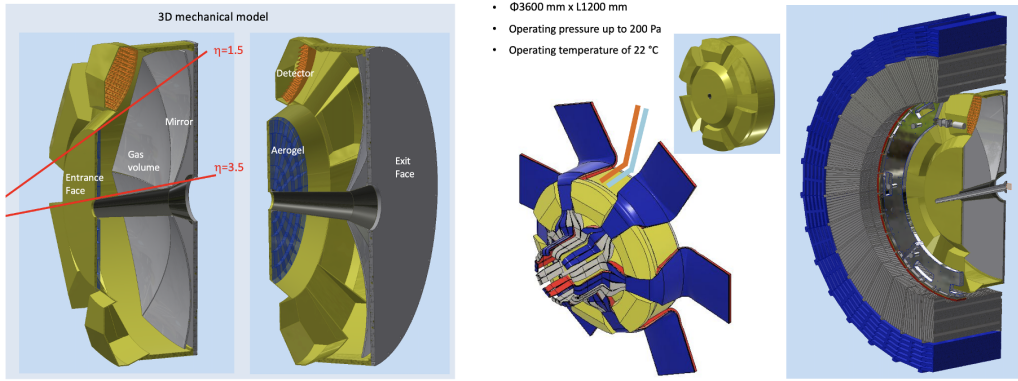


Figure 8.52: (Left) dRICH detector model with highlighted the major components. (Right) dRICH inside ePIC services lines at barrel HCAL end point.

Device concept and technological choice: The dRICH is a ring-shaped detector fitting inside the ePIC forward endcap, see Fig. 8.52. The essential components are a layer of aerogel radiator, a volume of gas radiator, and an array of mirrors focalising the Cherenkov light into compact areas instrumented with photo-sensors. The detector is designed in a modular way, with 6 sectors around the beam line of equivalent mirror set and detection area.

The aerogel radiator is a amorphous solid network of SiO_2 nanocrystals whose density regulates the refractive index and chromaticity [2]. The use of silica aerogel for RICH detectors is well established. It is available with refractive indices in the range 1.006–1.08 in between gases and liquids. The current manufacturing methods succeeded in improving the attenuation length Λ ($\lambda = 400 \text{ nm}$) from 20 mm (aerogel used in HERMES) to 50 mm (aerogel for CLAS12 and BELLE-II). The selected aerogel radiator has refractive index $n = 1.026$ at $\lambda = 400 \text{ nm}$. The chromatic dispersion has been measured during the R&D phase to be $dn/d\lambda = XX \text{ nm}^{-1}$ at 400 nm wavelength. Aerogel is typically produced in tiles of few cm thickness: in order to minimize edge effect, the dRICH tile side should be greater than 18 cm, approaching the word record value of 20 cm. The shape and surface flatness of the tiles are important parameters to consider for ensuring optimal PID performance. Typically, due to the fabrication process, aerogel tiles exhibit a slight meniscus shape. Measurements taken during the R&D phase on aerogel samples provided by Aerogel Factory Co. Ltd revealed deviations from the ideal parallelepiped shape by a few tenths of a millimeter, along with a thickness variation between the center and the edges of a similar magnitude. Based on the measurements conducted so far, this deviation from the ideal shape does not impact PID performance. Additionally, the manufacturer, Aerogel Factory Ltd (Chiba, JP), has confirmed that improvements in both flatness and thickness uniformity are feasible.

The selected reference gas radiator is hexafluoroethane (C_2F_6) (Appendix xxx), which matches the requirements being characterized by refractive index $n = 1.00086$ and excellent chromatic dispersion $dn/d\lambda = 0.2 \text{ nm}^{-1}$ at light wavelength $\lambda = 350 \text{ nm}$ [32].

The selected refractive indexes dictates a minimum thickness of 4 cm for the aerogel and O(1) m for the gas in order to ensure enough photon yield. Mirror focalisation is necessary to minimise the consequent uncertainty on the Cherenkov photon emission point. Being inside the detector acceptance, the mirror structure is made of carbon fiber reinforced polymer (CFRP) to ensure the necessary stiffness while being light. In order to preserve the Cherenkov angle information the mirror surface should have excellent optical quality, i.e. few nm roughness and better than 0.2 mrad angular precision (reflecting in a point-like image with more than 90% of the light intensity concen-

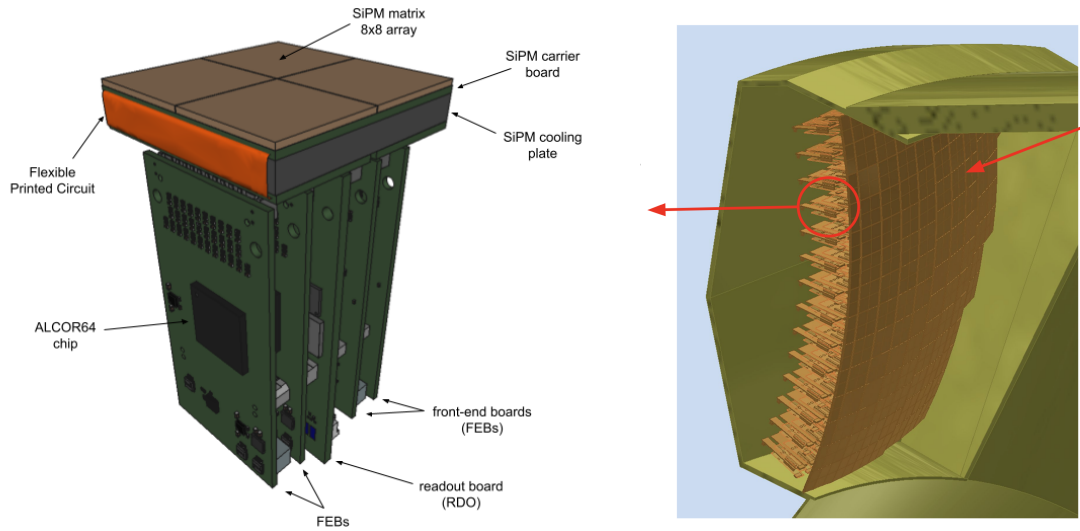


Figure 8.53: (Left) CAD model of the dRICH photodetector unit (PDU) module with its major components. (Right) dRICH detector box model with 208 PDUs forming a curved active surface.

3052 trated in a disk smaller than 2.5 mm). The single mirror dimension is limited to a ≈ 1 m maximum
 3053 diagonal when accounting for realistic forming mandrel and coating chamber dimensions. In the
 3054 dRICH mirror array, the radius of curvature should be replicated within 1% of the nominal value.

3055 The dRICH photon detector surface is shaped over a sphere of radius ~ 110 cm to best approach
 3056 the 3D focal surface of the mirror array. The Silicon Photomultiplier (SiPM) sensor technology is
 3057 selected for the photon detector. It ensures superior single-photon counting capability inside the
 3058 ePIC magnetic field and compact dimensions suitable for tessellating a shaped active surface. The
 3059 single SiPM sensor has a $3 \times 3 \text{ mm}^2$ area to provide the necessary spatial resolution with an intrinsic
 3060 time resolution better than 150 ps. The SiPM sensors are grouped into 8×8 arrays in a buttable
 3061 arrangement to minimize the dead area, which are eventually mounted side-by-side to form a $16 \times$
 3062 16 array defining the 256 channels of the dRICH photodetector unit (PDU). The selected front-end
 3063 ASIC is ALCOR, a 64-channel chip with coupling and rate capability optimized for SiPMs, and a
 3064 ToT architecture with better than 50 ps LSB¹ resolution in order the SiPM-ALCOR readout chain
 3065 could achieve an overall time resolution better than 200 ps RMS. To minimize the volume within
 3066 the dRICH envelope and to maximize the active area, the photodetector is organized in compact
 3067 photodetector units (PDU). The PDU integrates 256 SiPM channels with the ALCOR TDC readout
 3068 provided by four front-end boards (FEB), one readout board (RDO) to interface with the ePIC data
 3069 acquisition (DAQ) and detector control (DCS) systems. In addition, the PDU is designed to allow
 3070 sub-zero cooling of the SiPMs as well as high-temperature annealing operations. Figure 8.53 (left)
 3071 shows the conceptual design of the PDU and its main components. The present dimensions of the
 3072 PDU concept are approximately $52 \times 52 \times 140 \text{ mm}^3$.

Figure 8.54: (Left) dRICH aerogel model. (Right) dRICH mirror model [placeholder].

¹Least Significant Bit

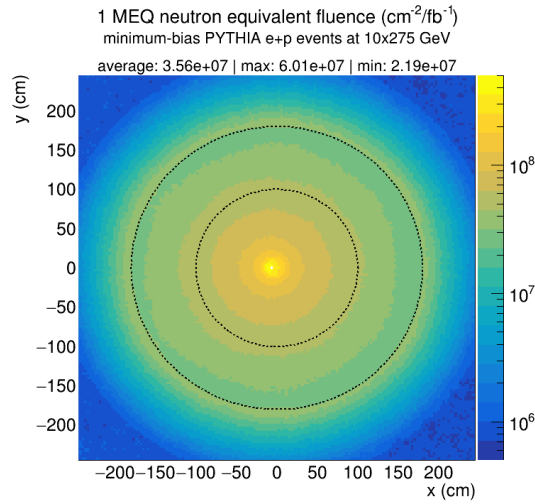


Figure 8.55: Transverse map of the expected 1-MeV equivalent neutron fluence per 1 fb^{-1} of integrated luminosity in e+p interactions at the maximum EIC center-of-mass energy at the location of the dRICH photodetector ($210 < z < 260 \text{ cm}$). The average, maximum and minimum values within the region of the dRICH photodetector ($100 < R < 180 \text{ cm}$, indicated by the dashed lines) are reported.

Subsystem description:

General device description:

Because at ePIC the electron and hadron beam collide at an angle of XX mrad, the common beam pipe cross-section is off-axis at the dRICH location and increasing in area with the distance from IP, imposing an asymmetric layout of the inner components, see Fig. 8.54. The aerogel wall is composed by five rings of tiles, each shaped in order to fit inside a 0.2 mm thin aluminum supporting structure. In each sector, focalization is provided by a compound of five mirrors covering a total area of about 2 m^2 with an optimized radius of curvature around 2200 mm. Six independent spherical active surfaces with curvature radius around 1100 mm, each made of 208 PDUs for a total of 53k readout channels, are mounted inside detector-boxes that provide thermal insulation, cooling for the electronics and connections to the services. Given the gas radiator open volume, the Cherenkov photons can be reflected into different detectors depending on the parent charged particle kinematics. The aerogel and photo-detector are separated from the radiator gas by transparent septa, and immersed in a dry (e.g. purged N_2) atmosphere to minimize contaminant absorption and prevent moisture formation. The mirrors are supported by a light carbon fiber structure that is mechanically decoupled from the vessel and allows fine alignment adjustments by means of piezo-electric motors.

Sensors:

The silicon photomultiplier (SiPM) [33, 34] is chosen as the sensor technology for the dRICH photodetector. The main baseline specifications demand sensors with a $3 \times 3 \text{ mm}^2$ single-channel active area, single photon detection over a broad spectral range from 300 to 900 nm and very high overall photodetection efficiency $> 40\%$ at the peak sensitivity wavelength $400 < \lambda_{\text{peak}} < 450 \text{ nm}$ (see Table 8.16 in Additional Material for the full list of the baseline parameters and specifications of the SiPM sensor devices for the dRICH photodetector). SiPMs fulfil the dRICH requirements being cheap and versatile devices with excellent

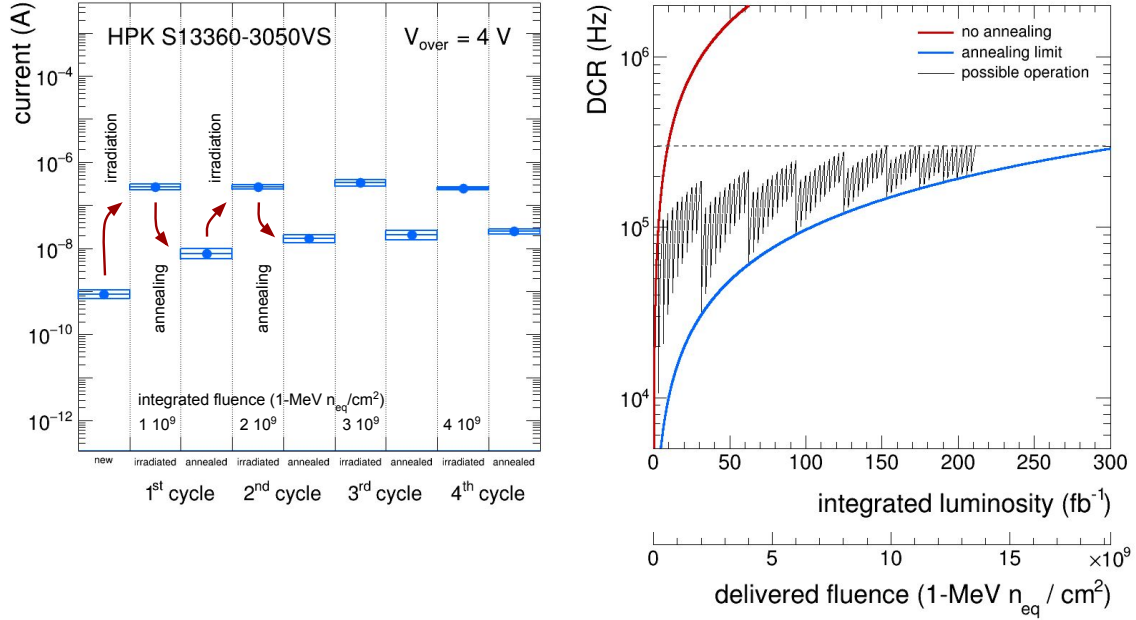


Figure 8.56: (Left) Dark current measurements on sample SiPM sensors for the studies of repeated irradiation-annealing. (Right) Projected increase of the DCR of SiPM as a function of the integrated luminosity (delivered fluence). The “no annealing” and the “annealing limit” curves show the limits of possible operations. The dashed line indicate the desired maximum DCR threshold.

photodetection efficiency (PDE) and time resolution. Their single-photon performance is unaffected by high magnetic fields [35,36], which makes SiPM the only photosensor that can efficiently operate in the field configuration at the dRICH photodetector location in the ePIC experiment, see Fig. ?? . SiPM sensors on the other hand have very high dark count rates (DCR) and are not radiation tolerant. The DCR in SiPM is mostly of thermal origin and it reduces significantly by lowering the SiPM temperature, typically halving every 7-10°C in new sensors [37]. Radiation damage in SiPM is mainly due to displacement damage in silicon, which causes a significant DCR increase and reduces the effectiveness of cooling [38]. At the moderate radiation levels expected at the location in the dRICH, no significant change in the SiPM parameters (PDE, gain, quenching resistor R_{quench} , pixel capacitance C_{pixel} , breakdown voltage V_{break}) is observed [39]. SiPM cooling is important to keep the DCR low and it becomes crucial after radiation damage [40], as the increase in DCR would be such to make SiPM unusable as single-photon detectors, otherwise. In the dRICH, the SiPMs will be operated at subzero temperature of $T = -40^\circ\text{C}$, or lower. A cooling block is placed in thermal contact with the back-side of the printed-circuit board hosting the SiPMs (carrier board). Cooling fluid in the cooling block will be circulated through a closed loop by a dynamic temperature control system circulating thermostat to regulate and maintain the SiPMs at low temperature. The circulating thermostat system will also be used to circulate fluid at high temperature ($T = 100^\circ\text{C}$, or higher) to provide heat during SiPM annealing. Therefore a low-viscosity silicone fluid is particularly suitable for cold and heat transfer. The radiation damage on SiPMs increases moderately with the integrated luminosity. At the location of the dRICH photodetector a maximum (average) fluence of $\Phi_{eq} = 6.0$ (3.6) $10^7 \text{ cm}^{-2}/fb^{-1}$ 1-MeV equivalent neutrons (n_{eq} in the following) is expected from e+p interactions at the

highest center-of-mass energy of the EIC (Figure 8.55). Beam-induced background from proton beam-gas events at 35 kHz are expected contribute with a maximum (average) of $\Phi_{eq} = 3.7 (1.6) 10^6 \text{ cm}^{-2}/\text{fb}^{-1} n_{eq}$ at the location of the dRICH photodetector, bringing the total maximum (average) expected radiation damage to $\Phi_{eq} = 6.4 (3.7) 10^7 \text{ cm}^{-2}/\text{fb}^{-1} n_{eq}$. As shown by the “no annealing” curve in Figure 8.56 (right), the SiPM DCR is expected to increase with the integrated luminosity at a rate of 31.8 (18.6) kHz/fb⁻¹, reaching a DCR of 300 kHz after an integrated luminosity of approximately 9.5 (16.1) fb⁻¹. These values are based on measurements performed on Hamamatsu S13360-3050 sensors operated at $V_{over} = 4 \text{ V}$ at $T = -30^\circ\text{C}$., more details in Section ??.

Annealing of SiPMs can be achieved exploiting the Joule effect []. When a SiPM is forward biased, the microcells composing the device behave as directly polarized diodes connected to their quenching resistors. The current flowing through the resistors eventually heat up the entirety of the sensor. In the dRICH, SiPM annealing will be performed up to temperatures of $T = 150^\circ\text{C}$ in “forward-bias mode”. The actual annealing temperature and annealing time will be tuned during detector operations according to the DCR reduction needs and available experiment down time. The “forward-bias mode” approach can cure approximately 97% of the radiation damage. It is therefore expected that a residual irreducible radiation damage (residual DCR) will build up during the dRICH lifetime. As shown by the “annealing limit” curve in Figure 8.56 (right), the SiPM residual DCR is expected to increase with the integrated luminosity at a rate of 950 (560) Hz/fb⁻¹, reaching a residual DCR of 300 kHz after an integrated luminosity of approximately 310 (530) fb⁻¹. In the dRICH, SiPM annealing will be performed with a technical implementation of the “forward-bias mode” which needs to be integrated both into the SiPM power-supply system, the front-end and control electronics, cooling and the temperature monitoring system. As previously mentioned, the circulating thermostat system used for low-temperature operation of the SiPM will be operated in heating mode to warm up the SiPM cooling plate during high-temperature annealing. This will allow one to perform the “forward-bias annealing” by delivering a lower current to the SiPM, as a fraction of the heating power is delivered by fluid. Nonetheless the required power to perform “forward-bias annealing” at once over the full dRICH detector is excessively large. Therefore annealing operations will be segmented in space and time across the dRICH detector and will be performed during periods with no Physics beam and depending on the DCR needs. As can be see from Figure 8.55 the sensors closer to the beam line will experience a radiation damage almost a factor 3 larger than those father from the beam line and will likely require a more frequent annealing. The “possible operation” curve in Figure 8.56 (right) shows a potential scenario for the DCR evolution for SiPM sensors closer to beam pipe (worst case). This is based on an operation model where more frequent (every $\sim 3 \text{ fb}^{-1}$) softer annealing cycles at lower temperature and/or of shorter duration, delivering a DCR reduction of 10 \times , are interleave by less frequent (every $\sim 30 \text{ fb}^{-1}$) full annealing cycles to reduce DCR as much a possible. A limit in the operation scenario is reached when the annealing is not capable to keep the DCR below the desired threshold or when the annealing frequency become too high. As it can be seen from Figure 8.56 (right), beyond an integrated luminosity of $\sim 200 \text{ fb}^{-1}$ to keep the DCR below the 300 kHz threshold requires to perform full annealing cycles every $\sim 5 \text{ fb}^{-1}$, which is not obviously a practical operation scenario anymore. Some or all of the SiPM sensors might be needed to be replaced at that stage with new ones or with SiPM sensors of improved performance and radiation hardness in a future upgrade of the dRICH photodetector. One has to keep in mind though that the 300 kHz limit is a conservative value that is connected to the present level of dRICH reconstruction and could be relaxed in future. Moreover, the model shown in Figure 8.56 (right) is based on measurement on Hamamatsu S13360-3050 sensors operated at $V_{over} = 4 \text{ V}$ in a climatic chamber at $T = -30^\circ\text{C}$. Possible SiPM operation in ePIC at a lower V_{over} of 3 V and at a lower

T of -40°C will allow one to achieve lower DCR overall.

FEE:

The ALCOR (A Low Power Chip for Optical Sensor Readout) ASIC, developed by the electronics laboratory of INFN Torino, is the baseline option for the readout of the dRICH SiPM sensors. The main goal of ALCOR is to provide single-photon time tagging of the incoming signals, while being able to cope with the SiPMs inherently high DCR: a maximum DCR value of 300 kHz/ch is expected before an annealing cycle is performed. A good time resolution, better than 200 ps RMS, is required to perform DCR suppression via time gating at both hardware and software levels. ALCOR is a mixed-signal ASIC comprising 64 channels arranged in a 8×8 pixel matrix. The ASIC includes in-pixel signal amplification, conditioning and digitization, with a fully digital output using 8 LVDS DDR Tx links operating at a clock frequency of 394.08 MHz, a multiple of the EIC clock frequency. The architecture of one ALCOR pixel is displayed in the left panel of Fig. 8.57. The amplifier input stage is a low impedance current conveyor based on a regulated common-gate topology suited for sensors with large capacitance such as SiPM sensors. The versatile front-end is able to work with positive or negative input polarity signals and includes four gain settings and two discriminators with 6-bit DAC programmable thresholds. Each channel also incorporates 4 low-power TDCs based on analogue interpolation providing precise timestamping with a 20-40 ps time bin. This architecture allows for single-photon time tagging and includes Time-over-Threshold (ToT) or Slew-Rate (SR) measurements for time walk correction. ALCOR is designed in a 110 nm CMOS technology and the power consumption is about 12 mW per channel. The ASIC adopts a time-based readout: every signal above the threshold is processed by the pixel control logic and digitized, without any external trigger. This data-push architecture matches well with the ePIC streaming readout approach, in which the detectors will be read out continuously. Limited by the 6.3 Gb/s bandwidth of the ASIC data transmission links, ALCOR can operate at a maximum event rate of about 2.4 MHz per channel in time-tagging mode and 1.2 MHz per channel when operating in ToT and SR mode. A programmable hardware shutter, implemented inside ALCOR pixel digital logic, can be enabled to filter out-of-time DCR and provide a significant bandwidth reduction to the system. The time window of interest is controlled off-chip by the RDO and can be adjusted using in-pixel programmable delays to compensate timing offsets among the 64 channels. With a time window of approximately 2-3 ns, considering that the EIC bunch crossing period is about 10.15 ns, data can be reduced by a factor of 3 or 5. One important point is that the shutter will be needed only when DCR becomes higher due to SiPMs taking radiation damage over time. Therefore, the first period of ePIC data taking can be used to optimize the shutter calibration. The ASIC will be integrated inside a BGA package, providing a compact and robust solution to be assembled on the FEB. A $16 \times 16 \text{ mm}^2$ flip-chip ball grid array (FC-BGA), with 256 balls and 1 mm ball pitch, is the option chosen for the ASIC packaging since it offers more interconnections and better performance w.r.t. standard packaging techniques and matches well with the pixel-matrix geometry of the ALCOR ASIC. A 3D model of the FEB is shown in the right panel of Fig. 8.57. Each FEB hosts one ALCOR BGA device and several components to ensure a stable and safe operation of the system. Linear regulators are employed to provide clean power supplies to the ALCOR ASIC and are coupled to I2C interface and current monitors to control the regulators and prevent potential damage from over-current conditions. The FEB also incorporates a dedicated PCB section for SiPMs bias voltage routing and also a circuit to enable the SiPM forward-biasing when annealing cycles are carried out. AC-coupling between the SiPM sensors and ALCOR inputs has been chosen to isolate them when the SiPMs are operated in forward bias. Several connectors, mounted on the FEB, provide the interface towards the RDO and the other FEB boards of the same PDU as well as towards the SiPMs carrier board and the LV-HV services.

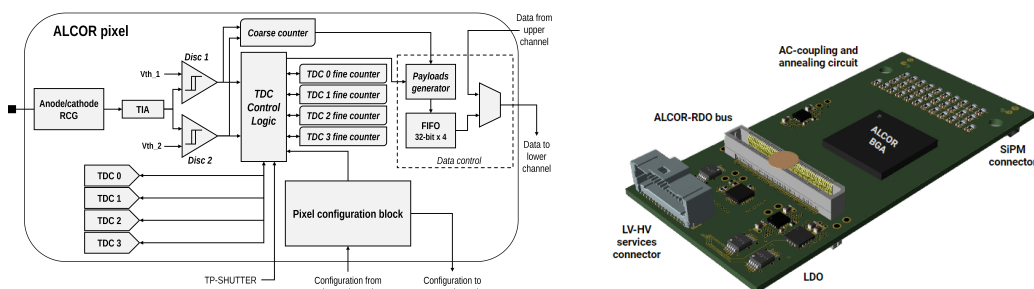


Figure 8.57: (Left) Block diagram of ALCOR pixel. (Right) 3D model of the dRICH FEB.

Other components:

The radiator gas in the RICH vessel is controlled by the gas radiator system (Fig. 8.58). Its main tasks are, during detector operation, (i) providing well controlled pressure conditions in the 12 m³ RICH vessel to avoid relevant pressure difference at the vessel walls and at the fused silica windows; (ii) removing oxygen and water vapor contaminates, in order to prevent building up impurities due to air leaks entering the gas system; (iii) performing detector vessel filling with hexafluoroethane before a data taking period and radiator gas recovery at the end of the period; the filling/recovery is from/to the storage tank. The main components of the radiator gas system are two oil-free compressors, working in parallel, which continuously extracts gas from the vessel at constant rate in order to ensure the gas circulation, a pressure sensor installed on top of the radiator vessel for continuous monitoring of the internal relative pressure and to dictate the opening level of a flow control valve on the input line, adjusting the opening so to preserve the relative pressure inside the vessel. Oxygen and water vapor traces are removed by filtering cartridges with molecular sieves and Cu-catalyst, which are permanently in series in the circulation system. The vessel is flushed with nitrogen during the shutdown periods. Nitrogen and hexafluoroethane separation during filling and recovery is under study and two options can be envisaged: (i) the use of osmosis via dedicated membranes or (ii) via a two-step procedure: replacing nitrogen with carbon dioxide and then performing distillation at -35°C. Hexafluoroethane is a greenhouse gas and, therefore, the residual C₂F₆ present in the nitrogen/carbon dioxide cannot be vent out: it must be collected and trapped for disposal with a dedicated recovery system. The control of the whole radiator gas system is performed via a Programmable Logic Controller (PLC). More details are provided in Appendix xxx.

Performance

For each recorded dRICH hit, the photon path is reconstructed taking into account the charged particle trajectory and the focalising optics of the detector, in order to provide an estimate of the Cherenkov angle at the emission point. The combined information of all the Cherenkov photons associated to a charged particle concur to a precise determination of its velocity (beta) and, knowing the momentum from the ePIC spectrometer, its mass. The dRICH model is part of the ePIC simulation framework and allows complete performance studies taking into account quality of the track reconstruction, bent trajectories (by magnetic field) and multiple scattering. To bypass the complexity of such a framework, some specific study can be anyway performed with private or simplified simulation chain. The laboratory characterization and the numerous test-beams have provided detailed inputs for modeling in a realistic way the single components and global detector response. In the dRICH, the contributions to the single-photon (SPE) angular resolution have a different weight depending on the radiator. The dRICH has been designed in order to keep most

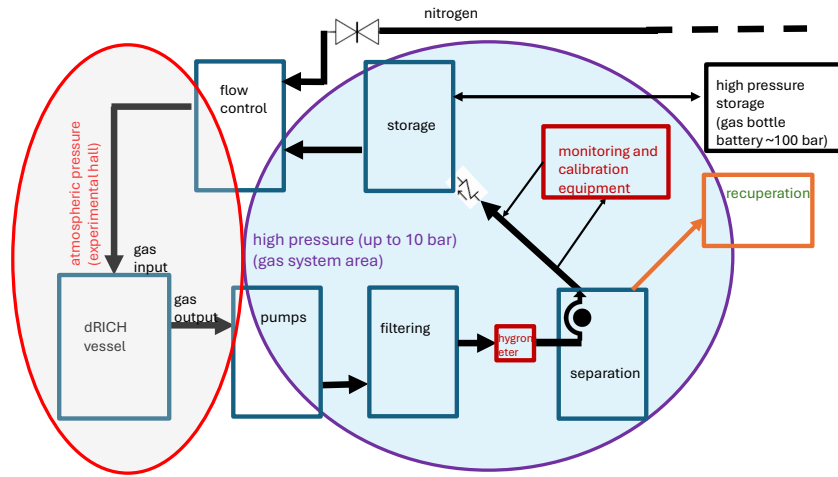


Figure 8.58: Block diagram of the dRICH gas system [graphically, a preliminary version].

of the contributions to the SPE angle resolution below 0.5 mrad, see Fig. 8.59, a value dictated by the tiny Cherenkov angle difference between pions and kaons at 50 GeV/c in the radiator gas. The single SiPM readout channel has been limited to $3 \times 3 \text{ mm}^2$ area. The MARCO coils and the dRICH position has been optimized in order to minimize the bending inside the radiator gas volume. The tracking resolution is assumed to cope with the same constrain. Note that combining N photons the angular precision scale with a maximum $N^{-1/2}$ factor only in case of a completely uncorrelated information, a condition that is not valid for the bending and tracking contributions. The uncertainty on the emission point is not an issue for a few cm layer of aerogel, but is critical for a 1 m long gas volume, especially within the limited space available in ePIC for the optics: this remains the major contribution to the SPE resolution of the radiator gas despite the mirror focalization and the curved dRICH detector surface. As the present model assumes a single radius for the dRICH mirrors, optimized for the forward rapidity region to boost the high-momentum reach, the resolution worsens with the polar angle increase. This is not a problem, because the average particle momentum decrease as well loosing the performance requirement. The chromatic error is well under control for gas but is the largest contribution to the angular resolution for the aerogel. This derives from the intrinsic nature of the radiator in conjunction with the quantum efficiency characteristic of the photosensor. The chromatic uncertainty limits the aerogel momentum reach to something above 15 GeV/c, a value well above the Cherenkov threshold of kaons in gas, high enough to provide the wanted overlap between the measured ranges of the two radiators.

The number of emitted photons varies with the pseudo-rapidity due to the different path of the particle within the radiators. The mean number of recorded photons is about 18 for the radiator gas and 12 for the aerogel for a particle with momentum well above the Cherenkov threshold. In average, few charged particles per event are expected to hit the detector, see left panel of Fig. 8.60. With a proper pattern recognition and photon path reconstruction, the information of the two radiators can be combined to extend the momentum coverage of ePIC PID from the TOF $\approx 2.5 \text{ GeV/c}$ upper momentum limit to above 50 GeV/c, see central panel of Fig. 8.60. In the forward direction with optimized focalization, an identification efficiency greater than 95 % at a corresponding 5 % percent mis-identification probability, is achieved, see right panel of Fig. 8.60. As expected from the resolution study, the momentum reach is reduced with the pseudo-rapidity, in accordance with the kinematics of the particles expected from physics reactions.

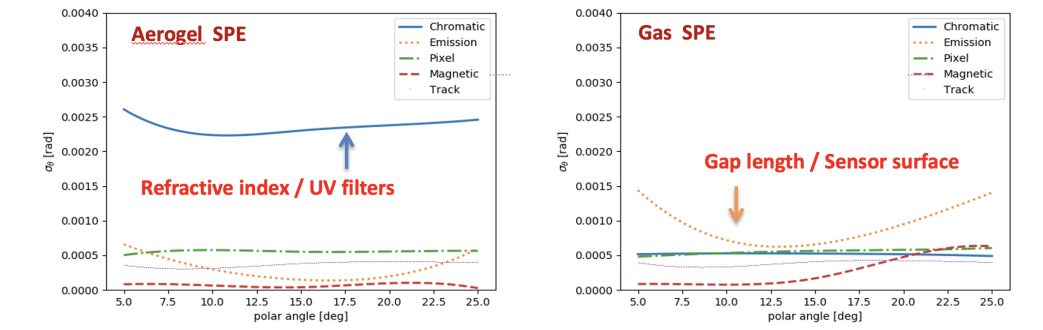


Figure 8.59: (Left) Contributions to the single-photon angular resolution for aerogel. (Right) Contributions to the single-photon angular resolution for radiator gas.

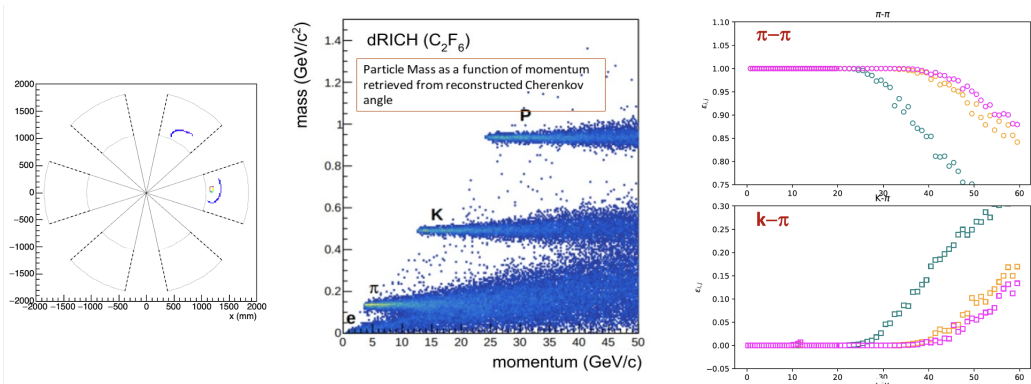


Figure 8.60: (Left) Event display. (Center) Reconstructed mass vs momentum. (Right) Pion identification efficiency and pion to kaon mis-identification probability as a function of momentum in three bins of rapidity.

Implementation

Services:

The dRICH services are grouped into power lines for sensors, electronics and slow control monitors, gas lines for the radiator gas volume, the aerogel inert gas volume, and cooling lines for the

Name	Voltage (V)	Current (A)	Channels	Boards	AWG gauge
Analog	1.4	10.0	312	39	10
Digital low	1.4	8.5	312	39	11
Digital high	2.7	6.0	312	39	12
Master panel	5.0	5.2	6	1	13
SiPM bias	64.0	1.3	12	2	19
Annealing	12.0	3.2	1248	156	15

Table 8.13: List of the voltage services to the dRICH electronics, indicating the number of primary power-supply channels and boards as well as the cross-section of the cables (AWG). The number of power-supply boards is defined assuming to use commercial 8-channel low-voltage boards.

sensors and electronics. Table 8.13 shows a list of the power services for the dRICH photodetector. 18 19" wide/8U mainframes (approximately $50 \times 40 \times 70 \text{ cm}^2$ each) capable to host 16 boards each are needed to accommodate the low-voltage and high-voltage boards. The primary power-supply channels will serve multiple modules at the same time, with a typical grouping of 1024 SiPM channels. Nonetheless, further segmentation is implemented on the detector electronics, reaching a low-voltage power segmentation of 64 SiPM channels and a high-voltage power segmentation of 32 SiPM channels. The circulating thermostat system should be capable of circulating approximately 50 l/min of fluid at a maximum pressure of 1.5 bar in a broad temperature range (from -60°C to 120°C). Possible commercial systems are available, but more time is needed to better investigate the options. It is expected that a potential circulating thermostat system with the desired characteristics will require space in the experimental hall for a volume of approximately $1.3 \times 0.8 \times 1.6 \text{ m}^3$. Manifolds are needed to split the fluid from the thermostat into 6 loops, each feeding one dRICH photodetector box. A solution without manifold and 6 smaller independent thermostat unit for each dRICH sector will be investigated as a possible optimization. Insulated pipes will be needed to transport the fluid from the thermostat to the detector, and back. The insulation must guarantee no frost and no water condensation on the pipes when operating at the lowest temperatures and is also required to limit transport losses in heating/cooling capacity. Cooling for the front-end electronics is required to remove the approximately 15 kW of heat generated by the dRICH photodetector ($\approx 2.5 \text{ kW}$ in each of the six photodetector boxes). Force-air circulation in the boxes with diffusers are being studied as a possible effective solution. It is important that the air-cooling system for the FEE electronics provides dry air with a dew point of $T = -70^\circ\text{C}$ or lower, well below the SiPM operating temperature. A system based on forced circulation of gaseous nitrogen might be well suited also to ensure an inert environment inside the detector boxes. Gaseous nitrogen will also be used to maintain the aerogel in a clean and inert environment. The radiator gas system and its related monitoring equipment require a surface of about 15 m^2 , in order to host 5 racks of instrumentation, the gas storage tank and a support for the spectrophotometer. This surface includes the space needed by the operators. Various sections of the gas system operate at a 2-3 bar pressure, while the cell to measure and monitor the gas transparency operates at 10 bar. Some gas bottles at typical high pressure (100-150 bar), organized in a battery, have to be included to provide the radiator gas at filling and house it when recovered. The pipelines connecting the gas system to the vessel are 70 m long with a diameter of 10 cm.

Subsystem mechanics and integration:

The dRICH structure can be described by two disks, one entrance window of 0.9 m radius supporting the aerogel radiator and one exit window of 1.8 radius mounting the mirror system, connected by two ring-shaped structures, one shell that mounts the six detector boxes and one inner pipe surrounding the ePIC beam pipe. All the elements are made in composite materials. The pipe and shell are made by a carbon fiber reinforced polymer (CFRP) bulk to provide support strenght. The two windows are a sandwich of two carbon fiber skins and a core honeycomb to limit the material budget to about 1% of radiation length. The shell and detector boxes are shaped in order to allow the passage of all the services of the inner barrel detectors, see left panel of Fig. 8.61. The dRICH services are concentrated on the shadow of the detector boxes and do not interfere with the routing of the others. A dedicated scaffolding would be realized to allow the installation of the detector, and the roll-in and roll-out movements to the service position without interference with the beam pipe to preserve the beam vacuum, see central and right panel of Fig. 8.61. The dRICH is suspended inside ePIC via brakets connected to the HCAL barrell.

Calibration, alignment and monitoring:

Dark counts in SiPMs are indistinguishable from photon-induced signals and owing the large SiPM

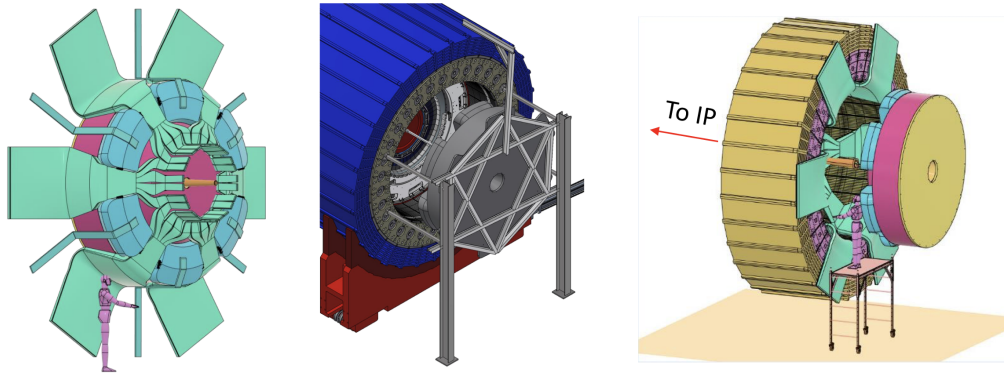


Figure 8.61: (Left) Service routing around the dRICH. (Center) Installation tool. (Right) Maintenance position.

DCR there is no need of a dedicated system to evaluate the functioning of any given readout channel. A measurements of the DCR as a function of the front-end electronics discrimination threshold can provide information on the signal amplitude. This technique can be used at different bias voltages. Using solely the dRICH readout system it is possible to measure the signal amplitude as a function of the bias voltage, hence to obtain information on sensor functioning and its breakdown voltage at different operation conditions. Timing calibration of the SiPM sensors can be achieved with a picosecond pulsed laser light system. The light from the laser is brought inside the dRICH volume via optical fibres. The light from the laser directly impinges on a diffuser that eventually illuminates the full area of one dRICH photodetector sector. At least one laser-fibre-diffuser system is needed for each dRICH sector. The time delay due to the different path of photons from the diffuser to the SiPM that detects the light is known and can be corrected to achieve a relative calibration of the times of SiPMs within the same sector. Absolute timing calibration can then be achieved with collision data. Samples particles from physics reactions can be used to perform fine adjustment of the calibration constants. Electron particles identified by other ePIC subsystems can be used to correct residual misalignment or calibrate the radiator refractive index thanks to the saturated Cherenkov rings. Known particles from meson decays ($\Lambda, \phi, K_S, \dots$) identified by kinematics criteria can be used to verify the parameters of the dRICH reconstruction and the consequent PID performance. The calibration and monitoring equipment of the radiator gas and gas system (Appendices xxx, yyy, ...) includes a set of temperature sensors placed inside the dRICH vessel and equipment on-line in the gas circulation loop. A commercial hygrometer and a commercial oximeter, a transparency measurement system by a commercial spectrophotometer equipped with a high pressure (≈ 10 bar) cell and a Jamin interferometer setup complete the set of the equipment. The interferometer, complemented with temperature and pressure sensors, will provide in real-time the refractive index of the gas in the vessel. The refractive index measurement has a twofold role: during filling/recovery, it monitors the hexafluoroethane level in the vessel, during operation it will provide in real time the refractive index of the radiator gas to make possible quasi on-line data reconstruction as foreseen in the ePIC streaming read-out model.

Status and remaining design effort:

R&D effort:

SiPM sensors. A station has been realized to characterize the SiPM sensors inside a climatic chamber to control the working temperature, see left panel of Fig. 8.62. The readout chain is based on ALCOR to reproduce the ePIC configuration. Such a station allowed detailed

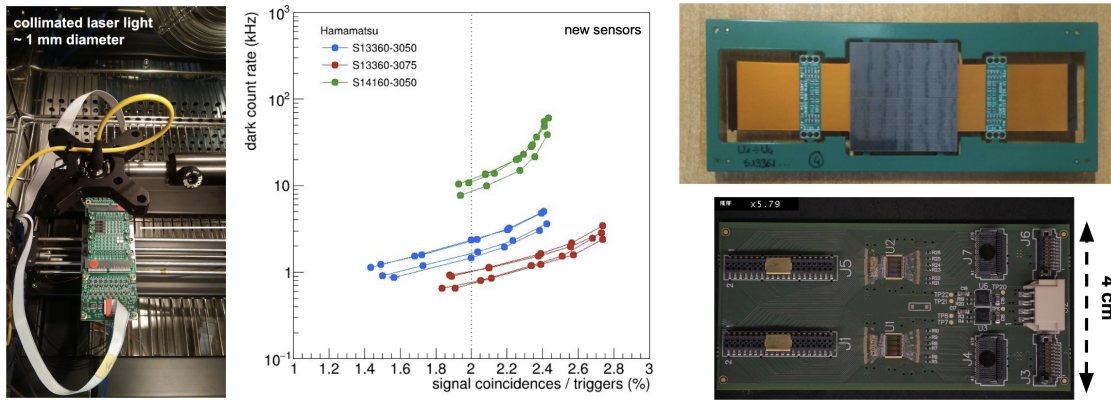


Figure 8.62: (Left) Test stand for SiPM characterization. (Center) Performance comparison between different SiPM models. (Right) Prototype version of the SiPM carrier board (top) and FEB (bottom).

performance comparison between SiPMs of different manufacturers and types, and different ageing due to radiation and annealing, e.g. see central panel of Fig. 8.62. The R&D results on photosensors reported here are those obtained with Hamamatsu S13360-3050 sensors operated at $V_{\text{over}} = 4 \text{ V}$ in a climatic chamber at $T = -30^\circ\text{C}$, unless otherwise specified. Nonetheless, the qualitative features of the results are valid also for other types of sensors. Irradiation tests and laboratory measurements on SiPM candidate samples show that after irradiation with a fluence of $\Phi_{\text{eq}} = 10^9 \text{ cm}^{-2} n_{\text{eq}}$ the DCR increases by approximately 500 kHz with respect to the DCR measured when new [41]. The dark current and the DCR of irradiated SiPM decreases by almost two order of magnitudes when placed in a thermostatic chamber at $T = 150^\circ\text{C}$ for 150 hours (“oven annealing”). Further tests performed to simulate a realistic experimental situation where SiPMs experience repeated irradiation and annealing cycles (see left panel of Figure 8.56) show that each irradiation cycle produces a consistent DCR increase (approximately 500 kHz for a $10^9 \text{ cm}^{-2} n_{\text{eq}}$ irradiation) and a consistent residual DCR (approximately 15 kHz for a $10^9 \text{ cm}^{-2} n_{\text{eq}}$ irradiation) remains after an “oven annealing” cycle. The fraction of damage cured by the “oven annealing” cycle is of approximately 97% of each newly-produced irradiation damage. The residual damage of 15 kHz/ $10^9 n_{\text{eq}}$ builds up after each irradiation-annealing cycle and seems to be irreducible within the details of this annealing protocol. The “oven annealing” protocol is not a practical approach for a central-barrel detector in a collider experiment, because of the limited access and because it would entail the removal of the sensors from the photodetector to place them the thermostatic chamber to perform annealing. Irradiation tests and laboratory measurements show that the “forward-bias annealing” mode can cure radiation-induced damage on SiPM (see left panel of Figure 8.63) to the same effectiveness level as the one measured for the “oven annealing” with a residual damage of approximately 3%. The benefit of the “forward-bias annealing” is significant: an extended SiPM sensors lifetime that can be achieved over the delivered radiation damage without the need to directly access the detectors in the experimental cavern. The fraction of damage, measured as dark current reduction, depends on the annealing temperature and the duration of the annealing. Higher temperatures and longer annealing times lead to more effective annealing. On the other hand, a limit seems to be reached already at $T = 150^\circ\text{C}$ and annealing at a higher temperature of $T = 175^\circ\text{C}$ does not lead to improved current reduction. Self-heating of the SiPM happens also when reverse biased, although given that the reverse I-V characteristics of SiPM is non-linear and depends

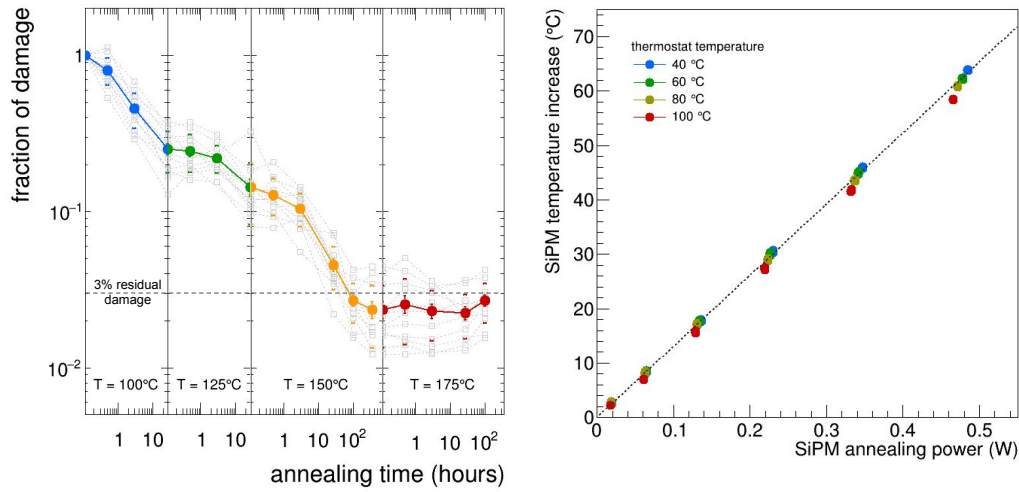


Figure 8.63: (Left) Fraction of residual irradiation damage measured on multiple SiPM candidate samples after “forward-bias annealing” cycles at increasing temperature and integrated annealing time. The measurements are shown for individual sensors (gray points) and as averages (coloured points, uncertainty of the average and RMS are indicated on the plot). (Right) Temperature increase of the SiPM sensor with respect to the temperature of the SiPM carrier board as a function of the “forward-bias annealing” power at different temperature values of the circulating thermostat system.

on the illumination state, currents can increase with less control making the reverse-bias annealing intrinsically more dangerous than forward-bias annealing. Laboratory measurements performed so far show that one can increase the temperature of the SiPM with respect to the temperature of the SiPM carrier board proportionally to the power delivered by the forward-bias current. Figure 8.63 (right panel) shows that, as expected, the increase of SiPM temperature linearly depends on the annealing power and it is the same at different values of circulating thermostat temperature. It is therefore sufficient to monitor the temperature of the SiPM carrier board and deliver the needed annealing power to have control of the SiPM temperature during “forward-bias annealing” and keep the process safely under control. Laboratory measurements reported here are performed in an open environment at room temperature. With the circulating thermostat temperature set at $T = 100^\circ$, we reach a SiPM annealing temperature of $T = 150^\circ$ with approximately a power of 0.5 W/sensor, which corresponds to a forward-bias current of approximately 60 mA/sensor. With the SiPM placed in a closed environment as the in dRICH photodetector box, one would expect a lower power needed that will be measured during detector construction. Laboratory measurements of the variation of the SiPM PDE as a function of the annealing temperature and annealing time show that for annealing temperatures up to $T = 150^\circ$ there is no observation of a significant degradation of the PDE up to annealing times of 150 hours. On the other hand, annealing at a temperature of $T = 175^\circ$ seem to cause a degradation of the transparency of the silicone protective window of the SiPM, which causes a decrease in the PDE to approximately 80% of the initial value after 150 hours. As already discussed, annealing at temperatures higher than $T = 150^\circ$ does not bring any advantage for what concerns DCR reduction. More studies will be done, but at the time of writing annealing at $T = 150^\circ$ can be considered safe for the expected dRICH operations.

FE Electronics. ALCOR has been extensively used within the ePIC dRICH Collaboration since 2021. The current version of ALCOR incorporates 32 channels, arranged in a 8×4 pixel matrix. It has been tested coupled to different SiPM models assessing its single-photon time-tagging capability and time resolution. A prototype version of the SiPM carrier and FEB board have been developed, see right panel of Fig. 8.62. The SiPM carrier provides electrical connections via thin kapton cables in order to bypass the sensor cooling plate. The prototype FEB hosts two 32-channel ALCOR chips which are directly wire-bonded on the PCB. It has been designed using specifications close to the ones for the final FEB, i.e. having the same dimensions and incorporating the same number of channels (64). It is served by a master-logic board that provide bias control and temperature monitor. These boards have been extensively used for the 2023-2024 dRICH activities, including two successful beam tests. ALCOR has been tested for radiation hardness with results showing only some small degradation on the TDC performance after a total ionizing dose (TID) of 300 krad, which is $O(100)$ times the expected TID in ePIC. These results confirm that the technology is sufficiently radiation tolerant to be used in the ePIC dRICH environment and that no special design techniques have to be adopted for the new version of ALCOR. The single-event upset (SEU) cross section has been measured to be $3.3 \cdot 10^{-15} \text{ cm}^2/\text{bit}$ for the pixel configuration registers and $8.5 \cdot 10^{-14} \text{ cm}^2/\text{bit}$ for the periphery configuration registers, which is significantly higher because these registers are not triplicated in the current version of ALCOR. From these results we can expect a mean time between failure due to SEU of about 190 hours for the entire dRICH detector.

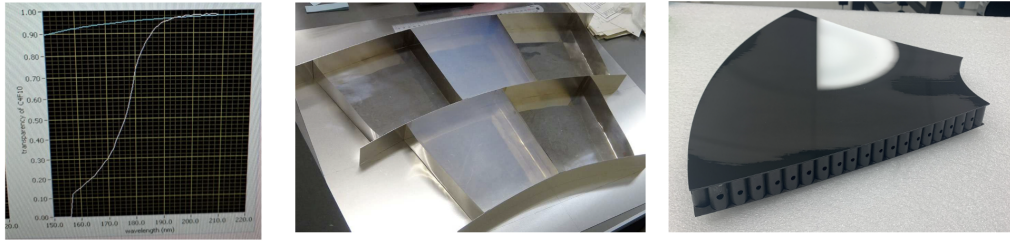


Figure 8.64: (Left) C_2F_6 measured transmittance. (Center) Aerogel large tiles assembling as obtained at BELLE-II [2]. (Right) Mirror demonstrator with an optimized dRICH core structure.

Radiator gas. The transparency in the near-UV benchmark region (most sensitive to the gas quality and contaminants) has been measured with a monochromator at CERN, resulting in values above 98% for a 1.6 m column of gas at wavelengths greater than 200 nm, see left panel of Fig. 8.64. The measurement has been done with a gas that was stored into bottles for about 4 years, indicating an excellent preservation with time.

Aerogel. Several measurements were performed to optically characterize the aerogel. The transmittance of silica aerogel is a measure of how much light passes through the material without being absorbed or scattered. Silica aerogel consists mostly of air. Indeed, it has a unique structure made of a three-dimensional network of interconnected nanopores, with diameters ranging from 2 to 50 nm, which allows visible light to pass through the material with minimal scattering or absorption. Specifically, in aerogel, light undergoes Rayleigh scattering, which is the elastic scattering of light by particles much smaller than the wavelength of the light. The transmittance is typically highest in the near-infrared region, where the absorption of radiation by the silica network is minimal. Its dependence on the radiation wavelength is usually defined by the Hunt formula [42] which assumes a λ^4 -dependence of Rayleigh scattering cross section. In silica aerogel, the low absorption is due to the absence

of impurities or defects in the silica network that could trap and dissipate the energy of the photons. Additionally, silica aerogel can be hydrophobic or hydrophilic. The tiles tested are highly hydrophobic, which means that they repel water and other liquids. This property helps to maintain the material's transparency even in humid or wet conditions. The aerogel scattering and absorption capability can be assessed through the transmission length as follows: $1/\Lambda_T = 1/\Lambda_{\text{scat}} + 1/\Lambda_{\text{abs}}$.

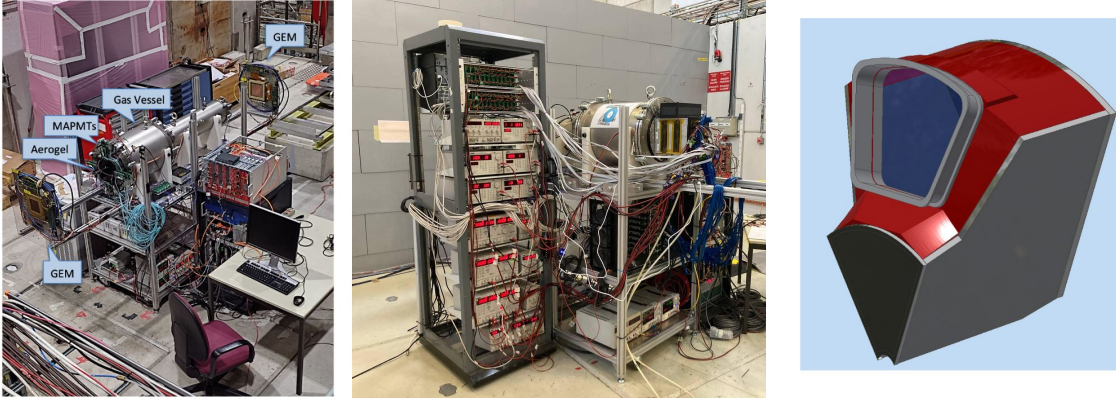


Figure 8.65: (Left) Baseline prototype with reference detector at the SPS-H8 beam line of CERN. (Center) First ePIC-drive detector box under test at the PS-T10 beam line of CERN. (Right) Real-scale prototype model mimicking the basic dRICH construction unit (sector).

We have characterized several $10 \times 10 \text{ cm}^2$ and $5 \times 5 \text{ cm}^2$ aerogel tiles produced as a spin-off the BELLE-II development in a broad range of refractive indexes. Table 8.17 reports a list of the tested samples, where for each tile its refractive index and expected thickness in the thinnest point of its meniscus geometry are reported. On each tile transmittance was measured on 15 different sampling points, to provide information on the dependence of the transmittance on the thickness as well as on the light wavelength (in a range from 250 to 800 nm). The maximum discrepancy along the tile is of the order of $\approx 0.3\%$, the transparency homogeneity is quite good. Transmittance as a function of the wavelength of a single tile was considered as the average of the transmittance value at each sampling point. The average transmittance was fitted by the extended Hunt formula suggested in [42] to extract scattering and absorption lengths. The results are presented in Fig. 8.69 for a tile with $n = 1.03$, which shows that the transmission length is nearly equal to the scattering length, whereas the absorption length is considerably higher. Therefore, the contribution of absorption can be considered negligible. A comparison of the results from all the tested tiles can provide valuable insights into the impact of the refractive index on the optical properties of the aerogel, see Fig. 8.70. The transmittance measurements reveal that the tiles with a refractive index close to $n=1.03$ exhibit higher transmittance length values at 400 nm compared with tiles of higher or lower refractive index, see Fig. 8.71. In the metrology laboratory at CERN, the thickness and flatness of the tile have been also measured. The measurement has been executed on a tile with $n = 1.03$ using the touch probe system (force applied = 2 g). The measuring system is the LEITZ PPMC with $\pm 0.3 \text{ }\mu\text{m}$ of precision. There is a variation in thickness from the center to the edges, of the order of 0.4 mm, and a different planarity in the two faces, one 0.7 mm, the other 1.27 mm. In general the tiles have the shape of a dome.

Mirror. A mid-size demonstrator (of 60 cm diagonal) has been realized with dRICH specifications, see right panel of Fig. 8.64. The CFRP core structure has been optimized for preserving the surface shape accuracy and a light body: it adopts the light LHCb structure in the

center, and the stronger CLAS12 structure on the edges. Before coating, the point-like source image test measures a D0 value, that represents a global surface quality estimator, of 1.8 mm, better than the specification of 2.5 mm. The same test indicates a radius of 2254.1 mm, slight above the request to be within 1% of the nominal 2200 mm value.

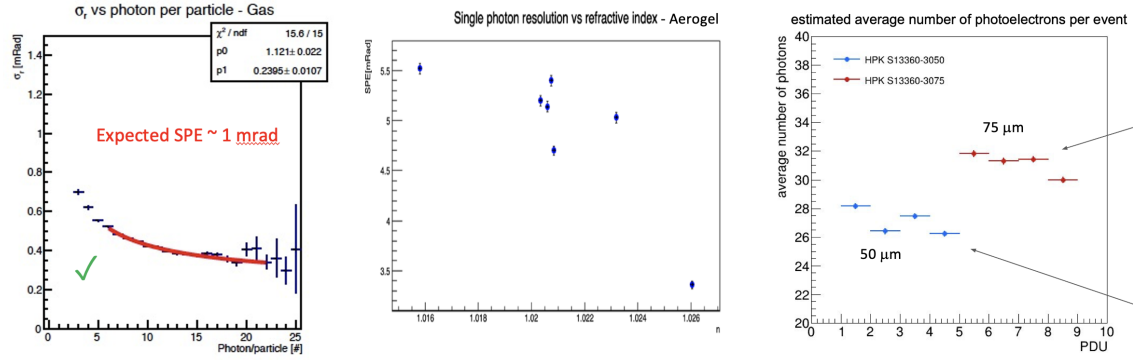


Figure 8.66: (Left) Cherenkov angular resolution obtained for C_2F_6 as a function of the recorded number of photons. The SPE values is consistent with expectations. (Center) SPE angular resolution measured on aerogel as a function of the refractive index. The expected resolution is obtained for an index greater than $n=1.025$. (Right) Comparison in photon yield of sensor with different SPAD size. All the measurements are obtained with the dRICH prototype.

Prototyping. A baseline prototype has evolved in time to serve the dRICH R&D development for few years, see left panel of Fig. 8.65. The gas vessel is a cylinder made of vacuum standards, to allow an efficient and safe gas exchange. The entrance flange can mount an external dark box separated from the inner gas volume by a UV-transparent lucite foil (or quartz window). An aerogel tile with possible additional UV filters, plus an array of alternative sensors and readout electronics, can be inserted into the dark box. Two mirrors inside the vessel have optimized focal lengths to image the Cherenkov light from the two radiators onto the limited active surface. The major achievements obtained during several test-beams have been the validation of the dual-radiator concept, the validation of the C_2F_6 gas radiator (see left panel of Fig. 8.66), the optimization of the aerogel refractive index (see central panel of Fig. 8.66), the performance study of the SiPM-ALCOR readout chain (see right panel of Fig. 8.66), and the development of an EIC-driven readout plane. A partially equipped EIC-driven plane has been realized in time for the October '23 test-beam with Hamamatsu S13360-3050 SiPM sensors of standard 50 μm pixel pitch, see left panel of Fig. 8.67. The plane has been complemented for the test-beam in May 2024 with sensors of 75 μm pixel pitch, to verify the potential benefit in timing and photon detection efficiency. This has allowed for the first time a full ring coverage, an essential requirement for precise radiator performance study and effective signal over background study, see central panel of Fig. 8.67. An effective interplay between the two radiators at intermediate energies has been demonstrated, see right panel of Fig. 8.67. The new detector box has allowed a preliminary study of the thermal gradients and possible effects on the gas performance, indicating that the possible temperature gradient of few degrees induced into the gas volume by the cool sensor plane can be largely mitigated by a gas re-circulation or by a double window.

E&D status and outlook:

A new version of the ALCOR ASIC is currently being designed to extend the number of channels to 64 and integrate the chip inside a BGA package, aiming to enhance the scalabil-

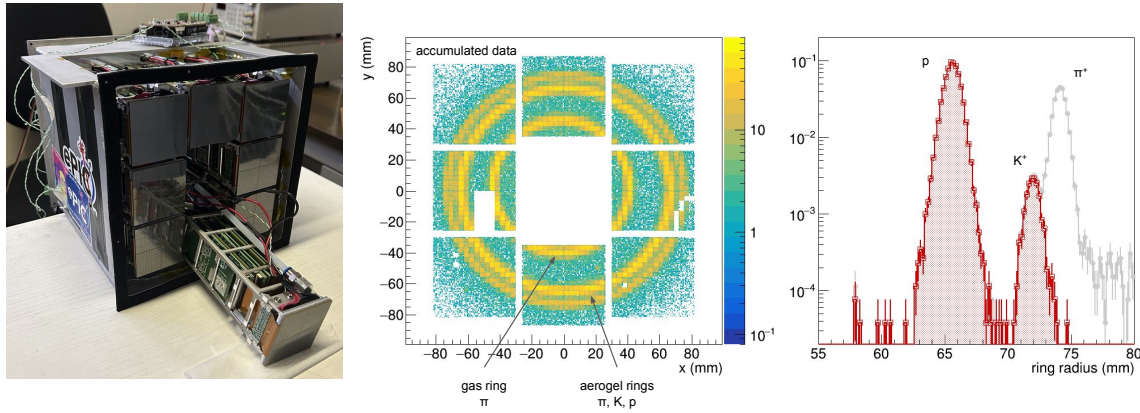


Figure 8.67: (Left) Prototype PDU and assembled detector plane. (Center) Cumulated ring imaging. (Right) dual-radiator interplay for a mixed hadron beam at 10 GeV/c. After the gas information is used to tag pions, an effective separation between kaon and proton is provided by the aerogel.

ity of the readout system and meet specific EIC-driven requirements. The ASIC package will use FC-BGA technology with 256 balls and 1 mm ball pitch. Since no re-distribution layer (RDL) is available for the 110 nm technology in which ALCOR is fabricated, a dedicated 10-layer 1.27 mm thick substrate in bismaleimide-triazine (BT) resin material is currently being designed. This BT epoxy provides a more advanced and reliable solution w.r.t. many FR4 grade materials, while being also commonly available from multiple vendors. In particular, its higher thermal conductivity and lower z-axis coefficient of thermal expansion (CTE) values make it more suited to cope with repeated thermal cycles, in which CTE mismatches may induce mechanical stress on the BGA solder joints. The new version of ALCOR will also include some internal design revisions. A programmable hardware shutter is being implemented to filter out-of-time DCR and thus significantly reduce the data throughput. The asynchronous digital shutter is implemented in ALCOR pixel logic using the external test-pulse signal and will be provided by the RDO board. Inside the ASIC programmable delay chains, with 4 configuration bits at channel-level (LSB \simeq 350 ps) and at the chip periphery (LSB \simeq 100 ps), allow the compensation of the offsets between different pixels and columns. In addition, the front-end will feature an increased bandwidth amplifier to improve the system time resolution while keeping the same power consumption and also an hysteresis circuit in the discriminator stage to avoid unwanted re-triggering on the SiPM signals slow tail, occurring when operating with very low thresholds. To improve its overall SEU tolerance, the new version of the ASIC will implement triple modular redundancy (TMR) also for the periphery registers as well as error-correcting Hamming encoding for the finite-state machines (FSM). Further irradiation tests are foreseen in 2025-2026 on ALCOR final version to fully validate the front-end electronics in terms of radiation tolerance for all of its components. The tape-out is scheduled during the first months of 2025. A thorough electrical characterization of this version of ALCOR, the first one assembled in a BGA package and including all the features required for the dRICH application, will be carried out to validate its new functionalities and measure its performance in order to complete the E&D activity and go ahead with ASIC mass production which is foreseen in 2026.

The development of the final front-end boards takes advantage of the work done for the prototype version in terms of space constraints, readout scheme and components selection. To finalize their layout several design optimization are required: define the best segmentation

and routing to provide the bias voltage to the SiPMs, optimize the AC-coupling circuitry between ALCOR and the SiPM sensors, include the annealing circuit required to operate the SiPMs in forward-bias, distribute the power lines and optimize the control and monitor protocols. In addition, all components that will be mounted on these boards need to be tested to verify their radiation hardness. The design of the final version of the SiPM carrier, FEB and master-logic boards will be completed in 2025 while the mass production is expected during 2026.

For the radiator gas, it is required to complete the design of the gas system and finalize the layout of the monitoring equipment. Each of these activities assumes an engineering study and its validation by laboratory studies. The remaining E&D activity is expected to be completed by the end of 2026.

An increase of the aerogel tile volume is instrumental to minimize the edge effects and contain the cost. During the R&D phase, tiles with side up to 15 cm and thickness up to 2 cm were realized. A feasibility study is ongoing to increase these limits towards a side of 20 cm or a thickness of 3 cm to support the successful assembling scheme adopted at BELLE-II, see central panel of Fig. 8.64. The aerogel production efficiency should be evaluated in conjunction with the optical quality obtained. This engineering work is expected to take time and not be completed before the end of 2026.

Coating of the CFRP mirror substrate should be realized and compare with the benchmark performance obtained with the same materials at CLAS12. This work will be completed by mid 2025.

A real-scale prototype is being realized with composite materials and a realistic geometry (mimicking a dRICH sector). This is instrumental to validate the mechanical elements and study the assembling details (e.g. of transparent septa), the mechanical stability, the gas tightness, and the thermal aspects. One of the major goals of the real-scale prototype is also to reproduce the final ePIC working conditions, mount an extended readout plane with the designed RDO board, operate demonstrators of the optical components as results of the ongoing developments, and optimize the performance in a realistic off-axis optics configuration. To this end, a test-beam is planned for mid 2025.

Other activity needed for the design completion:

Slow control, interlock and the calibration LED/laser system design is not started yet.

Status of maturity of the subsystem:

The R&D activity has been focused on the most innovative aspects of the detector that present technological challenges. These are the SiPM for single-photon detection in a strong magnetic field, a compact readout electronics to fit into the ePIC envelope and the use of two radiators to extend the momentum reach. The remaining effort is substantial, but is connected to more consolidated technologies, with possibly the only exception of the gas separation system for the peculiar C_2F_6 gas.

Environmental, Safety and Health (ES&H) aspects and Quality Assessment (QA planning):

Standard slow-control and interlock procedures will be implemented to control power and cooling while monitoring gas flow, humidity and temperature. The cooling system is complemented by a buffer tank to allow air flow and heat removal from the detector boxes in case of a failure of the recirculating system. The gas volume is maintained at +1 mbar with respect the atmospheric pressure on the top, with a consequent +5 mbar overpressure defined by the hydrostatic pressure of the radiator gas on the bottom, by means of pressure regulators connected to an UPS station and a two-way bubbler. Hexafluoroethane is non-flammable and it has limited toxicity, when below 1000 ppm level and for short exposure time [ref to be added]. In case of a major damage of the

Component	QA station 1	QA station 2	QA detail and backup
Aerogel	Temple U.	BNL	INFN-BA
Gas	BNL		INFN-TS
Mirror	JLab		Duke U.
Sensor (SiPM)	INFN CS-SA-CT	INFN-TS	INFN-BO
Readout	INFN-BO	INFN-FE	INFN-TO

Table 8.14: Planned quality assurance (QA) stations, organized in order to provide redundancy and support specific characterization studies.

supply pipeline or of the vessel itself, 12 m³ of hexafluoroethane at atmospheric pressure from the vessel (0.02% of the hall volume) will mix with the air present in the experimental hall, requiring the implementation of standard ODH procedures. Hexafluoroethane has a high Global Warming Potential (GWP): 12400 for a horizon time of 100 years [43] and it is, therefore, included in the group of GreenHouse Gasses (GHG). Environment protection imposes that GHGs are not released in the atmosphere. This is obtained by using them in closed circuits, where leakages are minimized, and by collecting and sending for disposal the fraction of gas purged during circuit filling and gas recovery at the beginning and at the end of an operation period, respectively. Both closed circuit gas circulation and purged gas trapping are characterizing elements of the dRICH radiator gas system design. The maximum expected leakage rate during operation is about 20 m³ / year assuming six-month operation. Experience in quality assurance protocols has been gained in parallel with the R&D activity. For each critical component two stations are being organized to provide essential QA and redundancy, with a (third) station able to support in-deep characterization on samples and serve as backup, see Table 8.14. The QA activity will be supported by manpower from all the dRICH groups. Essential QA parameters will be measured: integrity, refraction index, transparency, dimensions, and planarity of the aerogel; leak rate of the gas system (after completion); refractive index and transparency of the radiator gas (with the monitoring equipment of the gas system); dark count rate and PDE for the sensors; electrical connections, bias levels and data rate for the readout; dimensions, weight, reflectivity and D0 (point-like source image brightness) for the mirrors.

Annealing of SiPM will be performed during technical stops and/or during the annual stops of the EIC machine. All the dRICH front-end electronics (FEE) will not be powered, with the exception of a few components needed to monitor and control the annealing operations. An interlock-based system will inhibit the FEE power-supply units during annealing. The circulating thermostat system used to cool the SiPMs will be switched to heating mode to reach a temperature of up to T = 100°C. A slow heating ramp of < 1 °C/minute will be employed to reduce thermal stress on the system. The dRICH photodetector boxes will be thermally insulated as much as possible to reduce heat leaks into neighbouring detectors while performing annealing. It is expected that the inner volume of the detector box can reach a temperature of T = 100°C and will be monitored with temperature sensors. Temperature sensors will be placed on the outside of the photodetector boxes to monitor the external environment. Annealing of the whole dRICH photosensors at once requires up to 160 kW of power and will not be performed as such. Only a fraction of the dRICH SiPMs will perform annealing at a given time, to limit the total amount of power needs to about 20-40 kW. This is similar to the total power consumption of the FEE during normal operations and the same safety procedures apply. Annealing power will be distributed evenly across the dRICH SiPM. In case of a power outage, the annealing current will be promptly removed from the SiPMs and their temperature will promptly drop to the temperature of the thermostat. The latter will eventually slowly cool down.

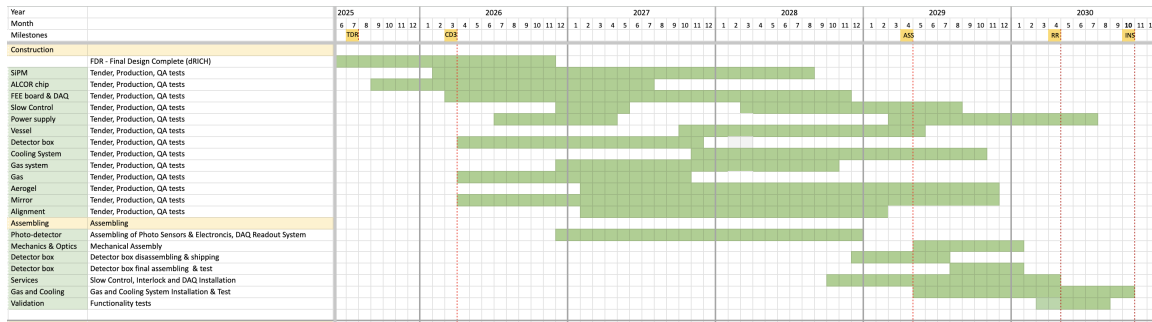


Figure 8.68: Construction plan

Construction and assembly planning:

The construction and assembling plan assumes to compress all the necessary tasks in a short time period in between the presently known EIC milestones: start with CD3 (at the beginning of 2026) and completion 6 months in advance of installation (in October 2030). This results in an aggressive schedule in terms of manpower and funding profile. The 6 months contingency time before installation will be used to perform functionality tests, and complete the services in the experimental hall at IP6. The assembling of 1248 PDUs comprising SiPM sensors and cooling, front-end electronics and RDOs, and their integration with the services inside six detector boxes will be staged over 2 years (mainly 2027 and 2028) by the dRICH DSC in Italy. This organized effort requires a timely procurement, starting with the ALCOR chip (wafer and packaging) followed by sensors, readout electronics, and box mechanics. Cooling infrastructure and DAQ system are expected to run in parallel to the detector box construction and be mainly covered by the EIC Project. First articles of DAQ, power supply and slow control could be used for the initial functionality tests of each single detector box, but the main effort on such services is concentrated on a later stage of the plan during assembling at BNL. The detector boxes will be completed in time to be shipped to BNL and mounted on the dRICH in the second half of 2029. The dRICH vessel construction, a joint venture of the dRICH DSC and the EIC Project, will start in 2028 in order to be ready for detector assembling mid 2029. Mirror production is expected to take 2 years and is staged as soon as possible, subject to the funding profile of the EIC Project, to reduce the sole source risk. The engineering of the aerogel production is expected to extend beyond the TDR, with the consequent production led by the dRICH DSC not happening before 2027 and lasting for at least 2.5 years. An early procurement of the C_2F_6 gas by the EIC Project is planned in order to reduce the risk of a market price increase. The principle design of the radiator gas system will be completed by the end of 2026 by the dRICH DSC. The executive drawings and the system realization by the EIC Project engineering team supported by adequate technical personnel is expected during years 2027 and 2028. The layout finalization and validation of the monitoring equipment will be completed by the end of 2026, while its realization is by the end of 2027 by the dRICH DSC. This equipment will be interfaced with the gas system in 2028, via synergistic effort between the EIC Project engineering team and the dRICH DSC. This combined group will perform the QA assessment of the gas system in 2029.

Collaborators and their role, resources and workforce:

INFN has agreed on a substantial in-kind contribution and the corresponding workforce has taken corresponding responsibilities in the construction within the DSC. The INFN in-kind will cover the design, production and quality assurance cost of the SiPM sensors, of front-end ASIC (ALCOR), of the front-end board (FEB), of the readout boards (RDO) as well as the assembly of the above components in a compact Photo Detector Unit (PDU), including the cooling circuitry and related

mechanics. It will cover the cost of the realization of the six detector boxes (containing the PDU of each sector) with the control panels and the electronic services attached (for HV/LV/daq links routing). It will contribute to the design and realization of the main vessel, the design/supervision of the powering and monitoring systems, the dRICH tagging system and data filtering in streaming mode, see Sec. ?? , and to the definition of specifications and quality assurance (QA) of all the other components and services (i.e. gas, power and cooling plants). The availability of the essential local resources as mechanical and electronic workshops and laboratory space have been negotiated. **INFN-FE (IT)**: is coordinating the DSC activity and is leading the mechanical design. The group will lead the design and production of the vessel in collaboration with the EIC Project and will take care of the realization of the detector boxes and corresponding control panels for the 6 sectors. The assembly of the detector boxes is expected to happen in its laboratories. **INFN-BO (IT)**: the group is leading the activity on photosensors (SiPM) and data-acquisition. It will be responsible of the procurement of SiPM, design and production the readout boards (RDO) and coordinate the integration of the various elements of the PDU. The PDU will be assembled in BO and tested/validated before being moved to INFN-FE for the installation in the detector boxes. **INFN-BA (IT)**: the group is leading the aerogel activity. It will coordinate the mass production and the quality assurance (expected to be operated in the US at Temple University and BNL). **INFN-CS-SA-CT (IT)**: this cluster of units will work on the QA of SiPM and front-end boards prior of the PDU assembling. They will equip test stations in SA and CS for this purpose. **INFN-GE (IT)**: is carrying out a feasibility study (and if successful, the realization) of an interaction tagger to filter the dRICH data stream. **INFN-LNS (IT)**: the group will contribute to the mechanical design effort. **INFN-RM1/RM-TV (IT)**: the RM1 group (and one staff person of RM-TV) has extensive experience on AI algorithm running on FPGA. They will develop algorithm for pattern recognition and data reduction on FELIX cards and the interface with the signals received by the dRICH tagger or from ePIC via GTU. **INFN-TO (IT)**: the group is leading on the design, test and production of the front-end ASIC ALCOR. The group will produce the chips and the front-end cards (FEB) mounting the ALCOR, and coordinate the quality assurance tests of the chip and FEB. **INFN-TS (IT)**: the group is leading the radiator gas activity. It will lead the design of the gas system and develop a continuous monitor system (critical to maintain a good chromaticity). It will also develop a test station of SiPM (with smaller capacity with respect to the CS-SA-CT cluster). **DUKE U. (US)** is leading the mirror activity. It will coordinate the mirror production, expected to happen in the States, the corresponding QA activity, and the coating process that possibly will be realized at Stony Brook. **Jefferson Lab (US)** is contributing to the mechanical design and developing tools for mirror characterization. **Brookhaven Lab (US)** is contributing to the mechanical design and integration study. It will lead the infrastructure (installation tools, services, safety control) realization with its design authority and technical resources. **Stony Brook (US)** is developing mirror coating capability. **Temple U. (US)** is developing an aerogel quality assurance facility. **M.S.Ramaiah U. (India)** is contributing to the simulation and performance study. **NISER (India)** is contributing to the performance study. **Haryana and Karnataka U. (India)** have started contributing to the performance study. Secondments of personnel from all the DSC groups will be organized to support the QA activity in US and the assembling phase at BNL. The EIC Project is expected to cover the procurement effort that can be more efficiently based on US, and all the safety, infrastructural and integration aspect that require specific engineering background. This include the cost of the gas, of the mirrors, of the installation tools, of the power-supply systems , of the cooling plant and the gas plant, and of the FELIX cards receiving the data from the RDO.

3674 **Risks and mitigation strategy:**

3675 The major risk of the dRICH gas radiator is the banning of the hexafluoroethane or more severe
 3676 restriction on its usage, that can also result in increased cost or difficult procurement. The only
 3677 alternative option to preserve the dRICH performance would be an eco-friendly gas with very

similar refractive index, an option not available in nature at atmospheric pressure. Argon at ≈ 3 bar absolute pressure mimics with great accuracy the hexafluoroethane characteristics. It is also non-expensive, non-toxic and non-flammable. R&D is being performed within the EIC generic R&D program to establish the validity of this approach as risk mitigation strategy. Radiation damage reduces the lifetime of the SiPM as good photodetector for the dRICH performance. Estimates of the radiation level on the dRICH photodetectors are expected to be accurate. The DCR model shown in Figure 8.56 (right) is for the sensors experiencing the largest radiation levels (closer to the beam line) and for detector operation at $V_{\text{over}} = 4$ V and $T = -30^\circ\text{C}$. Operation at lower $V_{\text{over}} = 3$ V and/or lower temperature $T = -40^\circ\text{C}$ would reduce the DCR without loss in performance, hence allowing one to accommodate larger integrated radiation levels (up to a factor 2-3) than those reported in the figure. The addition of small thermoelectric cooling (TEC) modules will be evaluated as a potential approach to boost the cooling performance, allowing one to reach an even lower operation temperature of $T = -50^\circ\text{C}$ and avoid possible dishomogeneities. Current R&D on new SiPM technologies for improved performance and radiation hardness are being followed up as a risk mitigation strategy and as a potential upgrade for the dRICH photodetector in the late 2030's or in the early 2040's. For two components, optical aerogel and carbon-fiber mirror, there is only one known supplier able to deliver the wanted specifications at the present stage. An early procurement should limit the risk of a market discontinuity. Within the ePIC RICH Consortium, the recently initiated R&D on mirrors at Purdue University are being followed up as potential sources of risk mitigation in the long term period, if the adaptation to the dRICH needs will be proven feasible. DSC members are part of the recent DRD4 initiative, that aims to create a worldwide collaborative environment to favor new technological breakthroughs in Cherenkov particle identification and photon detectors. Within DRD4, there are many development areas of interest for the dRICH program, in particular gasses or mixtures alternative to the greenhouse fluorocarbon gasses and radiation hard SiPM.

3754 **Additional Material** Planning of additional material for the gas radiator system/monitoring
3755 equipment:

- 3756 • Radiator Aerogel:
 - 3757 – aerogel characterization in lab and beam tests;
 - 3758 – details of the aerogel support and purging;
- 3759 • Radiator Gas:
 - 3760 – Hexafluoroethane characteristics;
 - 3761 – Detailed description of the gas system;
 - 3762 – Options for gas separation during filling and gas recovery operations;
 - 3763 – Trapping system to collect hexafluoroethane in the purged gas;
 - 3764 – Jamin interferometer for refractive index measurement;
 - 3765 – Measurement of the transparency with the spectrophotometer;
 - 3766 – Oxygen and water vapor contamination: measurement and removal;
 - 3767 – High-pressure Ar R&D;
- 3768 • Mirror:
 - 3769 – mirror characterization in lab and beam tests;
 - 3770 – details of the mirror structure;
 - 3771 – details of the mirror support;
 - 3772 – details of the mirror alignment;

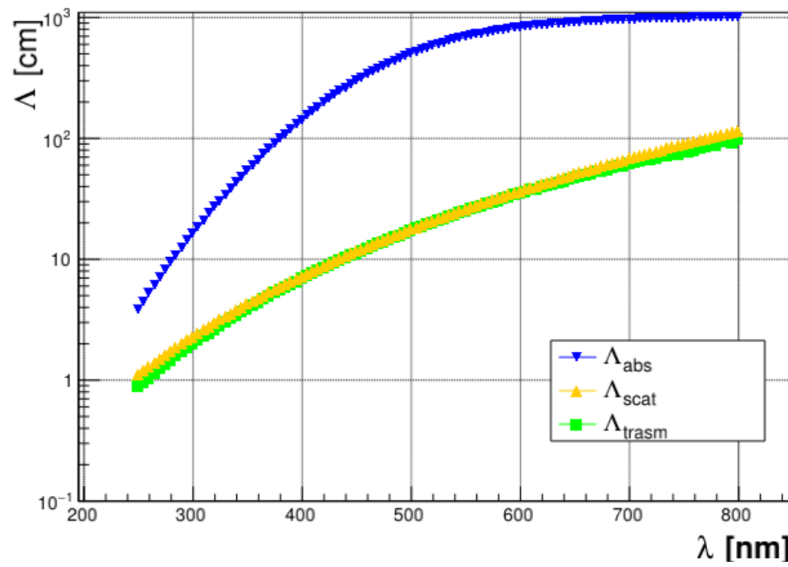


Figure 8.69: Transmission, absorption and scattering length curves as a function of the wavelength for the tile with $n = 1.03$.

3773 In the following the specifications of the main dRICH components are tabulated.

Detector element	Abbreviation	Elements/sector	Total elements
Photodetector box	PDB	1	6
Master panel board	MPB	26	156
Photodetector unit	PDU	208	1248
Silicon photomultiplier	SiPM	53248	319488
SiPM sensor arrays		832	4992
Readout board	RDO	208	1248
Front-end board	FEB	832	4992
ALCOR chips		832	4992

Table 8.15: Main elements of the dRICH photodetector system with the indication of number of elements per sector and the total.

Parameter	Value	Notes
Package type	SiPM array	
Package dimension	$< 26 \times 26 \text{ cm}^2$	
Mounting technology	surface mount	
Number of channels	64	
Matrix layout	8×8	
Channel size	$3 \times 3 \text{ mm}^2$	
Fraction of active area in package	$> 85\%$	
Microcell pitch	$50 - 75 \text{ }\mu\text{m}$	
Protective window material	silicone resin	radiation & heat resistant
Protective window refractive index	1.55 - 1.57	
Spectral response range	300 to 900 nm	
Peak sensitivity wavelength (λ_{peak})	400 - 450 nm	
Photon detection efficiency at λ_{peak}	$> 40\%$	
Breakdown voltage (V_{break})	$< 60 \text{ V}$	
Operating overvoltage (V_{over})	$< 5 \text{ V}$	
Operative voltage (V_{op})	$< 64 \text{ V}$	
Max V_{op} variation between channels	$< 100 \text{ mV}$	at $T = -30^\circ\text{C}$
Channel dark count rate (DCR)	$< 50 \text{ kHz}$	
DCR at $T = -30^\circ\text{C}$	$< 5 \text{ kHz}$	at $T = -30^\circ\text{C}$
DCR increase with radiation damage	$< 500 \text{ kHz}/10^9 n_{\text{eq}}$	at $T = -30^\circ\text{C}$
Residual DCR after annealing	$< 50 \text{ kHz}/10^9 n_{\text{eq}}$	at $T = -30^\circ\text{C}$
Terminal capacitance	$< 500 \text{ pF}$	
Gain	$> 1.5 \cdot 10^6$	
Recharge time constant (τ)	$< 100 \text{ ns}$	
Crosstalk (CT)	$< 5\%$	
Afterpulsing (AP)	$< 5\%$	
Operating temperature range	$-40 \text{ to } 25^\circ\text{C}$	
Single photon time resolution (SPTR)	$< 200 \text{ ps FWHM}$	

Table 8.16: Baseline specifications of the SiPM sensor devices for the dRICH photodetector. All parameters are defined at room temperature ($T = 25^\circ\text{C}$) and at the operating voltage V_{op} , unless otherwise specified.

Tile	Refractive index @405 nm	Nominal thickness (mm)
1	1.03	20.7
2	1.03	20.8
3	1.03	20.1
4	1.03	20.5
5	1.03	20.4
6	1.03	10.0
7	1.03	10.0
8	1.04	20.3
9	1.04	20.5
10	1.04	20.3
11	1.04	20.4
12	1.04	20.5
13	1.05	20.5
14	1.05	20.7
15	1.05	20.6
16	1.05	20.6
17	1.05	20.8
18	1.005	20.0
19	1.005	20.0
20	1.005	20.0

Table 8.17: Tiles list. Tiles from 1 to 17 were produced at the High Energy Accelerator Research Organization (KEK) in Japan and delivered in March 2021 [3], except tiles 6-7 which belongs to a 2000 production manufactured by Matsushita Electric Works (Japan).

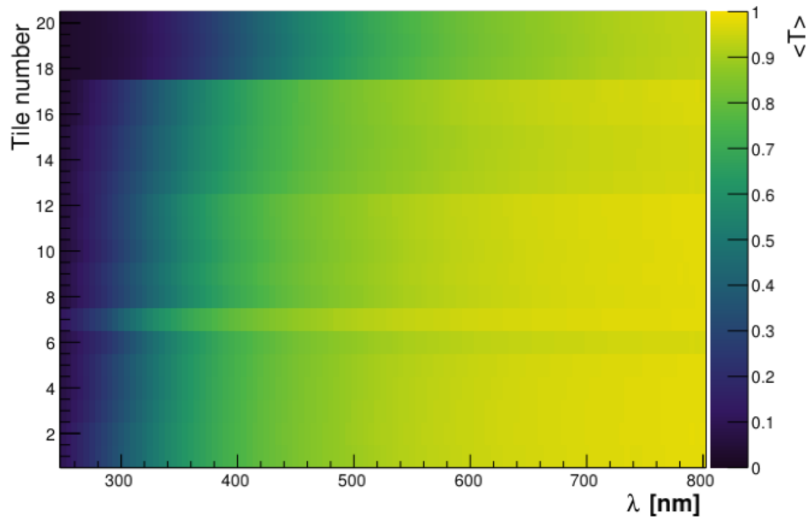


Figure 8.70: Transmittance as a function of the wavelength for all the tiles.

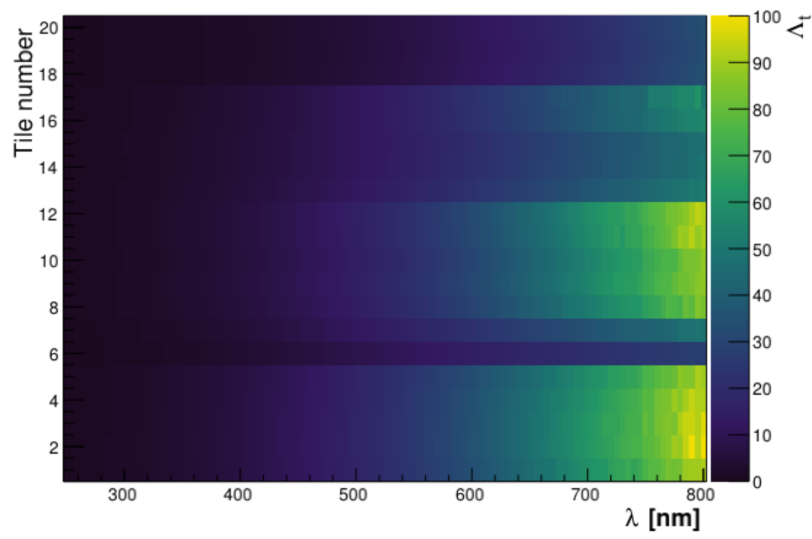


Figure 8.71: Transmission length as a function of the wavelength for all the tiles.

3774 8.3.5 Electromagnetic Calorimetry

3775 Add text here.

3776 8.3.5.1 The backward endcap electromagnetic calorimeter

3777 Requirements

3778 **Requirements from physics:** The electron-end-cap calorimeter will cover a dynamic energy
 3779 range of 0.1–18 GeV for electromagnetic showers of the scattered electron based on e+p Pythia
 3780 simulations at $18 \times 275 \text{ GeV}^2$. The EEMC is a high-resolution ECal designed for precision measure-
 3781 ments of the energy of scattered electrons and final-state photons in the electron-going region. The
 3782 requirements for energy resolution in the backward region is driven by inclusive DIS where precise
 3783 determination of the scattered electron properties is critical to constrain the event kinematics.

3784 An excellent energy resolution of $\sigma_E/E \approx 2\%/\sqrt{E} \oplus 1\%$ is required for the backward endcap elec-
 3785 tromagnetic calorimeter.

3786 **Requirements from Radiation Hardness:** The EEEMCal detector must operate at a radia-
 3787 tion level of $\sim 3 \text{ krad/year}$ (30 Gy/year) electromagnetic and 10^{10} n/cm^2 hadronic at the EIC top
 3788 luminosity

3789 **Requirements from Data Rates:** Add text here.

3790 Justification

3791 **Device concept and technological choice:** The EIC physics program requires high-precision
 3792 detection and identification of the scattered electrons emitted in the electron-going direction, as
 3793 well as final-state photons. The backward endcap electromagnetic calorimeter (EEEMCAL) pro-
 3794 vides a compact solution with excellent energy resolution over a large dynamic range and with high
 3795 granularity. The EEEMCAL meets the experiment requirements of fast timing to handle an inter-
 3796 action rate up to $0.5 \times 10^6 \text{ Hz}$ and acceptable radiation hardness up to $\sim 3 \text{ krad/year}$ (30 Gy/year)
 3797 electromagnetic and 10^{10} n/cm^2 hadronic at the EIC top luminosity. Furthermore, the EEEMCAL
 3798 achieves the required clean electron identification for energies greater than 2 GeV with a rejection
 3799 factor better than 10^4 when combined with other detector subsystems. The EEEMCAL has been
 3800 reviewed and passed the EIC Project detector technical review of electromagnetic calorimetry in
 3801 December 2022.

3802 A drawing of the EEEMCal mechanical design is shown in Figure 8.72. The EEEMCAL will be
 3803 located at a distance of 175 cm from the EIC interaction point where it is installed around the beam
 3804 line in a roughly cylindrical geometry. The particles of interest impinge on the front face of the
 3805 detector and pass through a radiator with adapted geometrical dimensions to contain the major
 3806 part of the electromagnetic shower. The produced scintillation photons are detected at the back of
 3807 the radiator by means of an array of Silicon PhotoMultipliers (SiPMs) and readout with back- and
 3808 front-end electronics. The entire detector is enclosed in a mechanical structure that also provides

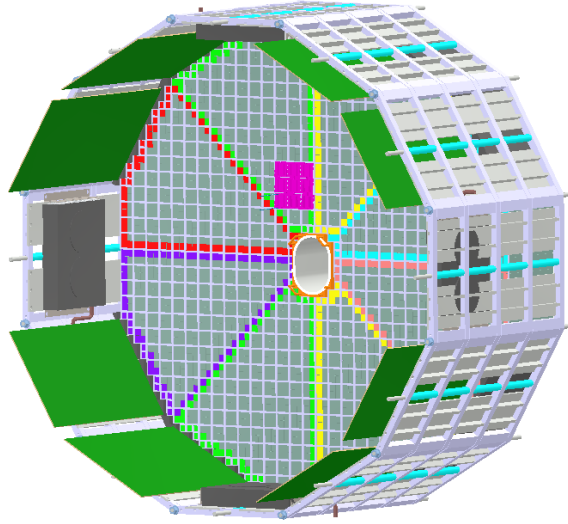


Figure 8.72: CAD drawing of the EEEMCAL. The small gray shapes are the scintillating crystals. The SiPM photosensor matrices are grouped over four crystals and indicated by the pink area. The green rectangles are part of the backend electronics. The dark gray rectangles and circles on the circumference are part of the cooling system.

3809 services like thermal monitoring and cooling and light monitoring. The entire assembly weighs on
3810 the order of three tons, which is consistent with the specifications of the EIC experimental area.

3811 Based on extensive simulation studies, the preferred material for the EEEMCAL radiator is lead
3812 tungstate (PWO), an extremely fast, compact, and radiation-hard scintillator providing sufficient
3813 luminescence yield (15 - 25 photoelectrons/MeV) to achieve good energy resolution. This material
3814 has been the most common precision calorimetry method of choice for hadron physics measure-
3815 ments with electromagnetic reactions, such as at multiple setups at JLAB and also at PANDA/GSI.
3816 To achieve good energy resolution including the so-called constant term typically requires 20 or
3817 more radiation lengths (X_0). For PWO in the EEEMCAL we have $22X_0$ (20 cm). The transverse
3818 block dimensions are matched to the Moliere radius to capture the major part of the transverse
3819 shower. The measured energy resolution for PWO is $\sigma_E/E \approx 2\%/\sqrt{E} \oplus 1\%$ [44]. To pinpoint the
3820 electron scattering kinematics, the EEEMCAL provides a position resolution of $\sim 2\text{mm}$ at 1-3 GeV
3821 with a granularity of 2 cm. The technology for mass production of PWO crystals that guarantees the
3822 needed homogeneity of the whole calorimeter has been well established with recent experiments,
3823 most recently with the Neutral Particle Spectrometer at JLab [45,46].

3824 An effective way to read out the EEEMCAL is through SiPMs that offer several advantages, e.g., a
3825 high gain and a medium photodetection efficiency of about 50%. Furthermore, SiPMs can be oper-
3826 ated in the magnetic field of order few hundred Gauss expected at the location of the EEEMCAL.
3827 Individual devices are grouped into an array to maximize surface coverage of the PWO blocks. In
3828 a recent beam test campaign, the readout concept was validated to work well with a Streaming
3829 Readout setup, the method of choice envisioned for the EIC [47].

3830 Subsystem description:

3831 General device description: In the EEEMCal the PWO crystals are arranged in the mechanical

support structure (Fig. 8.73). This provides the infrastructure to attach the readout components, cooling system, and cables, as well as the installation fixtures to mount the detector in the experimental hall. The support for the crystals is provided by a frame that is installed in the mechanical structure. Photosensors are located at the backend of the crystals. Mechanical grating in the mechanical structure allows the attachment of the SiPM PCBs there. The crystals are stacked with carbon fiber plates at front and back that allow one to guide the crystal into position. The cooling system provides thermal stabilization, which is important for crystal performance. Based on initial thermal calculations, this stabilization can be achieved with a combination of internal and external cooling aided by airflow.

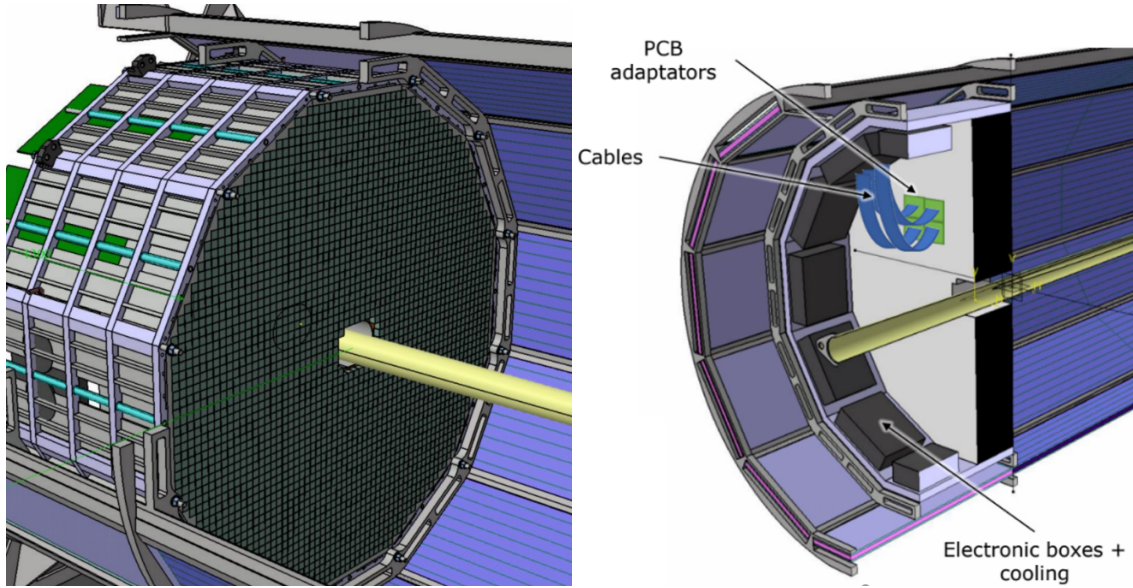


Figure 8.73: Conceptual design of the ePIC electron endcap electromagnetic calorimeter support.

Sensors: Hamamatsu S14160-1315 SiPMs have been identified as the optimal choice for the EEEMCal. Their gain of $3.6 \cdot 10^5$ and relatively low dark current rate (0.7 MHz) allow the measurement of very small signals, close to the single photo-electron (Fig. 8.74, left), while its high pixel density provided by a $15\text{-}\mu\text{m}$ pixel pitch provides very good linearity over several orders of magnitude (Fig. 8.74, right).

FEE: All calorimetry in ePIC will use SiPMs for their readout. However, the number of channels and input signals and capacitance varies greatly from detector to detector. The requirements of the EEEMCal are particularly stringent in terms of energy resolution, which in particular requires the detection of low energy signals (down to 5 MeV per crystal). The readout should provide sufficient dynamic range to accommodate for signals of energy up to 18 GeV.

A discrete readout solution based on commercial devices is currently the baseline for the forward and backward ECals. However, a readout based on the existing H2GCROCv3 chip (developed for the CMS HGCal) is currently under investigation for the backward ECal. It presents many advantages, in addition to exploiting the synergies with most of the other calorimeters in ePIC. Using an ASIC in the readout of the calorimeter is a very cost effective, more radiation tolerant and cooler (i.e. consuming less power) solution. The H2GCROCv3 chip was developed by the Omega group for the primary use for the High Granularity Calorimeter (HGCal) for the CMS detector at LHC, making it a great fit for any calorime-

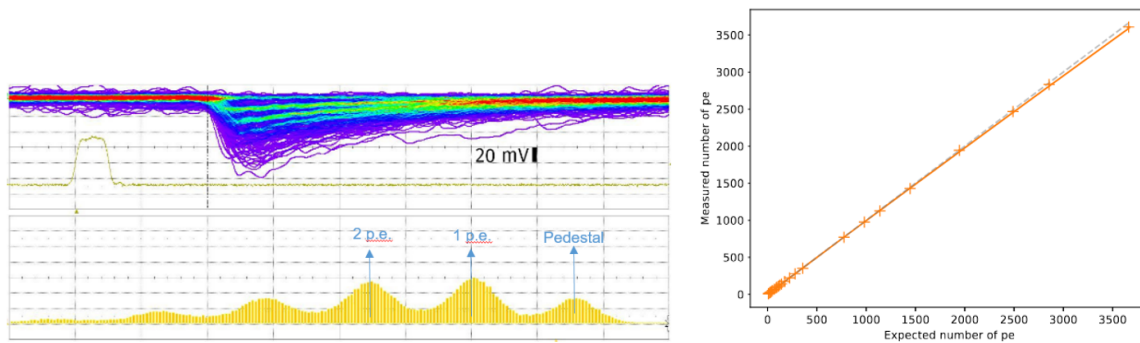


Figure 8.74: Left: waveform (top) and integrated signal (bottom) showing single photoelectron signals in Hamamatsu 15 μm pixel SiPMs. Signals are produced with a low-intensity LED. Right: Linearity measurement, showing 2% linearity up to 3500 photoelectrons.

ter readout. The ASIC requirements for the EEEMCal are very low noise level, low power consumption and very good ($< 1\%$) linearity throughout a very large dynamic range. The chip also has a current conveyor where each channel's bias voltage can be fine-tuned from the ASIC itself. A variation of the H2GCROCV3 chip (CALOROC) is currently under development by OMEGA in order to make it compatible with EIC.

Other components: Add text here.

Performance Our group has performed extensive simulations of the detector performance in the ePIC geometry, including a realistic material budget in front of the detector, which directly affects its resolution and PID capabilities. Figure 8.75 shows the performance of two key parameters: the energy resolution and the pion rejection factor. Results fulfill the physics requirements as outlined in the Yellow Report [4] and NAS study [ref].

Implementation The EEEMCAL project has been organized into a well-defined Work Break-down Structure (WBS). The WBS contains the work necessary to complete the project scope and will form the basis of planning, executing, and controlling project activities. The WBS ensures that no portions of the estimate are omitted. The level of the WBS reflect a logical breakdown of the work by major system as shown in Table 8.18.

The baseline schedule for the EEEMCAL Project is shown in Fig. 8.76. The EEEMCAL project aims at the beginning of the window of installation at BNL. The installation window dates are October 2028 to June 2030.

Services: PbWO_4 crystals are sensitive to temperature changes with a variation of $2\%/^{\circ}\text{C}$ in light output. Thus, the specification is to keep the crystal temperature stable within $\pm 0.1^{\circ}\text{C}$. To ensure this stability the additional heat generated by the electronics needs to be removed and the following cooling structures are being considered. As internal cooling structure several machined copper blocks with internal coolant circulation will be used around the beam pipe. To reduce the spatial extend support structures the EEEMCAL consortium is moreover planning to use cooling plates in between the readout cables which are linked to the support structure surrounding the EEMC with tubes. This system is composed of 12 plates with a 5-8 mm spacing in which water can

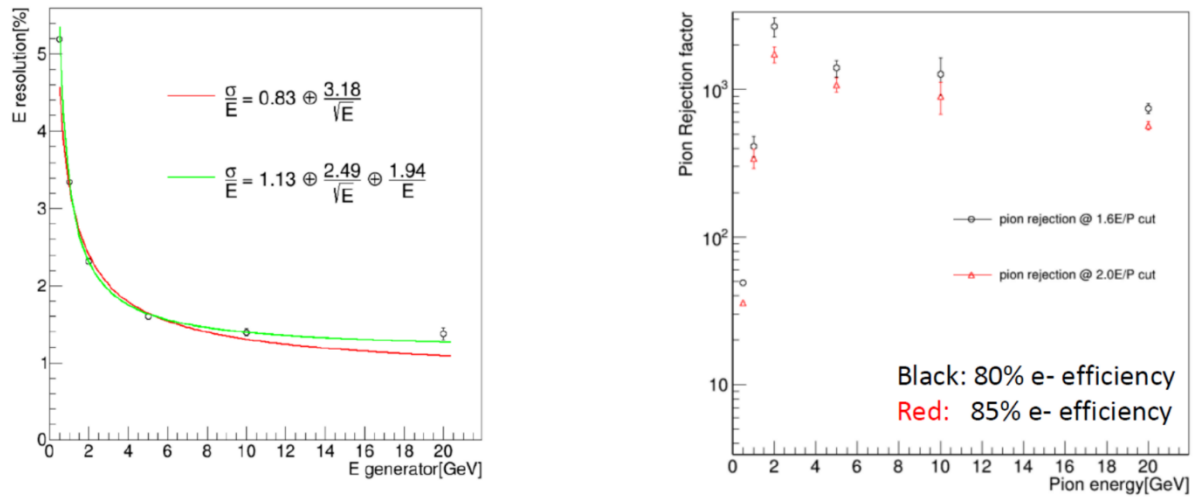


Figure 8.75: EEEMCal simulated performance using the ePIC detector framework including all materials. Left: energy resolution as a function of the incident particle energy. Right: pion rejection factor as a function of energy and different values of electron efficiency.

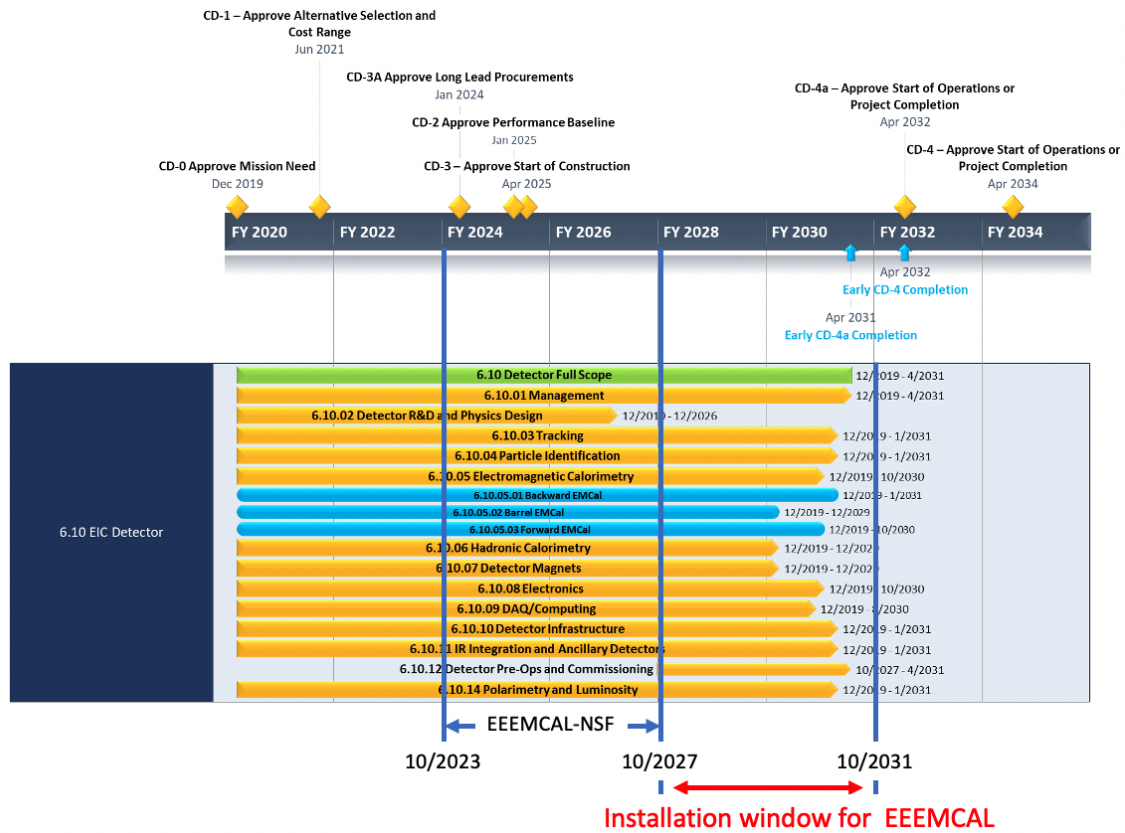


Figure 8.76: EEEMCAL integrated schedule.

WBS	WBS Title	WBS description
2.00	EEEMCAL Project	Construct the EEEMCAL. The EEEMCAL is an electromagnetic calorimeter for measurement of the inclusive process physics in the electron-going direction at the EIC
2.01	Radiator	Radiation detectors consisting of scintillating crystals (PWO) and thin reflector sheets. These provide the detection of energetic electrons
2.02	Photosensor	Photosensors consisting of multi-pixel photon counters grouped into an array to maximize surface coverage of the PWO blocks.
2.03	Mechanical	Mechanical structure including installation fixtures and a cooling system providing thermal stabilization, which is important for crystal performance.
2.04	Signal Processing/DAQ	Signal Processing/DAQ providing the front-end electronics to transmit the signals to the data analysis modules
2.05	Simulation/Software	Simulations/Software providing the software libraries and infrastructure foundation for extracting the physics from the detector

Table 8.18: EEEMCAL WBS Structure

be circulated. The cooling near the crystals will likely not be enough to meet specification. These challenges could be overcome by outside cooling with standard cooling blocks with airflow in front of the electronics or additional cooling added at the back of the assembly.

Subsystem mechanics and integration: The EEEMCAL installation fixtures are shown in Fig. 8.77. They include a mechanical structure that mounts the detector and positions it in the EIC experimental hall at the appropriate height above ground. The structure is envisioned to ride on rails for the installation. The rails could be on the floor as shown, but could also be within the cylindrical structure. In the latter case the outer structure would be bolted to the floor. Having the rails extend from the cylindrical structure has the advantage that it would not require rails on the floor of the experimental hall, which could interfere with other hall infrastructure, e.g., the magnet.

Calibration, alignment and monitoring: Add text here.

Status and remaining design effort:

R&D effort: Add text here.

E&D status and outlook: Add text here.

Other activity needed for the design completion: Add text here.

Status of maturity of the subsystem: Add text here.

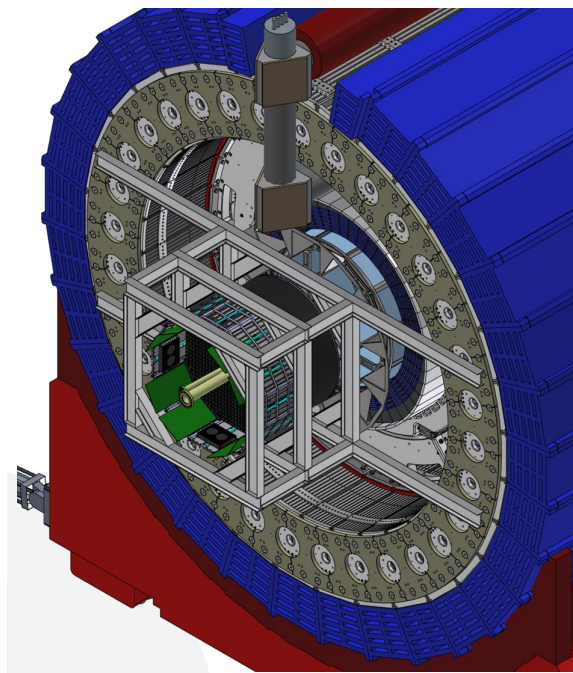


Figure 8.77: EEEMCal installation fixtures that allow for installing the detector safely into the ePIC detector barrel.

3902 **Environmental, Safety and Health (ES&H) aspects and Quality Assessment (QA plan-**
 3903 **ning:** Quality Assurance (QA) is an integral part of effective project management and will be
 3904 employed throughout the design, procurement, and construction of the project. An EEEMCAL
 3905 Project-specific Quality Assurance Plan has been developed to establish all applicable QA require-
 3906 ments for the design, construction, and operation of the EEEMCAL, consistent with the EIC Quality
 3907 Assurance Plan that implements the ten criteria defined in DOE Order 414.1D.

3908 **Construction and assembly planning:** Upon completion of its construction and initial test-
 3909 ing, the EEEMCAL will be situated at BNL. The EEEMCAL collaboration leaders will coordinate
 3910 the required equipment readiness for experiment and final integration of the EEEMCAL into the
 3911 EIC beamline with the EIC Project Management, the ePIC collaboration, and the BNL and JLAB
 3912 Technical leads. This is necessary for successful integration. For example, a special external sup-
 3913 port frame will be provided, installed, and surveyed by the BNL technical staff for this purpose.
 3914 All installations and the integration of the EEEMCAL will be handled by BNL technical staff with
 3915 expert's assistance to ensure appropriate interfacing of infrastructure and fulfillment of installation
 3916 and operation protocols.

3917 Once installed in the EIC experimental hall the EEEMCAL will be operated and maintained by
 3918 the EEEMCAL team and its stakeholders in collaboration with technical teams at BNL. The nor-
 3919 mal operating resources will be provided by BNL. The physics resources to operate and maintain
 3920 the EEEMCAL will be provided through research grants. These resources are critical for tasks that
 3921 are not directly related to the construction of the calorimeter, but instead to the integration of the
 3922 EEEMCAL into the ePIC detector. Examples include developing readout software and trigger algo-
 3923 rithms, implementing online GUIs and the slow controls interfaces required to operate and monitor
 3924 the detector during data taking, as well as designing clustering algorithms and calibration tools and

Item #	Risk Category	Risk Title	Description	Associated Cost (\$)	Pre-Mitigation Scores				Resolving Risk Scores				Risk Action	Mitigation Actions	Impact on Value	Post-Mitigation Scores				Status of Impact Estimation
					On Schedule	On Cost	On Scope	On Quality	On Schedule	On Cost	On Scope	On Quality								
1	Risk	Radiation safety delay	If the vendor safety limit is exceeded then the delivery of the detector block may be delayed.	2.00	High	High	High	High	High	High	High	High	High	High	High	High	High	High	High	Realistic to estimate to expect schedule
2	Risk	S&M hardware issues	If the vendor safety limit is exceeded then the delivery of the detector block may be delayed.	2.00	High	High	High	High	High	High	High	High	High	High	High	High	High	High	High	Realistic to estimate to expect schedule
3	Risk	COVID-19 delay	COVID-19 or other pandemic event occur, then it is possible that project schedule would be delayed.	2.00	High	High	High	High	High	High	High	High	High	High	High	High	High	High	High	Realistic to estimate to expect schedule
4	Risk	O&M issues	If the O&M issues assumed in the cost estimate are more than planned, then the project cost will be impacted.	2.00	High	High	High	High	High	High	High	High	High	High	High	High	High	High	High	Realistic to estimate to expect schedule
5	Opportunity	O&M issues	If the O&M issues assumed in the cost estimate are higher than planned, then the project cost will be impacted.	2.00	High	High	High	High	High	High	High	High	High	High	High	High	High	High	High	Realistic to estimate to expect schedule
6	Risk	Personnel costs, engineering and technical support	If labor resources are not available to address project scope while the project is in progress, then the project cost will be impacted.	2.00	High	High	High	High	High	High	High	High	High	High	High	High	High	High	High	This risk would need to be addressed in the number of days of personnel at any one time. The risk would be addressed in a dashboard.
7	Risk	Personnel costs, engineering and technical support	If labor resources are not available when needed and there will be higher cost and schedule delay.	2.00	High	High	High	High	High	High	High	High	High	High	High	High	High	High	High	
8	Risk	Personnel costs, engineering and technical support	If labor resources are not available when needed and there will be higher cost and schedule delay.	2.00	High	High	High	High	High	High	High	High	High	High	High	High	High	High	High	
9	Risk	Personnel costs, engineering and technical support	If labor resources are not available when needed and there will be higher cost and schedule delay.	2.00	High	High	High	High	High	High	High	High	High	High	High	High	High	High	High	
10	Risk	Personnel costs, engineering and technical support	If labor resources are not available when needed and there will be higher cost and schedule delay.	2.00	High	High	High	High	High	High	High	High	High	High	High	High	High	High	High	
11	Risk	Personnel costs, engineering and technical support	If labor resources are not available when needed and there will be higher cost and schedule delay.	2.00	High	High	High	High	High	High	High	High	High	High	High	High	High	High	High	
12	Risk	Personnel costs, engineering and technical support	If labor resources are not available when needed and there will be higher cost and schedule delay.	2.00	High	High	High	High	High	High	High	High	High	High	High	High	High	High	High	
13	Risk	Personnel costs, engineering and technical support	If labor resources are not available when needed and there will be higher cost and schedule delay.	2.00	High	High	High	High	High	High	High	High	High	High	High	High	High	High	High	
14	Risk	Personnel costs, engineering and technical support	If labor resources are not available when needed and there will be higher cost and schedule delay.	2.00	High	High	High	High	High	High	High	High	High	High	High	High	High	High	High	
15	Risk	Personnel costs, engineering and technical support	If labor resources are not available when needed and there will be higher cost and schedule delay.	2.00	High	High	High	High	High	High	High	High	High	High	High	High	High	High	High	
16	Risk	Personnel costs, engineering and technical support	If labor resources are not available when needed and there will be higher cost and schedule delay.	2.00	High	High	High	High	High	High	High	High	High	High	High	High	High	High	High	
17	Risk	Personnel costs, engineering and technical support	If labor resources are not available when needed and there will be higher cost and schedule delay.	2.00	High	High	High	High	High	High	High	High	High	High	High	High	High	High	High	
18	Risk	Personnel costs, engineering and technical support	If labor resources are not available when needed and there will be higher cost and schedule delay.	2.00	High	High	High	High	High	High	High	High	High	High	High	High	High	High	High	
19	Risk	Personnel costs, engineering and technical support	If labor resources are not available when needed and there will be higher cost and schedule delay.	2.00	High	High	High	High	High	High	High	High	High	High	High	High	High	High	High	
20	Risk	Personnel costs, engineering and technical support	If labor resources are not available when needed and there will be higher cost and schedule delay.	2.00	High	High	High	High	High	High	High	High	High	High	High	High	High	High	High	
21	Risk	Personnel costs, engineering and technical support	If labor resources are not available when needed and there will be higher cost and schedule delay.	2.00	High	High	High	High	High	High	High	High	High	High	High	High	High	High	High	
22	Risk	Personnel costs, engineering and technical support	If labor resources are not available when needed and there will be higher cost and schedule delay.	2.00	High	High	High	High	High	High	High	High	High	High	High	High	High	High	High	
23	Risk	Personnel costs, engineering and technical support	If labor resources are not available when needed and there will be higher cost and schedule delay.	2.00	High	High	High	High	High	High	High	High	High	High	High	High	High	High	High	
24	Risk	Personnel costs, engineering and technical support	If labor resources are not available when needed and there will be higher cost and schedule delay.	2.00	High	High	High	High	High	High	High	High	High	High	High	High	High	High	High	
25	Risk	Personnel costs, engineering and technical support	If labor resources are not available when needed and there will be higher cost and schedule delay.	2.00	High	High	High	High	High	High	High	High	High	High	High	High	High	High	High	
26	Risk	Personnel costs, engineering and technical support	If labor resources are not available when needed and there will be higher cost and schedule delay.	2.00	High	High	High	High	High	High	High	High	High	High	High	High	High	High	High	
27	Risk	Personnel costs, engineering and technical support	If labor resources are not available when needed and there will be higher cost and schedule delay.	2.00	High	High	High	High	High	High	High	High	High	High	High	High	High	High	High	
28	Risk	Personnel costs, engineering and technical support	If labor resources are not available when needed and there will be higher cost and schedule delay.	2.00	High	High	High	High	High	High	High	High	High	High	High	High	High	High	High	
29	Risk	Personnel costs, engineering and technical support	If labor resources are not available when needed and there will be higher cost and schedule delay.	2.00	High	High	High	High	High	High	High	High	High	High	High	High	High	High	High	
30	Risk	Personnel costs, engineering and technical support	If labor resources are not available when needed and there will be higher cost and schedule delay.	2.00	High	High	High	High	High	High	High	High	High	High	High	High	High	High	High	
31	Risk	Personnel costs, engineering and technical support	If labor resources are not available when needed and there will be higher cost and schedule delay.	2.00	High	High	High	High	High	High	High	High	High	High	High	High	High	High	High	
32	Risk	Personnel costs, engineering and technical support	If labor resources are not available when needed and there will be higher cost and schedule delay.	2.00	High	High	High	High	High	High	High	High	High	High	High	High	High	High	High	
33	Risk	Personnel costs, engineering and technical support	If labor resources are not available when needed and there will be higher cost and schedule delay.	2.00	High	High	High	High	High	High	High	High	High	High	High	High	High	High	High	
34	Risk	Personnel costs, engineering and technical support	If labor resources are not available when needed and there will be higher cost and schedule delay.	2.00	High	High	High	High	High	High	High	High	High	High	High	High	High	High	High	
35	Risk	Personnel costs, engineering and technical support	If labor resources are not available when needed and there will be higher cost and schedule delay.	2.00	High	High	High	High	High	High	High	High	High	High	High	High	High	High	High	
36	Risk	Personnel costs, engineering and technical support	If labor resources are not available when needed and there will be higher cost and schedule delay.	2.00	High	High	High	High	High	High	High	High	High	High	High	High	High	High	High	
37	Risk	Personnel costs, engineering and technical support	If labor resources are not available when needed and there will be higher cost and schedule delay.	2.00	High	High	High	High	High	High	High	High	High	High	High	High	High	High	High	
38	Risk	Personnel costs, engineering and technical support	If labor resources are not available when needed and there will be higher cost and schedule delay.	2.00	High	High	High	High	High	High	High	High	High	High	High	High	High	High	High	
39	Risk	Personnel costs, engineering and technical support	If labor resources are not available when needed and there will be higher cost and schedule delay.	2.00	High	High	High	High	High	High	High	High	High	High	High	High	High	High	High	
40	Risk	Personnel costs, engineering and technical support	If labor resources are not available when needed and there will be higher cost and schedule delay.	2.00	High	High	High	High	High	High	High	High	High	High	High	High	High	High	High	
41	Risk	Personnel costs, engineering and technical support	If labor resources are not available when needed and there will be higher cost and schedule delay.	2.00	High	High	High	High	High	High	High	High	High	High	High	High	High	High	High	
42	Risk	Personnel costs, engineering and technical support	If labor resources are not available when needed and there will be higher cost and schedule delay.	2.00	High	High	High	High	High	High	High	High	High	High	High	High	High	High	High	
43	Risk	Personnel costs, engineering and technical support	If labor resources are not available when needed and there will be higher cost and schedule delay.	2.00	High	High	High	High	High	High	High	High	High	High	High	High	High	High	High	
44	Risk	Personnel costs, engineering and technical support	If labor resources are not available when needed and there will be higher cost and schedule delay.	2.00	High	High	High	High	High	High	High	High	High	High	High	High	High	High	High	
45	Risk	Personnel costs, engineering and technical support	If labor resources are not available when needed and there will be higher cost and schedule delay.	2.00	High	High	High	High	High	High	High	High	High	High	High	High	High	High	High	
46	Risk	Personnel costs, engineering and technical support	If labor resources are not available when needed and there will be higher cost and schedule delay.	2.00	High	High	High	High	High	High	High	High	High	High	High	High	High	High	High	
47	Risk	Personnel costs, engineering and technical support	If labor resources are not available when needed and there will be higher cost and schedule delay.	2.00	High	High	High	High	High	High	High	High	High	High	High	High	High	High	High	
48	Risk	Personnel costs, engineering and technical support	If labor resources are not available when needed and there will be higher cost and schedule delay.	2.00	High	High	High	High	High	High	High	High	High	High	High	High	High	High	High	
49	Risk	Personnel costs, engineering and technical support	If labor resources are not available when needed and there will be higher cost and schedule delay.	2.00	High	High	High	High	High	High	High	High	High	High	High	High	High	High	High	
50	Risk	Personnel costs, engineering and technical support	If labor resources are not available when needed and there will be higher cost and schedule delay.	2.00	High	High	High	High	High	High	High	High	High	High	High	High	High	High	High	
51	Risk	Personnel costs, engineering and technical support	If labor resources are not available when needed and there will be higher cost and schedule delay.	2.00	High	High	High	High	High	High	High	High	High	High	High	High	High	High	High	
52	Risk	Personnel costs, engineering and technical support	If labor resources are not available when needed and there will be higher cost and schedule delay.	2.00	High	High	High	High	High	High	High	High	High	High	High	High	High	High	High	
53	Risk	Personnel costs, engineering and technical support	If labor resources are not available when needed and there will be higher cost and schedule delay.	2.00	High	High	High	High	High	High	High	High	High	High	High	High	High	High	High	
54	Risk	Personnel costs, engineering and technical support	If labor resources are not available when needed and there will be higher cost and schedule delay.	2.00	High	High	High	High	High	High	High	High	High	High	High	High	High	High	High	
55	Risk	Personnel costs, engineering and technical support	If labor resources are not available when needed and there will be higher cost and schedule delay.	2.00	High	High	High	High	High	High	High	High	High	High	High	High	High	High	High	
56	Risk	Personnel costs, engineering and technical support	If labor resources are not available when needed and there will be higher cost and schedule delay.	2.00	High	High	High	High	High	High	High	High	High	High	High	High	High	High	High	
57	Risk	Personnel costs, engineering and technical support	If labor resources are not available when needed and there will be higher cost and schedule delay.	2.00	High	High	High	High	High	High	High	High	High	High	High	High	High	High	High	
58	Risk	Personnel costs, engineering and technical support	If labor resources are not available when needed and there will be higher cost and schedule delay.	2.00	High	High	High	High	High	High	High	High	High	High	High	High	High	High	High	
59	Risk	Personnel costs, engineering and technical support	If labor resources are not available when needed and there will be higher cost and schedule delay.	2.00	High	High	High	High	High	High	High	High	High	High	High	High	High	High	High	
60	Risk	Personnel costs, engineering and technical support	If labor resources are not available when needed and there will be higher cost and schedule delay.	2.00	High	High	High	High	High	High	High	High	High	High	High	High	High	High	High	
61	Risk	Personnel costs, engineering and technical support	If labor resources are not available when needed and there will be higher cost and schedule delay.	2.00	High	High	High	High	High	High	High	High	High	High	High	High	High	High	High	
62	Risk	Personnel costs, engineering and technical support	If labor resources are not available when needed and there will be higher cost and schedule delay.	2.00	High	High	High	High	High	High	High	High	High	High	High	High	High	High	High	
63	Risk	Personnel costs, engineering and technical support	If labor resources are not available when needed and there will be higher cost and schedule delay.	2.00	High	High	High	High	High	High	High	High	High	High	High	High	High	High	High	
64	Risk	Personnel costs, engineering and technical support	If labor resources are not available when needed and there will be higher cost and schedule delay.	2.00	High	High	High	High	High	High	High	High	High	High	High	High	High	High	High	
65	Risk	Personnel costs, engineering and technical support	If labor resources are not available when needed and there will be higher cost and schedule delay.	2.00	High	High	High	High	High	High	High	High	High	High	High	High	High	High	High	
66	Risk	Personnel costs, engineering and technical support	If labor resources are not available when needed and there will be higher cost and schedule delay.	2.00	High	High	High	High	High	High	High	High	High	High	High	High	High	High	High	
67	Risk	Personnel costs, engineering and technical support	If labor resources are not available when needed and there will be higher cost and schedule delay.	2.00	High	High	High	High	High	High	High	High	High	High	High	High	High	High	High	
68	Risk	Personnel costs, engineering and technical support	If labor resources are not available when needed and there will be higher cost and schedule delay.	2.00	High	High	High	High	High	High	High	High	High	High	High	High	High	High	High	
69	Risk	Personnel costs, engineering and technical support	If labor resources are not available when needed and there will be higher cost and schedule delay.	2.00	High	High	High	High	High	High	High	High	High	High	High	High	High	High	High	
70	Risk	Personnel costs, engineering and technical support	If labor resources are not available when needed and there will be higher cost and schedule delay.	2.00	High	High	High	High	High	High	High	High	High	High	High	High	High	High	High	
71	Risk	Personnel costs, engineering and technical support	If labor resources are not available when needed and there will be higher cost and schedule delay.	2.00	High	High	High	High	High	High	High	High	High	High	High	High	High	High	High	
72	Risk	Personnel costs, engineering and technical support	If labor resources are not available when needed and there will be higher cost and schedule delay.	2.00	High	High	High	High	High	High	High	High	High	High	High	High	High	High	High	
73	Risk	Personnel costs, engineering and technical support	If labor resources are not available when needed and there will be higher cost and schedule delay.	2.00	High	High	High	High	High	High	High	High	High	High	High	High	High	High	High	
74	Risk	Personnel costs, engineering and technical support	If labor resources are not available when needed and there will be higher cost and schedule delay.	2.00	High	High	High	High	High	High	High	High	High	High	High	High	High	High	High	
75	Risk	Personnel costs, engineering and technical support	If labor resources are not available when needed and there will be higher cost and schedule delay.	2.00	High	High	High	High	High	High	High	High	High	High	High	High	High	High	High	
76	Risk	Personnel costs, engineering and technical support	If labor resources are not available when needed and there will be higher cost and schedule delay.	2.00	High	High	High	High	High	High	High	High	High	High	High	High	High	High	High	
77	Risk	Personnel costs, engineering and technical support	If labor resources are not available when needed and there will be higher cost and schedule delay.	2.00	High	High	High	High	High	High	High	High	High	High	High	High	High	High	High	
78	Risk	Personnel costs, engineering and technical support	If labor resources are not available when needed and there will be higher cost and schedule delay.	2.00	High	High	High	High	High	High	High	High	High	High	High	High	High	High	High	
79	Risk	Personnel costs, engineering and technical support	If labor resources are not available when needed and there will be higher cost and schedule delay.	2.00	High	High	High	High	High	High	High	High								

Figure 8.78: Screenshot of the EEMCal Risk Management Plan and registry.

integrating them into the ePIC workflow.

Collaborators and their role, resources and workforce: Add text here.

Risks and mitigation strategy: Risk planning details are included in the Risk Management Plan and the Risk Registry (see Fig. 8.78). The EEMCAL Risk Registry is a living document used and updated throughout the life of the project. The EEMCAL Risk Registry is reviewed and updated monthly by the EEMCAL Project Team and the Risk owners to reflect any reassessment of risks and opportunities to the project. It contains 14 risks and opportunities. Post mitigation, two of them are considered moderate impact due to the probability of occurrence and impact on cost, schedule, or scope, based on the Risk Matrix analysis. There are two risks on cost with a moderate risk score, but due to the low probability of occurrence, they are in the low-impact category. Post mitigation all risks on schedule and scope are in the low-impact category. In general, the schedule risks are relatively very modest relative to the schedule of the full EIC-DOE project.

Additional Material Add text here.

8.3.5.2 The barrel electromagnetic calorimeter

Requirements

Requirements from physics: The Barrel Electromagnetic Calorimeter (BEMC) must meet the stringent physics requirements set by the EIC program. It needs to identify scattered electrons and measure their energy, particularly in high Q^2 events, and also detect decay electrons from vector or heavy flavor meson decays, as well as DVCS photons (G-DET-ECAL-BAR.1). Electron identification, including electron-pion separation, is required up to 50 GeV and down to 1 GeV (F-DET-ECAL-BAR.1), with an energy resolution better than $10\%/\sqrt{E} \oplus (2-3)\%$ (P-DET-ECAL-BAR.1). Additionally, the BEMC must provide photon reconstruction from 100 MeV to 10 GeV (F-DET-ECAL.9, F-DET-ECAL-BAR.2). The system must also achieve photon-pion discrimination (γ/π^0 separation) up to 10 GeV, with the ability to distinguish two showers with an opening angle

down to 30 mrad (P-DET-ECAL-BAR.3). Furthermore, the BEMC will assist with muon identification (G-DET-ECAL-BAR.3) and provide a charged tracking point behind the DIRC to help with charged hadron PID (P-DET-ECAL-BAR.4), with a spatial resolution of less than 150 μm . Lastly, the system must have sufficient dynamic range to detect MIP signals (P-DET-ECAL-BAR.5).

Requirements from Radiation Hardness: The BEMC must be designed to operate in an environment where it may experience radiation levels of up to about 3.9×10^9 1-MeV neutron equivalent per cm^2 per year of running (6 months), corresponding to full luminosity and background conditions (F-DET-ECAL.6). All components, including sensors, electronics, and structural materials, must be sufficiently radiation-hardened to maintain performance under these conditions. This includes ensuring that the sensor response, energy resolution, and position reconstruction capabilities remain stable throughout the detector's operational lifetime.

Requirements from Data Rates: The BEMC and its readout technology must be designed to handle the high event rates expected at full luminosity, ensuring stable performance under expected background conditions, including radiation doses and neutron flux (F-DET-ECAL.6). The system must provide sufficient timing resolution to accurately discriminate between different bunch crossings (F-DET-ECAL.10), ensuring precise event separation and minimizing pile-up effects. The chosen detector and readout technologies must be capable of processing the high data rates without compromising performance or data integrity.

Based on global ePIC studies on rates from signal and backgrounds [48], the maximum channel rates for the Barrel Imaging Calorimeter are as follows. For electron-proton DIS at 18×275 GeV, the highest rate per channel is 0.66 Hz for the imaging layers and 0.5 Hz for the Pb/ScFi layers. In background simulations, the highest channel rates are achieved for the hadron beam background at 10×275 GeV, reaching approximately 10 Hz for the imaging layers and 8 Hz for the Pb/ScFi. For the 10 GeV electron beam background, the maximum channel rates are about 4.8 Hz and 8.0 Hz, respectively.

Justification

Device concept and technological choice: The ePIC BEMC is called the Barrel Imaging Calorimeter (BIC). The BIC combines two proven technologies to meet the stringent requirements of the EIC physics program. The first is a lead-scintillating fiber (Pb/ScFi) sampling calorimeter, providing robust energy measurement through light collection, based on the well-established GlueX Barrel Calorimeter (BCAL) design. This technology offers a reliable solution for high-resolution energy measurements, benefiting from its extensive use in other experiments.

The second key component is the AstroPix monolithic CMOS silicon sensors, which are interleaved with the Pb/ScFi layers to provide precise 3D imaging of particle showers. This hybrid approach enables excellent spatial resolution and position reconstruction, critical for separating particle showers and achieving the necessary photon and electron identification capabilities. AstroPix sensors, developed for the NASA space mission AMEGO-X, offer low power consumption, radiation tolerance, cost-effectiveness, and scalability, making them ideal for large-area applications in a high-radiation environment. For the AstroPix chip parameters refer to Tab. 8.19.

This combination of Pb/ScFi for energy resolution and AstroPix for spatial resolution was chosen to balance performance, cost-effectiveness, and long-term reliability under the expected operational conditions at the EIC.

Parameter	AMEGO-X Mission Requirements	BIC Requirements
Pixel size	500 μm x 500 μm	same
Power usage	< 1.5 mW/cm ²	\sim 2 mW/cm ² acceptable
Energy resolution	10% @ 60 keV	same
Dynamic range	25-700 keV	same
Passive material	< 5% on the active Si area	same
Time resolution	25 ns	3.125 ns (available in v5)
Si Thickness	500 μm	same

Table 8.19: Comparison of AstroPix requirements for AMEGO-X and BIC.

Subsystem description: The Barrel Imaging Calorimeter (BIC) consists of 48 trapezoidal sectors, with End-of-Sector Boxes (ESBs) at each end for readout. The calorimeter spans 17.1 radiation lengths (X_0) at central pseudorapidity, with the first layer being an AstroPix imaging layer, which provides a tracking point behind the DIRC. Each sector has six slots for AstroPix imaging layers, separated by 1.45 X_0 of Pb/ScFi at $\eta = 0$. In the baseline configuration, slots 1, 3, 4, and 6—counting radially outward—are filled with AstroPix sensors, while slots 2 and 5 are designated for future upgrades. Figure 8.79 presents the overall structure of BIC and its sectors and Fig. 8.80 shows the imaging AstroPix layers components.

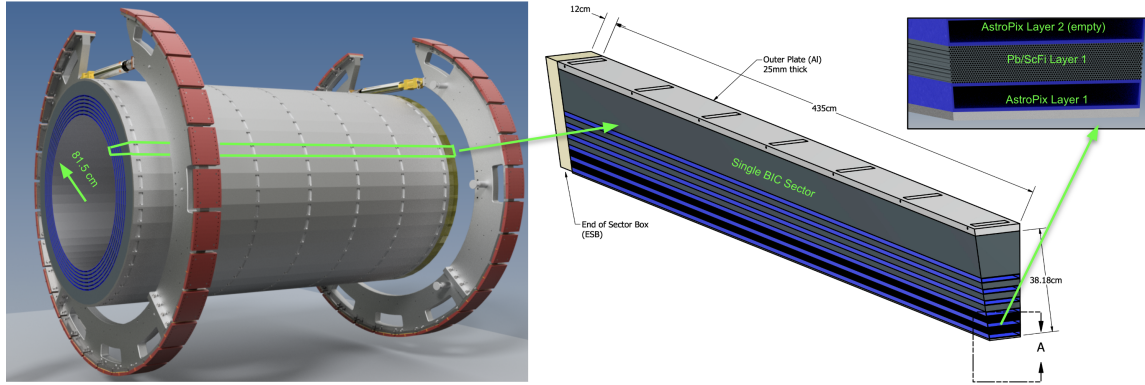


Figure 8.79: Drawing of the Barrel Imaging Calorimeter with its 48 sectors. The central drawing shows the structure of a single sector, featuring interleaved Pb/ScFi layers and slots for trays holding AstroPix chips, followed by the Pb/ScFi bulk section. On the right, a zoomed view of the first radially layers is presented.

Scintillating fibers for Pb/ScFi: The Pb/ScFi calorimeter system is based on the GlueX model with fibers positioned parallel to the z-direction with 2-sided readout for energy measurement and position reconstruction along the fiber. We will use single-clad scintillating fibers with 1 mm diameter embedded in lead and glue to provide reliable energy measurement through light collection.

Sensors for Pb/ScFi: The light from the scintillating fibers is subdivided into 12 rows of 5 columns per sector-end by light guides, which are optically coupled with cookies to the SiPMs. These sensors have a 50 μm pixel pitch to optimize dynamic range and photon detection efficiency.

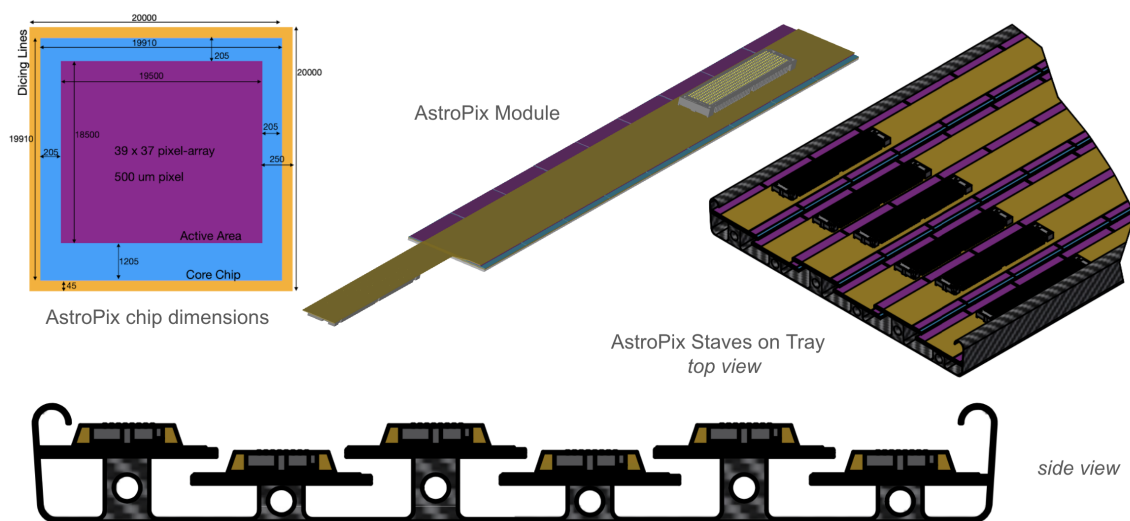


Figure 8.80: Components of Barrel Imaging Calorimeter imaging AstroPix layers.

FEE for Pb/ScFi: The FEE for the Pb/ScFi system, based on the CALOROC ASIC, processes the signals from the SiPMs. It provides sufficient time resolution for determining the z -position of events within the scintillating fiber, while maintaining low noise and high radiation tolerance.

Sensors and modules for imaging layers: The imaging layers use AstroPix monolithic silicon sensors with a $500\ \mu\text{m}$ pixel pitch, interleaved with the Pb/ScFi layers. These sensors are glued on a base plate and daisy-chained on a flexible PCB to form a module containing 9 chips, providing high-resolution spatial information for 3D imaging and particle identification.

Staves and trays: Each stave is formed by daisy-chaining 12 AstroPix sensor modules. A tray holds 6–7 staves based on the layer position, with each tray being half of the sector length and read out at its respective end in the ESB. This modular structure allows for flexible scaling and future upgrades to the system.

End-of-Tray Card (ETC): The ETC functions as the RDO unit in the ePIC DAQ scheme. It manages signal processing, data formatting, and communication with the DAM, ensuring efficient and reliable data flow from the sensors.

Performance Performance of BIC and its components has been tested at the bench and in beam tests at Fermilab Test Beam Facility and Hall D of Jefferson Lab. Selected performance results based on realistic simulations benchmarked against data are presented in this paragraph. Results from the beam and bench tests are covered in the R&D paragraph.

The realistic BIC geometry was implemented, including a detailed Pb/ScFi matrix with single clad fibers embedded in lead and glue, following the GlueX model. The AstroPix layers were implemented as staves, with AstroPix chips placed in realistic dead areas, and materials accounted for the sensors, electronics, cables, insulation, glue, and support structure. Realistic digitization and reconstruction were applied. For the Pb/ScFi component, an effective model for light attenuation in the fibers, photoelectron statistics, light guide efficiency, and SiPM thresholds was implemented

Detector parameters	Value
Active length (z-direction)	435 cm
Inner radius	81.5 cm
Number of sectors	48
η coverage	$-1.71 \lesssim \eta \lesssim 1.31$
Radiation Length X_0	1.45 cm
Total depth in X_0	from 17.1 ($\eta = 0$) to 42 ($\eta = -1.55$)
Molière radius	4.5 cm
Total sampling fraction of Pb/ScFi layers	about 9.5%, see Fig. 8.81
Total sampling fraction of AstroPix layers	< 0.4%
Scintillating fibers	\varnothing 1 mm, single clad fibers
Light guide length	5 cm
Number of light guides	60 per sector per side
Monitoring system	Blue LED, one LED per light guide
SiPMs	1.2×1.2 cm ² arrays, 50 μ m pixel
Number of SiPMs	60 arrays per sector per side

Table 8.20: Selected BIC Parameters.

based on beam and bench measurements as well as optical simulations. For AstroPix, each digitized readout unit corresponds to one pixel, while for the Pb/SciFi component, each readout cell covers the area of one light guide with an attached SiPM. More details about the specific implementations, benchmarks, and simulated performance described in the following paragraphs can be found in the Additional Material.

Energy resolution The energy resolution of the Pb/ScFi layers has been simulated within the full ePIC framework for different rapidity ranges and photon and electron energies. The energy response, corrected for the sampling fraction, was fitted using the Crystal Ball function, and the energy resolution was extracted as the σ of the Gaussian core of the fitted function. The obtained energy resolution is presented in Fig. 8.81 (a) and the results of the fitted stochastic and constant parameters a and b of the energy dependence $\sigma/E = a/\sqrt{E} \oplus b$ are presented in Tab. 8.21. The sampling fraction defined as energy deposited in the scintillating fibers divided by the true energy of generated photons is presented in Fig. 8.81 (b). The contribution of the low-energy tail of the energy losses was quantified and is presented in Additional Material together with the results for electrons. The expected energy resolution fulfills the detector requirements.

η range	a/\sqrt{E} [%]	b [%]
$(-1.7, -1.3)$	6.60 ± 0.03	0.66 ± 0.04
$(-1.3, -0.88)$	6.11 ± 0.01	1.24 ± 0.01
$(-0.88, -0.4)$	5.91 ± 0.02	1.24 ± 0.02
$(-0.4, 0)$	5.85 ± 0.01	0.88 ± 0.02

Table 8.21: Fitted energy resolution parameters for photons in BIC for different η ranges.

Energy response to both electromagnetic and hadronic showers has been also tested in the beam test

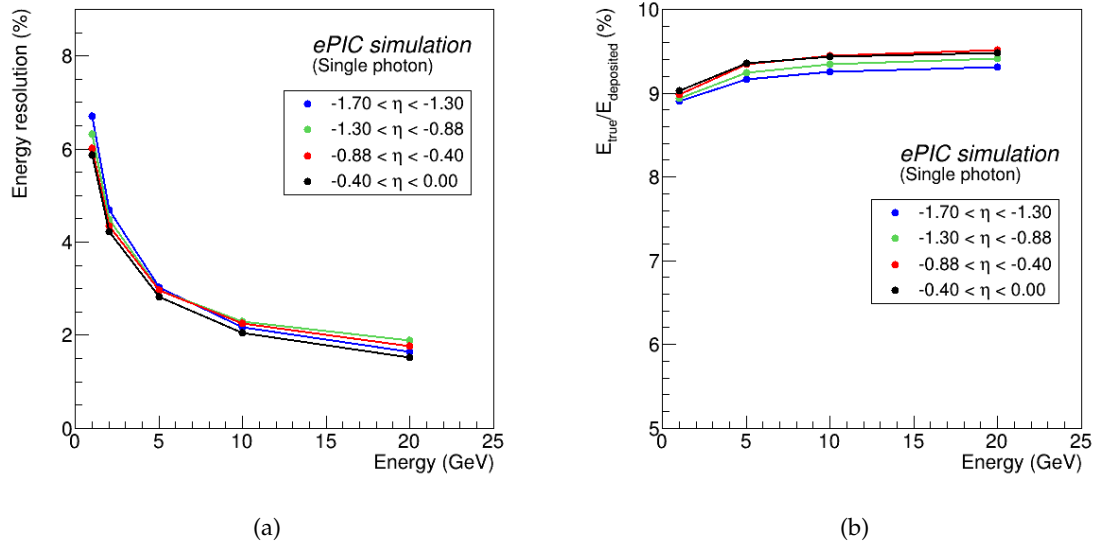


Figure 8.81: (a) Simulated energy resolution in from Pb/ScFi extracted as a σ of the Gaussian core of the Crystal Ball fit to the energy deposits of photons in different rapidity ranges at BIC. Repository to be added. (b) Sampling fraction for photons, defined as energy losses in scintillating fibers divided by the true photon energy, as a function of photon energy in different rapidity ranges. Repository to be added.

environment with a 60 cm long and $15.5 X_0$ deep Pb/ScFi bulk-section prototype based on GlueX BCAL geometry, termed *Baby BCAL*. At Hall D of Jefferson Lab, Baby BCAL was exposed to 3-6 GeV positrons hitting it at different impact angle and position depending on beam energy. Figure 8.82 (a) presents the measured energy resolution measured in those conditions. Note that the highest energy points reflect positrons hitting the prototype close to the end and at the impact angle that causes partial shower leakage. At Fermilab Test Beam Facility, Baby BCAL was exposed to mixed electron-pion-muon beam at energies of 4, 6, 8 and 10 GeV. The energy response to pion beam has been benchmarked in simulation of Baby BCAL implemented in ePIC environment, same as used for the BIC simulations. Fig. 8.82 (b) shows comparison between collected data and simulations benchmarking their realism.

Angular resolution The angular resolution for photons has been estimated using the AstroPix layers, based on full detector simulations across different rapidity ranges as a function of energy. The difference between the true and reconstructed azimuthal (θ) and polar (ϕ) angles has been extracted to assess the resolution as full-width-at-half-maximum (FWHM). In the current reconstruction algorithm, the angles are reconstructed from the hit with the maximal energy deposit in the AstroPix layer where the shower started. The resolutions for θ and ϕ are presented in Fig. 8.83. The results indicate a small dependence of the angular resolution on η . In all regions, the angular resolution remains well below 0.1 degrees, which is on the level of single pixel resolution. The example fit of the θ resolution in the rapidity region of $-0.88 < \eta < -0.4$ gives $(0.040 \pm 0.004) \text{ deg}/\sqrt{E} \oplus (0.016 \pm 0.003) \text{ mm}$. The ϕ resolution is worse than the θ resolution due to the smearing of shower particles by the magnetic field. Overall, the results show significantly better performance than what can be achieved with any tower-like calorimetry systems and fulfills the requirements for the barrel electromagnetic calorimetry for the EIC.

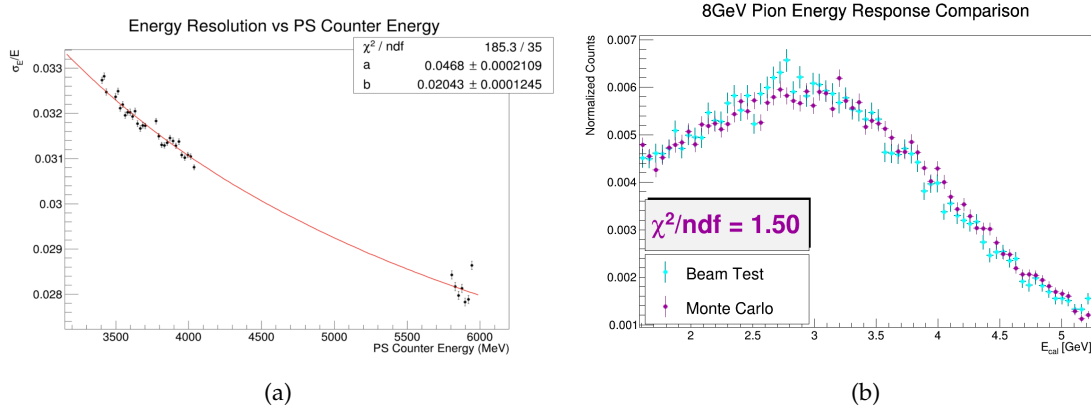


Figure 8.82: (a) Preliminary energy resolution of Baby BCAL exposed to 3–6 GeV positrons at Hall D of Jefferson Lab, with varying impact angles and positions depending on beam energy. The highest energy points correspond to positrons striking near the end of the prototype and at angles causing partial shower leakage. Red line shows the fitted function $\sigma/E = a/\sqrt{E} \oplus b$. Repository to be added (b) Preliminary energy response of Baby BCAL to an 8 GeV pion beam at the Fermilab Test Beam Facility. The plot compares the collected data (light blue) with simulations (purple) implemented in the ePIC environment, as used for BIC simulations, benchmarking the realism of the simulation model. Repository to be added.

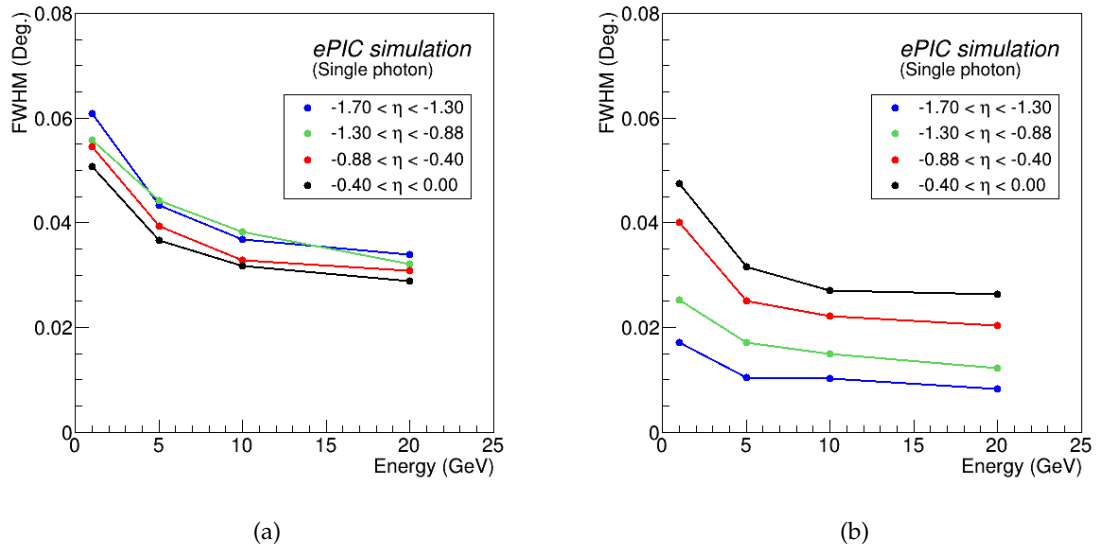


Figure 8.83: Simulated angular resolution for photons at different energies for the ϕ (a) and θ (b) angles reconstructed from the maximal-energy pixel from the first AstroPix layer where the shower started. The resolution is taken as FWHM from the distribution of the difference between true and reconstructed angle. Repository to be added.

Particle identification The design of the barrel calorimeter aims to provide high π^-/e^- separation, particularly in the momentum region below 5 GeV. The AstroPix layers capture snapshots of electromagnetic and hadronic showers, allowing for the reconstruction of a 3-dimensional profile of the shower development, supported by the longitudinal energy profiles from the Pb/ScFi layers. A deep-learning algorithm is employed alongside the traditional E/p cut to achieve accurate electron identification, meeting the detector requirements.

Charged pion rejection is carried out in a two-step process. First, an E/p cut is applied to the cumulative energy deposit in the Pb/ScFi layers. This cut is deliberately loosened to ensure high electron efficiency. The "cleaned" samples, following the E/p cut, are then fed into a classification neural network for supervised training to distinguish between electrons and pions. We used a 10-layer Visual Geometry Group-style Convolutional Neural Network to analyze combined AstroPix and Pb/ScFi data. The network utilizes energy and position features from both technologies capturing energy and spatial shower details. Future improvements may come from using Graph Neural Networks or Point Clouds.

The charged pion suppression factor for $\eta = 0$ rapidity is shown in Fig.8.84 (a), for a target 95% electron efficiency. The rejection exceeds 10^3 at low to mid energies, where rejection is most critical. For comparison, results from the upgraded system with six imaging layers are also presented.

The upper limit of the probability of merging two γ s from a π^0 decay into one cluster at $\eta = 0$ is shown in Fig. 8.84 (b). Neutral pions decaying into two γ s were simulated with various momenta. In different calorimeter technologies based on tower geometry, as outlined in the EIC Yellow Report [4], the separation criterion requires that the two γ s be separated by at least one tower size. However, for the BIC technology, which uses granular position information from AstroPix, a different criterion has been established. The probability of merging two γ s was determined using a separation of 6 times the FWHM of the shower profile, measured at the third imaging layer (where more than 90% of photons with energies above 0.5 GeV register at least one hit), providing a conservative estimate.

The upper limit for γ/π^0 separation is expected to be well above 10 GeV, based on studies incorporating AstroPix's position resolution and shower profile data. Additionally, initial results from a neural network approach, similar to the e/π studies but simplified for neutral pion identification, were applied using full detector simulations. Preliminary results suggest a pion rejection rate of approximately 82% at 90% electron efficiency for 10 GeV pions, based on the current status of model training.

Low energy response The performance of the Barrel Imaging Calorimeter (BIC) for detecting minimum ionizing particles (MIPs) was evaluated through simulations using 5 GeV muons at various rapidities. The deposited energy per readout cell, represented by the most probable value of the MIP peak, was extracted from simulations with Single-Clad Kuraray fibers that meet the FDR fiber specifications. This was compared against the 4-sigma pedestal peak from S14161-3050-04 SiPM array simulations, which also fulfill FDR specifications. Even with the dark count rate corresponding to the irradiation level of 1×10^9 1-MeV neq/cm², the MIP signal remains well-detectable with a 4-sigma cut on the pedestal. Figure 8.85 shows the extracted most probable value (MPV) of the MIP peak in terms of the number of photoelectrons (nphe) for muons at $\eta = 0$, which is the case where we observe the least photoelectrons from muons due to the combination of the distance the light has to travel in the fibers and the energy muons deposit at this angle in one Pb/ScFi layer. The pedestal 4-sigma value is marked in red. An example pedestal and MIP signal spectrum for 9 and 12 phe MIP signals, showing the worst-case scenario for the back Pb/ScFi layer of the BIC, is also presented.

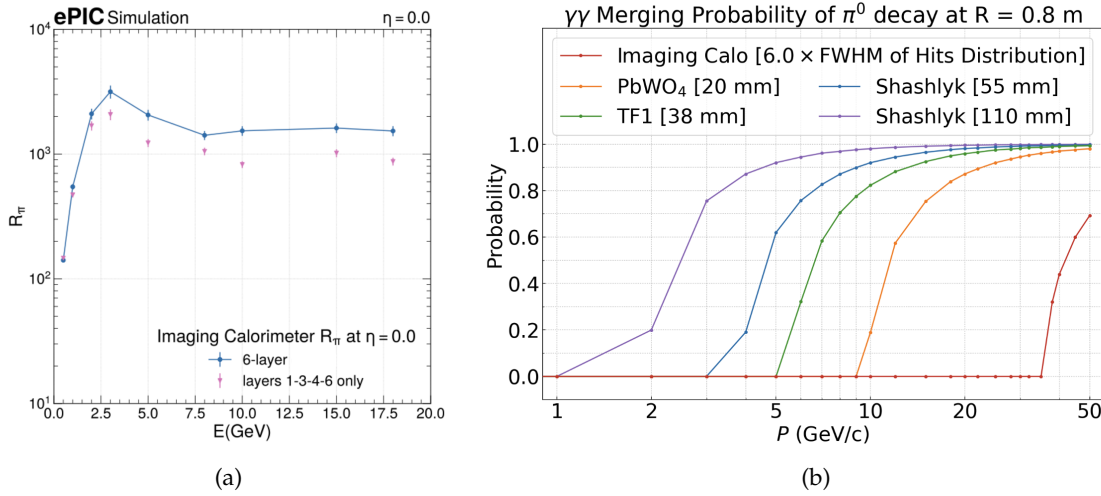


Figure 8.84: Simulated performance on particle identification from BIC. (a) The charged pion suppression factor for $\eta = 0$ rapidity for 95% electron efficiency as a function of particle energy E . Pink points show the baseline performance where slots 1, 3, 4, and 6, counting radially, of imaging layers are filled with AstroPix trays, blue points show performance with 6 imaging layers. Repository to be added. (b) Upper limit on cluster merging at $\eta = 0$ (shortest distance for particles to travel about 80 cm) from 2 photons from π^0 decay at particular π^0 momentum P . For calorimeter technologies based on tower geometry from [4] the separation by at least one tower size is required. For BIC the separation based on shower profile was assumed (see text). Repository to be added. (To be replaced by the NN results with full simulation when ready)

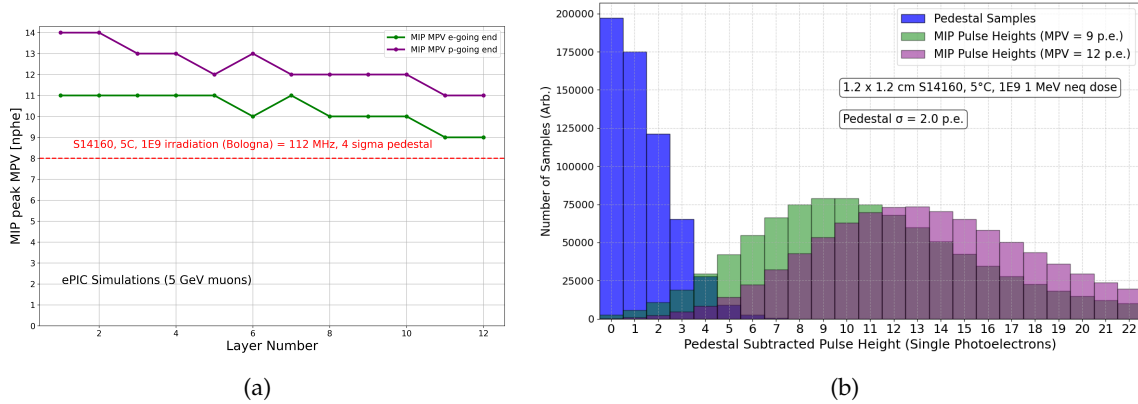


Figure 8.85: Simulated performance on MIP response in BIC. (a) The most probable value of the MIP peak in terms of the number of photoelectrons for 5 GeV muons at $\eta = 0$ at each of the BIC layers. The red line corresponds to 4 sigma of the pedestal simulated with realistic S14160 family SiPM responses at 5 degrees Celsius, irradiated with a dose of 1×10^9 1-MeV neq/cm². The green line corresponds to the electron-going end, while the purple line corresponds to the proton-going end readout cells. Repository to be added. (b) An example spectrum of the pedestal and MIP pulses at 9 and 12 phe signals, showing the worst-case scenario from plot (a) for the back Pb/ScFi layer of the BIC at $\eta = 0$. Repository to be added.

AstroPix chip performance studies The AstroPix chip has been extensively tested in both bench and beam environments. The AstroPix.v3, the first full-size chip with a 500 μm pixel pitch and row-and-column readout (35 rows and columns in a strip-like format), has demonstrated strong performance, as summarized, for example, in [49]. Key tests included a noise study and a radiation source test. In the noise study, less than 0.5% of the pixels exhibited a noise rate exceeding 2 Hz, with the chip's dynamic range starting at 25 keV, allowing thresholds over 200 mV above the baseline. These results meet the BIC's requirements for low energy thresholds and masked pixel yield. The radiation source test, using isotopes with calibration points ranging from 22.2 keV to 122 keV, as shown in Fig. 8.86, showed that 44% of pixels met the 10% energy resolution requirement at 59.5 keV, and 92.4% of pixels achieved the required 25 keV sensitivity for BIC. Although the AstroPix.v3 chip is not fully depleted, it demonstrated promising performance. The upcoming AstroPix.v5, designed with a dynamic range extending to 700 keV, is expected to meet energy resolution requirements for all pixels.

Beam tests at Fermilab further validated the AstroPix.v3 chip in both single- and double-layer configurations. In the single-layer test, data collected with a 120 GeV proton beam was used to match corresponding row and column hits, using matching timestamps and ToT to reveal a hit map that showed the proton beam profile presented in Fig. 8.86. Although the AstroPix.v3 does not yet have pixel-level granularity (which is implemented in AstroPix.v4 and higher), it demonstrated a pixel-level position resolution. In the double-layer configuration, two daisy-chained layers of AstroPix.v3 were tested, successfully reading events in coincidence and pinpointing hit pixel locations, providing a proof-of-concept for layer integration in a beam environment.

The characterization of AstroPix.v3 is ongoing, with specific tests designed to meet the ePIC detector requirements. Results show the chip is well-suited for the Barrel Imaging Calorimeter (BIC) and aligns with project goals. Remaining improvements, including enhanced dynamic range and energy resolution, will be addressed in the upcoming AstroPix.v5, which is expected to be fabricated by early 2025.

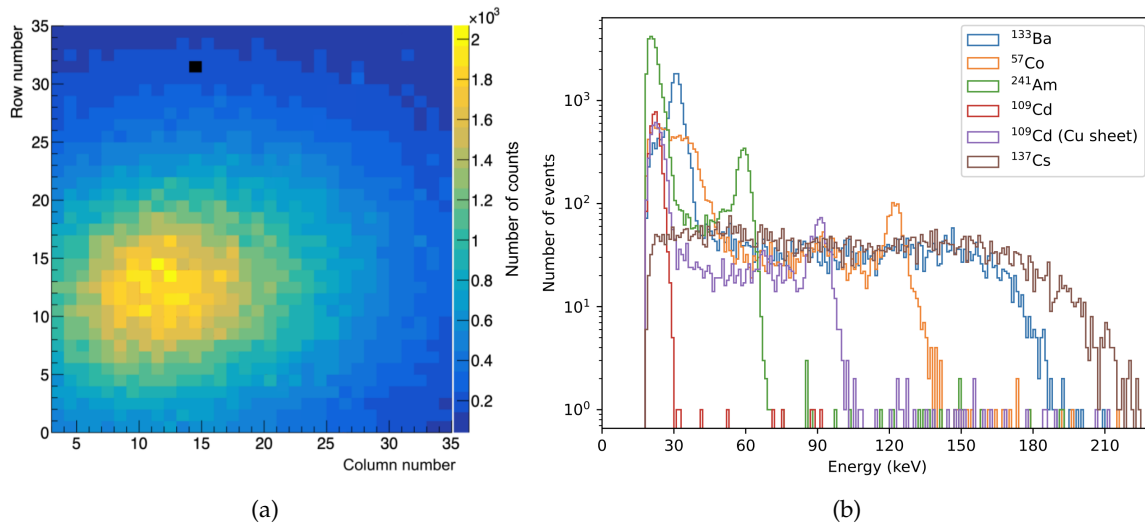


Figure 8.86: (a) Beam hit map recorded in the 120 GeV proton run in Fermilab Test Beam Facility with a AstroPix.v3 chip. The masked pixel has been marked in black. Repository to be added.(b) Calibrated energy responses from an example pixel of a AstroPix.v3 chip. Plot from [49].

4145 Implementation

4146 **Subsystem mechanics and integration:** The 48 BIC sectors are arranged in a self-supporting
 4147 Roman arch configuration. Once assembled, the full calorimeter is supported by the solenoid cryo-
 4148 stat support rings. In the hadron-going direction, a small gap must be bridged between the end of
 4149 the BIC and the support ring, while in the lepton-going direction, the system slightly overhangs,
 4150 creating a cantilevered structure.

4151 A BIC sector consists of six carbon fiber frames for the imaging layers, interleaved with five single
 4152 layers of a Pb/ScFi matrix (17 fibers tall), followed by a bulk segment consisting of seven Pb/ScFi
 4153 matrix layers. The back of the sector consists of an aluminum support plate with connectors de-
 4154 signed to link the sectors together, affix the ESB, and integrate with the global BIC support structure.
 4155 The sector is constructed as a monolith, with all components epoxied together to ensure structural
 4156 integrity.

4157 The inner face of each BIC sector consists of a 0.5 cm thick aluminum plate, designed to connect the
 4158 inner support rails to the detector. The inner support rails hold the inner detector support structure,
 4159 maximizing the use of available space while avoiding obstruction of the ESBs (the readout boxes),
 4160 ensuring that individual imaging layers can be added or removed as necessary for future upgrades
 4161 or servicing. Hence, the BIC plays a critical role in supporting the overall inner detector structure.

4162 Detailed FEA to validate the mechanical integrity of the sector design is ongoing. The design of
 4163 the support that connects the BIC to the solenoid cryostat support rings is still under development,
 4164 ensuring it meets the mechanical stability requirements while maintaining accessibility to readout
 4165 electronics and other critical components.

4166 **Calibration, alignment and monitoring:** The BIC calibration approach treats the Pb/ScFi and
 4167 AstroPix imaging layers as two separate systems, each calibrated independently. For the Pb/ScFi
 4168 calorimeter, we will follow well-established in-situ calibration methods, starting with MIP-based
 4169 calibration, then refining with meson decays, electrons, and kinematic techniques derived from
 4170 experiences with GlueX and HERA experiments. The energy calibration is further refined using
 4171 decay photons from neutral pion events ($\pi^0 \rightarrow \gamma\gamma$).

4172 For the AstroPix layers, the calibration process occurs in three steps. First, an absolute pixel energy
 4173 calibration is performed during stave assembly using a radioactive source. Next, in-situ position
 4174 and alignment calibration will be conducted similarly to standard tracker procedures, utilizing
 4175 cosmics. Finally, the overall imaging cluster energy calibration will be matched with the Pb/ScFi
 4176 calorimeter, leveraging the energy reconstruction methods described above.

4177 Metrology will be used for alignment during installation, though very precise alignment is not
 4178 critical, given the calorimeter's purpose. Cosmic and physics events will be used to calibrate the
 4179 relative positioning of detectors and sensors, ensuring accurate reconstruction.

4180 Calibration stability during operation will be ensured by using LED-based relative light monitoring
 4181 systems for continuous monitoring, along with additional checks on linearity and timing using
 4182 both cosmics and dedicated calibration runs.

4183 **Services:** The Pb/ScFi part of BIC, which utilizes SiPMs, requires two LV lines (plus ground) of
 4184 1.2 V and 2.5 V for each H2GCROC3-based front-end board (FEB), along with one HV line (plus
 4185 ground) operating at less than 50V for biasing SiPMs. The system features a total of 5,760 readout
 4186 channels distributed across 48 sectors, with one FEB per sector per side, each managing 60 readout

channels. Each FEB is connected to the RDO through four lines: two data lines, one clock line, and one slow control line, and 1 RDO maintains 24 FEBs.

For the AstroPix sensor layers, the LV services include 1.8 V and 1.2 V to power the analog part of the chip, along with 1.2 V for the digital part of the chip, and the HV of 200-400 V distributed to each stave. Each stave within an AstroPix tray connects to the data acquisition system through a FPGA-based End-of-Stave Card (one per tray), which is connected to DAM via an optical link. In total, each sector will include 27 staves per side. The ETC will be powered through Power over Ethernet (PoE) within the control cable.

The SiPMs require cooling to maintain a temperature of 5°C. Each ESB will have in/out lines for cooling water and a dry air system to prevent condensation. The estimated heat load per ESB is projected to be under 100 W, necessitating effective heat management. Liquid water cooling will be utilized for the SiPMs, their readout boards, and the ETCs. AstroPix sensors are highly heat efficient, consuming less than 2 mW/cm². The baseline cooling strategy involves thermal coupling to dissipate heat through the staves and trays, with cooling occurring at the edges along with the ETCs. If additional cooling is required, circulating liquid through the staves will be employed as a mitigation measure. A preliminary cooling design is expected by May 2025 as part of the Cooling FEA in the PED phase.

Status and remaining design effort: High-level schedule for the BIC design and production phase is available in Additional Material (See Fig. 8.87)

R&D effort: The R&D efforts for BIC focus on demonstrating the combined performance of Pb/SciFi and AstroPix in EIC-like environments. This involves measuring higher than GlueX energy response up to about 10 GeV, benchmarking high-energy electron and pion simulations, testing AstroPix in high-rate environments, and integrating the Pb/SciFi with AstroPix sensor layers. In FY23, responses to 6 GeV positrons in 60 cm long Pb/SciFi prototype were measured in Hall D of Jefferson Lab, showing a constant term of about 2%, consistent with simulations. The Baby BCAL was commissioned with proton, pion, and electron beams during a June 2024 FBTF test, where data collected allowed for pion simulation benchmarking. A proof-of-concept synchronization of AstroPix with Baby BCAL was achieved by triggering on the AstroPix analog signal. With extensive data from previous AstroPix tests in FY23, the R&D is ready for multi-layer beam tests, to be conducted in early FY25 pending delays at FTBF.

E&D status and outlook: The Project Engineering Design phase of our project that started with granting the funding to the participating institutions starting Q4 2024, encompasses a detailed roadmap for the design, testing, and integration of key components for BIC. Early milestones focus on the design and development of the Pb/SciFi sector, including short and long test articles and the structural framework needed for housing these components. Alongside this, efforts are directed toward the design and prototyping of the end-of-sector box, which includes light guide and light monitoring systems integration. The tracking layer, which features AstroPix sensors, undergoes simultaneous development. This includes performance characterization of the AstroPix chips, module design and assembly, and testing of components such as bus tapes and end-of-tray cards. By mid-PED-phase, both the Pb/SciFi and tracking layers will undergo rigorous integration testing to ensure seamless functionality within the full detector system. The final phase focuses on validating the designs and performing full integration testing of staves, modules, and tracking layers. Quality control procedures will be established for each component, ensuring that everything meets performance specifications before final assembly. The PED phase is expected to finish in Q1 2026.

Other activity needed for the design completion: Within the small-scale R&D and design funding in Korea, a focused effort is underway during the period from August 2024 to April 2027, covering the PED phase and pre-production phase. The primary objectives include the development of testing and assembly systems for the AstroPix chip, particularly emphasizing automatic wafer testing and module assembly. Additionally, this work involves designing the readout box for the Pb/SciFi system and producing test modules to conduct performance studies.

Status of maturity of the subsystem: The maturity of BIC is currently estimated to be between 30% and 60%, depending on the specific component. The entire BIC underwent an incremental Preliminary Design Review (PDR2) in September 2024. Scintillating fibers and SiPMs have reached the final design stage, as they are classified as long-lead procurement items. Recognizing the extensive requirements for these materials—around 4500 km of scintillating fibers and a large quantity of SiPMs for ePIC—the project identified the need for early procurement. The Final Design Reviews (FDR) for both the scintillating fibers and SiPMs were successfully passed in September 2023. The first portion of the scintillating fibers was included in CD3a, with further procurement scheduled for CD3b. Vendor selection is nearly complete, and the first long-lead orders are expected by Spring 2025.

Construction and assembly planning:

Pb/SciFi Sectors Construction: The production of Pb/SciFi sectors will take place at Argonne, where there will be two production lines. The sectors will be constructed by embedding single-clad scintillating fibers in lead sheets, arranged in a stepped “Mayan pyramid” configuration, following the GlueX model. Carbon fiber frames will be integrated with the sector as it is built, with each frame assembled from two C-channel-like sides and a top and bottom plate. The sector construction process will proceed at a pace of 0.5 to 1 matrix layer per day, with the ability to build two sectors in parallel. Once a sector is fully assembled, it will be sent to an external machine shop for precise machining. Upon return to Argonne, the sector will undergo metrology and QC before being prepared for shipment to BNL.

ESB Manufacturing: The construction process for the ESB is still in development. ESB construction will include large-scale SiPM testing, SiPM mounting, light-guide manufacturing, light-monitoring system integration, construction of structural and cooling components, and manufacturing of electronics boards. There will be at least two ESB production sites: one in Canada at U. Regina and one in Korea. As the procedure is finalized, further details on assembly and integration will be specified.

AstroPix Wafers: The AstroPix wafers will be produced at the AMS foundry. Due to the large scale of the detector, automatic wafer-level testing will be conducted at two sites: PNU (South Korea) and Argonne. This testing will ensure the functionality of each chip before dicing, including measurements of pixel performance, noise levels, and defect detection early in the production process. After testing, the wafers will be diced into individual AstroPix chips.

AstroPix Modules and Trays: AstroPix chips will be assembled into modules at three production sites: Argonne, UC Santa Cruz, and PNU (South Korea). Each module will consist of nine AstroPix chips, daisy-chained on flexible PCBs. After assembly, each module will undergo initial testing to ensure proper chip-to-chip communication, pixel functionality, and noise levels. Modules that pass this stage will be integrated into staves, with 12 modules per staff. To keep the production process scalable and efficient, only one flavor of staff will be used across the entire system. The staves will then undergo additional QC testing. Once validated, the staves will be integrated into trays. There are two flavors of trays: one for the

hadron-going side and the other for the lepton-going side of the detector, with each being a mirror image of the other. Each tray will contain 6–7 staves. These trays will then undergo final QC prior to shipping to BNL. The entire production and QC procedure is designed to catch any defects early and ensure that the trays are fully operational before final integration into the BIC sectors.

Assembly Planning: The assembly of the BIC will follow a carefully planned sequence. Upon arrival at the integration site, the Pb/ScFi sectors will be unpacked and prepared for assembly. The first step will involve attaching the light guides to the sectors. Once the initial sectors have been prepared, we can begin the barrel assembly while continuing to unpack and attach light guides to the remaining sectors. The BIC barrel will be assembled next to the solenoid and then inserted into the solenoid using existing sPHENIX tooling. Following the installation of the barrel, the imaging layer trays will be inserted using specialized tooling that is still under development. After all trays are installed, the electrical and cooling connections will be made, and the rest of the ESB will be installed to complete the installation. This phased approach ensures that all components are properly integrated before the system is brought online for testing.

Quality Control (QC) Planning: QC will be implemented at multiple stages of the BIC production and assembly process to ensure system integrity and performance. The system, particularly the imaging layers, is designed with both modularity and scalability in mind, allowing for efficient production, easier upgrades, and reworkability. Key QC procedures include:

Pb/ScFi Sector Assembly: The Pb/ScFi sectors will undergo thorough inspection during assembly. Scintillating fibers and lead sheets will be inspected for defects before embedding. After each matrix layer is completed, visual and metrological inspections will ensure proper alignment and uniformity. Final metrology checks will be performed after external machining to confirm dimensions prior to shipment.

AstroPix Wafer Testing: Automatic wafer-level testing will be conducted to assess chip functionality, including pixel performance, noise levels, and defect detection. Once tested, wafers will be diced, followed by additional electrical tests on individual AstroPix chips to ensure reliability before moving to the module assembly phase.

Module and Tray QC: Modules will be assembled from AstroPix chips and undergo functional tests to verify chip-to-chip communication, pixel functionality, and noise levels. Defective modules will be identified and replaced before progressing to stave assembly. Staves will be tested for electrical continuity, power consumption, and thermal performance under load. QC for staves and trays will use the actual readout electronics (ETC) to perform these tests. Once integrated into trays, final testing will check for alignment, electronic connectivity, and cooling performance, ensuring that trays operate as intended under operational conditions.

ESB QC: SiPMs will undergo rigorous testing to ensure proper photon detection efficiency, dark count rates, and timing precision before being integrated into the ESB. ESB integration with the sector first article will test the complete system, including electrical connections, data acquisition, and cooling systems, to ensure seamless functionality with the Pb/ScFi sectors.

Final Integration and Barrel Assembly: After attaching light guides to the Pb/ScFi sectors, alignment and metrology checks will be conducted during barrel assembly to ensure sector and tray alignment within tolerances. Electrical and cooling system checks will be completed

4324 post-installation to confirm proper functionality. System-wide tests, including cosmic ray
4325 runs and electronic readout, will validate the entire system before commissioning.

4326 **Environmental, Safety and Health (ES&H) aspects** The BIC design incorporates standard
4327 safety and environmental practices across all production sites. We will strive for standardized
4328 safety protocols while adhering to internal work planning and control processes at each institu-
4329 tion to identify hazards, implement mitigations, and document safety procedures. Main hazards
4330 associated with the BIC include:

4331 **Lead handling:** The handling of lead sheets for the Pb/ScFi matrix requires careful consider-
4332 ation. We are working closely with experts to determine the appropriate safety steps. These
4333 steps may include specific protocols to mitigate any hazards and the potential enrollment of
4334 personnel in continuous health monitoring programs to ensure long-term safety.

4335 **Epoxy usage:** Standard procedures for handling, mixing, and applying epoxy will be fol-
4336 lowed, with work conducted in fume hoods to ensure safety. Part of our PED work aims to
4337 deploy a custom mixing nozzle to reduce air contaminants and epoxy waste while improving
4338 consistency in the application process.

4339 **Scintillating fibers:** The fibers are made of flammable polystyrene, and with the total fiber
4340 mass exceeding 3.9 tons, proper fire safety measures and storage protocols are essential.

4341 **Pinch/nip hazards:** Automated systems, such as robots for wafer probing, pick-and-place,
4342 and glue application, present pinch hazards. Controls, such as guards and procedures, will
4343 be in place to mitigate these risks.

4344 **Crush hazards:** The use of presses and swaging equipment introduces crush hazards during
4345 assembly processes. Strict safety protocols, including the use of guards and operator training,
4346 will mitigate these risks.

4347 **Radioactive sources:** The use of radioactive sources for calibration introduces additional
4348 handling requirements, and proper shielding and storage protocols will be implemented as
4349 necessary.

4350 **Electrical safety:** Electrical safety procedures will also be applied for all electronics and
4351 power systems associated with the BIC production tooling and detector components.

4352 **Collaborators and their role, resources and workforce:** The full BIC WBS org chart is avail-
4353 able in Additional Material (see Fig. 8.90). BIC is supported by a diverse and robust international
4354 collaboration, with institutions from the United States, Canada, Korea, and Germany. These col-
4355 laborators bring together a wealth of expertise and resources, working collectively to advance the
4356 development of the BIC.

4357 In the United States, several institutions play a key role across multiple aspects of the project. Ar-
4358 gon National Laboratory is leading several crucial areas, including the design and assembly of
4359 modules and staves, sector production, cooling systems, and system testing and QC, while also
4360 overseeing the software, simulation, and benchmarks. Oklahoma State University leads efforts on
4361 stave bus assembly, and the University of California, Santa Cruz (UCSC) supports module design
4362 and assembly efforts. NASA Goddard Space Flight Center (GSFC) contributes via the ETC compo-
4363 nents, ensuring that electronic testing is integrated into the system.

4364 Canadian institutions play a critical role, especially in the production and quality control of ESB.
4365 The University of Regina contributes to multiple efforts, including the QC of scintillating fibers,

SiPM integration, light guides, and electrical design, while also contributing to the system's demonstration and testing. The University of Manitoba provides leadership in cooling system development and supports the SiPM integration efforts. Mount Allison University focuses on ESB production, aiding in the overall electronics support infrastructure.

Korean institutions are heavily involved in various production, design, and testing processes. Collaborators from Kyungpook National University (KNU) support both electronics and SiPM integration. Yonsei University plays a key role in the sector production process and testing, while Sungkyunkwan University (SKKU) focuses on sector development and production. Pusan National University (PNU) leads efforts on wafer testing and supports software development and simulation. Additionally, Hanyang University, Korea University, and other Korean institutions provide significant contributions across assembly, installation, and testing.

The Karlsruhe Institute of Technology (KIT, Germany) provides essential AstroPix chip support.

Risks and mitigation strategy: As outlined in the Construction and assembly planning paragraph, in the default scenario, sector production will take place at Argonne using two production lines, with one staffed by Korean collaborators. ESB production and quality control will be managed by Canada and Korea. Wafer testing will occur in both Korea and the US. AstroPix module and stave production will be distributed across three or more sites in the US and Korea. Depending on the level of in-kind funding, the baseline plan is to produce four to six layers. In the unlikely event of no in-kind funding from Canada and Korea, the project will cover all sector production labor costs, including Korean collaborators, and consolidate production to a single ESB site (Canada) and a single wafer testing site (US). AstroPix module/stave production will be limited to two sites in the US, requiring an increased workforce at each site or potentially facing a one-year delay to deliver the four baseline layers.

A potential risk in the production of AstroPix chips is related to the feasibility of using 12-inch wafers, which offer a more modern and cost-effective solution. However, if this option proves unviable, we will need to use 8-inch wafers, which would increase production costs. To mitigate this, we aim to offset the higher costs through in-kind contributions from collaborators.

Additional Material

Subsystem description

- More detailed description of subsystems: sector, ESB, tray, module, chip
- More details on AstroPix chip with timelines
- More details on SiPMs
- More details on readout scheme ETC and CALOROC

Schedule

- High-level BIC Schedule

Performance

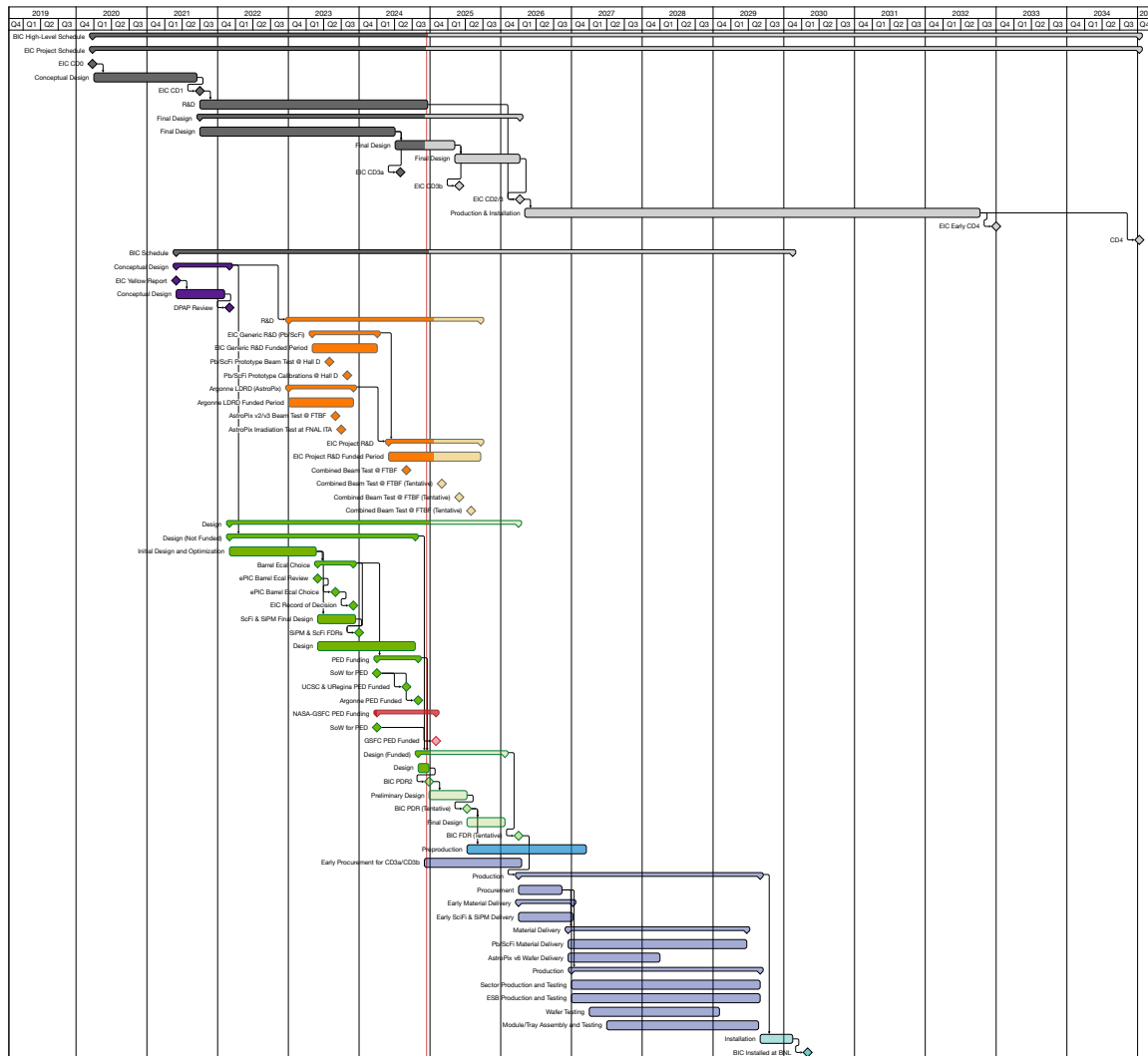


Figure 8.87: Barrel Imaging Calorimeter high-level schedule for design and production phases. (Updates expected)

4402 Realism of simulations

- 4403 • Geometry implementation description
- 4404 • How light response is simulated: folded in measurements of $n_{\text{phe}}/\text{GeV}$, fiber attenuation
- 4405 length, simulations of light guides and optical cookie, SiMP PDE and simulations
- 4406 • Comparison of data from beam tests and simulations benchmarking their realism: response
- 4407 to electrons and pions

4408 Energy resolution

- 4409 • Evaluation of the energy response tail

- Simulated energy response to electrons
- Energy resolution for low energy photons
- Energy resolution from FTBF FY24 beam test.

The contribution of the low-energy tail of the energy losses was quantified by calculating the difference between the area under the fitted Crystal Ball function and that of its Gaussian core marked in red in Fig. 8.88 (a). The tail contribution to the overall energy loss area is shown in Fig. 8.88 (b) and (c) for electrons and photons, respectively. The results of energy resolution and total sampling fraction as a function of energy for electrons is presented in Fig. 8.89.

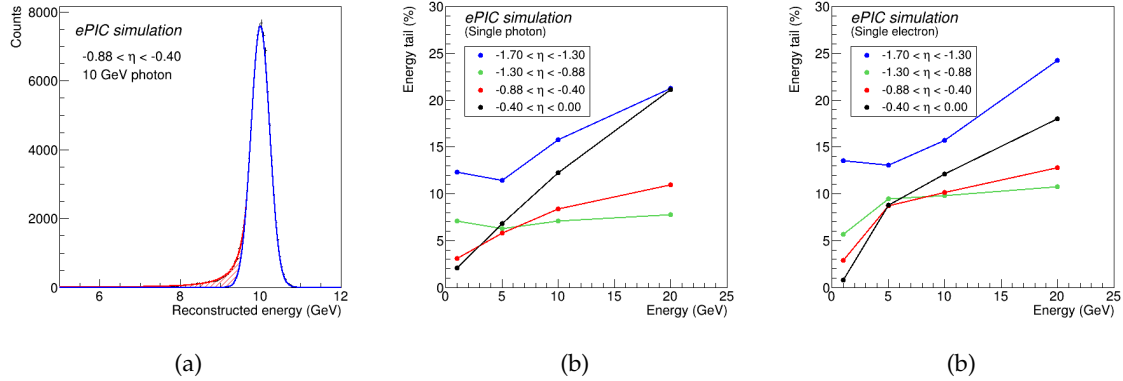


Figure 8.88: (a) Simulated energy losses in scintillating fibers of BIC for 10 GeV photons in the rapidity range $-0.88 < \eta < -0.4$. The distribution has been fitted with the Crystal Ball function; the Gaussian core of the function is marked in blue, and the power-law tail area is marked in red. (b) Percentage contribution of the low-energy tail-red area in plot (a)-to the overall area under the Crystal Ball fit to the energy losses of photon in Pb/ScFi as a function of photon energy and rapidity. (c) Same as (b) but for electrons.

4417

4418 Particle identification

- More details about the NN methodology
- Performance for different rapidity ranges and electron efficiencies
- Muon detection efficiency

For our π^-/e^- separation studies, we utilized a 10-layer Visual Geometry Group (VGG)-style Convolutional Neural Network (CNN) to process combined data from the AstroPix and Pb/ScFi parts of the calorimeter. This CNN architecture consists of 5 convolutional layers interspersed with 2 pooling layers, followed by 3 fully connected (dense) layers. Each event is formatted into an input array with dimensions $N_{\text{layers}} \times N_{\text{hits}} \times N_{\text{features}}$, where 4 primary features: energy deposit, η , ϕ , and radial position of the hit inside the calorimeter, to capture both energy deposition and spatial information about the particle shower.

We trained the network using supervised learning with a data set composed of a 10:1 ratio of pions to electrons. This ensured a sufficient number of pions remained after applying the energy-over-momentum (E/p) cut, which was crucial for training accuracy. Each training cycle consisted of 20

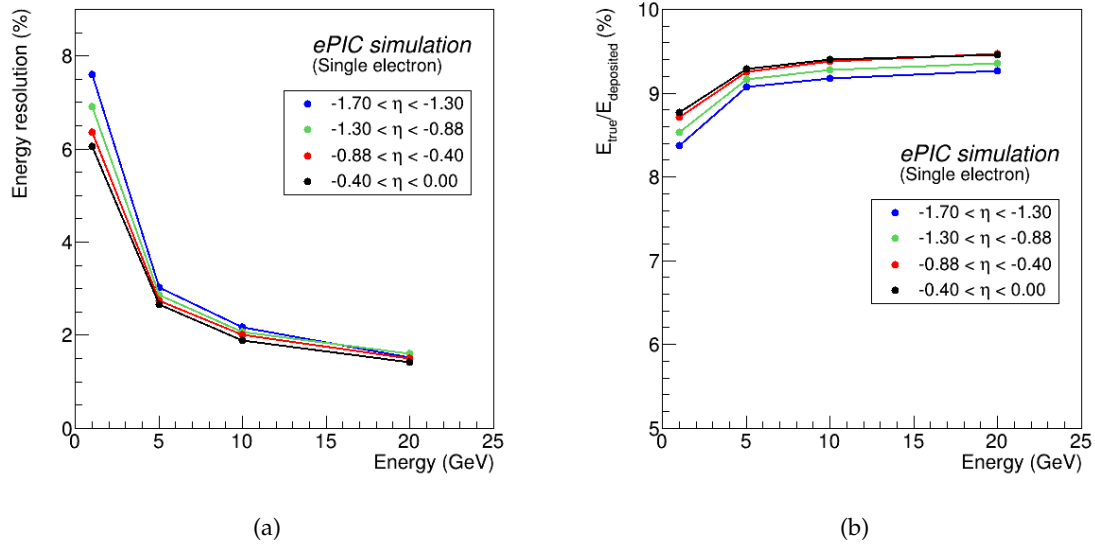


Figure 8.89: (a) Simulated energy resolution in from Pb/ScFi extracted as a σ of the Gaussian core of the Crystal Ball fit to the energy deposits of electrons in different rapidity ranges at BIC. (b) Sampling fraction for electrons, defined as energy losses in scintillating fibers divided by the true photon energy, as a function of photon energy in different rapidity ranges. (To be replaced with matching η regions and adjusted y-axis)

epochs, with data split into 70% for training, 10% for validation, and 20% for testing. On average, between 100,000 and 200,000 events were included in each training set, drawn from over 2TB of official singles productions simulations.

The CNN's performance is measured with uncertainties based on binomial statistics, providing robust estimates of classification accuracy. A similar but simplified approach was used for neutral pion identification. Initial results demonstrate promising pion rejection rates, which could be further enhanced by implementing algorithmic improvements. Future iterations of the model may explore Graph Neural Networks or Point Clouds to better capture the spatial and relational data inherent in these complex events.

MIP measurement capability

- More details about the SiPM simulations
- Performance for different rapidity ranges

Services and subsystem mechanics and integration

- More details about integration and services

Calibration, alignment and monitoring

- More details about calibration

4448 Status and remaining design effort:

- 4449 • Detailed timeline on R&D and PED efforts

4450 Environmental, Safety and Health (ES&H) aspects and Quality Assessment (QA) planning:

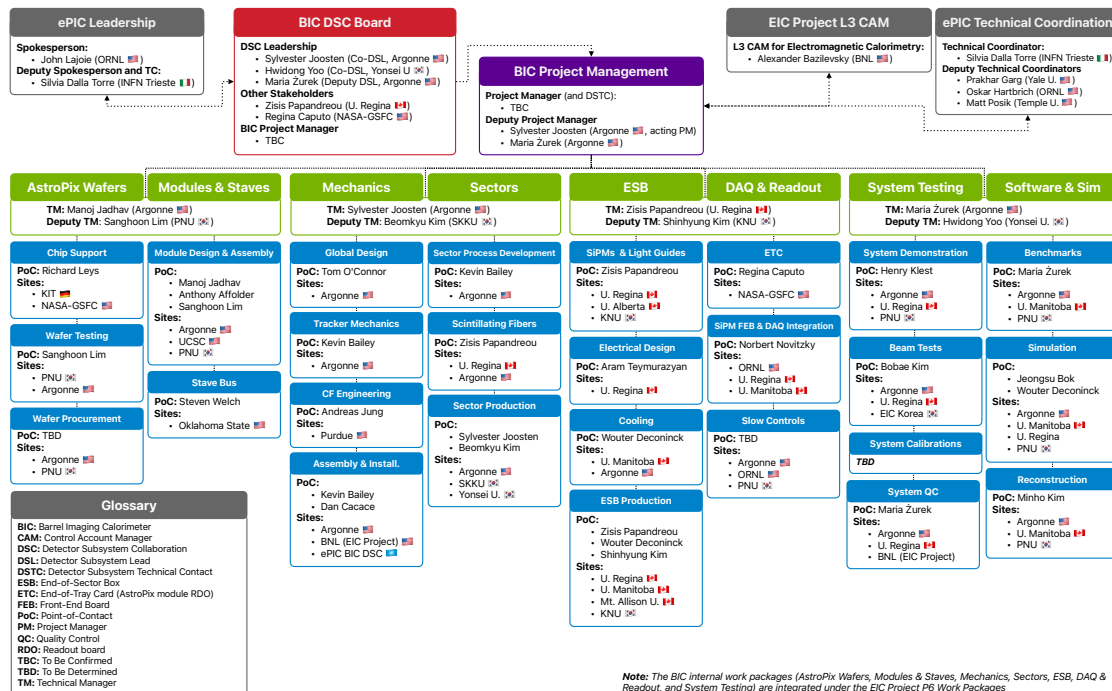
- 4452 • Remaining details on ES&H

4453 Construction and assembly planning:

- 4454 • Full construction plan with sites, FTEs, yields, etc

4455 Collaborators and their role, resources and workforce:

- 4456 • Full org chart



Note: The BIC internal work packages (AstroPix Wafers, Modules & Staves, Mechanics, Sectors, ESB, DAQ & Readout, and System Testing) are integrated under the EIC Project PB Work Packages

Figure 8.90: Barrel Imaging Calorimeter org chart. (Updates expected)

8.3.5.3 The forward endcap electromagnetic calorimeter

Introduction The ePIC forward electromagnetic calorimeter (fEMCal) is part of the hadron end-cap calorimeter system, complementing the forward hadronic calorimeter. Complete calorimetric coverage in ePIC is essential for detecting photons and electromagnetically decaying mesons, which are crucial for reconstructing parton-scattering kinematics through jets and to identify DVCS photons. fEMCal provides full azimuthal coverage within a pseudorapidity range of approximately $1.4 \lesssim \eta \lesssim 3.9$. At lower pseudorapidity, fEMCal overlaps with BEMC, ensuring continuous coverage by electromagnetic calorimeters in the hadron side of the ePIC detector. Coverage at higher pseudo-rapidity is restricted due to mechanical limitations (clearance required to accommodate the accelerator beam pipe).

The design requirements for the fEMCal were established through extensive studies of various detector concepts proposed for the EIC over the past decade. These concepts originated from the designs presented in the EIC White Paper [50] and Yellow Report [4], evolving through the ECCE [51] and ATHENA [52] proposals and culminating in the ePIC detector concept discussed here. It was concluded that an energy resolution of approximately $12\%/\sqrt{E} \oplus 2\%$, along with high granularity needed to distinguish single photons from DVCS events and photon pairs from π^0 decays up to 50 GeV, would meet the EIC's measurement objectives.

Though numerous electromagnetic calorimeter technologies were considered, as noted in the EIC Yellow Report [4], the stringent space limitation in ePIC detector (an integration length of only 27 cm along the Z-axis for fEMCal) ruled out all but one technology for the fEMCal: WScFi. This technology, developed during the generic EIC detector R&D program [53], has also been successfully implemented in the recently constructed barrel electromagnetic calorimeter of the sPHENIX experiment [54], which is comparable in scope with the ePIC fEMCal.

Some of the key requirements and parameters for the fEMCal are summarized in Table 8.2. The most critical challenges include the limited integration space and the need for a very large dynamic range, approaching 7000:1. Radiation doses and neutron fluxes are not expected to pose significant challenges for current technologies. For instance, the forward calorimeter system (FCS) constructed for the STAR experiment at RHIC has been successfully operational since 2021 under conditions—both in terms of radiation and neutron flux—similar to those anticipated at the highest luminosities of the EIC. The choice of photodetectors and front-end readout electronics for the fEMCal is partially based on the readout system developed for the STAR FCS.

Device concept and technological choice: Figure 8.6 depicts the front face of the ePIC hadron end-cap in its closed position, which is divided into two halves to allow access to the inner ePIC detectors in its open position. The end-cap features 1,145 fEMCal installation blocks, each of which is mounted to a one-inch-thick steel plate situated between the hadronic and electromagnetic calorimeters. Each installation block comprises 16 fEMCal towers and weighs approximately 18 kilograms, bringing the total weight of the fEMCal to around 21,000 kilograms. A 0.250 mm air gap separates each fEMCal installation block to accommodate production and installation fixtures tolerances. The readout system for the fEMCal is located at the front face of the blocks, ensuring easy access to the electronics. Cables and utilities run horizontally along each row of blocks to the perimeter of the fEMCal, where they bunched and passed through few openings in the light-tight external shell and connected to the RDOs positioned on the sides of the hadron end-cap.

Each fEMCal installation block is composed of four “production blocks,” with each production block consisting of a 2×2 arrangement of towers. All production blocks are identical, and precise mechanical tolerances are ensured by using identical production molds fabricated to high toler-

Table 8.22: Some requirements on performance of fEMCal and its parameters

Parameter	Requirements	Comments
Geometrical Acceptance	$1.4 \lesssim \eta \lesssim 3.9$	$R_{out} \sim 190$ cm, $Z_{frontface} \sim 341$ cm Hole for the beam pipe 30×30 cm ²
Integration envelope	$R_{max}=205$ cm, Depth = 27 cm	
E_{min} in a single tower	15 MeV	Minimal shower energy 50 MeV
E_{max} in a single tower	100 GeV	18×275 GeV, ep
Maximum rate in a single tower	10 kHz	$E_{thr}=15$ MeV, 10×275 GeV ep 500 kHz collision rate
Radiation doses	15 kRad	Integrated over 10 years
Neutron fluxes	4×10^{11} n/cm ²	1 MeV eq, integrated over 10 years
Energy resolution	$\lesssim 12\%/\sqrt{E} \oplus (2)\%$	Verified in the test beams
γ/π^0 separation	up to 50 GeV	$\sim 5\%$ mis-identification at 50 GeV
Depth	$23 X_0$	Minimize leakages
Detector parameters	Units	Comments
X_0, R_m	7 mm, 19 mm	Rad. length, Moliere radius
f_{samp}	2%	$e/h \simeq 1$ above 10 GeV
Scintillating Fibers	\varnothing 0.47 mm	Single clad sc. fibers
Light yield	~ 1600 pixels/GeV	Test beam results.
Transverse size of tower	2.5 cm \times 2.5 cm	Matches R_m
Transverse size of installation block	10 cm \times 10 cm	Block of 16 towers
Total number of towers	18320	Readout channels
Photodetector	S14160-6015PS	Four 6×6 mm ² SiPMs per tower 15 μ m pixels size
Monitoring system	Blue LED	LED integrated on SiPM board. One LED per four towers

ances, within a few tens of micrometers. The epoxy layer between production blocks is typically less than 100 micrometers thick. These thin epoxy layers, along with air gaps between installation blocks, represent the only dead material within the fEMCal volume. These dead zones have a negligible impact on the overall performance of the fEMCal.

The primary reason for using tungsten powder and scintillating fiber technology for fEMCal is that it is the only practical method to meet the stringent requirements outlined in Table 8.2. Specifically, the desired energy resolution with extremely compact tower dimensions can only be achieved by combining a small sampling fraction with a high sampling frequency. This high sampling frequency is attained by using 780 thin, 0.47 mm diameter scintillating fibers in each tower, arranged in a staggered pattern with a center-to-center distance of approximately 0.955 mm. Both the fiber diameter and spacing were optimized through Monte Carlo simulations to ensure fEMCal is nearly compensated and maintains the required energy resolution. Tungsten powder is used as the base material for the absorber structure to make the technology viable in practice. A set of specifications for tungsten powder and scintillating fibers for ePIC were established during generic detector R&D program for EIC and experience of constructing sPHENIX barrel EMCal utilizing WScFi technology.

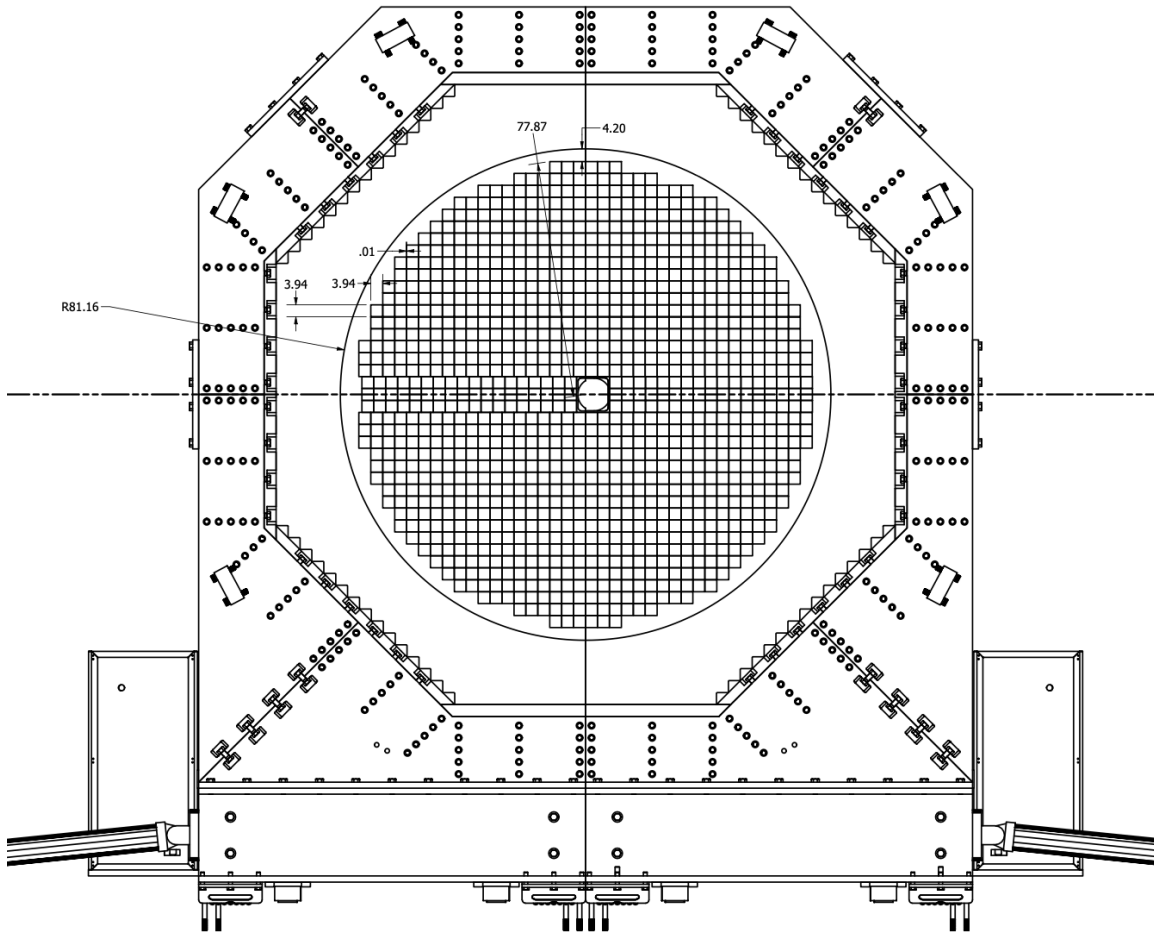


Figure 8.91: The front face of the ePIC hadron end-cap.

Despite the apparent simplicity of fiber calorimeters, constructing them is not straightforward. Detector components must be produced with extremely tight tolerances to maintain uniformity. Historically, techniques like extrusion, machining, or rolling were used to manufacture absorber plates, but these processes were complex and often required the creation of specialized machinery and tools. Building fiber calorimeters has traditionally been a labor-intensive process, with individual detector elements being handled one at a time, driving up costs compared to scintillating plate detectors. Moreover, traditional methods face challenges with increasing sampling frequency, as thinner absorber layers and fibers become more difficult to produce and manage. For example, construction and assembly techniques for H1 fiber calorimeter detailed in [55].

Our approach differs in that we first create a matrix of fibers and then pour the absorber material into the matrix. Unlike previous methods, this technique eliminates the need to handle individual calorimeter elements separately. Figure 8.7 shows a matrix of scintillating fibers and SEM image of tungsten powder used to build fEMCal prototypes. This powder has a particle size distribution of 90% between 70 and 160 microns, a tap density of 11.5 g/cm^3 , and a purity of $W \geq 99.9\%$, with Fe, Ni, and Co combined at $\leq 0.1\%$. Additionally, this tungsten powder exhibits excellent fluidity, a crucial property for our application. The only operation required for the absorber material is measuring the correct amount of powder before pouring it into the fiber matrix.



Figure 8.92: Matrix of scintillating fibers prepared to build production fEMCal blocks and SEM image of tungsten powder.

4535 The second key element is a straightforward method for forming the scintillating fiber matrix. This
 4536 matrix is defined by a set of precision brass meshes produced via photo-etching. These meshes have
 4537 mechanical tolerances of 30 microns on their overall dimensions for 300-micron thick meshes and
 4538 about 15 microns for the center-to-center distances between the holes for the scintillating fibers. The
 4539 fibers are cut to the desired length using a thermo-cutter, which melts the fiber ends to form small
 4540 drops that act as stoppers, preventing the fibers from slipping through the mesh holes. Once the
 4541 meshes are stacked, approximately 500 fibers at a time can be dropped into the container holding
 4542 the meshes, and with slight tapping, the fibers will flow through the set in seconds. For our recent
 4543 prototypes, a trained student could form a fiber matrix for a 2x2 tower production block with 3,120
 4544 fibers in around 30 minutes.

4545 The total production volume of scintillating fibers for the forward EMCal (fEMCal) is 3,000 km.
 4546 Only two companies, KURARAY and Luxium (formerly St. Gobain, BICRON), are capable of
 4547 producing the necessary fibers. Both companies' fibers were previously used to construct and
 4548 beam-test several WScFI EMCal prototypes for the EIC, with St. Gobain fibers also utilized by
 4549 the sPHENIX collaboration for their barrel EMCal. Recently, Luxium optimized the composition
 4550 of their standard BCF-12 fibers specifically for the shorter 17 cm fibers required for fEMCal, re-
 4551 sulting in a 20% improvement in light yield compared to their standard fibers. This was achieved
 4552 by adjusting the concentrations of primary and wavelength-shifting fluors, bringing them to the
 4553 same performance level as KURARAY fibers. Table 8.3 outlines the technical specifications and
 4554 requirements for the fEMCal fibers.

4555 To create a scintillating fiber matrix, it is essential that the fibers remain straight when placed into
 4556 the mesh framework. Fibers processed from spools tend to retain a bend due to "memory," which
 4557 leads to significant friction between fibers flowing through a set of meshes, which complicates the
 4558 assembly process. Among suppliers, only Luxium agreed to a delivery method that addresses this
 4559 issue, making them the sole provider of fibers for the fEMCal. These scintillating fibers are a long
 4560 lead procurement item, with a pre-production batch expected to arrive at ePIC by the end of 2024,

Table 8.23: Requirements and Technical specifications for fEMCal scintillating fibers.

Parameter	Requirements	Comments
Light Yield (LY)	≥ 8000 photons per MeV	Acceptance QA with Sr90 source Compared to a standard sample
Nominal Diameter	$0.47 \text{ mm} \pm 0.0094 \text{ mm RMS} \leq 0.02 \text{ mm}$	QA sampled on 10% boxes 100% at ramp-up prod. stage
Attenuation Length	$\geq 3 \text{ m}$	QA with UV LED
Batch-to-batch LY variation	$\leq 10\%$	QA with Sr90
Emission spectrum	Blue-green light	To match QE of SiPMs
Scintillation Decay Time	$\leq 3 \text{ ns}$	Bunch structure at EIC
Delivery Method	In cans, length of fibers +2%, -0%	Length $\geq 1 \text{ m}$, increment 20 cm

followed by monthly deliveries of the remaining fibers. Both the production and acceptance sites will adhere to agreed-upon QA and acceptance protocols to ensure that the fibers meet fEMCal specifications. Some of these QA steps are outlined in Table 8.3.

The concept of using tungsten powder as an absorber was briefly explored by the UCLA group in 2003, when they constructed and tested a small electromagnetic prototype at SLAC. At the time, the tower structure required a thin-walled brass container to hold the dry powder and fibers in place. However, this assembly technique proved imperfect, leading to significant transverse non-uniformities in detector response due to variations in the sampling fraction and potential displacement of fibers during packing. A compact calorimeter demands strict mechanical tolerances and a highly uniform internal structure to achieve theoretical energy resolution. To address these issues, we introduced intermediate meshes to secure fibers along the towers and developed a vacuum-assisted method to infuse epoxy into the tungsten powder/fiber assembly. Once assembled, the structure becomes rigid, eliminating the need for external containers and dead material in the tower. The homogeneity of the WScFi structure was verified by cutting multiple samples on small pieces which were analyzed and was found to exceed 1%. The mechanical properties of the WScFi structure were measured and they are comparable to construction steel.

This refined technique, with slight variations, was then employed in constructing the sPHENIX barrel EMCal and all recent fEMCal R&D prototypes.

Light Collection scheme and Photosensors The light collection scheme and photosensor setup adhere to the general requirements outlined in Table 8.2. The back of each installation block features a thin layer of optical epoxy (1.8 mm thick) mixed with 10% TiO_2 , which acts as a diffuse optical reflector for the scintillating fibers and provides a surface for bonding the 13 mm-thick aluminum “strong back.” This strong back plate is then bolted to the steel interface plate connecting the EMCal and HCal. On the front side of the installation block, a 21 mm-long light guide (LG) plate is attached. Made from a single piece of optically clear cast acrylic, this LG plate has 64 trapezoidal light guides to direct light from the fibers to the SiPMs. The front and back views of the LG plate with SiPMs attached can be seen in Fig. 8.8. The light collection efficiency of this setup is approximately 80%, which is sufficient to detect 15 MeV in a single tower, corresponding to 24 fired pixels. However, due to the short length of the light guide (typically much longer in fiber calorimeters), light “mixing” from individual fibers is minimal, resulting in spatial non-uniformities in light collection at the 10% level, as measured with a point light source.

The chosen photodetector for the fEMCal is the SiPM (Silicon Photomultiplier). Over the past 15

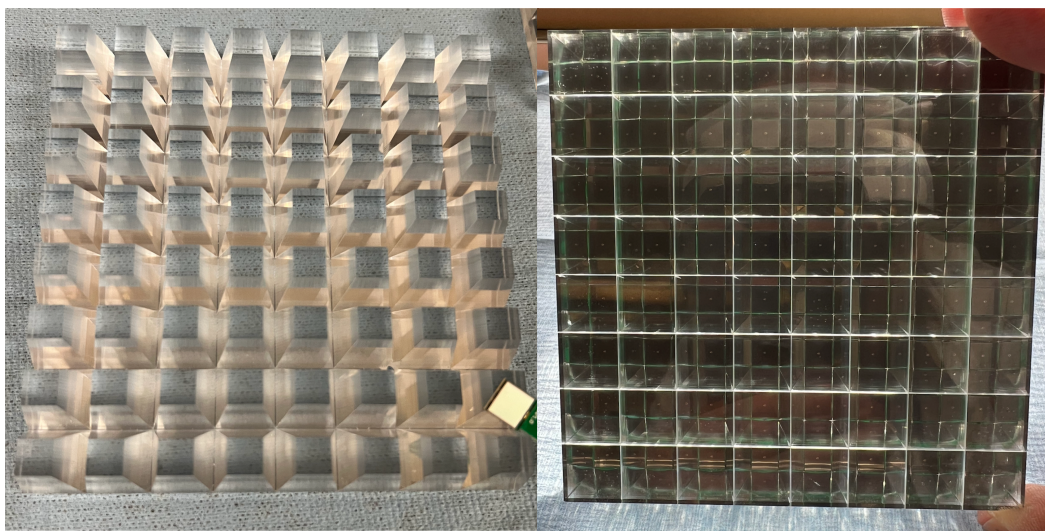


Figure 8.93: Front and back views of LG plates with installed SiPMs.

years, extensive R&D programs across the globe—including the generic detector R&D program for the EIC—have worked to bring SiPM technology to a mature and reliable level. Today, hundreds of thousands of SiPMs are in use in various high-energy physics and nuclear physics experiments. These detectors are extremely compact, robust, and well-suited for calorimetry readout in moderate radiation environments, such as the forward region of the ePIC detector, as shown in Table 8.2. The failure rates of SiPMs in calorimeter operations at facilities like JLab, BNL, and CERN have been remarkably low, typically less than 0.1%. Notably, the STAR Forward Calorimeter System (FCS) experienced zero SiPM failures during three years of operation under conditions similar to those expected in the high-luminosity EIC. Although neutron-induced damage will lead to increased leakage current and noise levels, these effects remain within tolerable limits. For example, it is anticipated that the equivalent noise level for fEMCal at ePIC will rise to around 6 MeV after 10 years of operation, particularly in areas near the beam pipe. This projection is based on scaling from the results observed in the STAR FCS. After this period, replacement of some of the SiPM boards near the beam pipe may be necessary. These considerations informed the design of the fEMCal readout system, ensuring a straightforward integration with the detector. The technical specifications and performance details of the SiPMs for the fEMCal are summarized in Table 8.4.

Mechanical Integration The mechanical integration, installation procedures, and structural tests for the fEMCal were validated using installation blocks at BNL. These blocks were produced following the final production protocols and using the same components that will be used for the actual installation. Structural tests on smaller samples demonstrated that the safety factor for the proposed mounting scheme is greater than 48. A full structural test (Fig. 8.9) was conducted by mounting an installation block on a mockup plate and applying five times the expected load. The deflections at the readout end of the fEMCal block were measured to be less than 100 μm , confirming that each installation block is self-supporting and does not exert any load on the blocks beneath it. Simple installation fixtures were designed, and the installation procedures were verified to ensure safety. Specifically, it was crucial to confirm that the fEMCal blocks could be safely installed with the SiPM-carrying boards glued to the LG plates. The tests confirmed that the blocks can be

Table 8.24: Requirements and Technical specifications for fEMCal SiPMs.

Parameter	Requirements	Comments
Active Area	6 mm \times 6 mm	Efficiency of light collection, E_{min} 15 MeV
Pixel Size	15 or 20 μ m	Dynamic Range, E_{max} 100 GeV
Peak Sensitivity	\sim 420 nm	Match scintillating fibers spectra.
PDE	\geq 30%	Efficiency of light collection, S/N
Gain	$\sim 2 \times 10^5$	at 3 V overvoltage, S/N
DCR	\leq 3000 kcps	at 3 V overvoltage, 25 C, S/N
Temperature Coefficient	\leq 40 mV/C	Stability, Unifformity
Direct Cross Talk	\leq 1%	Radiation, dark current
Terminal Capacitance	\leq 2 nF	FEE coupling
Packing Granularity	Multiple of 4 per tray	4 SiPMs per tower at same V_{op}
V_{op} variation within a tray	\pm 0.02 V	Uniformity of response

4620 safely mounted onto the hadron end-cap without causing any damage to the SiPM boards.

**Figure 8.94:** Structural and installation tests at BNL.

4621 **Performance** The performance of the fEMCal prototypes has been tested in several test beams
 4622 at FNAL over the past few years, initially as part of the generic detector R&D for the EIC and later
 4623 as part of the ePIC R&D program. In the summer of 2024, one installation block featuring the latest
 4624 version of the light guide (LG) and SiPM readout was tested at FNAL. Energy scans were conducted
 4625 at various impact angles covering the entire fEMCal acceptance range. As expected, some variation
 4626 in response across the surface was observed, as shown in Fig. 8.10, due to the compact nature
 4627 of the LG. However, this variation represents an improvement compared to earlier versions [56].
 4628 Position-dependent corrections, based solely on the data from fEMCal, were applied to account
 4629 for non-uniformities. This method is similar to the approach used in the 2014 test [56] and for

the sPHENIX barrel EMCal. As anticipated, the uniformity of response improves with shallower impact angles. The energy resolution, shown in Fig. 8.10, corroborates previous measurements with this type of electromagnetic calorimeter [56] and aligns with the performance requirements outlined in Table 8.2. The measured absolute light yield is 1580 pixels/GeV.

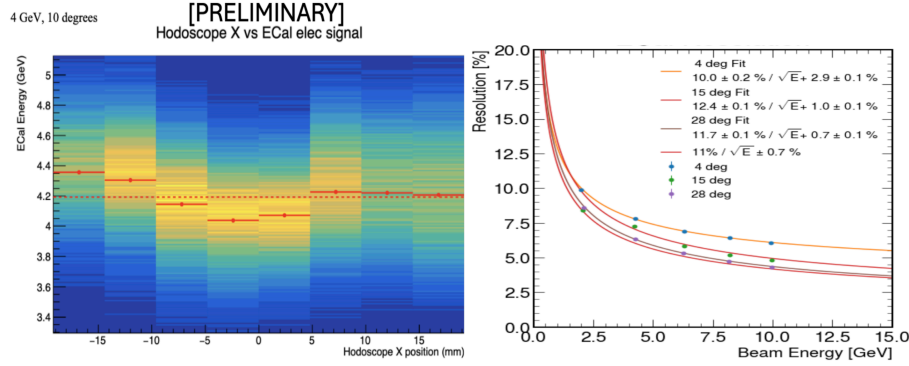


Figure 8.95: Response of calorimeter vs position in hodoscope (left panel). Energy resolution for different impact angles (right panel).

The remaining performance parameters were extensively tested using MC simulations, incorporating the full ePIC simulation chain with the latest detector geometry updates. A material scan indicated the presence of approximately $0.2 X_0$ of “dead” material in front of the fEMCal in ePIC, but its impact on performance was found to be negligibly small. Simulations conducted with PYTHIA8, using minimal Q^2 cuts for all energy configurations at the EIC, examined occupancy, rates, and dynamic range. These studies informed the set of requirements listed in Table 8.2.

An initial investigation into γ/π^0 separation, based on the traditional shower shape analysis method outlined in the EIC Yellow Report (Fig. 11.46, [4]), revealed potential for improvement. A significant enhancement in γ/π^0 separation was achieved by applying machine learning algorithms. As shown in Fig. 8.11 (left panel), the misidentification rate at 60 GeV dropped to approximately 10%, compared to 80% with traditional methods [4].

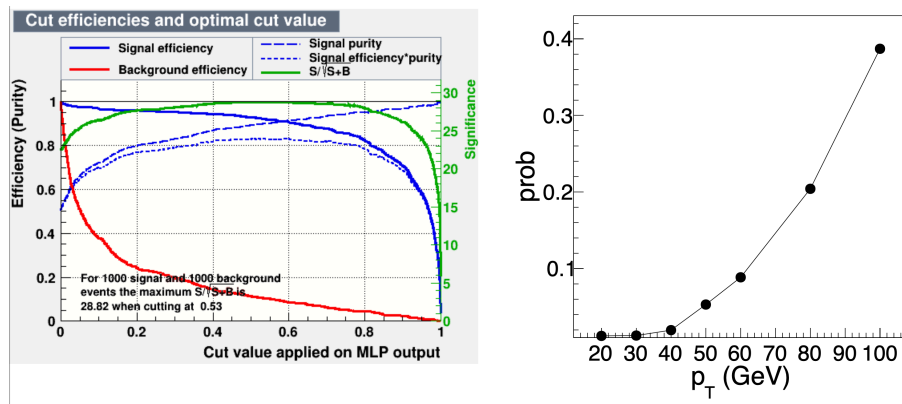


Figure 8.96: Signal (single photon) efficiency and background (merged di-photons) contamination for different cut value of the NN output for 60 GeV (left panel). Probability of misidentifying π^0 as a single photon vs energy (right panel)

Readout Electronics The fEMCal readout electronics face three primary challenges: achieving a large dynamic range of 7000:1, ensuring precise discrimination for streaming small signals (24 pixels) amidst dark counts of up to 45 GHz caused by radiation damage to SiPMs, and integrating everything within a compact space—around 5 cm for SiPM boards, front-end boards (FEBs), cooling, and cables. Table 8.7 summarizes requirements for the FEB.

Table 8.25: Requirements for the FEB

Parameter	Requirements	Comments
SiPM & overvoltage	4xS14160-6015PS, 2-3V	
Min signal	15 MeV (@ 1.6 pix/MeV)	
Max signal	100 GeV	
Hit rate	10 kHz	per channel
Charge reso.	$\sim 210\% / \sqrt{npix} \oplus (0.9)\%$	contribute 10% of fEMCal resolution
Charge nonlinearity	$\leq 1\%$	
Time resolution	$\ll 10$ ns	for ≥ 100 MeV signals only
SiPM bias voltage stability	≤ 10 mV	including T compensation
Bias voltage setting range	33 to 47 V	sufficient for meaningful IV curve
Bias current range & mon. resolution	2 mA, 200 nA	4 SiPMs per tower at same V_{op}
LED drive control	var. amplitude, masks	fired by global command

Building on the successful design of the STAR FCS readout, fEMCal’s readout system transfers SiPM signals to a low impedance load, shapes and amplifies the resulting voltage, and digitizes the waveform. Hits are detected in the digital waveform via threshold crossing (which may be filtered). In streaming readout mode, regions of interest in the digital waveform are identified, timestamped, and sent to an output FIFO/merging scheme, before being transmitted to the readout (RDO) board. At the RDO, data from up to 16 FEBs are buffered, merged, and sent to the DAM. Feature extraction, converting raw waveform samples to estimated pulse amplitude and timing, may be done either at the FEB or RDO level to reduce data volume. If hardware feature extraction is not used, this will be performed during preliminary online analysis.

Waveform digitization for fEMCal will operate at either 39.4 MSPS or 49.25 MSPS. The digitization clock must be phase-locked to the beam bunch crossing clock at 98.5 MSPS to extract hit timestamps in real-time within the streaming DAQ system. Sampling at 98.5 MSPS is not feasible due to power and FPGA resource constraints. To meet the 15 MeV readout threshold and achieve the dynamic range, the ADC resolution must be 14 bits. The analog waveform will be shaped before digitization to achieve a peaking time of approximately $2.8/f.SAMPLE$, which ensures less than 1% error in pulse amplitude measurement while minimizing noise from dark count pileups. For instance, a 57 ns peaking time is optimal at 49.25 MSPS.

The FEB will individually regulate bias voltage for each tower, providing temperature compensation for each SiPM board (covering 2×2 towers) and monitoring current with built-in protective current limits. Each tower’s four SiPMs will be connected in parallel, sharing a common bias voltage, requiring precise matching of the breakdown voltages (V_{BR}) among the four SiPMs to ensure uniform gain. The bias regulation circuits, developed from the STAR Forward Calorimeter, have proven effective, though radiation sensitivity in a voltage reference IC was noted. To mitigate this, fEMCal’s bias regulator will use a remote reference on the power distribution boards, ensuring the required 0.03% stability. Less critical internal voltage references require only 1% stability. The bias regulation channels provide sharp current limiting to protect the SiPMs from overload, maintaining 10 mV bias voltage stability up to the current limit (2 mA).

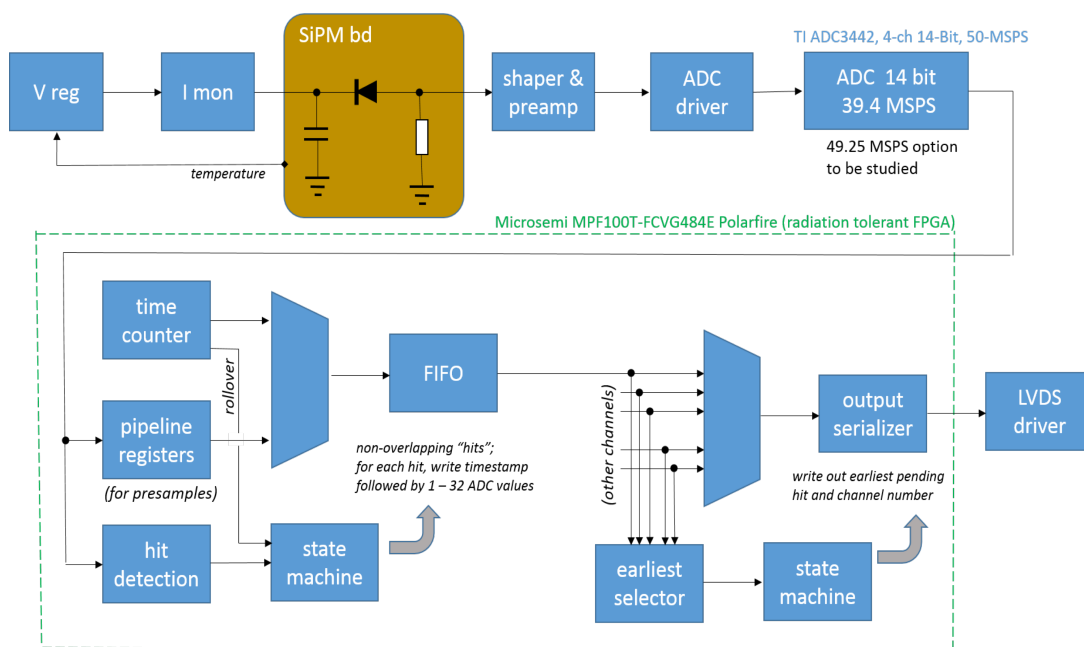


Figure 8.97: fEMCal front end electronics.

Signal routing from the SiPM boards to the FEBs is achieved through board-to-board connectors, eliminating the need for cables. These connectors can accommodate mechanical tolerances of ± 0.5 mm between the FEB and SiPM boards and overlap with space allocated for the cooling water tube. Should radiation damage impact the innermost FEBs, a backup plan would route SiPM signals via 2m coaxial cable bundles to FEBs mounted at the block periphery.

Connections between the FEBs and RDO will use shielded Cat6 Ethernet cables, routed horizontally through the FEB rows and out of the magnet to racks housing the RDOs. One rack will be placed north of the north detector half, and another south of the south detector half. Cable lengths are estimated at 15 meters, and it has been confirmed that LVDS signals can be properly received at 200 Mb/s over this distance, meeting performance requirements.

Each rack will also house a Wiener MPOD crate with low-voltage (LV) power supplies, with one crate serving the north half and one for the south half of the detector. Each FEB will require approximately 250 mA at +16 V, 180 mA at -2 V, and up to 67 mA (depending on SiPM radiation damage) at +50 V.

The FEBs will be cooled conductively via a copper bracket attached to the main board (housing the ADCs, FPGA, and power supply circuits) and connected to a water cooling line. The water line will consist of standard $\frac{1}{4}$ inch (potentially $\frac{3}{16}$ inch) diameter copper tubing. A negative pressure system will mitigate the risk of water leaks. Two rows of FEBs will be served by a single water line in a U-shaped loop, with no fittings at each FEB, only at the loop ends. Reliable flare fittings will be used for the connections. Custom water manifolds, located in the “service gap” at the outer perimeter of the calorimeter blocks, will manage water distribution. The arrangement will likely consist of two supply and return manifold sets—one for the upper and one for the lower half of the detector.

Each water circuit will need to cool about 750 W of power from 148 FEBs, requiring chillers with at least 1.5 kW capacity for each half of the detector. One chiller will serve the north half and another

the south, cooling two water circuits each.

Slow controls for fEMCal will fall into two categories: hardware registers on the FEBs (communicated through DAQ software and the DAM/RDO) and controls for commercial equipment such as the water chillers and power supplies (Wiener MPOD), connected via Ethernet. SoftIOC interfaces will manage EPICS variables, providing GUI control, logging, and alarms.

Table 8.8 summarizes the control and status registers for the FEB.

Table 8.26: Control and status registers on the FEB

Function/description	Qty per FEB	R/W	Notes
SiPM bias voltage (base)	32	R/W	
Bias temp. comp. slope	1	R/W	
actual compensation	8	R	i.e. temperature
SiPM current monitor	32	R	extra diagnostic info
input LV supply monitor	2	2	
FEB temperature monitor	3	R	
FEB & SiPM board serial numbers	9	R	read once at startup
firmware revision	1	R	read once at startup
firmware update interface	1	R/W	maintenance use only
hit threshold channel mask	32	R/W	
hit detection options registers	4	R/W	
LED firing mask	1	R/W	
hit scalers	32	R	
fifo overrun scalers	32	R	
ADC configuration interface	1	R/W	might be internal use only

Calibration The fEMCal faces the hadron beam, and at mid to high energies, its signals will predominantly come from photons produced by π^0 decays. Tower-by-tower absolute energy calibration of the forward electromagnetic calorimeter will be performed by reconstructing π^0 mesons through the invariant mass of two photons from π^0 decays. It is expected that π^0 calibration for each tower can be achieved in approximately one day of data collection, followed by semi-online analysis using only forward fEMCal data. The method involves associating reconstructed π^0 mesons with the tower showing the highest response, adjusting the tower's gain based on the π^0 mass location, and repeating the process over several iterations. This technique has been successfully implemented in forward calorimeters at RHIC, including the STAR FCS.

Electrons from DIS events, combined with tracking information, can be used to cross-check the calibration. However, this approach requires a large dataset and will be performed offline. Additionally, Minimum Ionizing Particle (MIP) signals from hadrons can be utilized for calibration at the low-energy end. For high energies, where the two photons from π^0 decays are too close together for the forward EMCal to distinguish them, η mesons can be used to verify energy non-linearity.

Monitoring system An LED system will be installed on the FEE boards to illuminate four towers using a trigger pulse. The LEDs will be preselected to provide equal light output to the towers, serving as a critical monitoring system. This will be essential for initial testing during installation, verifying mapping, and ensuring long-term stability of the detector, SiPMs, and FEE board gain,

as well as detecting any potential radiation damage. A dedicated short LED run will be performed daily to monitor the calorimeter's performance.

Additionally, the current and voltage on the FEE boards will be continuously monitored. Periodic I-V curve measurements will be conducted, on a weekly or bi-weekly basis, to assess the health of the SiPMs and FEE boards.

Status and remaining design effort:

R&D effort: eRD106 will be completed in early 2025 with finalizing analysis of the test beam data.

E&D effort: Detailing of mechanical design, and formalizing production drawings.

Other activity needed for the design completion: Produce and test first versions of final design FEB and SiPM boards.

Status of maturity of the subsystem: $\sim 70\%$

Environmental, Safety and Health (ES&H) The project will strictly adhere to all Environment, Safety, and Health (ES&H) regulations to ensure the safety of personnel, the integrity of the equipment, and the protection of the environment throughout the construction and operation phases. Comprehensive risk assessments will be conducted for all activities, including the handling of hazardous materials, electrical components, while implementing proper controls to minimize exposure to risks. Personnel will receive specialized training in safety protocols and emergency response procedures, and regular audits will be conducted to ensure compliance with ES&H standards. Additionally, the design of systems such as power management will prioritize environmentally friendly practices, incorporating energy-efficient technologies and minimizing waste and emissions. Continuous monitoring of environmental impact and adherence to radiation safety guidelines will be maintained to ensure the long-term safety and sustainability of the project.

Collaborators and their role, resources and workforce: Collaboration plays a pivotal role in the success of this project, as it brings together a diverse group of experts from various institutions, each contributing specialized knowledge and skills. The development of the fEMCal detector, for instance, relies on coordinated efforts between physicists, engineers, and technicians working on different aspects such as design, testing, and integration. Collaborative efforts ensure that challenges in areas like electronics, cooling systems, and data acquisition are addressed through shared expertise and innovative problem-solving. Additionally, partnerships with other research labs, such as BNL and international institutions, allow for the exchange of ideas, the pooling of resources, and the sharing of key R&D advancements. This collaborative environment fosters a culture of learning and inclusivity, which is critical for the project's long-term success, allowing it to meet both scientific and technical goals.

8.3.6 Hadronic Calorimetry

Add text here.

8.3.6.1 The backward endcap hadronic calorimeter

The backward hadronic calorimeter, here called **nHCal** meaning **Negative-eta/Neutral Hadronic Calorimeter** is a tail catcher calorimeter to be installed in the electron going negative-z direction. As illustrated in the ePIC detector schematic REFERENCE, the nHCal is surrounded by an outer collar, backed by a flux return plate and an oculus ring placed in front. Experience from H1 experiment at HERA shows the need for such a calorimeter for low- x measurements [57,58].

Requirements

Requirements from physics: The main requirements for nHCal originate from physics processes in events with low Q^2 and low $x \sim 10^{-3} - 10^{-2}$ as well as high inelasticity y . This requires the acceptance of $-4.14 < \eta < -1.18$.

The processes of interests include diffractive vector meson overproduction $J/\psi \rightarrow \mu^+\mu^-$, $\phi \rightarrow K_L K_S$, $\phi \rightarrow K^+ K^- \rightarrow \mu^+\mu^-$ and diffractive dijets. It will be also used as a veto for jet studies with neutral energy component and help in scattered electron identification along with backward EMcal. Finally, it will be used as a hadron beam background veto for dRICH in conjunction with LFHCAL for which a good timing resolution is required. In order to measure vector meson production with muons a good μ/π separation of tracks with MIP signal in calorimeters is required. The low energy neutron detection for neutral jet identification requires low hit thresholds to achieve more than 90% detection efficiency for 2 GeV neutrons. Furthermore neutral clusters have to be identified after charged hadron correction which require a track matching and cluster position resolution to distinguish showers which are 30 cm apart. This is achievable with tiles of up to 25 cm size.

Requirements from Radiation Hardness: In general, the radiation dose in the electron endcap area is expected to be low. A study was performed and is summarized here: https://wiki.bnl.gov/EPIC/index.php?title=Radiation_Doses

The low radiation dose compared to the forward region makes the use of SiPMs and FEE safe. SiPMs are required to have good low dark count rate after 10 years of running. This is possible with the selected Hamamatsu S14160-1315PS model.

Requirements from Data Rates: Data rates were studied by considering the following sources:

- Deep Inelastic Scattering (DIS)
- Synchrotron Radiation
- Electron Beam Gas
- Hadron Beam Gas

The values are taken from background studies found here:

- <https://wiki.bnl.gov/EPIC/index.php?title=Background>

Justification

bkg. type	hit rate in detector [Hz]	max single channel hit rate [Hz]
DIS	$\sim 10^6$	1233.24
Synchrotron rad.	$\sim 2 \cdot 10^4$	-
e+gas	403899	6644.8
h+gas	$\sim 7 \cdot 10^5$	303.781

Table 8.27: Maximum expected background rates for backward HCal. The assumed threshold is 170.

4796 **Device concept and technological choice:**

4797 **Subsystem description:**

4798 General device description: The nHCal is planned to be a sampling hadronic calorimeter
 4799 with 10 layers of alternating steel and plastic scintillator of 4 cm and 0.4 cm thickness respec-
 4800 tively. Such arrangement provides compensation. The structure of the calorimeter will be
 4801 that of a flattened cylinder with the outer radius of 276 cm and the inner radius of 14 cm to
 4802 provide room for the hadron and electron beampipes. The thickness along the beam direc-
 4803 tion is going to be 45 cm in total. The plastic scintillator layer is going to be made of tiles with
 4804 $10 \text{ cm} \times 10 \text{ cm}$ (TBD) size. Two light collection solutions are under consideration with either
 4805 the use of WLS fibers with SiPM readout or SiPM on tile design as for LFHICAL, which was
 4806 developed by CALICE [59]. The SiPM on tile is possible with smaller tiles close to the beam
 4807 ($\eta \sim -4$), while larger tiles need to use WLS+SiPM combination.

4808 Sensors: The Hamamatsu S14160-1315PS model SiPMs will serve as light sensors. They will
 4809 either be connected to the WLS fibers or placed directly on tile.

4810 FEE: HGCROCv3 will be used as an FEE similar to ther calorimetry systems in ePIC.

4811 Other components: Add text here.

4812 **Performance** Performance of the nHCal was studied with single particles. Thresholds for neu-
 4813 tron detection were studied vs. kinetic energy and integration time.

4814 **Simulated DIS events** One of the basic studies is a check of energy and momentum distri-
 4815 butions going into backward HCal. This study used DIS $e + p$ events at $18 + 275 \text{ GeV}$ with
 4816 $Q^2 > 1 \text{ GeV}^2$. The Fig. ?? shows total energy E and p distributions of each particle species in
 4817 nHCal acceptance $-4.0 < \eta < -1.0$.

4818 Energy and momentum distributions of particles in nHCal acceptance in $e + p$ DIS events at $18 +$
 4819 275 GeV with $Q^2 > 1 \text{ GeV}^2$ was studied with the full official simulation of the ePIC detector. These
 4820 are presented in Fig. 8.100 as well as vs. η in Fig. 8.101, Fig. 8.102 and Fig. 8.103. This was used to
 4821 check the average energy of neutrons and optimize the detector for measuring that.

4822 **Vector meson reconstruction** Vector meson reconstruction and acceptance was studied in $e + p$
 4823 and $e + A$ events with PYTHIA8 with the focus on exclusive diffractive photoproduction. Large
 4824 fraction of J/ψ cross section was found to be produced in the backward direction making it espe-
 4825 cially important. It has to be noted that J/ψ study is one of the major goals of EIC as listed in the

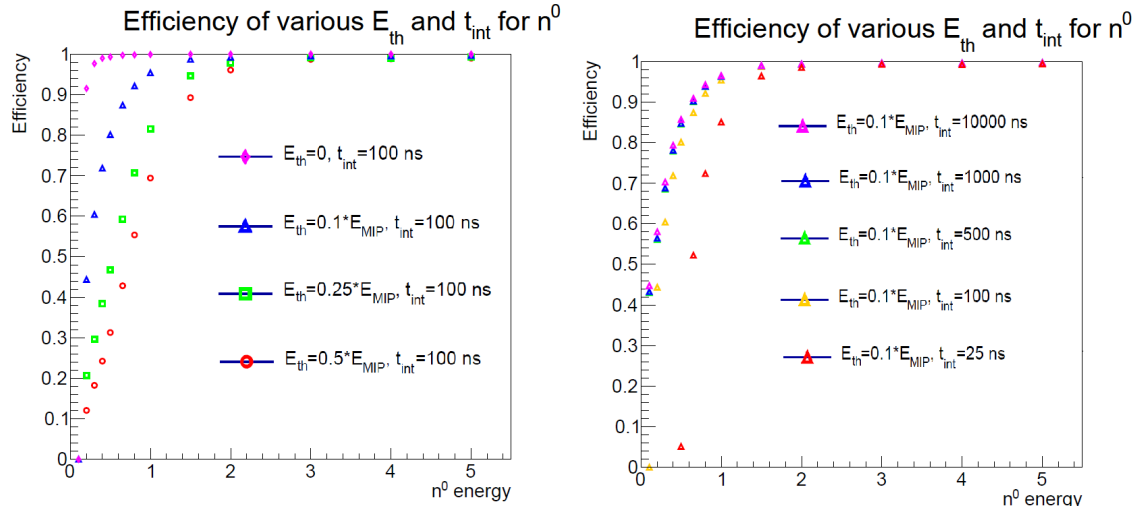


Figure 8.98: Left: Neutron detection efficiency vs. kinetic energy E_{kin} , dependence on threshold as a fraction of MIP energy deposit. Right: Same as left, but showing dependence on integration time.

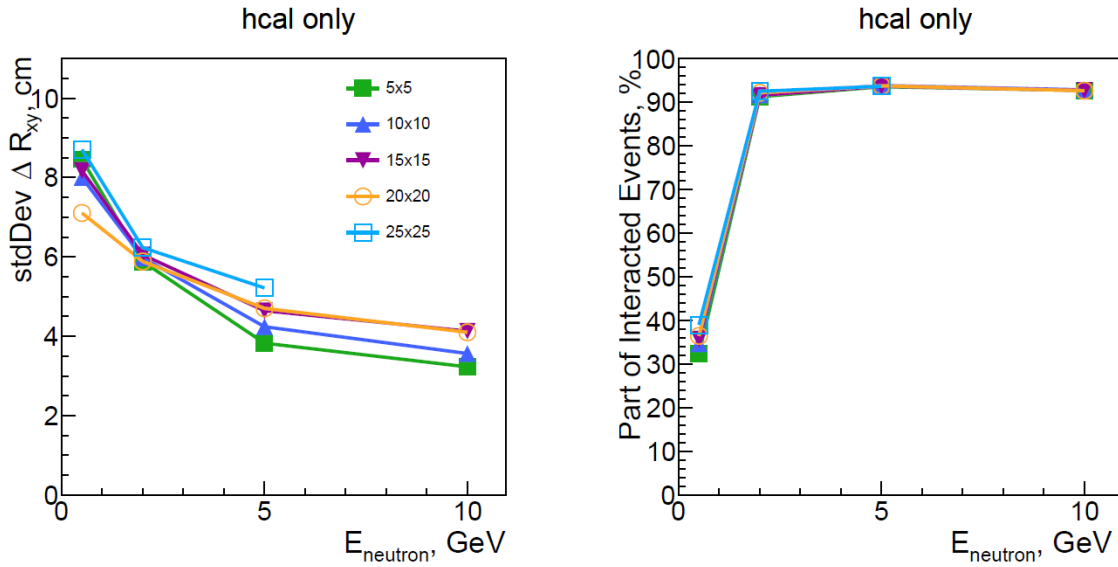


Figure 8.99: Position resolution R_{xy} and cluster efficiency vs. E for different tile sizes.

4826 Yellow Report [?]. Acceptance of J/ψ is shown in Fig. 8.104 vs. $-t$, Bjorken x_{BJ} and Pomeron x_p .
 4827 The figure also illustrates the acceptance when decay daughters are measured in different detectors.
 4828 Similar study was performed for $e + A$ collisions and presented in Fig. 8.105.

4829 Studies of $\Phi \rightarrow K^+ K^-$ were also performed as shown in Fig. 8.106 for $e + p$ and in Fig. 8.107 for
 4830 $e + A$ collisions.

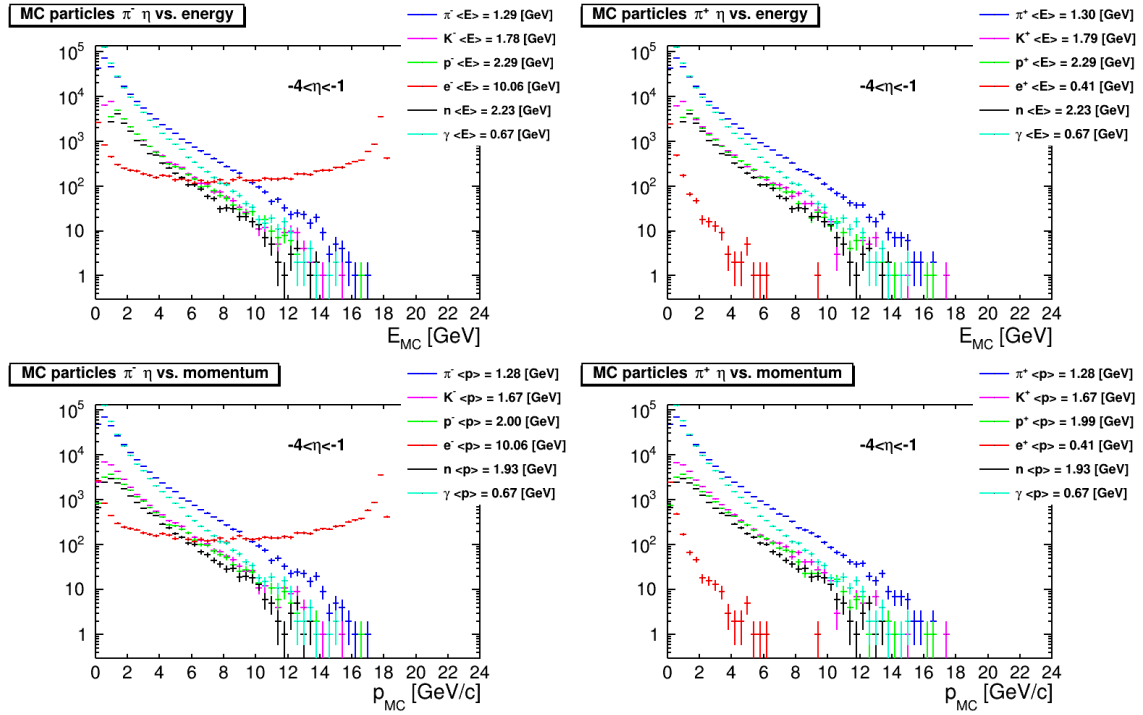


Figure 8.100: Top: Primary, generated particle E distributions in nHCal acceptance $-4.0 < \eta < -1.0$. Bottom: Primary, generated particle p distributions in nHCal acceptance $-4.0 < \eta < -1.0$.

These studies indicate that nHCal is needed to measure J/ψ and Φ in events with $x \sim 10^{-3}$ and lower.

Diffraction dijet measurement

Jets with neutral component Another purpose of nHCal is to help identify jets with neutral energy component, especially low energy neutrons of around $E = 2.23$ GeV. By distinguishing these 2 samples the jet energy resolution can be improved. This was studied with full ePIC simulation and track matching to MC particles or clusters using MC information. The jet energy resolution for the cases of inclusive(squares) and charged-only jets(triangles) is compared in Fig. 8.108. Results show $\sim 20\%$ improvement in jet energy resolution.

Cluster reconstruction

Implementation

Services:

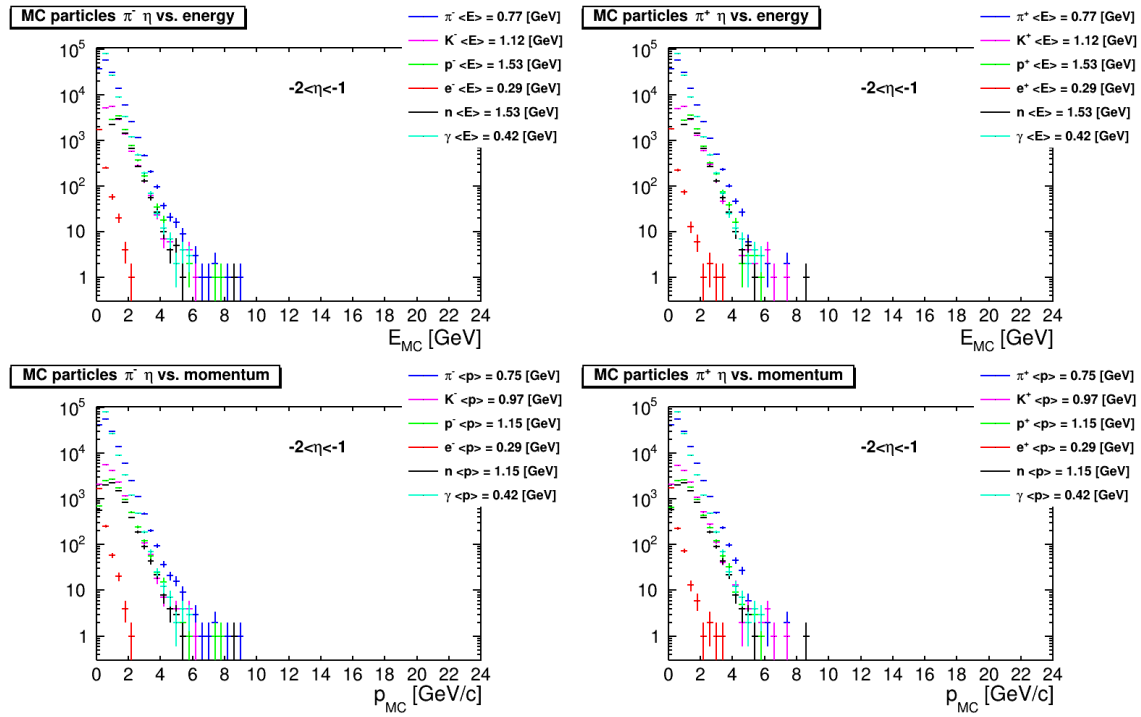


Figure 8.101: Top: Primary, generated particle E distributions in $-2.0 < \eta < -1.0$ range. Bottom: Primary, generated particle p distributions in $-2.0 < \eta < -1.0$ range.

4843 **Subsystem mechanics and integration:** TO BE DONE

4844 **Calibration, alignment and monitoring:** Calibration will be performed with the use of LEDs
 4845 on tile or additional clear fibers to guide the laser/LED light(similar to STAR EEMC calibration
 4846 system) to the scintillator tiles. The system will allow for simulation of custom shower shapes in
 4847 a similar way as for LHCAL. The response will be studied and used to calibrate the gains of the
 4848 SiPMs by adjusting bias voltage to compensate for variation and difference in response as well
 4849 as potential radiation damage to SiPM and tiles. This allows for monitoring the system during
 4850 operation.

4851 Alignment will be performed during assembly. During operation, physics events and cosmic rays
 4852 will be used to study the relative position of the calorimeter with respect to trackers. We will follow
 4853 standard alignment procedures performed at many collider experiments.

4854 Since SiPM gains are sensitive to temperature variations, temperature monitoring system using
 4855 thermocouples will be employed. These need to be only coarsely placed, because SiPMs generate
 4856 very little heat. In addition the absorber steel with large heat conductivity will allow to spread the
 4857 heat evenly over a large volume.

4858 **Status and remaining design effort:**

4859 R&D effort: Finalize simulations and confirm optimal tile size.

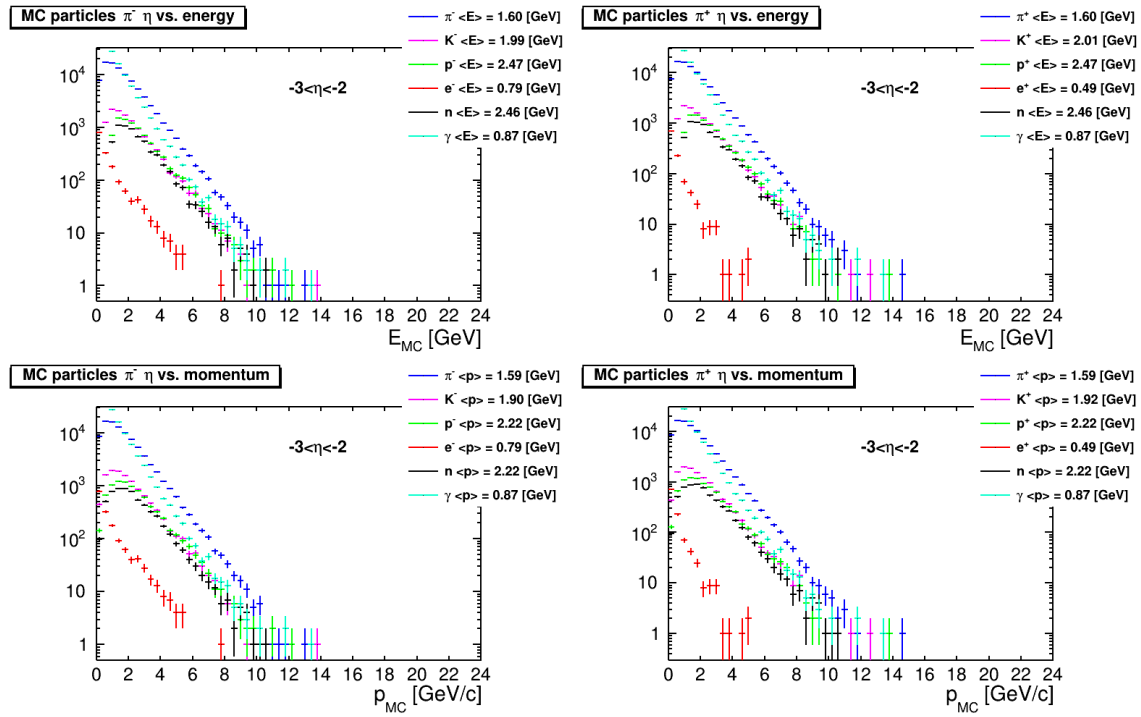


Figure 8.102: Top: Primary, generated particle E distributions in $-3.0 < \eta < -2.0$ range. Bottom: Primary, generated particle p distributions in $-3.0 < \eta < -2.0$ range.

E&D status and outlook: Design of support structures to follow the confirmed tile design.

Other activity needed for the design completion: Finalize simulations to confirm the tile size and design.

Status of maturity of the subsystem: Technologies and design are mature. Dependent on the outcome of performance simulations.

Environmental, Safety and Health (ES&H) aspects and Quality Assessment (QA planning): We will follow standard ES&H procedures observed at all participating institutions. Quality of the tile, fiber and SiPM interfaces as well as optical isolation will be tested after assembly of individual modules. This will be performed with the calibration system of the nHCal.

Construction and assembly planning: Add text here.

Collaborators and their role, resources and workforce: Add text here.

Risks and mitigation strategy:

Additional Material Add text here.

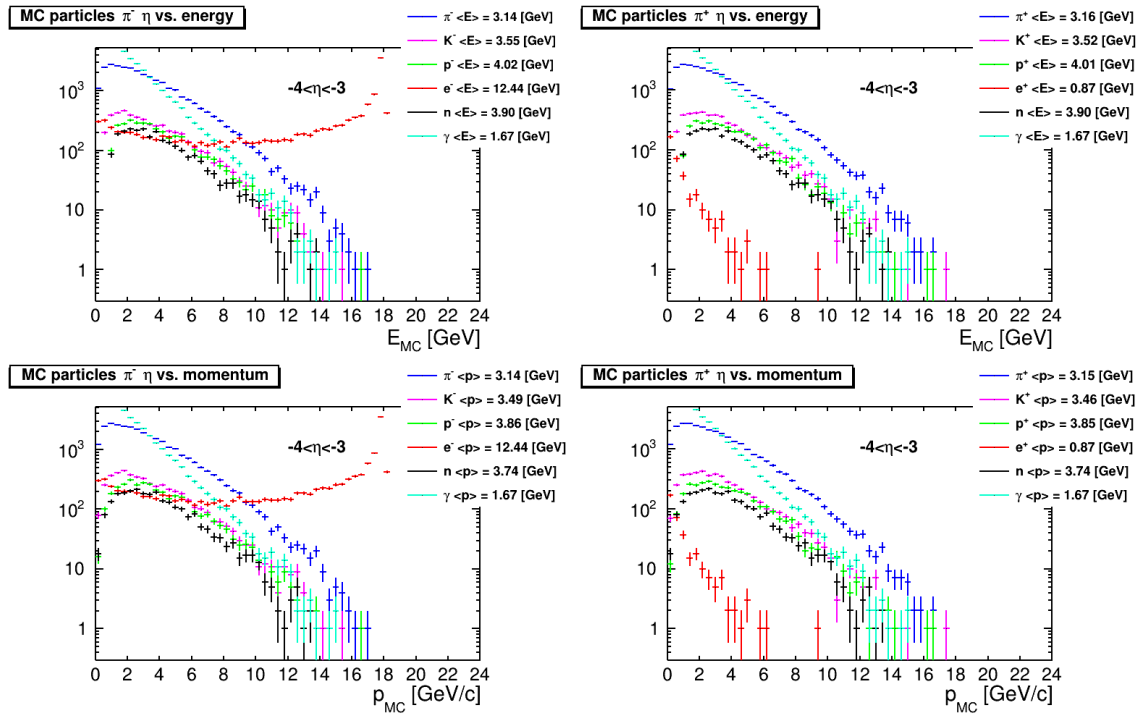


Figure 8.103: Top: Primary, generated particle E distributions in $-4.0 < \eta < -3.0$ range. Bottom: Primary, generated particle p distributions in $-4.0 < \eta < -3.0$ range.

8.3.6.2 The barrel hadronic calorimeter

Requirements The yellow report states the energy resolution of the mid-rapidity hadron calorimeter should be $85\%/\sqrt{E/\text{GeV}} + 7\%$. This requirement is driven by single jet measurements. While approximately 90% of the jet energy will be measured in the high precision tracking and electromagnetic calorimetry, the hadronic calorimeter is crucial for capturing the neutral hadron contribution. Figure 8.109 demonstrates the significance of the neutral hadron component.

A simple inclusion of the HCal energy does not necessarily improve the energy measurement. This is because of energy smearing of neutral particles. However, the HCal can be used as a neutral veto to select jets that do not contain neutral hadrons. This will provide the best energy resolution as demonstrated in Fig. 8.110.

Requirements from Radiation Hardness: Compared to LHC detectors, the various subsystems of the ePIC detector have moderate radiation hardness requirements. The Yellow Report states that at the calorimeters, the radiation level will be up to ≈ 3 krad/year electromagnetic and $10^{11} n/\text{cm}^2$ hadronic at top luminosity. However at the BHCAL, the radiation level will be only 10 rad electromagnetic and 0.1 rad hadronic, orders of magnitude lower than, *e.g.*, at the fHCAL. The on-detector electronics (SiPMs, H2GCROC3) are radiation tolerant. While the read-out boards (RDOs) contain FPGAs and therefore are radiation sensitive, they will sit well outside the detector, and therefore there is no concern for single-event upsets (SEUs). The neutron fluence will be low enough that it is not an issue for SiPMs. The neutron fluence is lower than in sPHENIX, where

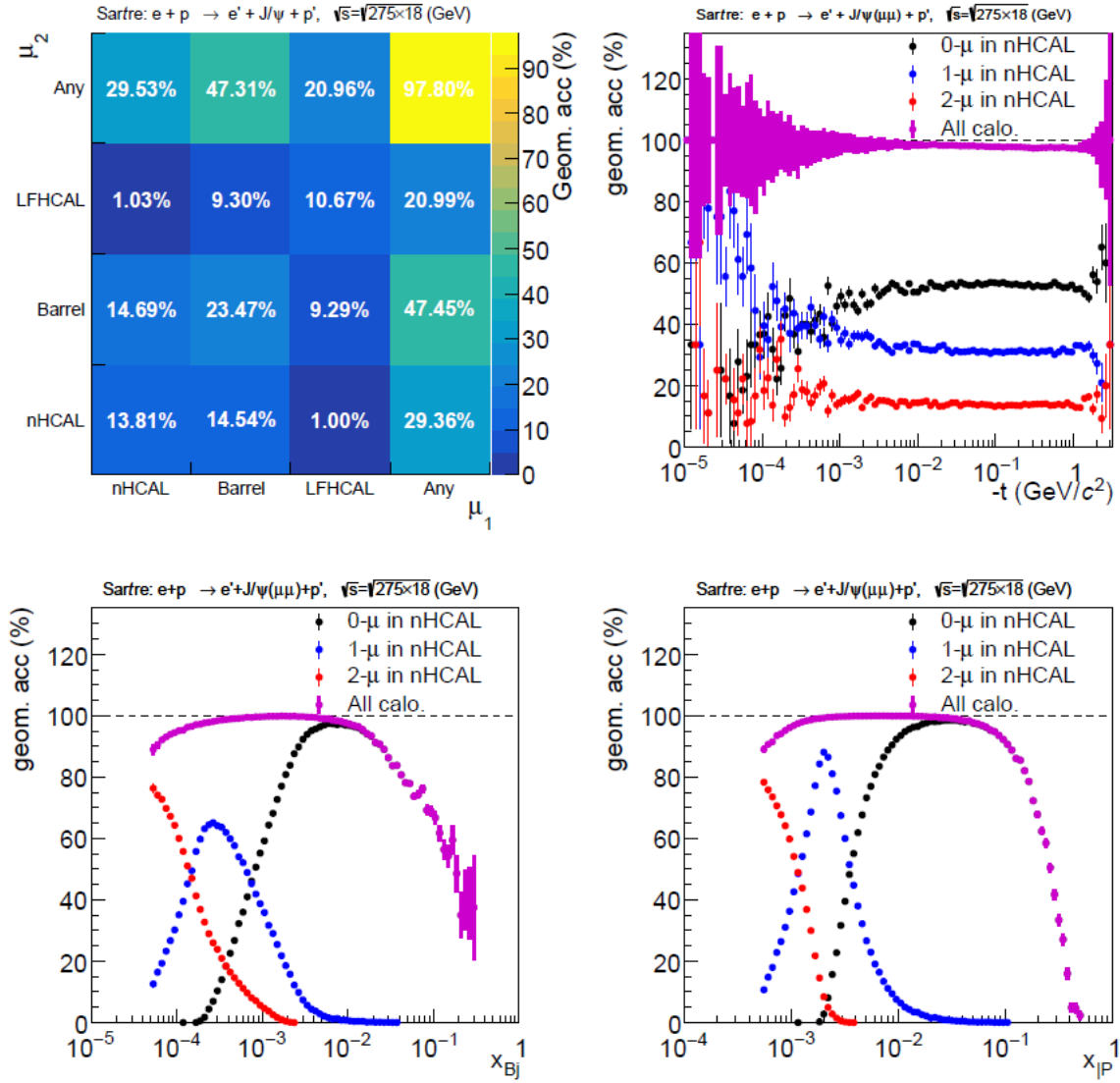


Figure 8.104: Acceptance of photoproduced $J/\psi \rightarrow \mu^+\mu^-$ in $e + p$ collisions at 18 + 275 GeV. Top left: Acceptance vs. μ_1 and μ_2 hitting different HCals. Top Right: Acceptance vs. $-t$ for different number of μ in nHCAL. Bottom Left: Acceptance vs. Bjorken x_{Bj} for different number of μ in nHCAL. Bottom Right: Acceptance vs. Pomeron x_P for different number of μ in nHCAL.

the dark current increase after the first year of running is consistent with expectations. Since the H2GCROC3s are used for the other calorimeter systems as well, there is no concern for the BHCAL.

Justification

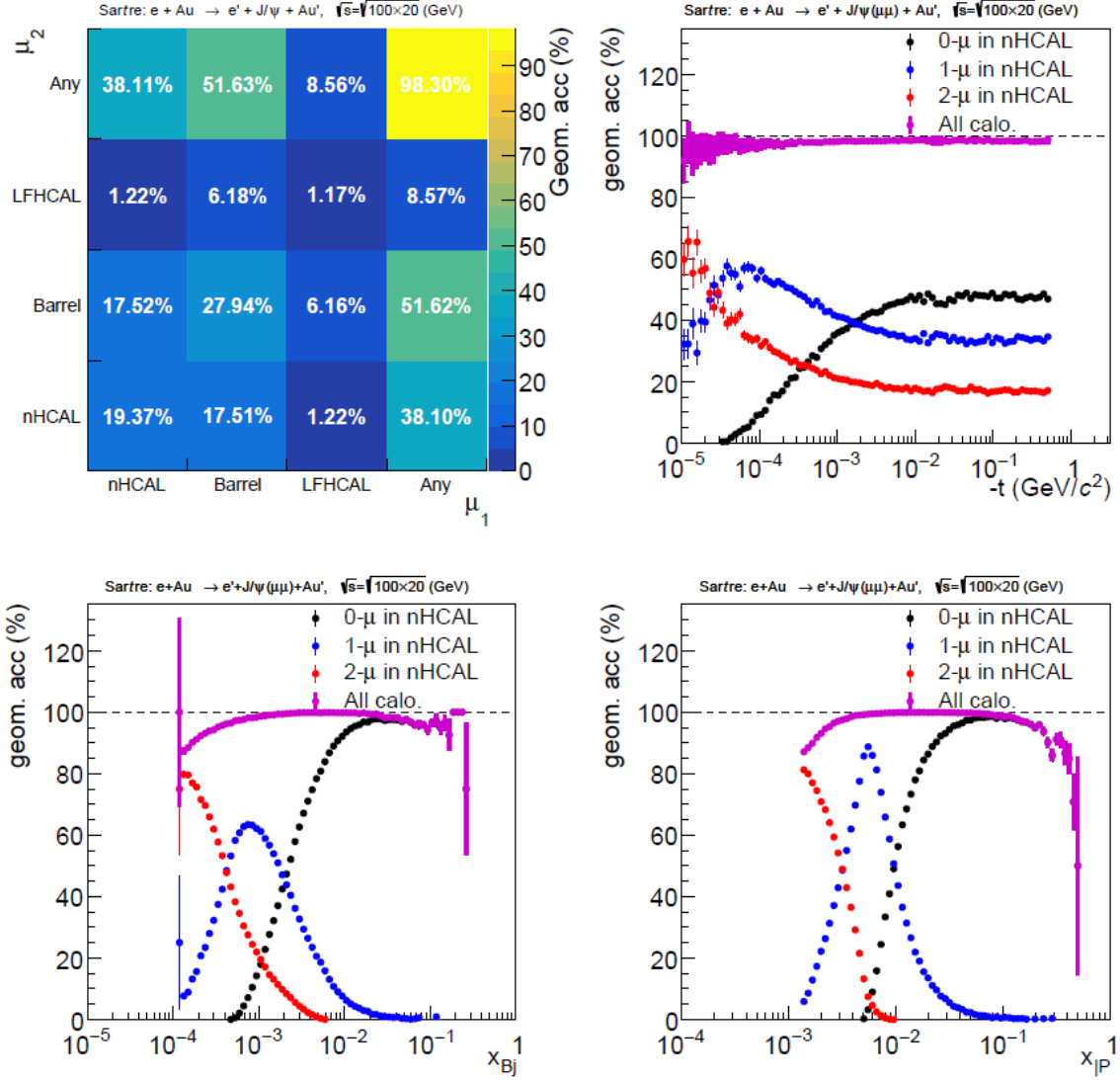


Figure 8.105: Acceptance of photoproduced $J/\psi \rightarrow \mu^+\mu^-$ in $e + p$ collisions at 20 + 100 GeV. Top left: Acceptance vs. μ_1 and μ_2 hitting different HCals. Top Right: Acceptance vs. $-t$ for different number of μ in nHCAL. Bottom Left: Acceptance vs. Bjorken x_{Bj} for different number of μ in nHCAL. Bottom Right: Acceptance vs. Pomeron x_P for different number of μ in nHCAL.

Device concept and technological choice: The sPHENIX outer HCal, which was demonstrated to have a single particle energy resolution of $75\%/\sqrt{E} \oplus 14.5\%$, will be repurposed for the EIC. It generally satisfies the requirements described in the previous section. The constant term of the energy resolution may be further improved by reading out the individual scintillator tiles instead of in towers.

The absorber material for the central hadronic calorimeter will also serve as the flux return for the solenoid magnet. Additional absorber will be added to the existing sPHENIX HCal steel plates to

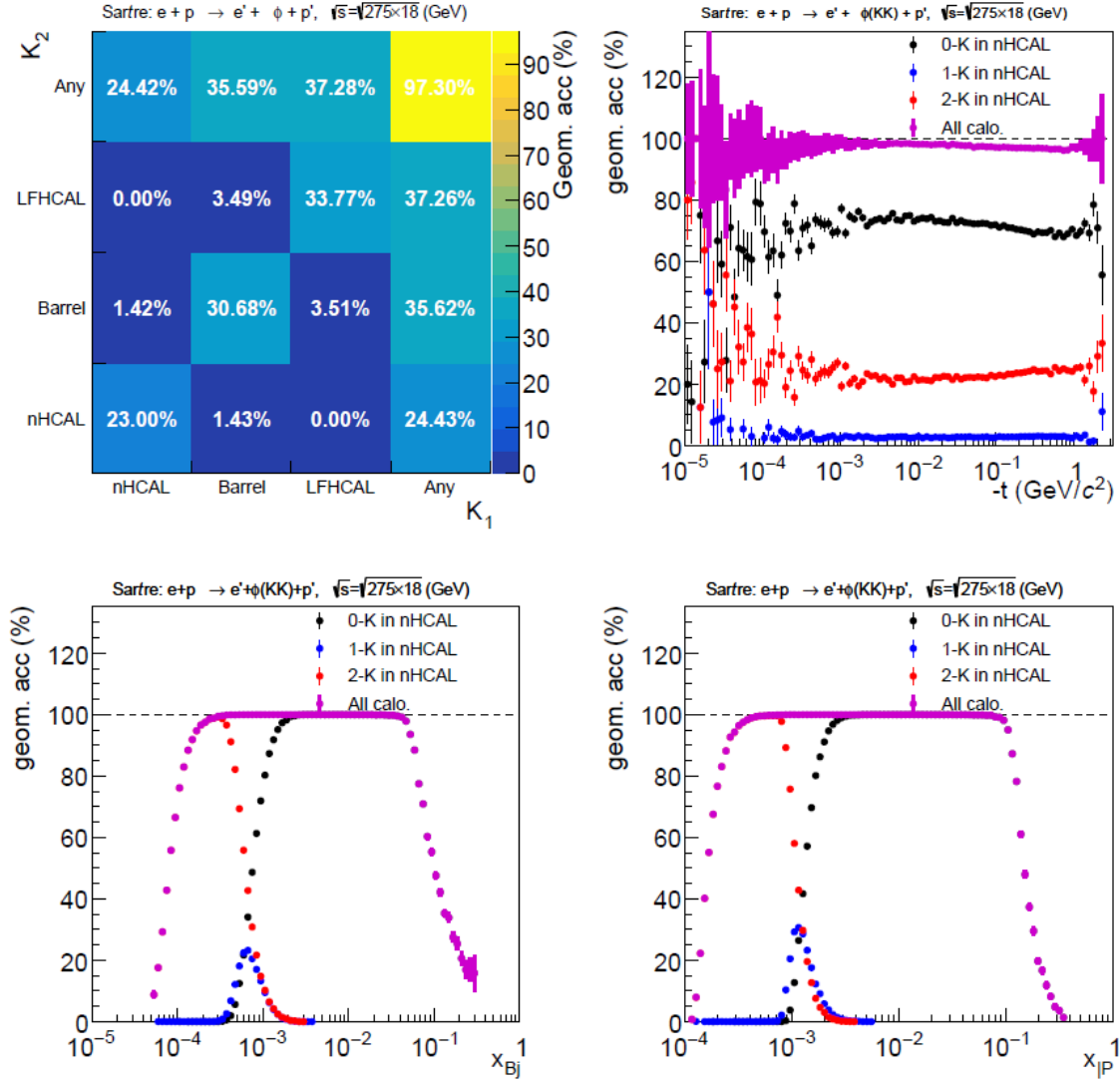


Figure 8.106: Acceptance of photoproduced $\Phi \rightarrow K^+K^-$ in $e + p$ collisions at $18 + 275$ GeV. Top left: Acceptance vs. K_1 and K_2 hitting different HCals. Top Right: Acceptance vs. $-t$ for different number of K in nHCAL. Bottom Left: Acceptance vs. Bjorken x_{Bj} for different number of K in nHCAL. Bottom Right: Acceptance vs. Pomeron x_P for different number of K in nHCAL.

4902 further contain the magnetic field.

4903 Subsystem description:

4904 General device description: The sPHENIX Outer HCal will be used as the basis of the ePIC
 4905 Barrel HCal. The sPHENIX OHCal design was developed and optimized through a series
 4906 of simulation and prototype studies. The sPHENIX hadronic calorimeter system consists of

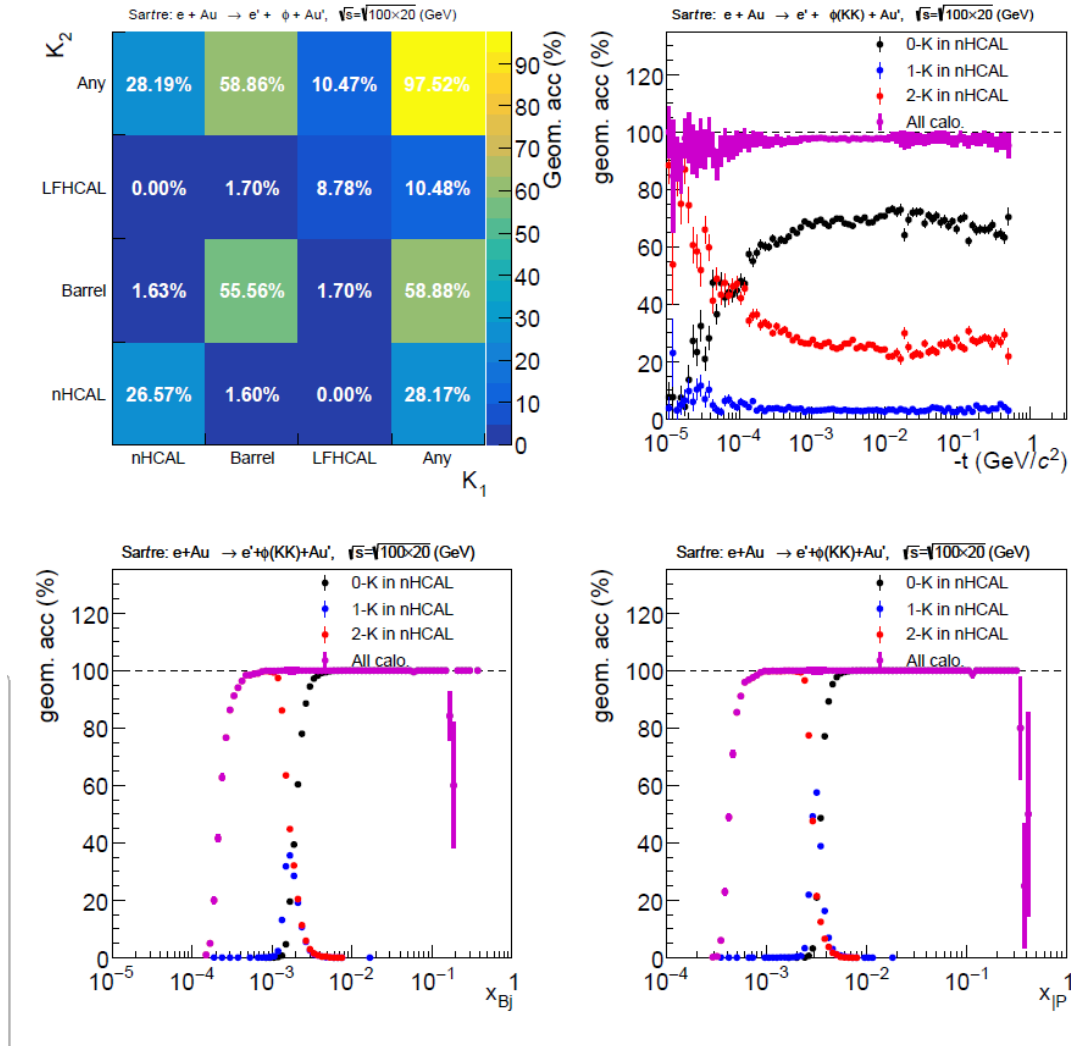


Figure 8.107: Acceptance of photoproduced $\Phi \rightarrow K^+K^-$ in $e + p$ collisions at 20 + 100 GeV. Top left: Acceptance vs. μ_1 and μ_2 hitting different HCals. Top Right: Acceptance vs. $-t$ for different number of K in nHCal. Bottom Left: Acceptance vs. Bjorken x_{Bj} for different number of K in nHCal. Top Right: Acceptance vs. Pomeron x_P for different number of K in nHCal.

two longitudinal compartments of calorimeter, one inside the solenoid, which serves both to measure the longitudinal development of electromagnetic showers thus providing additional discrimination between electrons and hadrons beyond determination of E/p in the electromagnetic shower, and as the first nuclear interaction length of the hadronic calorimeter. In the ePIC design the electromagnetic calorimeter will fill the space before the magnet. Therefore only the sPHENIX Outer HCal will be adopted in ePIC.

The basic calorimeter concept is a sampling calorimeter with tapered absorber plates tilted from the radial direction to provide more uniform sampling in azimuth. Extruded tiles of

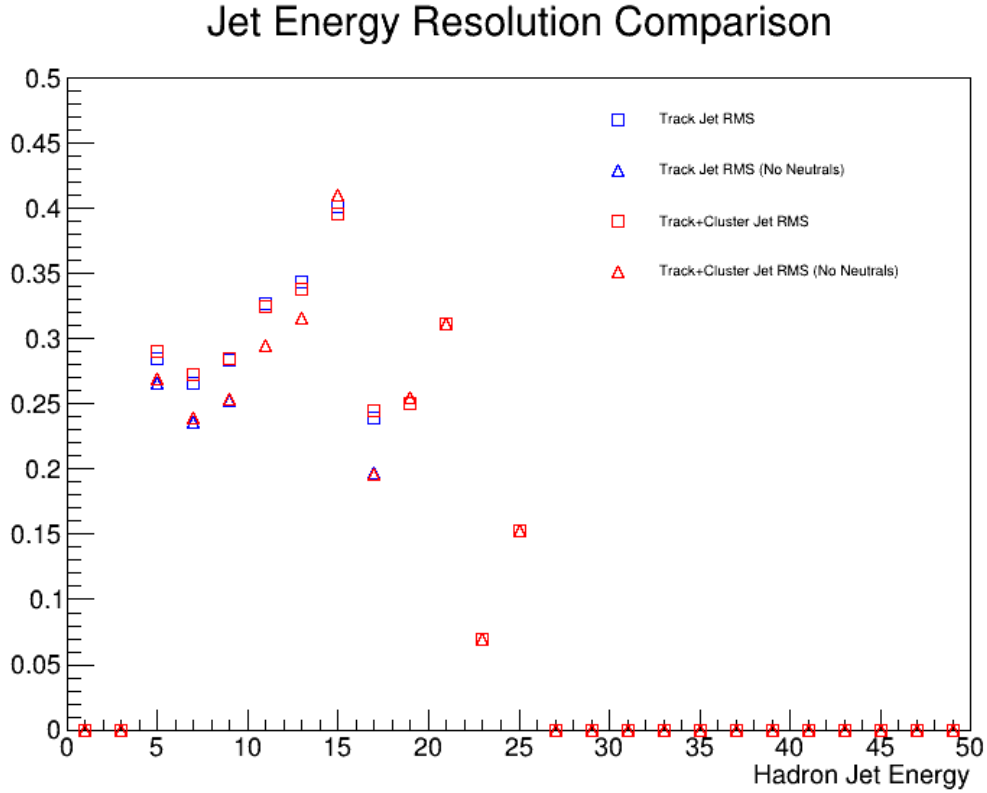


Figure 8.108: Energy resolution of jets vs. jet energy E compared for inclusive jets(squares) and jets with neutral veto(triangles). Track only jets(blue) are also compared to track and nHCal cluster jets(red).

plastic scintillator with an embedded wavelength shifting fiber are interspersed between the absorber plates and read out at the outer radius with silicon photomultipliers. The tilt angle is chosen so that a radial track from the center of the interaction region traverses at least four scintillator tiles as shown in Figure 8.111.

Each tile has a single SiPM. In the sPHENIX design, the analog signal from five SiPMs are ganged to a single preamplifier channel to form a calorimeter tower. In ePIC, each SiPM will be read out directly. Twelve tiles span 1.1 units of pseudorapidity in each direction as shown in Figure 8.112. Therefore the overall segmentation is $\Delta\eta \times \Delta\phi \sim 0.1 \times 0.02$.

Scintillator description:

The properties of the HCAL scintillating tiles are listed in Table 8.28. There are 12 different shaped tiles which span half of the η range of the detector. The detector is mirror-symmetric in η except in the region where the chimney for the cooling of the magnet reduces the depth of the HCAL.

A wavelength shifting (WLS) fiber is embedded in the tile to direct the light to the SiPM. The Kuraray single clad fiber was selected due to its flexibility and longevity which are critical for the multiple fiber bends in the design. The routing of the fiber was carefully designed to maximize the uniformity of light collection across the various tile shapes and avoid light

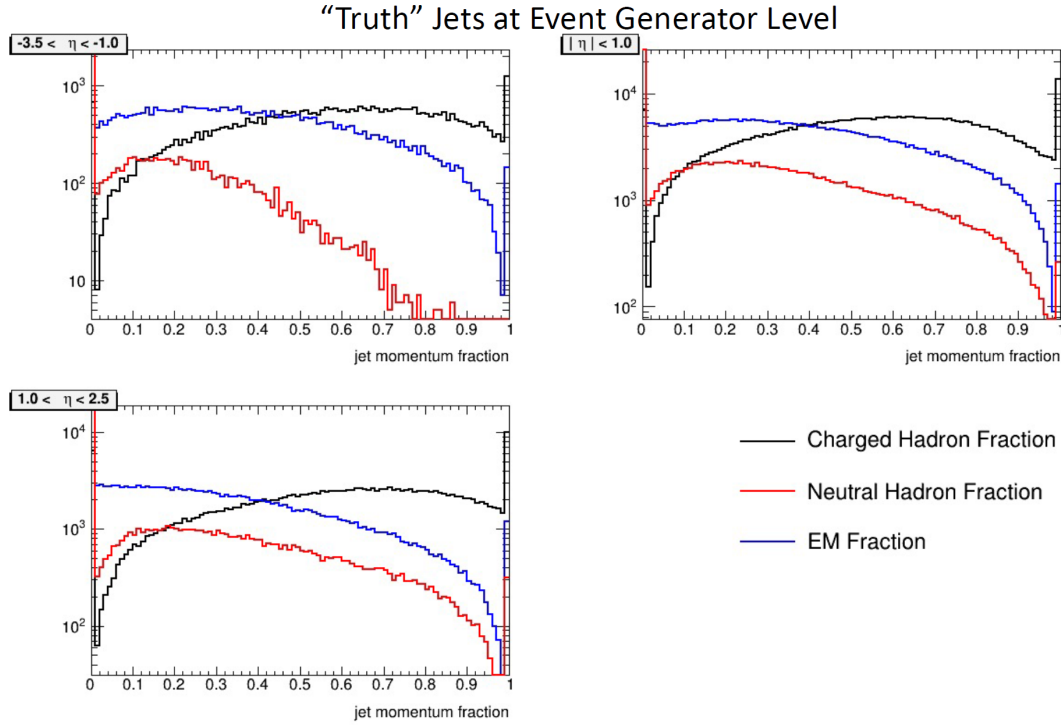


Figure 8.109: Jet charged and neutral Fractions in ECCE: The charged (black lines), neutral EM (blue lines), and neutral hadron (red lines) fractions of jets at the truth level in $\eta \in (-3.5, 1.0)$ (upper left panel), $|\eta| < 1$ (upper right panel), and $\eta \in (1.0, 3.5)$ (lower left panel). This illustrates that while jets are dominated by charged and neutral EM particles, there are still a distinct population of jets at central rapidity with a substantial neutral hadronic component.

leaks in the bends.

The Kuraray single clad fiber was chosen due to its flexibility and longevity which are critical in the geometry with multiple fiber bends. The properties of the HCAL wavelength shifting fibers are listed in Table 8.29

The fiber routing was designed so that any energy deposited in the scintillator is within 2.5 cm of a WLS fiber, and the bend radius of any turn in the fiber has been limited to 35 mm based on T2K and our own empirical experience with test tiles.

The two ends of a fiber are brought to the outer radius of a tile where a small plastic holder carries a 3×3 mm SiPM at 0.75 mm from the end of the polished fibers.

Table 8.30 summarizes the major design parameters of the HCAL, which is illustrated in Figure 8.111.

The Outer HCAL SiPM sensors and electronics are to be arranged on the outer circumference of the detector which reduces the radiation exposure of the SiPMs.

Sensors: The SiPMs used in sPHENIX will be replaced with newer S14160-3015PS Hamamatsu SiPMs. The SiPMs are still 3 mm X 3 mm and will be attached to a board that will fit

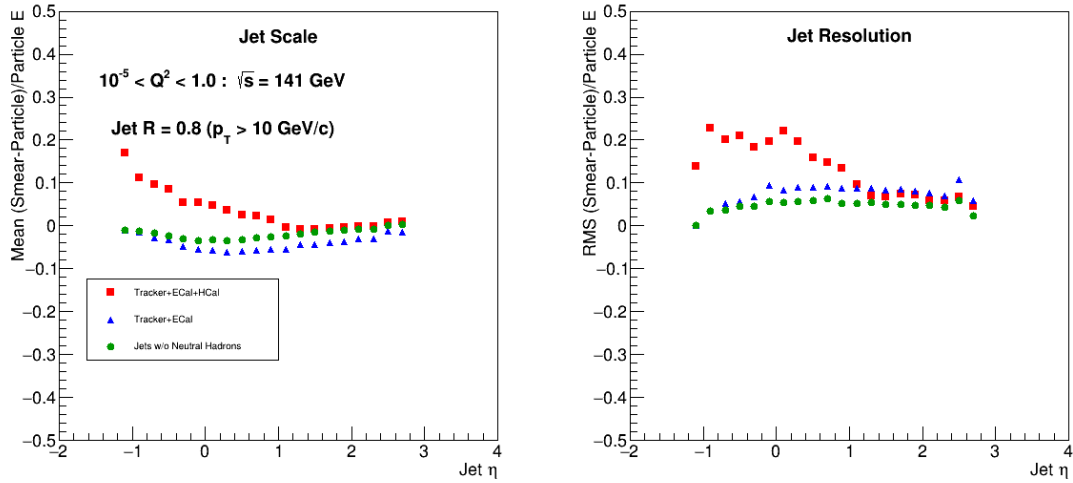


Figure 8.110: Demonstration of the effect of selecting only jets which do not contain a neutral hadron (green circles) on the jet energy scale (left) and resolution (right) as compared to the cases when all subsystems are used in jet finding (red squares) and when HCal information is excluded (blue triangles). Detector simulation and reconstruction was carried out using a fast simulation using Delphes. Figure 8.57 from the EIC Yellow Report.

Component	Description
Plastic	Extruded polystyrene
Scintillation dopant	1.5% PTP and 0.01% POPOP
Reflective coating	Proprietary coating by surface exposure to aromatic solvents
Reflective layer thickness	50 μ
Wrapping	one layer of 100 μ Al foil, one layer of 30 μ cling-wrap, one 100 μ layer of black Tyvek
Attenuation length in lateral (with respect to extrusion) direction	~ 2 -2.5 m
Wavelength shifting fiber	Single clad Kuraray Y11
Fiber size	1 mm round
Fiber core attenuation length	> 2 m
Optical cement	EPO-TEK 3015

Table 8.28: Properties of HCal scintillating tiles.

4947 in the same plastic connectors used in sPHENIX to mount the SiPM to the tile. Each SiPM
 4948 will be read out individually via the CALOROC. The electronics developed for the BHCal is
 4949 similar to other calorimeters and are described in a separate section.

4950 LED system: Each tile has a fiber that can be illuminated by an LED. The fibers will extend
 4951 to the edges of the detector where the electronics are also stationed.

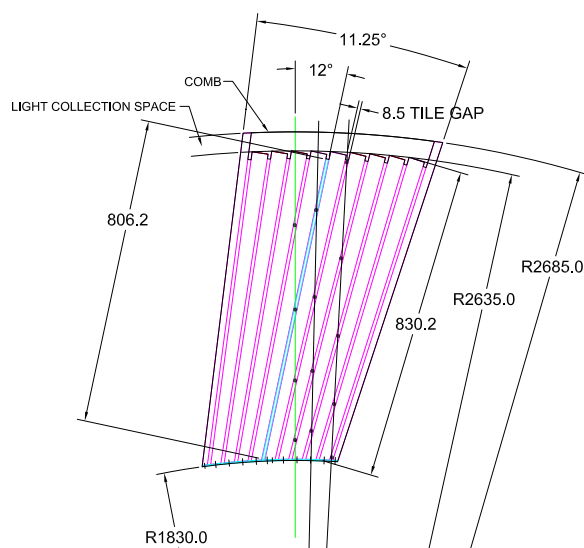


Figure 8.111: Transverse cutaway view of an sPHENIX Outer HCal module, showing the tilted tapered absorber plates. Light collection and cabling is on the outer radius at the top of the drawing.

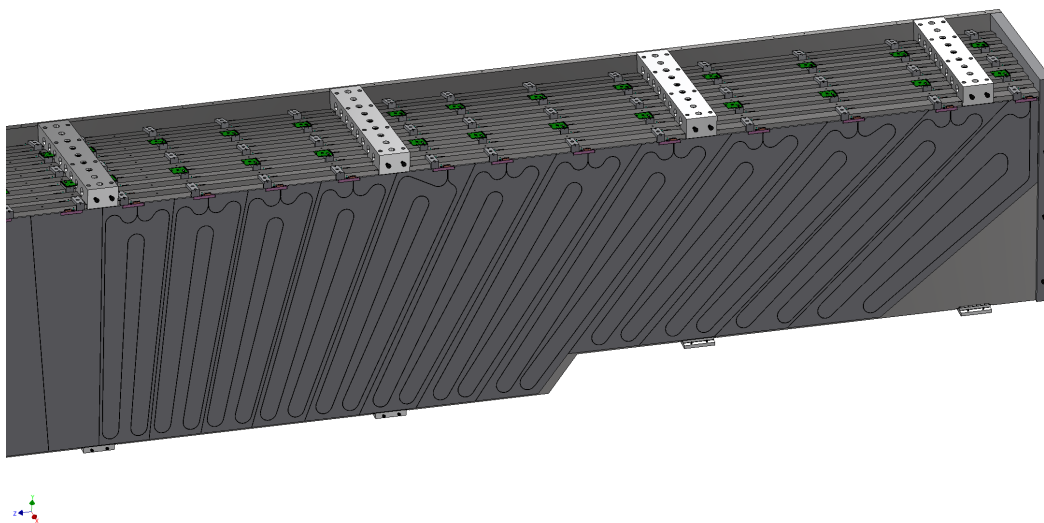


Figure 8.112: Scintillator tiles in a layer of the Outer HCal.

4952 **Performance** The performance of the BHCAL for ePIC has been studied in simulation as well as
 4953 tested through the experience of the HCals in sPHENIX. Thus far the sPHENIX HCal system has
 4954 performed very well in Au+Au and p+p collisions. One concern with using SiPM sensors is the
 4955 potential radiation damage in high energy collisions. The radiation exposure causes an increase in
 4956 the leakage currents and the measured noise. The leakage current measured in the commissioning
 4957 run for sPHENIX shows that leakage currents even an extrapolated are well below the limit. This is

Property	Description
Fiber diameter	1.0 mm
Formulation	200, K-27, S-Type
Cladding	single
Cladding thickness	2 percent of d (0.02 mm)
Numerical Aperture (NA)	0.55
Emission angle	33.7 deg
Trapping Efficiency	3.1 percent
Core material	polystyrene (PS)
Core density	1.05 g/cc
Core refractive index	1.59
Cladding material	Polymethylmethacrylate (PMMA)
Cladding density	1.19 g/cc
Cladding refractive index	1.49
Color	green
Emission peak	476 nm
Absorption Peak	430 nm
Attenuation length	> 3.5 m
Minimum bending radius	100 mm

Table 8.29: Properties of Kuraray Y-11 (200) wavelength shifting fibers.

Parameter	Units	Value
Inner radius (envelope)	mm	1820
Outer radius (envelope)	mm	2700
Length (envelope)	mm	6316
Material	1020 low carbon steel	
Number of tiles in azimuth ($\Delta\phi$)		320
Number of tiles in pseudorapidity ($\Delta\eta$)		24
Number of electronic channels	$320 \times 24 =$	7680
Number of modules (azimuthal slices)		32
Total number of absorber plates	$5 \times 64 =$	320
Tilt angle (relative to radius)	$^{\circ}$	12
Absorber plate thickness at inner radius	mm	10.2
Absorber plate thickness at outer radius	mm	14.7
Gap thickness	mm	8.5
Scintillator thickness	mm	7
Module weight	kg	12247
Sampling fraction at inner radius		0.037
Sampling fraction at outer radius		0.028
Calorimeter depth	λ	3.8

Table 8.30: Design parameters for the Barrel Hadronic Calorimeter w/o additional absorber, based on the sPHENIX Outer Hadronic Calorimeter.

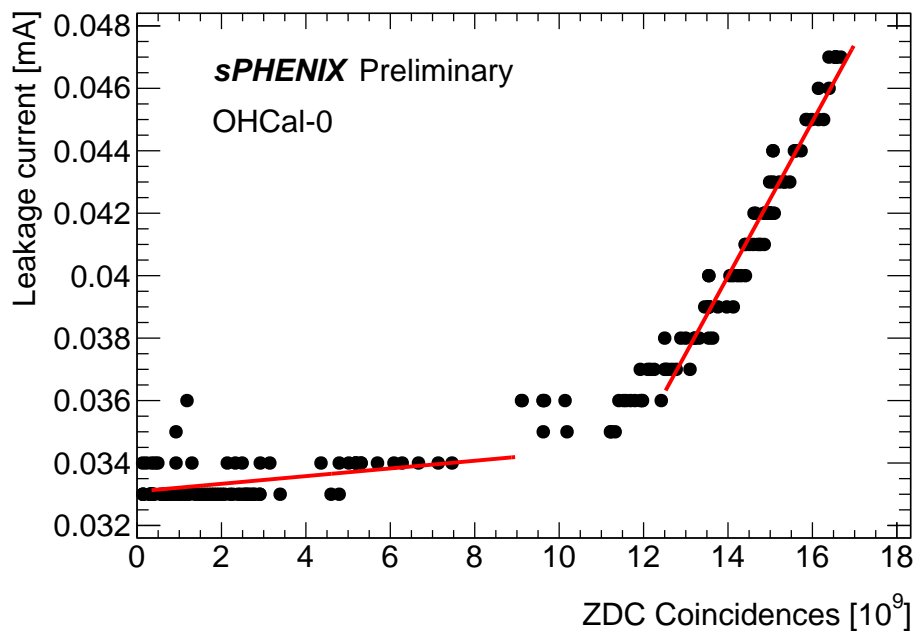


Figure 8.113: Leakage current in HCal measured once per fill as a function of total number of ZDC coincidence hits

4958 expected since the large amount of material in front of the SiPMs reduces their radiation exposure.

4959 Fig. 8.113

4960 Simulations demonstrate the energy deposition for muons and DIS events. For muons, a clear MIP
4961 peak is observed as shown in 8.114. In contrast, energy distributions for DIS events are shown in
4962 8.115.

4963 The resolution of calibrated single pion energies is shown in Figure 8.116

4964 Implementation

4965 **Subsystem mechanics and integration:** The BHCal is the outermost central detector and will
4966 need to be installed first. The steel serves as the flux return for the solenoid magnet.

4967 **Calibration, alignment and monitoring:** The sPHENIX HCal was primarily calibrated using
4968 cosmic ray measurements. In addition to cosmic ray measurements LEDs are used to monitor the
4969 tiles. These monitoring systems will be crucial for properly calibrating the detector over time to
4970 account for aging effects of the tiles and radiation damage to the SiPMs.

4971 Status and remaining design effort:

4972 R&D effort: The basic design is set by reusing the sPHENIX outer HCal. However, the elec-
4973 tronics and details of the LED system are still being developed.

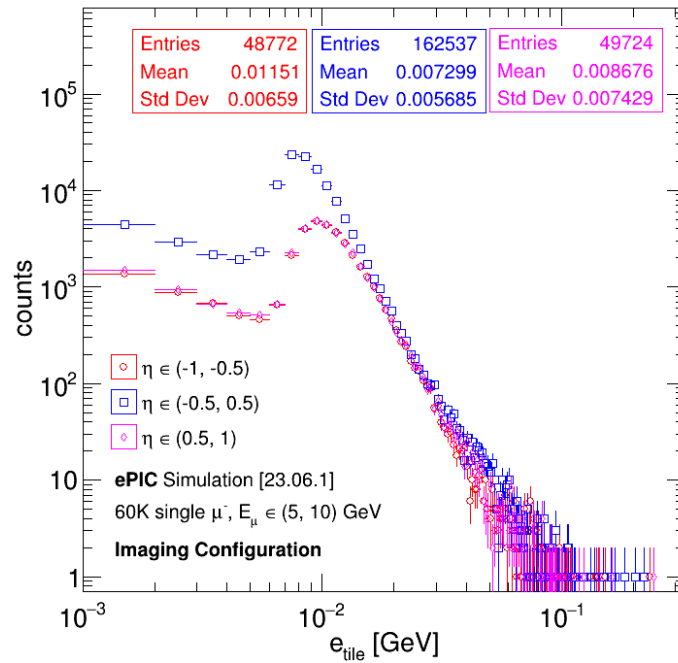


Figure 8.114: Muon energy deposited on tile: energy deposited on a given scintillator tile (i.e. the sum of G4 hits for a tile) by single GeV/c μ^- with energies between 5 and 10 GeV/c as a function of μ^- pseudorapidity. Distributions were simulated using the 2023.06.1 simulation geometry. A clear MIP peak is observed.

4974 **Environmental, Safety and Health (ES&H) aspects and Quality Assessment (QA plan-**
 4975 **ning:**

4976 **Construction and assembly planning:** After RHIC running concludes, sPHENIX will be dis-
 4977 assembled. When a sector of the outer HCal is removed from sPHENIX, the tiles within the sector
 4978 will be extracted. The tiles will be shipped to Georgia State University and University of New
 4979 Hampshire where test stands are ready to quantify the response of the tiles to cosmic rays
 4980 and record their relative performances. These initial tests proved to be very useful in the initial
 4981 calibration procedure in sPHENIX. For sPHENIX these tests were also crucial in the quality assess-
 4982 ment procedure which required that the tile performance deviate no more than 20% from the mean
 4983 for that tile shape. Similar performing tiles were also grouped together into towers for calibration
 4984 purposes.

4985 After the tiles have been tested, they will be shipped back to BNL to be installed in the new sec-
 4986 tors. Additional material will have been added to the sPHENIX steel sectors. Stefan Bathe from
 4987 Baruch College will oversee the assembly process at BNL. He served as the level 3 manager for the
 4988 sPHENIX HCals and likewise oversaw the assembly of the inner and outer HCals for sPHENIX.
 4989 After inserting the tiles in the proper sector locations, an SiPM will be connected to each tile. The
 4990 cables will be installed and connected to a test set up for the electronics to confirm that each tile can
 4991 be readout. Cosmic ray tests of each sector will also be performed which will confirm the relative
 4992 tile by tile calibration factors.

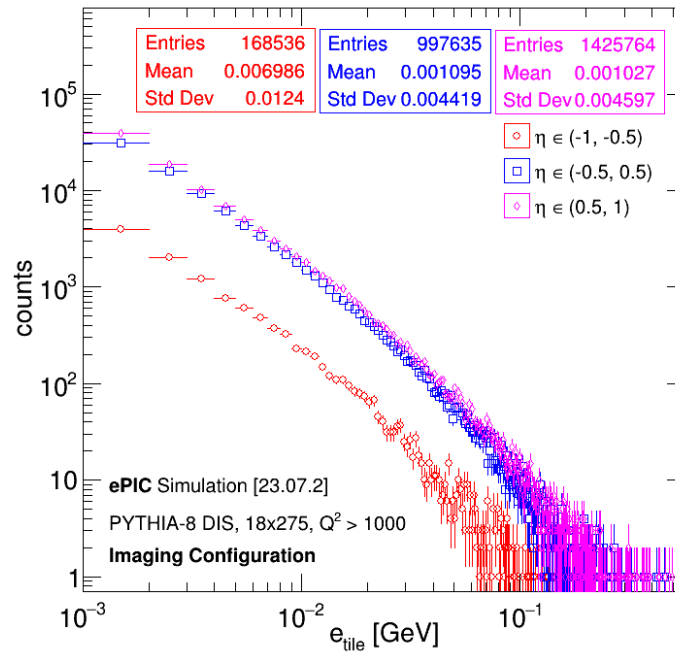


Figure 8.115: DIS energy deposited on tile: energy deposited on a given scintillator tile (i.e. the sum of G4 hits for a tile) in 18×275 NC DIS events for $Q^2 > 1000 \text{ GeV}^2$ for all particles in the events as a function of their pseudorapidity. Distributions were simulated using the 2023.07.2 simulation geometry.

Collaborators and their role, resources and workforce: Baruch College and GSU groups led by Bathe and Connors respectively have extensive experience working with the sPHENIX HCals. They will oversee the assembly and tile testing procedures for the ePIC BHCAL as they did for sPHENIX. In addition, UNH, BNL and others will be extremely important for ensuring the assembly timeline is achieved. Norbert Novitzky from Oak Ridge National Lab is developing the electronics and is collaborating with members of the BNL group that conducted the sPHENIX RD to test the electronics with the sPHENIX HCal prototype.

Risks and mitigation strategy: The BHCAL depends on previously tested technologies which minimizes the risks associated with it. A limited number of spare tiles exist at Georgia State University in case any tiles are damaged. There are two ways we can monitor the tiles once they are installed into EPIC. The LED system is useful for quickly testing the tiles on a regular basis while the cosmic ray studies require a long time to collect sufficient data.

8.3.6.3 The forward endcap hadronic calorimeter

Requirements

Requirements from physics:

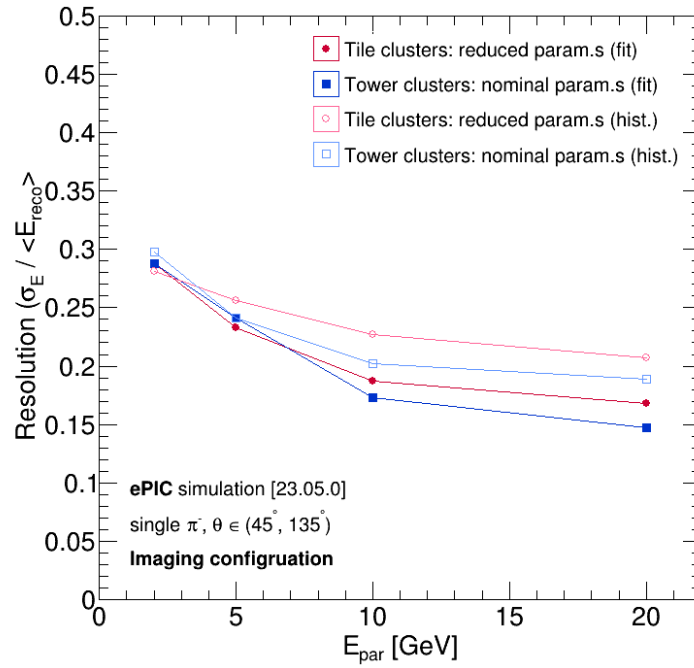


Figure 8.116: Resolution of calibrated single pion energies: Resolution of calibrated single π^- energies. Distributions were simulated using the 2023.05.0 simulation geometry. Red markers indicate the output of the calibration using tile-based clusters from the BHCAL, while blue markers indicate the output of the calibration using tower-based clusters from the BHCAL. The closed markers indicate the resolution as obtained by comparing the mean of a gaussian fit to the calibrated energies vs. the particle energies, while the open markers indicate the resolution as obtained by directly comparing the mean of the calibrated energies vs. the particle energies. Calibration is carried out by the LD model.

5008 **Requirements from Radiation Hardness:**

5009 **Requirements from Data Rates:**

5010 **Justification**

5011 **Device concept and technological choice:**

5012 **Subsystem description:**

5013 General device description:

5014 Sensors:

5015 FEE:

5016 Other components:

5017 **Performance**

5018 **Implementation**

5019 **Services:**

5020 **Subsystem mechanics and integration:**

5021 **Calibration, alignment and monitoring:**

5022 **Status and remaining design effort:**

5023 R&D effort: Add text here.

5024 E&D status and outlook: Add text here.

5025 Other activity needed for the design completion: Add text here.

5026 Status of maturity of the subsystem: Add text here.

5027 **Environmental, Safety and Health (ES&H) aspects and Quality Assessment (QA plan-**
5028 **ning:**

5029 **Construction and assembly planning:**

5030 **Collaborators and their role, resources and workforce:**

5031 **Risks and mitigation strategy:**

5032 **Additional Material** Add text here.

5033 **8.3.7 Far forward detectors**

5034 The ePID far-forward detectors are required to enable essentially the entirety of the exclusive
5035 physics program at the EIC, where final-states involve protons, neutrons, photons, and various
5036 other particles at $\eta > 4.5$. There are four subsystems, all integrated with the outgoing hadron
5037 beamline between ~ 5.5 and 39 meters from the interaction point. The far-forward subsystems are
5038 summarized in Fig. 8.117, and details are presented in subsequent subsections.

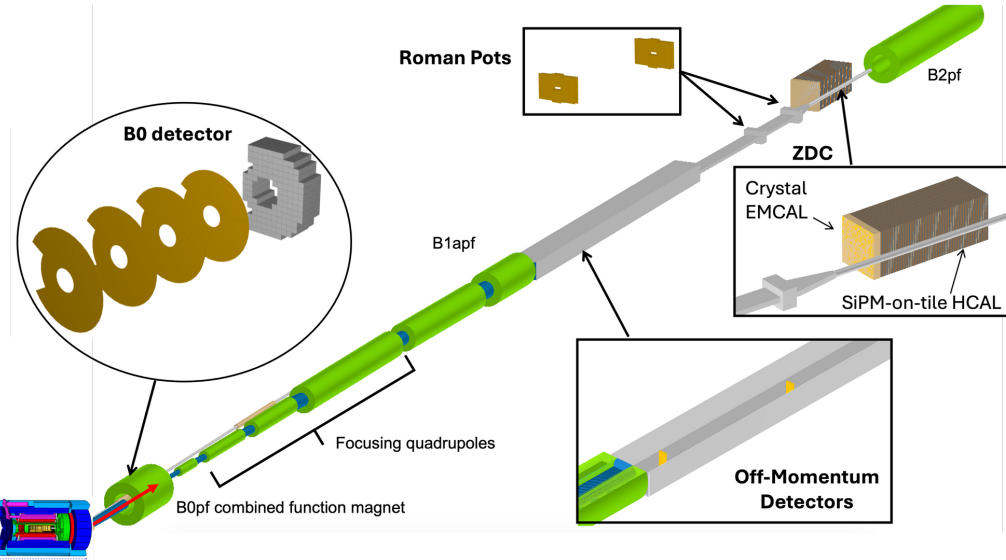


Figure 8.117: All four far-forward subsystems in the outgoing hadron beam direction. The green cylinders are accelerator dipole and quadrupole magnets.

8.3.7.1 The detectors in the B0 bending magnet

Requirements

Requirements from physics: The B0 magnet bore will contain two detectors: a charged particle tracker and an electromagnetic calorimeter. Both will have acceptance covering the angular region from 5.5 to 20 mrad. Given the mechanical constraints imposed by the detectors' location in the magnet (and respecting the beam lines themselves) the detectors will be highly asymmetric for angles greater than ~ 13 mrad. To maximize acceptance it's required that there be minimal dead areas in the instrumentation especially for angles less than ~ 13 mrad. The tracker should have momentum resolution up to 6% for protons, and timing precision sufficient to deal with vertex smearing. The calorimeter should have a large dynamic range with sensitivity to both soft, $O(100 \text{ MeV})$, and hard, $O(100 \text{ GeV})$, photons. The energy resolution should be less than $8\%/\sqrt{E} \oplus 4\%$, with position resolution $\lesssim 10 \text{ mm}$. We note that for some analysis use cases the calorimeter will function as a photon 'tagger' rather than an actual calorimeter, and so in some regions of acceptance (where the mechanical constraints are acute) this resolution may not be achieved but having the acceptance instrumented is still valuable.

Requirements from Radiation Hardness: The expected non-ionizing radiation dose at a longitudinal distance of 692 cm from the interaction point (near the fourth tracking layer and the front of the calorimeter) is approximately 3.1×10^{11} 1 MeV neutron equivalent per square centimeter for 100 fb^{-1} . At this location the ionizing dose can reach $O(100) \text{ kRad}$.

Requirements from Data Rates: Add text here.

5059 Justification

5060 **Device concept and technological choice:** The charged particle tracker will be composed of
 5061 four layers instrumented with silicon. The layers are approximately equidistantly placed at dis-
 5062 tances between 590 and 690 cm from the interaction point, which given the field inside the mag-
 5063 net allows satisfactory proton measurement and momentum reconstruction. The electromagnetic
 5064 calorimeter is composed of 135 scintillating PbWO_4 crystals, each one $2 \times 2 \times 20 \text{ cm}^3$ (the long
 5065 direction is on the z axis). We note that the crystals are the same as those used in the EEEMCal.

5066 Subsystem description:

5067 General device description: Each tracking layer has a transverse layout to cover as much of
 5068 the angular acceptance as possible given the mechanical constraints, as illustrated in Figure
 5069 ???. The crystals of the calorimeter are arranged in a similar way for the same reason.

5070 Sensors: For the tracking detectors AC-coupled low-gain avalanche diodes (AC-LGADs) are
 5071 chosen due to their capability to provide both high-precision space and time information. In
 5072 order for the spatial resolution to meet the performance requirements charge sharing must
 5073 be implemented in the reconstruction. We note that this technology is broadly in use within
 5074 ePIC, and its particular implementation for the B0 detectors should be very similar to the
 5075 Roman Pots/Off Momentum Detectors. For the calorimeter the PbWO_4 crystals produce
 5076 light peaking at $\sim 420 \text{ nm}$, which will be read out by SiPM. Four $6 \times 6 \text{ mm}^2$ SiPM will be
 5077 used per crystal, 3 with 15 micron pitch and one with a 10 micron pitch (likely Hamamatsu
 5078 S14160-6015PS and S14160-6010PS, respectively). The larger pitch SiPM have fewer pixels
 5079 but higher efficiency making them appropriate for smaller signals, whereas the smaller pitch
 5080 SiPM will be utilized for the higher energy particle signals.

5081 FEE: Following the Roman Pots/Off Momentum Detectors, the ASICs will be readout using
 5082 LPGBT in-place of FPGAs due to the high-radiation environment in which these detector
 5083 will be located. AC-LGAD + ASIC modules will be connected to the LPGBT, which will
 5084 be coupled to a VTRX+ to convert the signals to a fiber to send off to the DAW system. The
 5085 electronics to process the SiPM signal are still to be worked out but expected to follow closely
 5086 the scheme of the EEEMCal.

5087 Other components: Add text here.

5088 **Performance** The key physics task of the B0 tracker system is the measurement of protons, and
 5089 this is summarized by the acceptance and transverse momentum resolution shown in Figure 8.118.
 5090 The B0 calorimeter's acceptance for photons is shown in Figure 8.119. The calorimeter seeks to
 5091 measure photons over a very large range. The performance of the detector, in particular the energy
 5092 resolution, is shown separately for low and high energy photons in Figure 8.120. The higher energy
 5093 photons are evaluated based on a signal to a single 10 micron pitch SiPM, whereas the lower energy
 5094 photon performance assumes three 15 micron pitch SiPM per crystal.

5095 Implementation

5096 **Services:** For the trackers low voltage ($\sim 3\text{V}$) and high voltage ($\sim 150\text{V}$) supplies for the operation
 5097 of the ASICs and the bias supply, as well as slow controls for the voltages and the DAQ system.

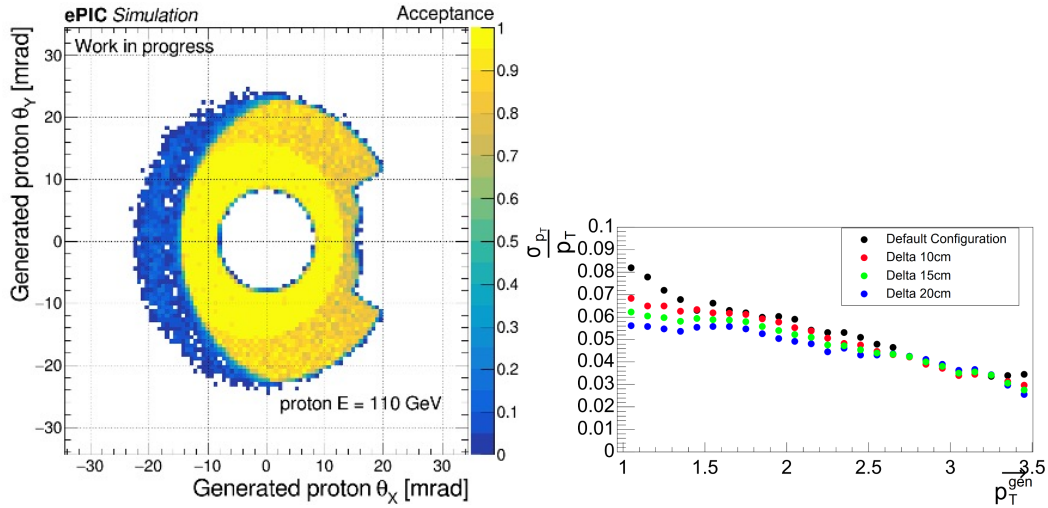


Figure 8.118: Left: The B0 tracker's acceptance of protons ($E=110$ GeV), as a function of θ_x and θ_y . **PLACEHOLDER NEEDS TO BE REMADE W/REAL B FIELD** Right: The p_T resolution for protons reconstructed in the B0 tracker. **PLACEHOLDER NEEDS TO BE REMADE WITH FINAL LOCATIONS, FINAL TRACKING, PROPER LABELLING ETC**

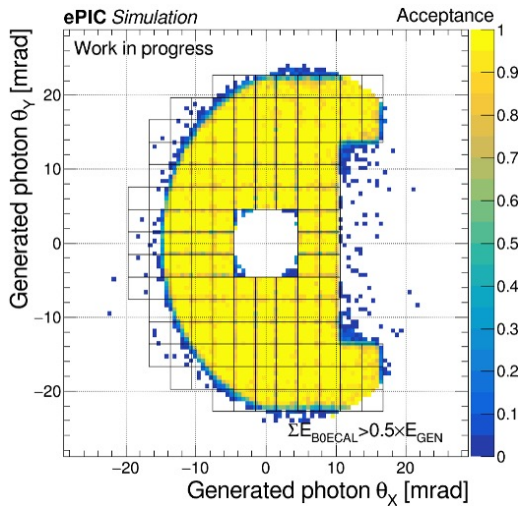


Figure 8.119: The B0 EM calorimeter's acceptance of photons with a **substantial (for now half their energy)** deposit in a calorimeter crystal. **PLACEHOLDER - SPLIT HARD SOFT, FIX CRYSTAL ALIGNMENT**

5098 The SiPM for the calorimeter need a bias of ($\sim 5V$). The cooling system is still to be worked out, but
 5099 is expected to be air based (unlike the in-vacuum challenge of the similar instrumentation for the
 5100 Roman Pot/Off Momentum Detectors).

5101 **Subsystem mechanics and integration:** The integration of the detectors into the B0 magnet
 5102 bore is a significant undertaking. The space for the detectors (and services) is quite limited and the
 5103 installation procedure introduces more constraints. After the vacuum valve is closed there is only

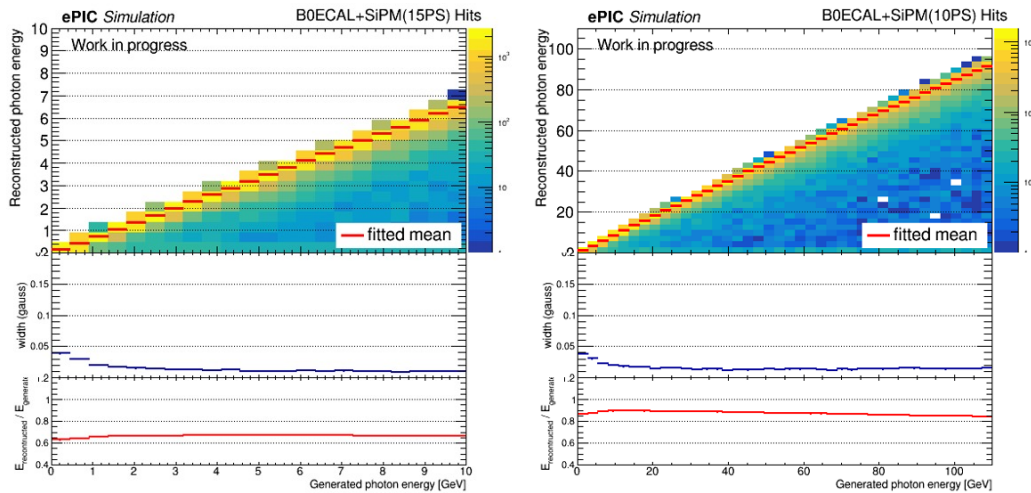


Figure 8.120: The energy reconstructed and associated resolution for the B0 EM calorimeter of photons with $\theta < 13$ mrad in the soft (left) and hard (right) energy reconstruction regimes.
 PLACEHOLDER - zoom soft photon, update reflectivity

about 10 cm of clearance in front of the magnet and this precludes installation of the 20 cm crystals. To address this difficulty, the crystals will be installed prior to closing the valve closing and the beam commissioning. At this point *only* the crystals will be installed to avoid the risk of damaging the other components during the commissioning. Following this the SiPM and electronics of the calorimeter will be installed. Both installations as well as the final positioning of the detectors will be via a rail system: detector components will be loaded onto the rails system outside the magnet and inserted in to it. We note that the detectors will be installed as sub-detectors not as monolithic pieces covering the entire acceptance.

Calibration, alignment and monitoring: Add text here.

Status and remaining design effort:

R&D effort: There is still work to be done for full detector operation. For the trackers especially demonstrating effective reconstruction using charge sharing and for the calorimeter the multi-SiPM readout. For both the trackers and calorimeter this includes optimizing the acceptance in concert with the installation procedure.

E&D status and outlook: Add text here.

Other activity needed for the design completion: Completion of the mechanical rail system is underway and this includes a final scheme of subdividing the detectors into sub-detectors accordingly.

Status of maturity of the subsystem: Add text here.

Environmental, Safety and Health (ES&H) aspects and Quality Assessment (QA planning: Add text here.

Construction and assembly planning: The tracking system should benefit from the BNL local expertise and production capabilities for AC-LGAD and from there ‘directly’ to installation readiness. The calorimeter sub-components may be prepared either on or off site, but in any case the final assembly can not be separated from the installation procedure.

Collaborators and their role, resources and workforce: The Israeli ePIC consortium (in particular BGU and TAU) are playing the main role in the detector development and this will continue through installation/operation. There is also very significant participation from BNL generally, and especially for the common AC-LGAD instrumentation.

Risks and mitigation strategy: For the trackers the largest risk is the necessity to utilize charge sharing in the reconstruction to obtain the needed momentum resolution. Other detection technologies have been considered to mitigate this risk (with smaller pixels) but to this point none has been identified as an appropriate alternative. For both detectors (and even more acutely for the calorimeter) the installation challenge risks limiting the detector acceptance.

Additional Material Add text here.

8.3.7.2 The roman pots and the off-momentum detectors

Requirements

Requirements from physics: Measurement of protons at various rigidities, with rigidity defined by ratio of the proton momentum to that of the beam itself, and with scattering at angles $< 5\text{mrad}$ requires detectors integrated directly into the hadron beamline in the form of Roman pots (RP). The Off-Momentum detectors (OMD) enable tagging and reconstruction of spectator protons from the breakup of light nuclei (e.g. deuterons and He-3), which produce protons at rigidities $< 65\%$, with deuterons producing protons at an average of $\sim 50\%$ rigidity. For the Roman pots, achieving acceptance down to 0 mrad is impossible due to the presence of the hadron beam itself, so the low- θ (low- p_T) acceptance is essentially entirely driven by the focusing quadrupoles (machine optics) before and after the interaction point. For IP-6, the choice of low- β^* optics to maximize luminosity (so-called “high divergence”) means the transverse beam size, $\sigma_{x,y} \approx \sqrt{\beta_{x,y}(z_{RP}) \times \epsilon_{x,y}}$, where $\beta_{x,y}(z_{RP})$ are the beta-functions in (x,y) at the Roman pots location and $\epsilon_{x,y}$ is the emittance for the machine, is larger, worsening the acceptance at the expense of luminosity. Generally, $10\sigma_{x,y}$ is the average “safe distance” for the Roman pots to operate. Conversely, a choice can be made to reduce luminosity to improve low- θ acceptance at the Roman pots location, normally referred to as “high acceptance” optics. Given this set of operational parameters for the machine itself, it is required that the sensor packages have minimal dead area at the edges to take maximum advantage of the machine optics during data taking runs.

For resolution, the detectors must deliver p_T -resolution better than 10%.

Requirements from Radiation Hardness: Maximal radiation doses are shown to be $< 10^{12}$ 1 MeV neutron equivalent for NIEL radiation, while ionizing doses are around 1 krad for the Roman pots region of ePIC [will add plot here, or reference section on the radiation].

Requirements from Data Rates: Rates during normal operations, with expected vacuum of 10^{-9} mbar, are a few Hz/channel. However, the beam halo could potentially provide rates of 30-50kHz at $\sim 10\sigma$ from experience of Roman pots at STAR. While the EIC hadron beam will have many differences to the RHIC hadron beam, it's hard to estimate the full rate impact of the beam halo without an appropriate simulation. This is something to be done in the coming year as the machine develops.

Justification

Device concept and technological choice: The basic concept of Roman pots detectors for measuring protons near the beam is not new and has been employed at HERA, RHIC, and the LHC, among other collider facilities. In the case of the EIC, the Roman pots (and OMD) need to be able to make measurements with challenges different to those in previous facilities. Studies from the EIC generic R&D program, in particular eRD24, demonstrated that the RP detectors need to have both high spatial ($\sim 140\mu\text{m}$) and timing ($\sim 35\text{ps}$) resolutions, a challenge to deliver with one subsystem. As silicon detector technology has advanced, an evolved version of the DC-coupled Low Gain Avalanche Diode (DC-LGAD) sensor, normally used for high-resolution timing detectors [Add reference here later], has come to the fore in the form of an AC-coupled version, known as the AC-LGAD. The AC-LGADs allow for pixilization and can meet the requirements of the RP and OMD subsystems, as was the goal of eRD24.

An additional challenge with operation of the RP and OMD systems is the operation of these detectors in vacuum. The subsystems themselves are large enough to prohibit use of the conventional "pot" vessels used to protect the detectors in other colliders, and therefore necessitate the inclusion of the sensor planes directly into the machine vacuum, providing unique challenges for cooling and shielding.

add figures of full detector layout here later when I have a better CAD picture to use.

Subsystem description:

General device description: The Roman pots and off-momentum detectors are both vacuum-based silicon sensors arranged into two stations for fully reconstructing protons at various magnetic rigidities, where rigidity here refers to the fraction of the momentum the proton has with respect to the steering dipoles design orbit momentum.

Sensors: AC-coupled low-gain avalanche diodes (AC-LGADs) are the technology of choice for these two subsystems due to their capability to provide both high-precision space and time information. add references here for testbeam results on SENSORS.

FEE: ASICs will be readout using LPGBT in-place of FPGAs due to the high-radiation environment in which these detector will be located. Up to sixteen AC-LGAD + ASIC modules will be connected to a single LPGBT, which will be coupled to a VTRX+ to convert the signals to a fiber to send off to the DAW system. The stave design is aimed to have the minimal amount of components inside the vacuum to ensure smooth operations and ease of access during maintenance periods.

Other components: Design of the front-end board and power distribution is still in a very early stage for the RP and OMD systems.

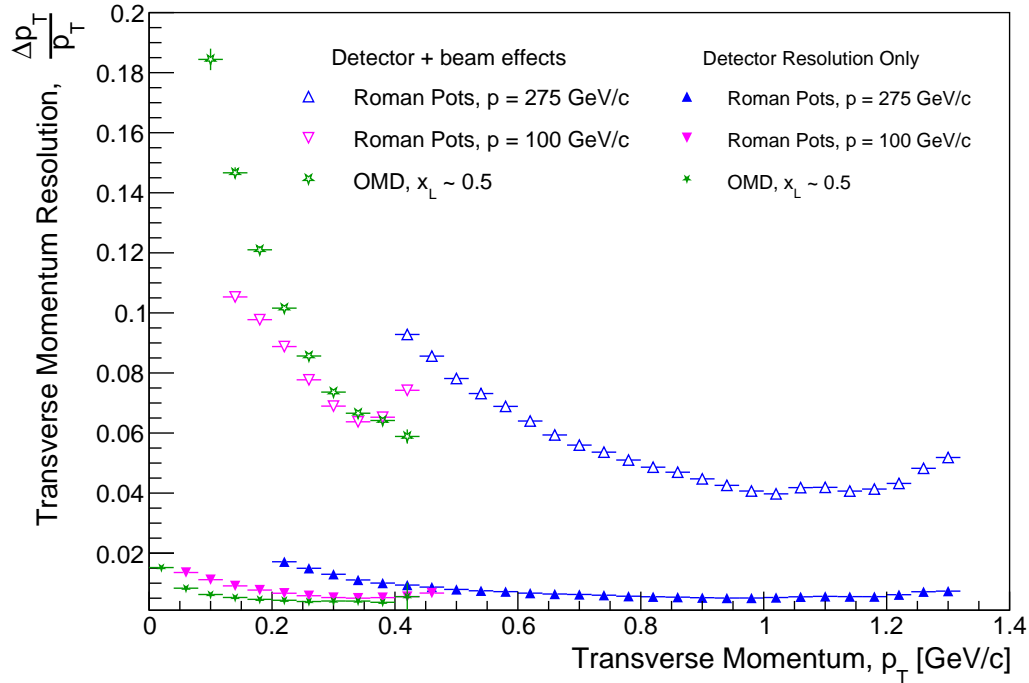


Figure 8.121: Summary of transverse momentum resolutions for the Roman pots and Off-Momentum Detectors. Contributions are separated by those induced by intrinsic detector choices (e.g. pixel sizes) and those from beam effects (e.g. angular divergence), which have an outsized impact on momentum measurements at very-forward rapidity. **Will be replaced with DD4HEP version**

Performance The performance of the Roman pots and Off-Momentum Detectors is summarized in Fig. 8.121. The overall momentum resolution is also affected by the detailed understanding of the hadron magnet lattice, which is used to be able extract the normal transfer matrices used to reconstruct momenta in Roman pots detectors. There is also a software solution in place using deep neural networks to further improve the momentum resolution performance, especially for the off-momentum detectors.

Implementation The basic detector component will be a “stave” which contains 3-4 “modules” comprised of bump-bonded AC-LGADs and ASICs attached a PCB, arranged in a 1x4 or 1x3 layout with modules on either side of the PCB to enable partial transverse overlap of the sensors to cover the dead area at the edges (e.g. guard ring location). The staves are proposed to only contain the sensors and ASICs, plus cooling services, with all other services coming from a readout board place outside the vacuum which contains the LpGBT and VTRX+ components and power distribution. The details of the this concept still need to be properly worked out with engineering support, but strawman versions of these concepts can be found in Figs. 8.122 and 8.123.

Services: The Roman pots and OMD have the same essential needs for services, which include cooling using conductive strips coupled to an external chiller to allow cooling in-vacuum, low volt-

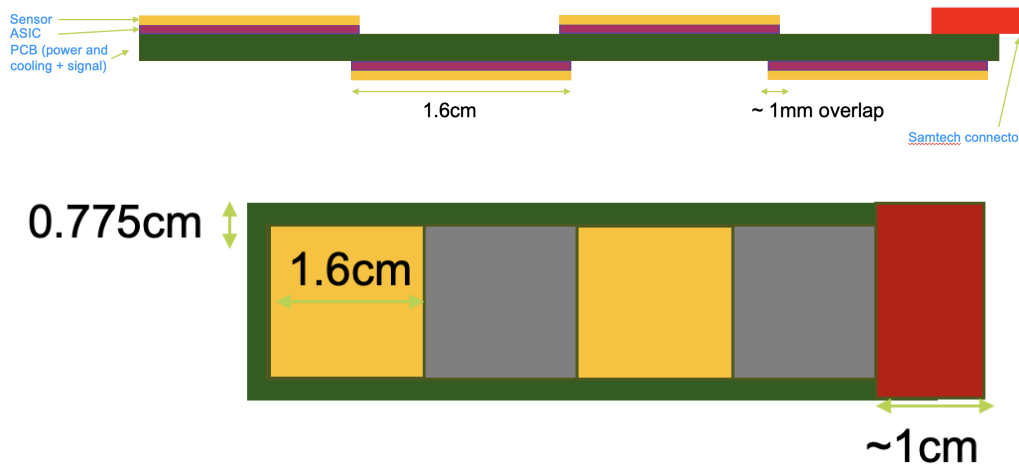


Figure 8.122: Strawman concept for the layout of the RP and OMD sensor staves. A 1x3 configuration is also being consider to reduce the size of the necessary Samtech connector for the staves, but more study is needed to assess impact of either choice, both in terms of construction feasibility and performance.

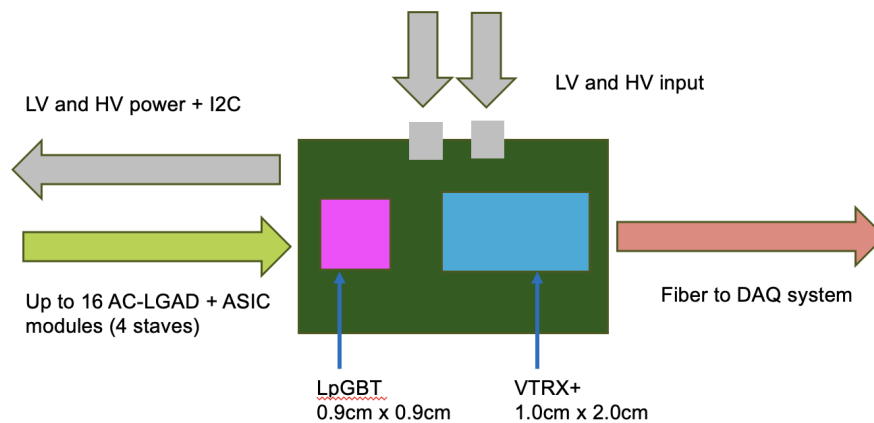


Figure 8.123: Strawman concept a readout board concept to communicate with and readout RP and OMD sensor staves. Work needs to be done to solve the issue of power distribution, and to ensure the EICROC ASIC can indeed be readout by the LpGBT.

age ($\sim 3V$) and high voltage ($\sim 150V$) supplies for the operation of the ASICs and the HV bias supply for the sensor, and slow controls to control both voltages and the DAQ system, and also to control the moving stages necessary for the detector operations. There will also need to be communication between the slow controls and the machine for safety interlocks for fast beam abort systems, and for permits to enable motion control of the detectors when beam conditions are stabilized.

Subsystem mechanics and integration: The primary support systems only need to be able to support very light staves with 3-4 modules per PCB. However, the entire subsystem needs to be

a on motor-driven rail system to enable movement near the hadron beam, especially in order to achieve acceptance at very-low $p_T \sim 0.2 \text{ GeV}/c$.

Calibration, alignment and monitoring: AC-LGAD sensors will be calibrated with MIPs, while alignment of the detector systems will need to be carried out using beam-based alignment with dedicated, short, very-low luminosity runs, which enable the detectors to approach the beam much closer than the standard 10σ distance such that the beam halo itself can be seen on the sensor planes. This, combined with conventional survey information used to align the motion system to the machine should enable alignment at a level much less than 1mm.

5233 **Status and remaining design effort:**

R&D effort: Much work is still needed to demonstrate full system operations with full size sensors + ASICs, and the cooling concept using conductive strips. As of now, only 4x4 channel versions have been tested.

E&D status and outlook: Engineering design is still very preliminary, but necessary design choices are being evaluated as engineering support becomes available.

Other activity needed for the design completion: The design of the front-end PCB which carries the sensors, ASICs, and necessary services needs to be carried out. Presently, only a strawman concept which will meet our requirements exists.

Status of maturity of the subsystem: The design maturity of the system will be at $\sim 60\%$ by Q2 of FY25.

Environmental, Safety and Health (ES&H) aspects and Quality Assessment (QA) planning: Since these detectors are embedded directly into the machine vacuum, special considerations must be made for integration with the machine. We expect that the detectors will be interlocked against operation until permits are received from the machine, pending stable operations of the machine in terms of stable beam losses, collisions at the IP, and background conditions. The cooling system will also have to be integrated with the machine envelope and likely must pass an evaluation from the machine group.

Construction and assembly planning: Sensors and EICROC ASICs will be manufactured in different foundries, but bump-bonding of the sensors + ASICs can be done for the far-forward at BNL, since these detector subsystems are very small compared to other ePIC sub-systems. The assembly will have to take place in stages which include the following steps. First, preparation of stave printed circuit boards and quality assurance testing to ensure traces pass continuity tests to the Samtech connectors will have to be carried out. In parallel, diced sensors need to be tested to ensure they can maintain bias voltage safely, and other electrical tests. ASICs will undergo similar tests to ensure they are ready for bonding into full modules. Once sensors and ASICs are prepped, modules of 32x32 channel size (one sensor, one ASIC) will be bump-bonded. Once sensors are bump-bonded, QA will need to be performed on the final modules before they are integrated into stave PCBs.

Collaborators and their role, resources and workforce: BNL and JLAB will take the primary role in constructing the Roman pots and Off-Momentum Detectors, with engineering support for cooling possibly supplied by IJCLab in France.

Risks and mitigation strategy: The primary risks to the successful construction of the Roman pots and OMD are late receipt of the final 32x32 channel EICROC ASICs and issues with the bump-bonding and construction of the final staves. There are additional risks related to machine integration.

Additional Material Will add sufficient reference to support documents as they are compiled.

8.3.7.3 The zero degree calorimeter

Requirements

Requirements from physics: The Zero-Degree Calorimeter (ZDC) plays an important role in many physics topics. The production of exclusive vector mesons in diffraction processes from electron-nucleus collisions is one of the important measurements. For the coherent processes, where the nucleus remains intact, the momentum transfer (t) dependent cross section can be related to the transverse spatial distribution of gluons in the nucleus, which is sensitive to gluon saturation. In this case, however, the coherence of the reaction needs to be determined precisely. Incoherent events can be isolated by identifying the break-up of the excited nucleus. The evaporated neutrons produced by the break-up in the diffraction process can be used in most cases (about 90%) to separate coherent processes. In addition, photons from the de-excitation of the excited nuclei can help identify incoherent processes even in the absence of evaporated neutrons. Therefore, in order to identify coherent events over a wide t range, neutrons and photons must be accurately measured near zero degrees.

The geometry of the collision is important to understand the characteristics of each event in electron-nucleus collisions. It has been proposed that collision geometry can be studied by tagging it with the multiplicity of forward neutrons emitted near zero degrees. Determining the geometry of the collision, such as the “travel length” of the struck partons in the nucleus, which correlates with the impact parameters of the collision, is very useful in the study of nuclear matter effects. Determining the geometry of the collision will allow us to understand the nuclear structure with greater accuracy.

Requirements from Radiation Hardness: In the ePIC radiation doses and particle fluences, ZDC neutron fluence is smaller than 10^{12} neutron/cm² for 6 month operation. It is not demanding, but degradation may occur for crystals and/or photon sensors due to radiation

Requirements from Data Rates: Dynamic range of the crystal calorimeter is a clear challenge. ~ 100 MeV photons from e+A “quasi-coherent” reactions and ~ 10 -100 GeV photons possible from other exclusive processes (Λ decay, u -channel DVCS) should be covered.

Justification

Device concept and technological choice: Add text here.

5299 **Subsystem description:**

5300 General device description: The Crystal calorimeter needs a good measurement of low-
 5301 energy photons. The first part of ZDC is designed to use a layer of crystal calorimeter towers
 5302 which is $8X_0$ in thickness. The layer consists of $2 \times 2 \text{ cm}^2$ crystals in an array of 30×30 .
 5303 LYSO is considered as the material choice for the crystal. SiPM and APD are considered as
 5304 photo-sensors. The FEE and other components are also under consideration.

5305 Sensors: Add text here.

5306 FEE: Add text here.

5307 Other components: Add text here.

5308 **Performance** Test beams for crystal calorimeter prototype have been performed and its data
 5309 analysis is underway. Its prototype modules have been made by Taiwan group. Two simulation
 5310 calculations and evaluations have been ongoing; Λ identification and low-E photon identification.
 5311 Angular resolution is a common thread. They have been less-emphasized early-on, but absolute
 5312 requirements for successful exclusive physics program should be given.

5313 **Implementation** ZDC implementation would have a benefit from a creative approach; poten-
 5314 tially non-static configuration which can be “changed” for different running conditions. The crystal
 5315 calorimeter need depends on physics channel; some level of conflict in the final states and associ-
 5316 ated requirements. Having the ability to bring the crystal calorimeter in/out of configuration, as
 5317 needed, would provide clear benefit to specific physics needs.

5318 **Services:** Add text here.

5319 **Subsystem mechanics and integration:** In the current crystal calorimeter prototype module
 5320 made by Taiwan group, by glueing modules together, 4×4 crystals are made, and then 4 modules are
 5321 put 64 crystals together. Support and mechanical structure need to communicate with US experts.

5322 **Calibration, alignment and monitoring:** Add text here.

5323 **Status and remaining design effort:**

5324 R&D effort: Add text here.

5325 E&D status and outlook: Add text here.

5326 Other activity needed for the design completion: Add text here.

5327 Status of maturity of the subsystem: Add text here.

5328 **Environmental, Safety and Health (ES&H) aspects and Quality Assessment (QA plan-**
 5329 **ning:** Add text here.

5330 **Construction and assembly planning:** Add text here.

5331 **Collaborators and their role, resources and workforce:** Add text here.

5332 **Risks and mitigation strategy:** Add text here.

5333 **Additional Material** Add text here.

5334 8.3.8 Far backward detectors

5335 The luminosity system at the Electron-Ion Collider plays a critical role in achieving high-precision
 5336 measurements in nuclear physics experiments. By determining, monitoring and optimizing the
 5337 number of particle collisions, the luminosity system ensures that the collider operates at peak per-
 5338 formance, enabling detailed exploration of the structure of matter. When electrons collide with
 5339 protons or nuclei, Bremsstrahlung (BH) photons are generated, with a well know cross section [].
 5340 This process thus provides us with the mean to indirectly determine the luminosity by accurate
 5341 and precise determination of the Bremsstrahlung photons generated in the interaction region of
 5342 the collider.

5343 Accurately determining luminosity is essential for addressing the fundamental physics questions
 5344 that underpin the construction of the Electron-Ion Collider. The Yellow Report specifies the EIC
 5345 requirements for luminosity determination to be 1% in absolute uncertainty and 10^{-4} in relative
 5346 luminosity [?]. This requirement will be fulfilled by two complementary detectors in the lumi-
 5347 nosity monitoring system: the Pair Spectrometer (PS) and the Direct Photon Detector (DPD). It was
 5348 demonstrated at HERA – the first electron-hadron collider – that the bremsstrahlung process can be
 5349 successfully used to precisely measure the luminosity of high-energy ep collisions (ZEUS achieved
 5350 an absolute uncertainty of 1.7% [?, ?]). The luminosity monitors designed for the EIC utilise the
 5351 same approach with implementation that mitigates large systematic uncertainties.

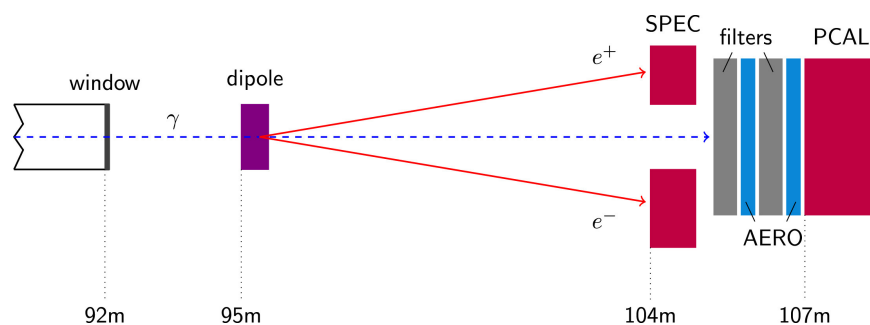


Figure 8.124: The layout of the luminosity monitor in the ZEUS experiment [?].

5352 The two subsystems, Pair Spectrometer, and Direct Photon Detector, are sensitive to different sys-
 5353 tematic effects; on one hand the Direct Photon detector is placed downstream the photon beam with
 5354 full acceptance, but within the synchrotron radiation fan and needs to be shielded. In addition,
 5355 at nominal luminosities planned for the EIC several photons will hit the DPD in each bunch cross-
 5356 ing. Thus the counting of bremsstrahlung photons is done through the total energy determination
 5357 deposited in DPD and is associated with systematic uncertainties related to gain stability. On the

other hand, the PS is outside the synchrotron radiation fan and overall rates can be controlled with a dedicated converter. The luminosity determination from the PS is sensitive to systematic effects related with the acceptance determination.

The PS and DPD detectors in the ZEUS luminosity monitor are shown in figure (8.124). The PS system consists of an analysing dipole magnet and two electromagnetic calorimeters, while the DPD system includes absorbing plates and an electromagnetic calorimeter. BH photons generated in the interaction region exit the vacuum chamber through a thick exit window. About 10% of these photons (depending on the window's thickness) undergo pair conversion into electron-positron pairs, which are then detected by the PS calorimeters. The remaining unconverted photons are detected by the downstream DPD. Additionally, the luminosity monitor includes a collimator positioned just after the exit window to produce a uniform, narrow cone of photons and pair-converted particles. This simple steel block also protects the PS system components from direct synchrotron radiation (SR), BH radiation, and unwanted stray particles.

The PS was needed at ZEUS due to challenges introduced by upgrades to the HERA accelerator, which significantly increased luminosity and, consequently, the rate of BH events [?]. The stronger beam focusing and increased synchrotron radiation (SR) — radiation resulting from the bending of electrons by the magnet—led to a higher pile-up of photons in the DPD, increasing the uncertainty in luminosity measurements from 1% to 3% [?]. The PS, positioned outside the SR fan and unconverted photon flux, experienced a lower pile-up due to fractional pair conversion. This introduction reduced the uncertainties in rate measurement to 2% [?], and additionally both detectors were utilized to monitor real-time detector inefficiencies and manage systematic uncertainties.

8.3.8.1 The luminosity system

This ZEUS luminosity monitor design serves as a baseline for EIC but the expected luminosity at EIC will be about 10^2 to 10^3 times that of ZEUS [?]. This directly leads to several challenges faced during the upgrade of HERA, such as beam size effects (BSE), increased SR backgrounds, and higher pile-up from BH radiation, becoming much more pronounced at the EIC. In addition to these, the EIC will also feature electron beams colliding with a diverse range of hadron species, from protons to heavy nuclei like gold, lead, and uranium. This in turn dramatically increases the BH rates by a factor of Z^2 , making pile-up at detectors even more difficult to manage. Furthermore, both the electron and light hadron beams will be polarized, adding another layer of complexity. In the following section, we will discuss these challenges in more detail and outline how the "upgraded" luminosity monitor of EIC will overcome them.

Beam Size Effect - The BH process in electron-proton collisions is notable for its extremely small momentum transfers between the radiating electron and the proton. It is kinetically possible for both particles to continue along their initial paths without angular scattering, while the BH photon is emitted in the direction of the electron's momentum. This specific configuration results in the smallest virtuality (Q_{\min}^2) of the exchanged photon [?]. At high-energy colliders, this minimal photon virtuality becomes incredibly small. For instance, at HERA, the Q_{\min}^2 for a photon energy of 1 GeV can be as low as 10^{-8} eV². Consequently, the typical transverse momentum transfer (q_{\perp}) reaches values around 10^{-4} eV/c. Since the BH differential cross section is proportional to Q^{-4} , photon virtualities near Q_{\min}^2 dominates the process and allows for the approximation,

$$Q^2 = Q_{\min}^2 + q_{\perp}^2$$

and not to forget the scenarios with $q_{\perp} = 0$ is also feasible. Analyzing the process in impact parameter space reveals that these small q_{\perp} values correlate to large impact parameters ($b = \hbar/q_{\perp}$), explaining the precision of Bethe-Heitler cross-section calculations in the Born approximation.

The derivation of the two-particle rate (R) relation with the collision luminosity (L) and cross-section (σ)

$$R = L\sigma \quad (8.1)$$

assumes both beams to be modeled as simple plane waves with a uniform impact parameter distribution. However, this assumption falls short when beams are strongly focused at the interaction point, as focusing suppresses large impact parameters. Consequently, the BH differential cross section is predominantly "over-sampled" at low impact parameters where the cross-section value is smaller. This results in an effective suppression of BH. This is particularly pronounced at lower photon energies, since typical q_{\perp} is proportional to E_{γ} .

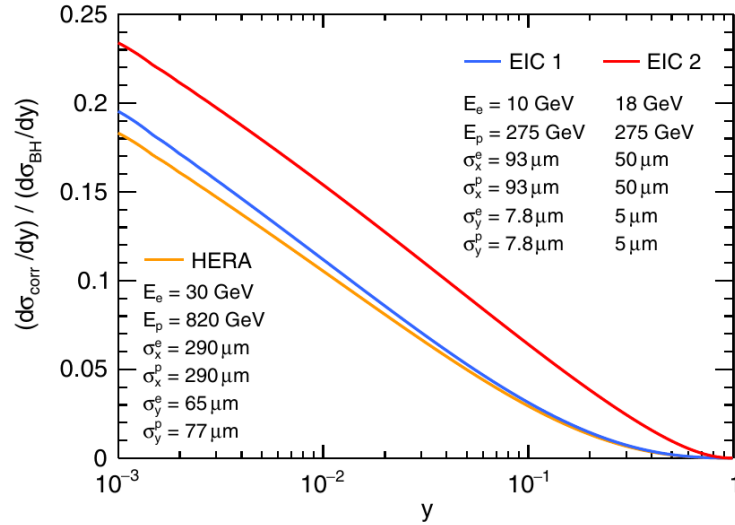


Figure 8.125: Relative suppression due to the BSE $(d\sigma_{corr}/dy)/(d\sigma_{BH}/dy)$ is shown as a function of $y = E_{\gamma}/E_e$ for three cases of collider parameters, HERA, EIC 1 & EIC 2. The corresponding beam energies and Gaussian lateral beam sizes at the interaction point are listed [?].

Relative corrections to the standard Bethe-Heitler cross-sections due to the BSE is shown in figure (8.125). Here the observed suppressed BH cross-section is related to the Bethe-Heitler cross-section as $(d\sigma_{obs}/dy) = (d\sigma_{BH}/dy) - (d\sigma_{corr}/dy)$. It is worth noting that even after higher beam energies at HERA, the BSE will be higher at EIC due to a stronger focused beam as evident from beam size parameters. In a recent study, the BSE is proposed to be corrected by a precise measurement of the BH spectra as a function of lateral beam displacements (indirectly the impact parameter) at the interaction point. This will be achieved using Van der Meer scans, commonly performed at hadron colliders. This involves systematically varying the beam positions and crossing angles to find the L as a function of lateral beam displacement, which can be described by the formula

$$L(B) = L(0) \exp \left(-\frac{B}{2(\sigma_1^2 + \sigma_2^2)} \right)$$

Here, B represents the lateral displacement of one of the beams within either the horizontal or vertical plane, σ_1 and σ_2 are the two Gaussian widths in a given plane, often assumed to be equal, and $L(0)$ corresponds to the luminosity of nominal, head-on collisions. However, in the case of BH, its photon spectrum will also be modified in a very specific manner, reflecting the BSE.

High rate of BH radiation and SR background - The bunch crossing rate at EIC will be set to 100 MHz for 5 and 10 GeV electron beam and 25 MHz for 18 GeV electron beams [?]. When this rate is multiplied by the BH photon production rate per bunch crossing, as illustrated in Figure (8.126), the resulting photon rates reaching the detectors looks substantial. For instance, with a 5 GeV electron beam and a 41 GeV proton beam, the coincidence rate (the rate when both the pair converted pairs are detected simultaneously) at the Photon Spectrometer (PS) can reach approximately 90,000 photons per second. The BH photon rates during electron-nuclei interactions will be proportional to the square of nucleus's atomic number. Therefore for the same setup but 41 GeV Gold nuclei beams will result coincidence rate equivalent to $79^2 \times 90000 = 56 \times 10^7$ photons per second.

SR, similar to BH radiation, is emitted at very small angles ($\sim m_e/E_e$) relative to the instantaneous direction of an electron beam's motion. At the EIC, the electron beam exiting the interaction region passes through two quadrupole magnets, Q1eR and Q2eR, followed by a dipole magnet, B2eR. The electron beam passes through the center of the quadrupoles and consequently, the B2eR magnet is the sole source of direct SR impacting the far-backward region. [\[Calculation of SR rates at EIC? Comment quantitatively on how much sweeper helps in subsequent paragraph.\]](#)

To address the issue of high photon flux and its associated pile-up, as well as to mitigate the high SR background, the luminosity monitoring system has been redesigned to include two new components: a sweeper magnet and a thin converting foil, both positioned between the EW and the spectrometer magnet, as illustrated in Figure (8.127). The enormous BH radiation and SR pass through the exit window, resulting in substantial pair conversions. These converted particles are deflected by the Sweeper magnet, leading to a reduced photon flux, with a large percentage being BH photons. These photons then encounter a thin converter made of the same material as the exit window. This setup results in fewer pair conversions reaching the PS and an overall reduced photon flux to the DPD.

For electron beams at 10 and 18 GeV, the SR flux is substantial, with power reaching the exit window potentially exceeding 4 kW. To mitigate this, it was proposed to divide the dipole magnet into two segments. The first segment, relevant to luminosity detectors, has a magnetic field about four times weaker than that of B2eR. This modification is crucial to minimize the direct SR flux, which is vital for accurate luminosity measurements, as it influences both PS and DPD readings [?].

Beam Polarisation - The electron and light ion beams at the EIC will be polarized both longitudinally and transversely. A recent study investigated the impact of longitudinal beam polarization on the Bremsstrahlung cross-section in the low- q^2 region [?]. Numerical calculations revealed that the polarized component is significantly suppressed compared to the unpolarized component, by a factor of $m_e^2/E_e E_p$. Figure (8.128) illustrates the unpolarized component first calculated by Bethe-Heitler, alongside the polarized component. However, no calculation exists for transversely polarised beams and also with the effect of nuclear recoil.

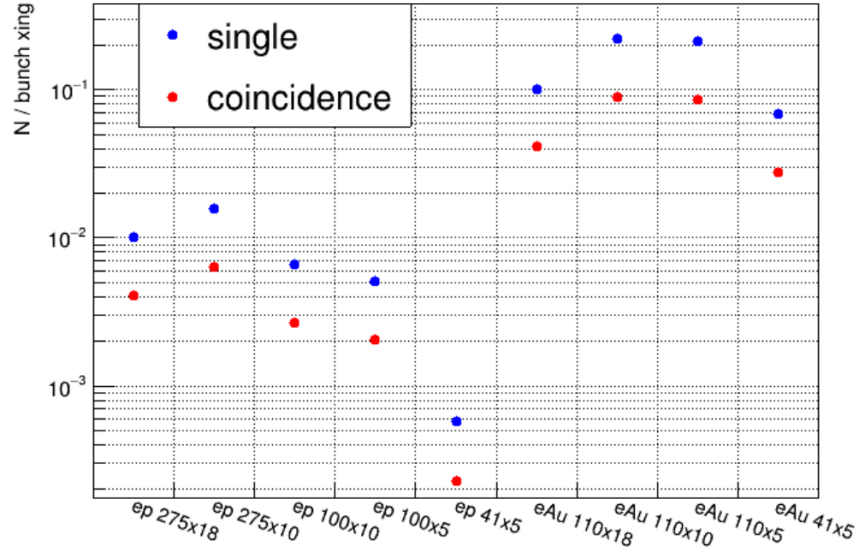


Figure 8.126: Rate of single and coincidence events for the PS detectors calculated by Dr. Gangadharan

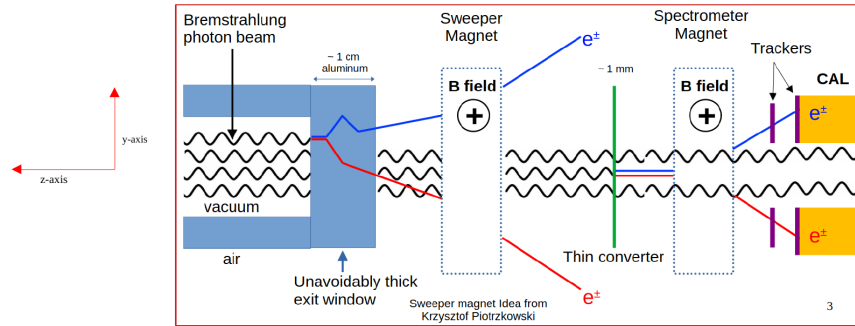


Figure 8.127: The layout of the luminosity monitor in the ePIC experiment of the EIC.

Physical Constraints - The components of the luminosity monitoring system are placed within the beam tunnels and are therefore constrained by the beam pipes and the equipment required to maintain the beam, such as magnets and cooling systems. The majority of the system is located sixty meters back from the interaction region to provide sufficient space for the magnets and detectors to operate without interfering with the beam. The long air column between the exit window and the PS calorimeters is approximately 46 meters. The “unconverted” photon beam from the exit window undergoes pair conversions, which are quite significant (approximately 10%) and indeterminate during experimentation due to variability in air composition. Most of the unwanted pair conversions occur between the exit window and the sweeper magnet and are swept away by the sweeper. To reduce pair conversions in the air column between the sweeper magnet and the spectrometer magnet, a helium or partial vacuum chamber will be installed between the magnets. The thin converter will remain at the same location but will be placed inside this vacuum chamber.

Add paragraph outlining requirements on magnets imposed by physical space limitations.

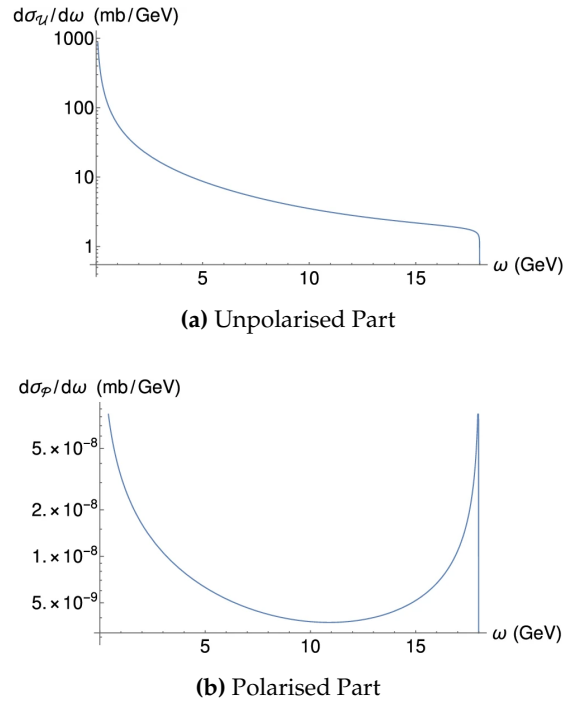


Figure 8.128: Unpolarised and polarised Bethe-Heitler Cross-Section. [?]

Systematic Uncertainties - The systematic uncertainty in the luminosity measurement at ZEUS was 1.7 %, and our goal is to reduce this value to below 1 %. Table 8.31 summarises the main systematic uncertainties that contributed to the ZEUS luminosity determination. In our current design, we ensure we mitigate the largest of these sources with the introduction of trackers for the PS, that would enable an accurate determination of the detector acceptance and beam size effects, and a sweeper magnet that allows us to have more control on the converted pair rates in the PS.

Source	DPD detector (%)	PS detector (%)
Acceptance	1.0	1.0
x-position of photon beam	1.2	1.2
Pair conversion in EW		0.7
RMS Cut Correction		0.5
Pedestal Shifts	1.5	
Pile up	0.5	
Total	2.2	1.8

Table 8.31: Summary of systematic uncertainties at ZEUS DPD and PS detector. [?]

5478

Design and Components A two-level review of all the components of luminosity monitor is presented below. First, a short review on the component's material, location & dimension, and a longer version with detailed description of each component requirement, design with simulation or test-beam results. Note that all length measurements are in centimeters unless otherwise

5483 mentioned.

- 5484 • Exit Window
 - 5485 – Material - Aluminum
 - 5486 – Location - (0.0, 0.0, - 1850.5)
 - 5487 – Dimension - (4.0, 4.0, 1.0)
- 5488 • Collimator
 - 5489 – Material - Stainless Steel
 - 5490 – Location - (0.0, 0.0, - 2260.0)
 - 5491 – Hollow Structure, Outer Dimension - (6.5, 6.5, 30.0), Inner Dimension - (4.832, 4.832,
 - 5492 30.0)
- 5493 • Sweeper Magnet
 - 5494 – 0.5 T horizontal magnetic field.
 - 5495 – Location - (0.0, 0.0, - 5600.0)
 - 5496 – Main Body Structure, Outer Dimension (75.972, 94.0, 120.0), Inner Dimension - (42.032,
 - 5497 61.262, 120.0)
 - 5498 – Magnetic Coils Structure (How to describe ?)
- 5499 • Photon Vacuum Chamber
 - 5500 – Material - Pipe : Aluminum & End caps : Beryllium
 - 5501 – Location - (0.0, 0.0, - 5800.0)
 - 5502 – Pipe Structure, Outer Dimension (6.3119, 2π rad, 555.0), Inner Dimension (6.119, 2π
 - 5503 rad, 555.0)
- 5504 • Converter Foil
 - 5505 – Material - Aluminum
 - 5506 – Location - (0.0, 0.0, - 5800.0)
 - 5507 – Disk Dimension - (6.119, 2π , 0.1)
- 5508 • Spectrometer Magnet
 - 5509 – Location - (0.0, 0.0, - 6000.0)
 - 5510 – Main Body Structure, Outer Dimension (75.972, 94.0, 120.0), Inner Dimension - (42.032,
 - 5511 61.262, 120.0)
 - 5512 – Magnetic Coils Structure (How to describe ?)
- 5513 • PS Trackers
 - 5514 – Type - AC-LGAD
 - 5515 – Locations
 - 5516 * Module 1 : Top (0.0, 15.76, - 6397.6) and Bottom (0.0, - 15.76, - 6397.6)
 - 5517 * Module 2 : Top (0.0, 15.76, - 6407.6) and Bottom (0.0, - 15.76, - 6407.6)
 - 5518 – Dimension - (18.06, 18.06, 0.044)

- 5519 • PS Calorimeters
 - 5520 – Type - Electromagnetic sampling (spaghetti) calorimeter
 - 5521 – Material - Active : Scintillating Fiber (ScFi) and Passive : Tungsten (W)
 - 5522 * Tungsten as powder, held together with optical epoxy.
 - 5523 – Location - Top (0.0, 15.76, -6408.6) and Bottom (0.0, - 15.76, - 6408.6)
 - 5524 – Dimension - (18.06, 18.06, 17.2)
- 5525 • DPD Calorimeters

5526 **Exit window**

- 5527 • Needs exact study of its composition and irradiation studies.

5528 **Collimator**

- 5529 • Do we need any further study ?

5530 **Sweeper and Spectrometer magnet**

- 5531 • Mapping the magnetic field. Need info from magnet experts

5532 **Photon Vacuum Chamber**

- 5533 • need info from accelerator

5534 The thickness of the exit window for electrons and positrons must be minimized to reduce mate-
 5535 rial interactions. However, if a vacuum chamber is selected instead of helium filled, a minimum
 5536 thickness of the exit window is required to withstand a pressure difference of 1 atm. The minimum
 5537 thickness of beryllium should exceed 3 mm to ensure structural integrity under these conditions.

- 5538 • Mapping the Pressure
- 5539 • Study of exact composition and thickness of two end caps.

5540 **Converter Foil** The converter foil is expected to operate in a vacuum, necessitating heat removal
 5541 due to synchrotron radiation (SR). Heat removal from the converter can be achieved through the
 5542 holder, utilizing one of two options: passive cooling or circulation of a coolant.

- 5543 • Study of exact composition, thickness and radiation dose.
- 5544 • Study of pair conversion percentage.
- 5545 • How this will reduce the error in position resolution.
- 5546 • Heat removal due to SR radiation.

5547 **PS Trackers**

- 5548 • PS trackers are required to reconstruct the vertex position at the conversion foil, which has a
5549 direct impact on determining acceptance. A vertex resolution of less than 6 mm is necessary
5550 to achieve an acceptance determination uncertainty of less than 1%.
- 5551 • This has not been studied yet; however, since the PS system is located away from the IP and
5552 positioned behind collimators and magnets, and not within the BH cone, the radiation levels
5553 are expected to be manageable.
- 5554 • AC-LGADs are chosen for their excellent position and timing performance. Due to the rela-
5555 tively small detection area and the fact that this technology is planned for FTOF, PS trackers
5556 will utilize a similar design.
- 5557 • Initial studies with the nominal 500 μm pitch are expected to provide a 2 mm resolution at
5558 the vertex (conversion foil).

5559 The tracking layers for the PS system are based on AC-LGAD technology with pixelated sensors.
5560 Each side will consist of two tracking layers, resulting in a total of four layers. AC-LGAD sensors
5561 will be placed on modules similar to the FTOF design. The pitch between the readout pads, set at
5562 500 μm , is expected to provide approximately 70 m position resolution at the detector plane and
5563 around 2 mm at the vertex (conversion foil). Current estimations indicate that, in order to achieve
5564 acceptance uncertainties below 1%, the vertex resolution in the dispersive direction must be less
5565 than 6 mm. With a 500 μm pitch, the number of readout channels is estimated to be about 130,000
5566 per plane. To minimize the number of DAQ channels, the number of pixels in the non-dispersive
5567 direction could be combined.

5568 **PS Calorimeters** The two electromagnetic calorimeters (CALs) used for the PS are of the sam-
5569 pling type, colloquially known as spaghetti CALs. The active component of the CAL consists of
5570 plastic scintillating fibers (ScFi), while the passive, or "hard," component is tungsten (W). The vol-
5571 umetric ratio of W to ScFi in each CAL is 4:1. The CALs are composed of 20 layers, with the fibers
5572 in alternate layers oriented parallel to either the x-direction or y-direction in the transverse plane.
5573 This alternating orientation in 10 layers along each direction aids in reconstructing the shower pro-
5574 file of hits, thereby enhancing the position resolution of hits. Each layer has a thickness of 0.86 cm
5575 and a transverse size of $18.06 \times 18.06 \text{ cm}^2$. Additionally, the layers are segmented into three mod-
5576 ules, each with a width of 6.02 cm. Each module contains well-distributed 448 ($14 \times 2 \times 16$) fibers.
5577 Finally, a group of 16 fibers forms a single channel for readout. Each readout will be associated
5578 with a silicon photo-multiplier (SIPM).

5579 The two PS CALs are symmetrically positioned in the vertical plane, perpendicular to the photon
5580 flux i.e., along the y-axis. The gap between the two CALs is approximately 3σ , which is sufficient
5581 for the detectors to not obstruct the final photon flux from reaching the DPD. The PS CALs serve
5582 the purpose of measuring the energy and the transverse coordinates of the pair-converted photons,
5583 which enables the reconstruction of the photon energy spectrum and thus the determination of the
5584 beam luminosity.

5585 The acceptance of PS system is effected by four major parts of the PS system.

- 5586 • The collimator which obstructs some part of BH photons.
- 5587 • The sweeper magnet which removes the pair-conversions from EW.
- 5588 • The front end cap of the vacuum chamber whose pair-conversions are not detected in CALs.

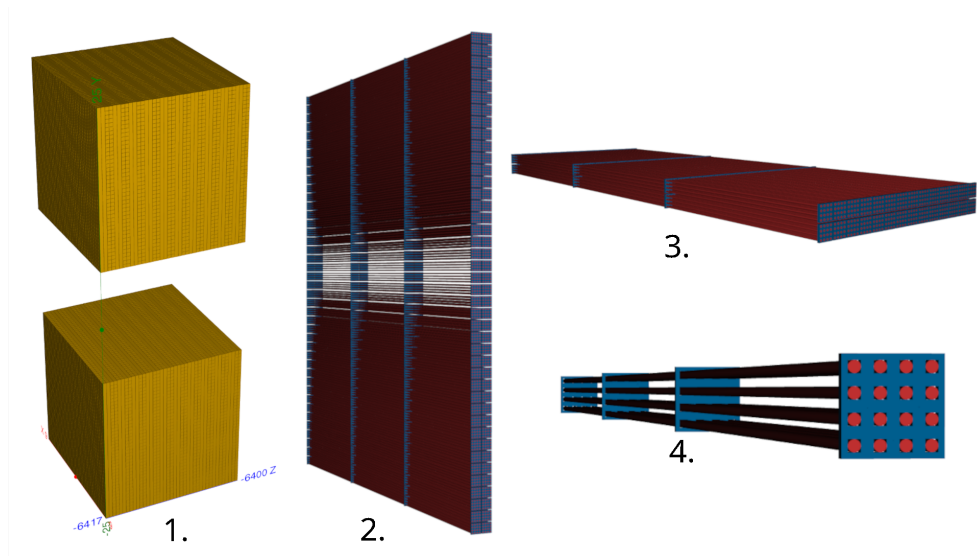


Figure 8.129: DD4hep implementation of PS Calorimeters.

- The fiducial areas of the CALs whose signals are rejected.

Plot the acceptance curve.

DPD

Collaborators and their role, resources and workforce: The main collaborating institutions for the PS calorimeter are York and Houston. The roles of each institution are outlined below -

- University of York, United Kingdom
 - Design and construction of calorimeters
 - Calorimeter simulation
 - Calorimeter reconstruction and analysis
 - DAQ and electronics for calorimeter
- University of Houston, Texas, USA
 - Calorimeter simulation
 - Calorimeter reconstruction software
 - Calorimeter design support
- Tel Aviv University, Israel
 - Design and integration of PS trackers.
 - Simulation.

The workforce at each institution is comprised of -

- 5607 • University of York, United Kingdom
 - 5608 1. Dan Watts, academic staff (20-25 % FTE)
 - 5609 2. Nick Zachariou, academic staff (25-30% FTE)
 - 5610 3. Mikhail Bashkanov, academic staff (10-15% FTE)
 - 5611 4. Stephen Kay, PDRA (100% FTE)
 - 5612 5. Alex Smith, PG Student (100% FTE)
 - 5613 6. Pankaj Joshi, academic support staff (5% FTE)
 - 5614 7. Julien Bordes, Geant4/simulation support (10-15% FTE)
 - 5615 8. Technical Support Staff
 - 5616 – Electrical engineering
 - 5617 – Mechanical engineering
 - 5618 – CAD support
- 5619 • University of Houston, Texas, USA
 - 5620 1. Dhevan Gangadharan, academic staff (X% FTE)
 - 5621 2. Aranya Giri, PG Student (100% FTE)
- 5622 • Tel Aviv University, Israel
 - 5623 1. Igor Korover, academic staff (15% FTE)
 - 5624 2. Avishay Mizrahi, Mechanical engineer (50% FTE).

5625 Note that where an FTE range is presented, this represents a min/max value.

5626 **Risks and mitigation strategy:** Add text here.

5627 **Additional Material** Add text here.

5628 8.3.8.2 The low Q^2 taggers

5629 **Requirements** The Low- Q^2 Tagger sits close to the electron beamline and consists to two mod-
 5630 ules - each with a silicon trackers and calorimeter. This is shown in Figure 8.130.

5631 **Requirements from physics:** The acceptance for the low- Q^2 tagger should complement the
 5632 central detector to reach the coverage close to the limits given by the divergence of the beam and
 5633 beamline magnets. Low- Q^2 tagger will have one or more stations to cover the maximum momen-
 5634 tum acceptance. The Low- Q^2 tracking system shall have a spatial resolution providing a momen-
 5635 tum resolution ; 5%. Low- Q^2 trackers will have Q^2 acceptance between 0 and 0.1 GeV².

5636 More on resolution here? Too much here on spectroscopy - maybe reduce and more from the ArXiv
 5637 paper blurb. Or add other sections with other physics titles. I added two.

5638 8.3.8.3 TCS

5639 Add text

5640 8.3.8.4 Vector Meson production

5641 Add text

5642 8.3.8.5 Spectroscopy

5643 Electron-ion collisions, where the electron is scattered through a very shallow angle, correspond
5644 to the case where the exchanged photon is almost real. Such photoproduction processes are of
5645 interest in their own right, but also can enable a program of hadron spectroscopy. Furthermore, as
5646 the virtual photon flux is highest in this region, yields may be relatively high or rare states may be
5647 searched for.

5648 A topic of particular interest is the photoproduction of exotic charmonium-like mesonic states.
5649 Commonly referred to as XYZ spectroscopy, these states were originally seen in decays containing
5650 J/ψ mesons and additional products. Despite there being many missing charmonium states these
5651 states do not fit the quark model expectations in terms of numeracy, masses or widths. While the
5652 Z_c^+ states were manifestly exotic as their charge required additional constituent quarks to a $c\bar{c}$ pair.

5653 The production cross section of these states is expected to be low, of order 1 nb and branching
5654 ratios to particles that can be detected can also be small. Therefore tagging a large fraction of the
5655 virtual photon flux is essential for making measurements of exclusive production of these states.
5656 The energy of the tagged photon can be used to determine the reaction invariant mass, W , and
5657 provide exclusivity discrimination when combined with the measured meson state from the central
5658 detector and hadron from the far-forward region.

5659 Reconstruction of the azimuthal angle for the electron would provide an effective linearly polarised
5660 photon beam, with polarisations up to 1 when the tagger electron energy is close to the beam en-
5661 ergy. Reconstructing this angle will be challenging and probably only possible with sufficiently
5662 high scattering angles. Provided this information alongside the virtual photon degree of polari-
5663 sation, which will mainly depend on the measured energy, would allow additional constraints to
5664 be used in partial wave analysis of the meson decay allowing the production amplitudes to deter-
5665 mined.

5666 The Q^2 of the scattering is not directly of use for these reactions, however ultimately it can be used
5667 to reject bremsstrahlung electrons which would improve the analysis.

5668 Count rate estimates were performed for a number of exotic states in [?] including branching ra-
5669 tio through to detected particles and using the models developed in [?] . To summarise for the
5670 charmonium-like XYZ states they are expected to be of the order 1000 per day at luminosities of
5671 $10^{34} \text{cm}^2 \text{s}^{-1}$, while for double J/ψ or Z_b decays there may be 10s per day.

5672 Given just providing evidence of the existence of these states in photoproduction would be a great
5673 result, as few of these states have been seen in more than one production mechanism, tagging
5674 efficiencies of 10% would be sufficient. However to perform detailed physics studies to determine
5675 quantum numbers and production amplitudes, which may provide insight into their exotic nature,
5676 or to measure rarer states such as the Z_b , large data samples would be required.

Requirements from Radiation Hardness:

The Low- Q^2 trackers are in the far backward region, where the incident flux is predominantly from bremsstrahlung electrons (MIPS). This means there is no requirement for a radiation hard classification for the trackers. However, the intensity is focused on a narrow band in the bend plane (see Figure 8.131), particularly close to the beam line, and trackers should be designed to *spread the load* by period vertical translation, and exchange of modules.

Requirements from Data Rates:

The Low- Q^2 system must operate at a full projected EIC luminosity.
 The Low- Q^2 system must operate in extreme background conditions (synchrotron radiation, bremsstrahlung events and beam gas) at the levels specified by the simulation studies.
 The Low- Q^2 trackers shall provide timing resolution sufficient to resolve 10 ns beam buckets.
 The Low- Q^2 tagger will be able to measure the momentum of more than 10 electrons per bunch crossing.

The rate distributions, based on simulation, are illustrated in Figure 8.131. It is clear that the raw rates on the detectors are dominated by bremsstrahlung, with increasing intensity closer to the bend plane, and to the beam line. These results can be used to calculate the integrated data rates for DAQ and storage, and the bottom right plot can be used to estimate the maximum rate which the tracker must be able to handle, in terms of pixel, column, sensor and board. The rates are summarised in Figure 8.132.

Justification

Device concept and technological choice: As described above, the Low- Q^2 detector will consist of two separate taggers, each with a silicon tracker and a calorimeter. For the trackers, the positions and layer spacing are still to be optimised on the basis of simulations. The essential characteristics are angular resolution (since all other quantities are derived from polar and azimuthal angles), rate capability and background rejection. For pixel detectors, the angular resolutions relate to pixel size, or, more precisely, to the position resolution of the centroids of pixel clusters. From the simulations it is clear that $55\ \mu\text{m}$ pixels (Timepix4 pixel size) would provide very good resolution. Bigger pixels would still provide acceptable resolution, but high segmentation is even more important for rate capability, where the efficiency for separating multiple tracks within a single event needs to be as high as possible: For an electron-ion collision event there are typically ten background bremsstrahlung electrons within the same beam bucket, each passing through all layers of a tagger and creating hits. Furthermore, in each layer there will be *singles* resulting from rescattering, or synchrotron radiation, together with hits from detector noise. However, we already have enough information to set some constraints on detector and readout technologies. We have used Timepix4 as the template for much of the development, and have had its dimensions, readout and rate capabilities as a strong influence in the development of the current design. However, where possible, we used *generic* pixel detectors - particularly in the Geant4 simulations, with the aim of being able to evaluate other current, or emerging, technologies.

It is already clear, both from a basic knowledge of the kinematics of bremsstrahlung and quasi-real events, and from preliminary simulations, that the intensity of electrons passing through the trackers will be distributed in a highly non-uniform way, with the bulk of the events close to the plane of the accelerator, and the flux increasing strongly towards the electron beamline. In particular, the rates on Tagger 2 are significantly higher than Tagger 1, with the hottest zone closest to

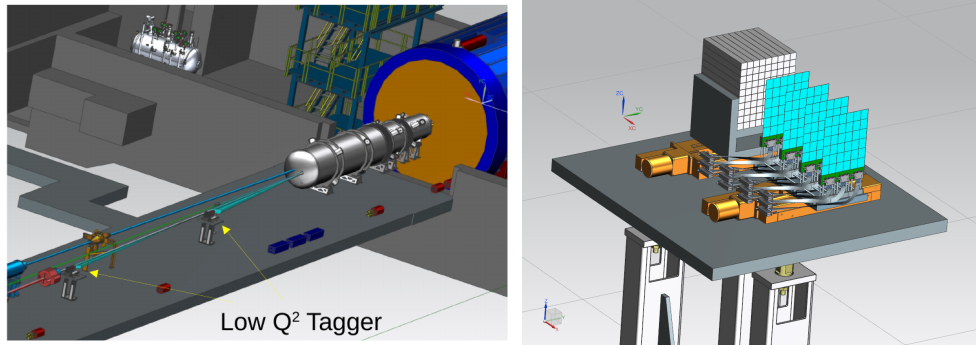


Figure 8.130: Left: Low- Q^2 taggers in relation to beamlines and central detector. Right: Tagger module with calorimeter and tracker from recent CAD model.

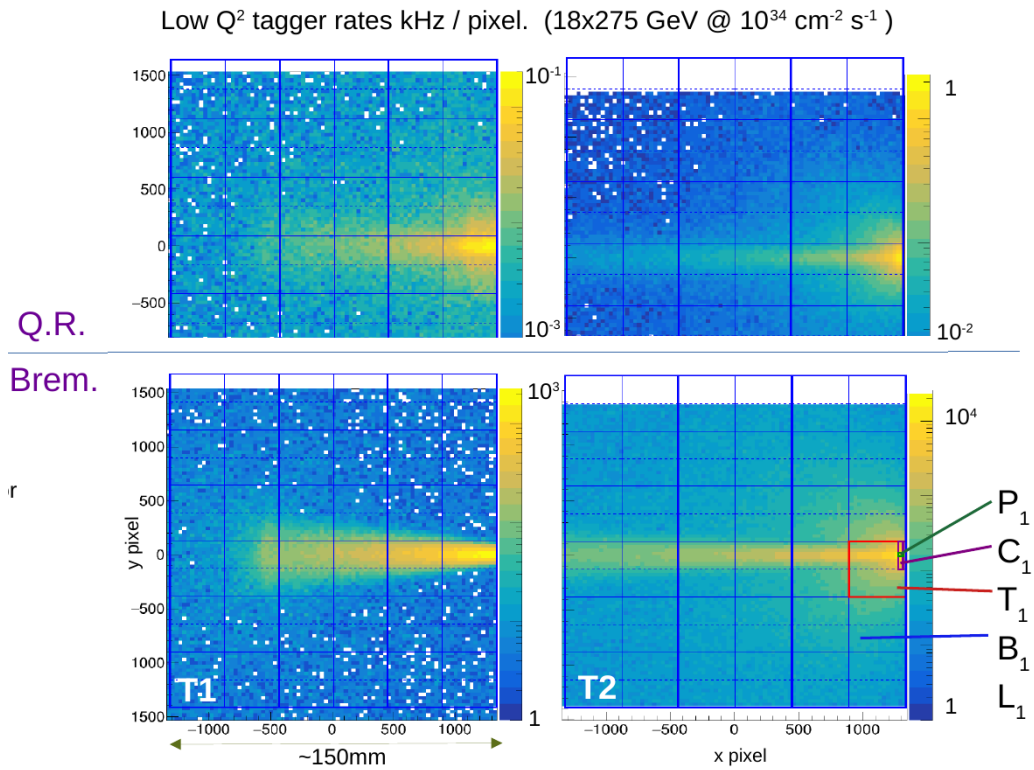


Figure 8.131: Hit rates on tracker layers for Quasi Real (Top) and bremsstrahlung (bottom) electrons, incident on Tagger 1 (left) and Tagger 2 (right). This design is based on layers with three carrier boards, each containing twelve Timepix4 hybrid sensors. The dashed lines indicated the centre lines of the Timepix4 ASICs, where the vertical columns terminate.

the beamline (Figure 8.132). For an estimate of the relevant rates we focus on the bremsstrahlung distribution in Tagger 2 and superimpose a tracking layer geometry based on two boards, each consisting of 12 Timepix4 hybrids, as shown in Figure 8.131. The four Timepix4 detectors running across the centre of board 1 (B1) take the bulk of the events, with the very highest on the one closest to the electron beam (T1). The small vertical offset between the centre of the board and the accelerator plane is to ensure that the centre line (dashed), where the top and bottom vertical 255 pixel columns meet, does not coincide with the very high rate band. The maximum rate estimates can be obtained by integrating over the relevant bins of the 2D histogram, and are shown in Figure 8.132. Although the dimensions of pixels and sensors are from Timepix4, these rates are *detector agnostic*, in the sense that they merely quantify numbers of electrons passing through the $55\mu\text{m}$ pixels in the tracking plane. After comparison with other technologies with other technologies proposed for the ePIC detector (MAPS, AC-LGAD) it became clear that Timepix4 is the only solution which can provide the required combination of rate capability, timing resolution and position resolution. The calorimeter paragraph.

The final configuration and position of the Low-Q2 tagger is still to be decided, since it depends on the position and structure of the magnets and beamline configuration in the backward regions. These are not yet finalised.

Subsystem description Tracker :

There are two trackers, each consisting of four layers on pixel sensors. The sensors are mounted on carrier boards (12 sensors per board) which connect to a readout modules. Readout modules perform some presorting and pass data to cluster and tracking modules and data buffers. Tracks which are in coincidence with a hadron in the central detector are saved in the main DAQ readout.

Sensors: Timepix4 ASIC with Silicon sensor.

FEE: SPIDR4 readout to custom FPGA clustering and tracking modules.

Other components: Frame / infrastructure with cabling and cooling for layers with removable carrier boards. Cabling from boards to readout modules (housed below on platform).

Subsystem description Calorimeter: Main purpose of the calorimeter is direct energy measurement for cross check with energy obtained from trackers, where it is measured indirectly via ML methods. Also alignment and fake-track reduction will benefit from the use of the calorimeter.

General device description: In the initial running at lower luminosity when in-bunch pileup from Bethe-Heitler bremsstrahlung is relatively small it is assumed to share the same technology as luminosity pair spectrometer, i.e. scintillating fibers embedded in tungsten-powder epoxy (SciFi), read-out by SiPMs. General layout of the SciFi calorimeter is indicated in Fig. 8.133, giving tower arrangement of 4 layers. Total perpendicular size is given by the trackers. The towers are arranged perpendicular to shower axis. Fibers inner radius is 0.25 mm, fiber spacing is 1 mm. Optical photons are detected by SiPMs, shown as yellow rings at the end of each fiber. It is assumed that groups of 4x4 fibers in the same cell act as a single SiPM. Opposite ends of the fibers are ended by aluminum mirrors, shown as green caps.

For the case of nominal collider luminosity, reached in later runs, the in-bunch pileup from Bethe-Heitler bremsstrahlung will cause calorimeter rates to reach bunch crossing frequency,

5763 giving some signal every 10 ns at top luminosity for 10x100 GeV beams. Calorimeter tech-
 5764 nology will be shared with luminosity direct photon detector, where only Cherenkov fibers
 5765 can fulfill the rate requirement. Expected energy resolution is shown in Fig. 8.134 Diameter
 5766 for quartz fibers 1.5 mm, fiber spacing is 2.5 mm. The resolution is mainly driven by limited
 5767 Cherenkov photon yields. Photon detection efficiency of 0.41 is included.

5768 Sensors: SiPM, specific SiPM with fast capacitive coupling is required for nominal luminosity,
 5769 possible example is Onsemi 30035 series.

5770 FEE: fADC250 (flash ADC, 250 MSPS, 12 bit) for nominal luminosity

5771 Other components: Add text here.

5772 **Performance** Don't know what that means in this context ?

5773 **Implementation**

5774 **Services:** No special services.

5775 **Subsystem mechanics and integration:** The taggers are housed on platforms which need to
 5776 be movable in vertical and horizontal (towards beamline) directions. Lower platform for readout
 5777 modules in close proximity for readout modules. Bias and LV per board (24 total). Chiller (800W)
 5778 per tagger.

5779 **Calibration, alignment and monitoring:** Procedures for calibration and equalisation of indi-
 5780 vidual sensors are already well established within the Medipix collaboration. These will be mapped
 5781 to a dedicated Slow Controls interface for the tracker. Alignment and timing calibrations require
 5782 tracks; they can be developed locally using cosmic rays and more rigorously tested in beam at Jlab
 5783 or one of the European facilities.

5784 **Status and remaining design effort:**

5785 R&D effort:
 5786 Electron tracker
 5787 Total expected from UK Infrastructure project in FTE years:
 5788 Academic 1.5
 5789 Senior Researchers 2.5
 5790 Postdocs 10.0
 5791 Technical 3.0
 5792 PhDs 10
 5793 Additional Requirement: Postdoc 6 FTE Years
 5794

5795 R&D status and outlook:

5796 Electron tracker:

5797 A test rig with SPIDR4 and Timepix4+Si sensors is complete, and fast readout tested. The
 5798 development of prototype tracker with single sensor layers in progress. To be tested in stand-
 5799 alone mode in Mainz, Dec24, with a further test using preliminary ePIC DAQ at Jlab in

5800 2026. Carrier board for 12 x Timepix4 sensors to be developed and approved by Dec 2027.
 5801 Procurement and fabrication of layers from Jan 2028 - 2030. Completion of taggers including
 5802 mechanical infrastructure, cooling, readout to be completed in Glasgow by Dec 2030 with
 5803 delivery to BNL Jan 31.

5804 Other activity needed for the design completion
 5805 Final decision on positioning, layer dimensions and spacing is still to be made. The requires
 5806 completion of designs for magnets, beamline and vacuum windows in the backward region.

5807 Status of maturity of the subsystem:

5808 Electron tracker

5809 The Timepix4 sensor is well established, and is the latest in a series of detectors by the CERN
 5810 Medipix collaboration. Current applications used the wire-bonded readout mode, but the
 5811 TSV (through silicon vias) mode is in fast development, and we anticipate having a test setup
 5812 within the next few months. The TSV mode is required to allow 4-side buttability, and fabri-
 5813 cation of the layers with no dead space. The current readout uses SPIDR4 from the NIKHEF
 5814 group in Amsterdam. We will collaborate with the developers to make an upgraded version
 5815 of their carrier boards and readout to handle the data from the 12 sensor layer modules.

5816 **Environmental, Safety and Health (ES&H) aspects and Quality Assessment (QA plan-**
 5817 **ning:** We will follow all procedures laid out by BNL and other labs where production test and
 5818 development are carried out. During the engineering design phase, we will include production of
 5819 mockups and engineering test articles to insure the proper functionality and quality, and will have
 5820 full production chain tests for each sub-system.

5821 For operation with HV and cooling we will ensure that these are mechanically secure and not a
 5822 trip hazard, have proper warning signs and follow the lab procedures for electrical safety, and
 5823 for operation near the beam-pipe and vacuum, anyone working near the far-forward/backward
 5824 detectors will wear ear protection, and will post signage to that effect.

5825 **Construction and assembly planning:** The tracker modules will be constructed assembled
 5826 and tested in Glasgow as Work Package 2 (WP2) of the UK's EIC Infrastructure project. We will fol-
 5827 low closely the fabrication and quality control procedures developed for the LHCb Velopix detector
 5828 by the Glasgow experimental particle physics group.

5829 **Collaborators and their role, resources and workforce:** The electron trackers are a *deliver-*
 5830 *able* within the UK's EIC Infrastructure project. The resources for constructing and delivering the
 5831 trackers are expected to be mostly met by this. However, the project is still to be passed through a
 5832 peer review panel and the costings for the tracker work package officially approved. As outlined
 5833 above, we anticipate that we need and additional 6 FTE postdoc years for simulation, analysis and
 5834 thermal modelling relating to detector development.

5835 **Risks and mitigation strategy:** The Timepix4 tracker is being developed in close collaboration
 5836 with colleagues in the Medipix collaboration. We will use suppliers and services recommended by
 5837 them for wafers and production. For local production, fabrication and testing we have more that
 5838 one person trained in bonding and quality control in case of staff changes. Our maximum rates
 5839 have been calculated on the basis of EIC maximum luminosities, so in the initial running we will
 5840 be well below capacity

5841 **Additional Material** Add text here.

5842 **8.3.9 Polarimeters**

5843 Add text here.

5844 **8.3.9.1 The electron polarimeters**

5845 **Requirements**

5846 **Requirements from physics:** Add text here.

5847 **Requirements from Radiation Hardness:** Add text here.

5848 **Requirements from Data Rates:** Add text here.

5849 **Justification**

5850 **Device concept and technological choice:** Add text here.

5851 **Subsystem description:**

5852 General device description: Add text here.

5853 Sensors: Add text here.

5854 FEE: Add text here.

5855 Other components: Add text here.

5856 **Performance**

5857 **Implementation**

5858 **Services:** Add text here.

5859 **Subsystem mechanics and integration:** Add text here.

5860 **Calibration, alignment and monitoring:** Add text here.

5861 Status and remaining design effort:

5862 R&D effort: Add text here.

5863 E&D status and outlook: Add text here.

5864 Other activity needed for the design completion: Add text here.

5865 Status of maturity of the subsystem: Add text here.

5866 **Environmental, Safety and Health (ES&H) aspects and Quality Assessment (QA plan-**
5867 **ning:** Add text here.

5868 **Construction and assembly planning:** Add text here.

5869 **Collaborators and their role, resources and workforce:** Add text here.

5870 **Risks and mitigation strategy:** Add text here.

5871 **Additional Material** Add text here.

5872 8.3.9.2 The proton polarimeters**5873 Requirements**

5874 **Requirements from physics:** Add text here.

5875 **Requirements from Radiation Hardness:** Add text here.

5876 **Requirements from Data Rates:** Add text here.

5877 Justification

5878 **Device concept and technological choice:** Add text here.

5879 Subsystem description:

5880 General device description: Add text here.

5881 Sensors: Add text here.

5882 FEE: Add text here.

5883 Other components: Add text here.

5884 **Performance**

5885 **Implementation**

5886 **Services:** Add text here.

5887 **Subsystem mechanics and integration:** Add text here.

5888 **Calibration, alignment and monitoring:** Add text here.

5889 **Status and remaining design effort:**

5890 R&D effort: Add text here.

5891 E&D status and outlook: Add text here.

5892 Other activity needed for the design completion: Add text here.

5893 Status of maturity of the subsystem: Add text here.

5894 **Environmental, Safety and Health (ES&H) aspects and Quality Assessment (QA plan-**
5895 **ning:** Add text here.

5896 **Construction and assembly planning:** Add text here.

5897 **Collaborators and their role, resources and workforce:** Add text here.

5898 **Risks and mitigation strategy:** Add text here.

5899 **Additional Material** Add text here.

5900 **8.3.10 Readout Electronics and Data Acquisition**

5901 **Requirements** The electronics and data acquisition systems are required to digitize and readout
5902 the data provided by the sensors of all ePIC detectors. The Electronics must tag hits with a time
5903 resolution sufficient to identify the bunch crossing (10.16ns) and provide high resolution time ref-
5904 erences as stringent as 5ps according the specific detector needs. The ePIC readout system must
5905 provide high data volume links to front end electronics up to 10Gb/s for selected components. The
5906 readout system must provide very high live times, with the goal of zero-system wide deadtime
5907 in normal operation, despite the possibility of by-channel deadtime according the specific readout
5908 technology of each detector.

Detector	Noise (hz/channel)
ITS3, Astropix, Timepix	0.01
AC-LGAD	30
HRPPD	230
dRICH(initial)	3000
dRICH(Max)	300,000
All Others	$4.5\sigma = 340$

Table 8.32: Noise Estimates

The Data Acquisition will group streaming data into time frames of $O(0.6\text{ms})$. The readout systems are expected to digitize up to $O(2\text{Tb/s})$ and must be capable of reducing this data volume to an output rate of $O(100\text{Gb/s})$ using techniques to compress signal and remove noise with minimal impact to signal integrity. The data from all running detectors for each time frame will be gathered together in a single buffer for transfer to the echelon 1 computing facilities located at BNL and JLAB for archive and analysis.

Requirements from Physics The scientific mission of ePIC is reflected in the requirements of the Electronics and DAQ through the scale and technology of the ePIC detectors shown in figures 8.135 and 8.136. Large channel counts combined with low occupancy lead to the need for multiple levels of aggregation at the Front End Boards (FEB), the Readout Boards (RDO) and the Data aggregation and Manipulation Boards (DAM).

The performance of the EIC Collider also impacts the requirements of the readout system. The collision rates and background rates are detailed in section ???. Two aspects are particularly important for the Electronics and DAQ.

The first is the maximum event rates, which we expect to be as high as 500kHz for DIS, 3.2Mhz for Electron Beam Gas and 32kHz for hadron Beam Gas. These rates are of primary interest within DAQ to estimate the data volumes which are described below.

The second consideration is that individual bunch crossing can have different polarization states. This implies that the luminosity and polarization of the beams must be tracked by bunch and produces the requirement that events must be associated to the bunch crossing from which they originated.

Requirements from Radiation Hardness The electronics installed in the ePIC detector will be subjected to significant radiation doses. Radiation doses are described in section ???. Electronics placed in the central detector (SVT, eTOF, bTOF, and MPGDs) will utilize radiation hard components to minimize the effect of radiation.

Electronics must be chosen and placed to minimize failure rates. Transient failures such as single bit upsets (SEUs) must have a recovery process which automatically senses, initiates, and accomplishes recovery while running in order to avoid downtime. There are commercial IP cores available for FPGAs that can support recovery from simple SEUs. More complex (multi-bit) failures will require an automated reset and reload feature for FEBs and RDOs.

Requirements from Data Rates The triggerless readout of the ePIC detector uses zero-suppression to help manage the volume of data read out. The streaming model's sensitivity to noise, beam background, and collision data make the understanding of these effects critical. Collision, synchrotron radiation and beam gas backgrounds from both the electron and hadron beams have been studied extensively by the ePIC collaboration, and the methods are presented in section ???. The hits have been converted to data volumes using our current understanding of zero suppression and data formats of each detector readout. Furthermore, the distribution of hits to each component has been estimated by arbitrarily assigning readout components to the sensitive planes of the detectors in order to estimate the impact of potential bottlenecks.

The hit rate for the collision signal is taken from simulated hits for DIS events generated by the ePIC physics and detector simulations. The simulated data set was taken for 18x275 GeV collisions with $Q^2 > 0$ with luminosity $1.54 \times 10^{33} \text{ cm}^{-2} \text{ s}^{-1}$. The collision rate was 83kHz, but the hit rates were scaled to the maximum rate of the EIC collider of 500kHz. Hadron and electron beam gas events were generated using the simulated vacuum profile after 10,000Ah of pumping. Noise calculations are currently based on the ePIC detector group expert estimates and shown in table 8.32.

One additional factor that must be considered is dark currents in the SiPM detectors which increase with radiation damage. In particular, this issue affects the dRICH, in which the SiPM threshold must remain low enough to be sensitive to single photons. There are several features planned to reduce these dark currents including annealing, and implementation of timing windows to synchronise readout with collision times. These are described in section ???. The DAQ system must be designed with the capability to manage the highest rates expected by the dRICH and must also apply filters to reduce the dRICH noise, either by applying a firmware trigger or by using specialized AI algorithms to determine which hits correspond to a dRICH physics signal.

Finally, noise is expected to be a potential issue in all other detectors as well. Generally, the noise level can be controlled with thresholds. The acceptable noise levels by detector is planned to be set according to the bandwidth requirements. The maximum data volume per RDO with estimated noise is summarized in table 8.138.

Device Concept and Technological choice: Streaming Readout The ePIC readout system will implement a flexible, scalable, and efficient streaming DAQ as outlined by the EIC Yellow Report. This design will provide the advantages of streaming include the replacement of custom L1 trigger electronics with commercial off-the-shelf (COTS) computing, virtually deadtime-free operation, great flexibility in event selection using full event data along with offline analysis, and the opportunity to study event backgrounds in detail. These advantages come at the cost of greater sensitivity to noise and background. A schematic of the readout system is show in figure 8.139.

The components in the ePIC readout system are shown in figure 8.140. Readout will be accomplished using detector specific front end sensors and adaptors. Even though the organization of the front end electronics varies by detector needs the custom electronics of each system generically referred to as Front End Boards (FEBs). There is no global trigger system in ePIC, instead each FEB is required to self-trigger, providing a stream of hit data. Digitization and zero-suppression is typically handled with ASIC support. Each FEB has similar needs for clocks, configuration, and serial data links. These needs are provided by Readout Boards (RDOs). The RDOs also aggregate data from the FEBs. The RDOs are driven by either FPGAs or IpGBT. The RDO serves as an interface between custom, technology driven, readout schemes of specific detectors and the ePIC DAQ. While there are a number of variations of the RDOs depending upon the FEB technology, all of the RDOs support a unified ePIC DAQ fiber protocol. They distribute high-resolution time reference, configuration, and control to the FEBs and transmit hit data and monitoring information to the Data Aggregation and Manipulation Boards (DAM).

The DAM boards have significant processing available for implementing firmware triggers and other data reduction algorithms. They also provide further aggregation and function as the interface between the electronics and the first level of COTS computers called the Frame Builder Data Collectors (FBDC). The farm of COTS DAQ computers dedicated to readout, data reduction, logging, monitoring, QA and data buffering and transfer to data centers is integrated in the ePIC computing model and referred to as echelon 0.

Synchronizing the front end electronics and provide high resolution time reference to beam crossings is an important requirement of the streaming DAQ. The Global Timing Unit (GTU) is the interface to EIC collider controls. It receives the 98.5Mhz bunch crossing clock and distributes it via the DAM boards to the RDOs and FEBs. The GTU is the only global source of real time information provided to the FEB/RDOs, so it must provide information a trigger system would normally provide. These functions include the ability to synchronize data from different detectors, to send flow control signals, to pass bunch information such as spin orientations and bunch structure, the ability to provide user defined signals for signaling special data formatting or calibration needs, and the ability to implement a hardware trigger for debugging or as a fallback option to solve unforeseen readout issues.

The communication between the RDOs, DAM, and GTU will use an unified data protocol serving four functions:

- The distribution of configuration information from the DAQ System to configure the RDOs, and to distribute configuration information to the FEBs via the RDOs using their serial links,
- The distribution of real-time control information to the RDO and FEBs,
- The distribution of a high-resolution beam crossing timing signal to the RDO and FEBs,
- The high performance ($\sim 10\text{Gb}$) transfer of hit data and monitoring information from the FEBs and RDO to the DAM boards.

Subsystem Description (components)

Readout Electronics and ASICS

Overview Readout electronics is being developed based on the sensor technologies. Common requirements among various sub-detectors have been identified to maximizing synergy. The readout electronics conforms to the ePIC streaming readout model with triggerless operation and serial interfaces. To facilitate calibration and debugging, capability for triggered operation is also implemented. The development of the readout electronics and ASICs are summarized in figure 8.141.

Discrete The Discrete readout implementation addresses the readout from calorimeters with SiPMs where high resolution digitization is required and commercial devices (COTS) are employed. The design and technologies will be validated for specific locations within the ePIC detector, where radiation hardness of COTS devices will need to be verified. The block diagram is shown in figure 8.142.

The circled area in fig. 8.142 delineates the Adapter section with SiPMs and bias circuitry; the remaining parts make up the FEB PCB, which includes signal conditioning, ADCs and readout logic. The Adapter and FEB PCBs are located at the detector, as a stack, and CAT6 cables are

employed for serial interfaces. Key specifications are shown in figure 8.144. Prototypes of the Adapter and FEB PCBs are shown in figure 8.143.

CALOROC The CALOROC ASIC is currently under development to address readout from calorimeters with SiPMs and for which a 10-bit resolution digitization with wide dynamic range capabilities is applicable. The CALOROC design is based on the existing H2GCROC ASIC for SiPMs with similar frontend and a backend, or digital section with interfaces, conforming to the needs of the streaming readout approach at the EIC. In parallel, tests with the H2GCROCv3 chip continue to provide input and validation into the design of the CALOROC ASIC. There are, however, two frontend variants being considered: CALOROC1A uses an ADC, a TOA and a TOT for wide dynamic range, similar to the H2GCROC; CALOROC1B uses a different frontend architecture making use of dual gain switching techniques to extend its dynamic range. The CALOROC block diagram is shown in figure 8.145 and its specifications summarized in figure 8.146.

EICROC The EICROC ASIC is currently under development to address readout from AC-LGAD pixel detectors with low detector capacitance (C_{din}) and very stringent timing precision requirements. The EICROC design is based on the existing HGCROC ASIC for Si and PMTs with similar frontend and a backend, or digital section with interfaces, conforming to the needs of the streaming readout approach at the EIC, which is already being designed for the CALOROC. Main IP blocks consist of preamp, discriminator, TOA, ADC and TDC. The EICROC block diagram is shown in figure 8.147 and its specifications are summarized in figure 8.149. Figure 8.148 shows the EICROC timing performance with varying charge from input signals.

FCFD The FCFD ASIC is currently under development to address readout from AC-LGAD strip detectors with medium detector capacitance (C_{din}) and very stringent timing precision requirements. The FCFD design implements the constant fraction discriminator technique for high precision timing without time-walk corrections. The backend, which is currently being considered, may be based on the existing ETROC ASIC or the EICROC development. The FCFD block diagram is shown in figure 8.150 and its specifications are summarized in figure 8.152. Figure 8.151 shows the FCFD timing performance with varying charge from input signals.

ALCOR The ALCOR ASIC is currently under development specifically for the readout of the dRICH detector with SiPMs due to its single photo-electron sensitivity requirement. The ALCOR design includes trans-impedance amplification (TIA) with regulated common gate (RCG) bias for low noise, inhibit or shutter operation to limit contribution from dark-rate SiPM noise and TDCs to allow for single-photon tagging or time and charge digitization. The shutter function is a critical aspect of this ASIC and it is programmable for width and latency. The ALCOR Die and block diagram are shown in figure 8.153 and its specifications are summarized in figure 8.154.

SALSA The SALSA chip is an ASIC currently under development, foreseen to do the readout of the different MPGD trackers, namely the barrel cylindrical Micromegas, the barrel RWELL and the end-cap RWELL detectors. The purpose of SALSA is to amplify, shape and digitize signals coming from the MPGD detectors, and then perform basic data processing on the digitized samples before to transmit them to the next element of the data acquisition chain. It gathers in a single die a CSA pre-amplifier, a shaper and an ADC for each of the 64 channels, followed by a DSP which performs baseline corrections, digital shaping and a zero-suppression in order to reduce the output data bandwidth. Furthermore, to reduce data output even more, a peak finding algorithm is

implemented to extract from samples information like amplitude and time of detected hits. It will be able to work both in the streaming readout environment foreseen at EPIC, and in a triggered environment.

The characteristics, performances and configurability of SALSA are designed to make the ASIC very versatile, being able to be adapted to several kinds of MPGD detectors and to several applications. It will be able to work with a large range of signal amplitudes, a large range of electrode capacitance and large range of signal rise times. Its target specifications are summarized in the Table 8.33.

Specification	Values	Remarks
Number of channels	64	Reasonable gain up to 1 nF
Input capacitance	50-200 pF	
Peaking time range	50 - 500 ns	
Max gain range	50 fC to 5 pC	Fast CSA reset
Max input rate	100 kHz/channel	
Signal polarity	Negative and positive	
ADC max sampling rate	50 MS/s	More than 10 effective bits
ADC dynamics	12 bits	
DSP processing	Baseline correction, filter, zero-suppression, peak finding	
Readout modes	Streaming readout, triggered	1 only used at EPIC
Output data links	4 Gigabit links	
Die technology	TSMC 65nm	
Die size	$\sim 1 \text{ cm}^2$	
Power consumption	$\sim 15 \text{ mW/channel}$	
Radiation hardness	Up to 300 Mrad and $10^{13} \text{ n}_{eq}/\text{cm}^2$	

Table 8.33: Main specifications of the SALSA chip.

Scope of the Effort The scope of the electronics and ASICs developments is summarized in figure 8.155, based on the number of readout channels, technologies employed and institutions developing these readout solutions.

It is noted that the pFRICH and the hpDIRC detectors benefit from the FCFD and the EICROC developments due to their timing precision requirements. The FCFD is, however, the nominal choice due to its lower channel density packaging for these applications with higher detector capacitances, which enable tailoring their timing performance via detector bias adjustment.

FEBCOMPONENTS

DC/DC converters DC/DC converters are employed throughout ePIC for the efficient distribution and regulation of the various sub-systems. The bPOL12V and bPOL48V DC/DC modules are selected for their radiation hardness and high magnetic field tolerances. Designs based on the LTC36xx family of devices will also be employed after proper validation.

Target Detector	Input	Output	technology
TOF Pre-Prototype, Calorimeters	copper	SFP+ fiber	FPGA
dRICH	copper	VTRX+ fiber	FPGA
SVT, MPGD, AC-LGAD second level	fiber	fiber	FPGA
AC-LGAD	copper	VTRX+ fiber	lpGBT
Imaging Calorimeter (Astropix)	copper	fiber	FPGA
Low Q^2 Tagger (Spyder3 Board)	copper	up to 12 fiber	FPGA
Direct Photon Detector	copper	fiber	flash

Table 8.34: Types of RDO

lpGBT The low power Giga-Bit Transceiver (lpGBT) chip will be extensively used in ePIC sub-systems to provide aggregation and serial communications of up to 2.5 Gbps. The lpGBT is radiation hard with Serializer/Deserializer (SERDES) functionality.

VTRX+ The VTRX+ module is an electro-optical receiver/driver which will be extensively used in ePIC to interface to multi-mode optical fibers with MT optical connectors. One (1) receiver Rx (2.5 Gbps) and four (4) transmitters Tx (10 Gbps) are implemented. The VTRX+ is radiation hard and it is tolerant to high magnetic fields; it has a small footprint, has low power consumption and interfaces directly to the lpGBT transceiver devices.

RDOs The RDO aggregates ASIC information from the multiple front end boards. The RDO also has the function of delivering a high resolution clock (≤ 5 ps jitter) to the front end boards. This clock is reconstructed from the data downlink fiber. The final function of the RDO is act as the interface between the detector specific function of the ASICs to the global ePIC DAQ fiber protocol. This protocol labels bunch crossings, organizes time frames, uses user defined fast commands to communicate with the ASICs and provides the capabilities for firmware triggering and flow control.

However, several detectors: the SVT, the MPGD based detectors, and all AC-LGAD based readouts will make use of lpGBT or lpGBT-like aggregation using VTRX+ transceivers. The lpGBT aggregates ASIC information, and delivers a high resolution reconstructed clock. However, it attempts to give a transparent interface to the ASICs. It does not have the capability of implementing the full ePIC protocol. For these RDOs the protocol will be implemented at the next level, either inside the DAM board or in a second level fiber to fiber RDO.

There will be several versions of the RDO depending on the needs of the specific detectors. The different RDO types are summarized in table 8.34

TOF pre-prototype RDO (FPGA based copper to SFP+ The TOF pre-prototype RDO was designed to use elements common to most ePIC detector RDOs. These elements include Xilinx Artix+ FPGA, SFP+ fiber optics interface, clock cleaner PLLs, and clock recovery. The pre-prototype has been produced and is undergoing measurements of power usage and clock jitter. The board is shown in figure 8.156.

dRICH RDO The dRICH RDO is part of the dRICH Photo Detector Unit PDU (see section ??, 1248 PDUs will serve the dRICH). It provides read-out of four 64-channel ALCOR ASIC, installed

each on a separate FEB. The space constraints are particularly demanding: the total RDO area is 40x90 mm² - quite similar to a credit card - requiring a devoted design, given the high integration of data buses and services within the PDU. The FPGA providing readout of the ALCOR is an AMD Artix Ultrascale+ AU15P-SBVB484, complemented by a PolarFire FLASH-based FPGA MPF050T-FCSG325. The latter will support remote programming and continuous scrubbing of configuration bits of the SRAM-based AMD FPGA, to protect against SEU. Given the space constraints and the need to curb power consumption (total RDO power is expected ≈ 4 W) the CERN-developed VTRX+ optical transceiver has been selected, directly connected to the AMD FPGA SERDES. The maximum throughput per link (reached at maximum radiation damage before annealing) is foreseen not exceeding 2 Gbps, safely within VTRX+ specifications. The ALCOR will be read out at 394 MHz, with a clock multiplier and jitter-attenuator (Skyworks Si5326) deriving this clock from the reconstructed EIC clock. A Microchip microcontroller provides power management and acts as watchdog against SEL. The first prototype of this card is under production and will be intensively tested during 2025, including irradiation tests. A 3D-rendering of the card is shown in Fig. 8.157.

Fiber to Fiber RDO The fiber to fiber RDO is to be used with lpGBT-like FEBs to convert the transparent ASIC interface to the ePIC DAQ protocol. They are also necessary to further aggregate the fibers, particularly in the case of SVT and bTOF large numbers of low-data utilization fibers are required.

lpGBT based copper to fiber RDO This RDO is yet to be designed, but is required for the lpGBT based readout of the inner detectors.

Astropix End of Stave Card (RDO) This RDO is to be developed by NASA for use with the Astropix sensors.

Low Q^2 RDO This is a RDO specifically for the low Q^2 taggers. It is expected to be an updated version of the Spyder3 board. These use the timepix sensor and have high potential data volumes, requiring several uplink fibers per RDO.

Flash based RDO The Flash RDO is a specialized interface for the Direct Photon Detector. This detector has only about 100 channels, but is expected to have very high occupancy, and as such the appropriate technology is to digitize all data at 200MHz and stream it directly to the DAM boards which will summarize the information, writing out only the summed energy deposited each bunch crossing, or histograms of the bunch crossing energies according to bunch number.

DAM - Data Aggregation and Manipulation Hardware For the ePIC DAQ system the DAM boards will be used as the primary aggregation point for the “raw” detector data streams. Because these boards are also the final aggregation points for the front-end (hardware managed) DAQ, there will need to be some well-defined but configurable algorithms for merging streams and managing potential congestion and data loss both for the incoming detector streams and the outgoing aggregated streams being queued up for online processing.

In Addition, the DAM boards will interface with the Global Timing Unit (GTU) hardware via a proprietary communication protocol that supports a synchronized EIC clock distribution to all sub-systems and general DAQ/Run control and configuration. Finally, the DAM will act as the slow

control interface for configuration and monitoring of all detector subsystem front-end boards (e.g. ASICs and other digitizing electronics).

We have identified an ideal candidate for the DAM hardware. An updated version of the FELIX board (Model FLX155) is currently being produced at BNL for ATLAS at the HL-LHC. Its features are substantial and the updated components ensure a longevity of production, performance and support that match very well with the EIC timeline. The board is built around the new Xilinx Versal FPGA/SoC family. This will facilitate using the board both as a PCIe device (supporting both PCIe Gen4 and Gen5 standards) in a server or as a standalone “smart” “aggregation” switch running a Linux OS. It can support up to 48 serial links to RDOs at the front-end running at speeds up to 25Gbps as well as an LTI interface (8 fibers) supporting a high-resolution direct clock along with our GTU-DAM communication protocol. There is also a separate 100Gb ethernet link off the board. A DDR4 RAM slot is available to support buffering and more complex algorithms for data reduction or interaction tagging. The board supports JTAG and I2C communications.

We expect to procure several FLX155 boards for testing and software/firmware development in 2025.

GTU - Global Timing Unit The design of the global timing distribution system (GTU) will be central to the operation of the streaming readout model. The timing system must provide signals to ensure that the data from different detectors can be synchronously aggregated. It must provide a copy of the accelerator bunch crossing clock (running at 98.5Mhz) to all front-end systems. A subset of these systems (e.g. TOF) will require a phase aligned system clock with a jitter of $< 5\text{ps}$ in order realize required timing resolutions for these detectors (20-30ps).

The GTU is also the only source of real time information provided to the FEB/RDOs, so it must provide information a trigger system would normally provide. These functions include the ability to synchronize data from different detectors, to send flow control signals, to pass bunch information such as spin orientations and bunch structure, the ability to provide user defined signals for signaling special data formatting or calibration needs, and the ability to implement a hardware trigger for debugging, calibration or as a fallback option to solve unforeseen readout issues. It will also need to track potential phase changes of the beam relative to the accelerator clock due to the transitive loading specific to the EIC acceleration scheme.

Figure 8.158 shows a schematic layout based on required functionality of the GTU. The physical concept is shown in figure 8.159. In general the GTU will be custom rack-mounted hardware in the DAQ room. It will be based on a multi-FPGA architecture including a single Zync SoC FPGA supporting gigabit ethernet and a full Linux OS to facilitate both ePIC Run Control and other user-based applications. It will include an interface for the EIC Common platform (Clock, beam orbit and other collider information) and an interface for feedback from the local IP-6 beamline to support bunch crossing clock phase corrections

The jitter-cleaned and phase corrected clock then is fanned out for distribution to all DAM boards via a multi-fiber communications link (We intend to support up to 150 of these links for current needs as well as potential future requirements). In addition we plan to support up to 250 direct clock links to the RDO/FEB electronics. This is to mitigate potential limitations with the distribution of the low jitter ($< 5\text{ps}$) clock via the DAM path communication protocol.

Protocols The ePIC fiber protocol is used to communicate information between the GTU, DAM and RDO boards. The DAM to RDO communications are limited by the type of interface, and can be described in three categories as shown in table 8.36.

DarkGray		Decoded Synchronous Command Structure								
Gray		[0:7]		[8:15]	[16:23]	[24:31]	[32:39]	[40:47]	[48:55]	[56:64]
Gray	Flexible Command Data Encoding			FAST CMD		Comma				
type				type specific				FAST CMD		Comma

Table 8.35: DAM/RDO Decoded Synchronous Command Structure. This structure is defined to allow continuous availability of the critical beam related bits and more rare commands. The data in the 40 bits worth of flexible command data encoding remains flexible but must contain enough control bits to select what structure it has. The "type", "type specific" division is an potential holding this flexibility

type	clock (MHz)	downlink rate (Gb/s)	downlink word length (ns)	downline word width (bits)
FPGA Standard	98.5	10	10.15	64
FPGA VTRX+	98.5	2.56	10.15	16
lpGBT VTRX+	39.4	2.56	25.375	64

Table 8.36: RDO downlink words

The ePIC fiber protocol depends upon a synchronous command structure (table 8.35 which simultaneously encodes fast commands, to be delivered to the RDO or ASICs with fixed latency relative to the bunch crossing and control information such as the current bunch crossing. The RDO acts upon delivered synchronous commands to provide headers defining the time frames, and to implement required features. The lpGBT provides a transparent fiber interface to the ASICs and does not have features capable of implementing the full ePIC DAQ protocol, so this functionality must be provided later in the chain, either in a second layer fiber to fiber RDO, or in the DAM board itself.

The maximum timeframe length, in bunch crossings will be defined to fit within 2^{16} , which implies a time frame length of $\approx 0.6\text{ms}$. This is also a convenient time as it corresponds to a manageable maximum time frame size of $\approx 10\text{MB}$. The need to support both the 10.15ns EIC clock and the synchronized 25.375ns clock support by cern lpGBT and CERN developed asics demands that time frame lengths be limited to multiples of 5 EIC clocks, if the time frame's are to be synchronized in time.

The features encoded in the Synchronous command protocol are

1. Synchronize bunch counters among all detector readouts
2. Define the time frame boundaries
3. Provide RDO and DAM Data processing flags
4. Configure ASICs and RDOs
5. Firmware based triggering
6. Flow control
7. Transfer Data
8. Transfer Slow Controls Data

Firmware Trigger One example of the operation of the protocol is in the firmware trigger to be implemented to reduce dRICH noise. It's important to note that the the firmware trigger under discussion is not (or not necessarily) a global trigger that would remove full events from the readout of the ePIC detector. Instead, this trigger is expected to affect only the data from particular detectors with unusually high data volumes. In this example, the dRICH.

The path of the commands sent is show in figure 8.160. Data arrives at DAM boards with 10us from digitization. It is stored in the DAM boards. After 10us FPGA based algorithms provide a description of the data (for example number of hits above a specified threshold) from each fHCAL DAM board. This information is encoded into 64 bits and sent to the GTU which aggregates data from fHCAL DAM boards and sends the keep/drop bunch bit to the dRICH DAM boards. The dRICH DAM boards drop or transmit data based upon this message. The decision comes after a fixed latency of about 11us which is very small compared to the buffering available on the DAM board.

Note that a similar approach can be implemented with a hardware signal into the GTU. In this case a fixed delay is applied to the hardware signal, but the decision mechanism uses the same data path.

dRICH Internal trigger There is also another scheme for implementing a dRICH trigger using only dRICH data under investigation by the dRICH group ?? In this scheme, 8 of the data ports are dedicated to connect a second layer of DAM boards which implement a multi FPGA ML algorithm with deterministic time. The results of this calculation are transmitted to the GTU in the same manner as in the previous firmware trigger.

Resource	Totals
DAM/FELIX boards	136
EBDC Servers	92
DAQ Compute Nodes	108
File Servers (Buffer Box)	6

Table 8.37: DAQ Computing Resources

DAQ/Online Computing - Echelon 0 Table 8.37 outlines the planned resources for the ePIC detector DAQ and Online computing needs. This is based on the elements shown in the DAQ schematic in Figure 8.139. Several thousand fibers from the RDOs will be aggregated in the DAM boards and presented to the Online Farm. To be clear each online farm node represents one multi-core server. The expectation is that they will minimally support 32-64 cores, and selected nodes will support PCIe-based GPUs and/or FPGAs in addition to the DAM boards in the FBDC (Frame Building Data Concentrator) nodes. The high performance DAQ network is expected to support 100/400Gbps bandwidth connections. As the majority of the Online computing is expected to be COTS hardware, much of it will be acquired as late as is reasonable in the construction phase.

All Echelon 0 resources are fully dedicated to operation of the ePIC Detector and are included as part of the EIC Project. One open question under consideration, however, is to split these resources between the DAQ Room at IP-6 and the SDCC (BNL main data center) and to integrate them as a single enclave under ePIC control. There are several advantages to this configuration. First it will reduce the overall cost of infrastructure upgrades to the DAQ Room cooling systems. Also, having a subset of ePIC computing resources available in the SDCC will allow better network

6259 access to DAQ and electronics labs during construction (when the DAQ Room will not be available.
6260 Finally, during operations having DAQ tiered storage of production data in the SDCC will facilitate
6261 distribution of that data to both Echelon 1 processing sites (BNL and JLAB).

6262 At the DAM stage the aggregated data streams will have substantial buffering and available net-
6263 work bandwidth for online processing that will be primarily focused on event identification and
6264 background/noise reduction. While we do not currently have solid estimates on the necessary
6265 computing resources to complete the required tasks, we have tried to provide conservative esti-
6266 mates of computing resources that would allow a full reconstruction of a 500kHz trigger rate of
6267 events from similar scale detectors that exist now (e.g. GlueX and CLAS12 at Jefferson Lab and
6268 sPHENIX at RHIC). More likely the necessary computing resources for online filtering to get the
6269 expected data rates of O(100Gbps) to files will be somewhat smaller.

6270 **Time Frame Building** In the streaming model, the primary consideration is ensuring that
6271 enough bandwidth and buffering will be available to handle the digitized data at each stage of
6272 the DAQ. At the front-end stage time frames for the individual streams are created, managed and
6273 aggregated. Given current background and noise estimates the planned bandwidth off the detector
6274 to the DAM boards O(10Tbps) should be more than sufficient.

6275 Streams at the DAM boards will support time frames using a 16 bit bunch crossing counter which
6276 would represent a configurable time window of up to $65536 \times 10.15\text{ns} = 665\mu\text{s}$. Although the front-
6277 end DAQ will be synchronized using a single common clock from the EIC, not all ASICs/digitizers
6278 at the FEBs will be running at the same frequency. Hence the timestamps coming from hits in
6279 different detectors will need to be wrapped in smaller "time slices" within the full time frame to
6280 establish an absolute time for each hit.

6281 Time frames buffered at the DAM boards will be able to utilize the online farm to complete a full
6282 build of complete time frames with data from all detectors. Effectively N streams from the DAM
6283 boards will generate $M < N$ streams of time frames containing the time frame fragments from the N
6284 original streams. This will greatly facilitate additional event identification and processing at both
6285 the Echelon 0 and Echelon 1 stages.

6286 **Data Processing** The ePIC readout system must support data reduction techniques. The imple-
6287 mentation of firmware based triggering has already been described, but there are many additional
6288 techniques that might be implemented in echelon 0. These include zero loss techniques like aggre-
6289 gation of headers from ASICs or DAM board data. It could include standard or ML based compres-
6290 sion techniques. It could involve analysis techniques such as cluster finding or track reconstruction.
6291 There could also be ML based noise reduction techniques. And there could be analysis done for
6292 specific purposes such as the creation of scalers for monitoring or collider feedback.

6293 The framework for the code generating these features must allow the code to be shared with the
6294 offline software, for operational transparency, and for algorithm evaluation.

6295 The results of the code must be incorporated into the time frame data using data formats that allow
6296 for independent data banks to co-exist. The policy of ePIC is expected to be to avoid dropping any
6297 data unless data volumes make it necessary. There should also be a sample of unprocessed data
6298 even if the readout of raw data banks are suppressed due to data volume limits. This implies that
6299 the write out of specific data banks be controlled by configurable prescales.

6300 **Configuration Databases** Configuration information must be stored and made accessible to
6301 the ePIC Collaboration.

6302 **Slow controls interface to RDOs/FEBs** The primary configuration and slow control com-
6303 munications interface to all the ASICs and other digitizing electronics (FEBs) will be through our
6304 proprietary data link between the DAM board and the RDOs. Our current plan is to take advan-
6305 tage of the Versal SoC FPGA dual-core ARM Cortex processor. ALL DAM boards will support a
6306 full LinuxOS and gigabit ethernet access. This will facilitate running an EPICS soft IOC as well as
6307 user-based server applications for local and remote communication with the front-end electronics.

6308 Slow control communication on the DAM-RDO link must be bidirectional which means that slow
6309 control communications must share the link with streaming data coming from the detectors. Nom-
6310 inally, we will be providing more than adequate bandwidth to support this slow control piece even
6311 if the stream is active, but provisions will be made to ensure that stream time frames will take
6312 priority.

6313 Software and firmware development of drivers and libraries necessary to access all the FEB "fla-
6314 vors" is supported as part of the Project. The majority of the FEBs will support standard I2C control
6315 communications.

6316 **Monitoring / Logging** A unified system for centralized logging of informational and error mes-
6317 sages is required. These messages should be ideally be available and archived in web-accessible
6318 form.

6319 A unified system for monitoring of the real time behaviour and utilization of online components is
6320 also needed.

6321 **Interface to Echelon 1** As discussed in Section X (computing), the ePIC DAQ (Echelon 0) is an
6322 integral part of the computing system, and the output of the DAQ data triggers the calibration and
6323 reconstruction pipeline in Echelon 1, located at the computing centers of the host labs. From the
6324 DAQ buffering disks, two identical copies will be sent to the buffer file system at the BNL SDCC
6325 via a dedicated fiber link and at the JLab Data Center via the 400Gbps ESnet link, respectively. Each
6326 data center's data buffer has the capability of about three weeks' ePIC data taking to allow for mul-
6327 tiple iterations of calibration jobs and reconstruction passes. Data will also be copied to permanent
6328 archival storage (presumably HPSS-like tape system), one copy at each site, which allows for re-
6329 processing of the data in the future in case a problem identified in the prompt reconstruction pass
6330 or an improved reconstruction becomes available in the future. Nevertheless, in a steady state, the
6331 prompt calibration and production are expected to make the final analysis-ready data for physics
6332 working groups within days of the data taking, significantly expedited compared to many ongoing
6333 Nuclear Physics experiments.

6334 **Slow Controls** There will be a myriad of slow controls information associated with both the
6335 EIC collider and the ePIC detector. These include various systems associated with the beamline,
6336 magnets, detector biases, gas flows, temperatures, pressures, etc. . . While the design and imple-
6337 mentation of these slow control systems will be driven by the relevant subsystems they are asso-
6338 ciated with, it is the defined responsibility of the DAQ to provide software tools to facilitate the
6339 integration of all this information with the streaming physics data. This will include synchronizing
6340 the times associated with readout of slow control systems and the bunch-crossing clock that will be
6341 driving the DAQ system. Online slow control databases to support calibration and reconstruction

Scenario	Yearly Database Storage (TB)	Network Traffic (Mbps)
estimated	53.9	22.8
worst case	173.5	73.4

Table 8.38: Slow Controls data volume and network traffic

processing will also be developed. Finally, a general network infrastructure in the experimental hall and control room, independent of the high performance DAQ network, will be provided to support integration of all slow control systems

A schematic of the proposed slow controls network topology is shown in figure 8.161. The implementation uses EPICS 7 on an ethernet network to control detector operation and read and archive conditions information. Allen-Bradley PLCs are to be used for controlling power to racks in the IR and for detector interlocks.

Resource requirements for the slow controls system were obtained by surveying detector managers. These resulted in approximately 500,000 channels to be read and stored. The yearly storage estimates and network traffic estimates are show in table 8.38.

Implementation

Calibration, alignment and monitoring: During run time, predetermined calibration and alignment will be used in configuring the readout electronics and data reduction computing tasks. These calibration and alignment are managed by detector groups, extracted from dedicated prior-to-beam calibration runs, such as pedestal runs and zero field runs. When necessary, such as changes in detector condition, new calibration will be extracted and updated to be used in data taking. The calibration constant used will be archived in the run database and made available for reference in the offline analysis.

Constant monitoring for detector status and data pipeline healthiness is key to high-efficiency data taking and a successful run. We expect a multi-level of monitoring that includes monitoring the metrics on (1) detector statues (2) each stage of the data pipeline (3) sampled data content for decoding and analysis. In addition, in the Echelon-1 computing facility, full reconstruction will be performed for a small fraction of time frames expediently to provide holistic feedback of the experiment capability down to analysis level observable such as π_0 and K_0 s.

Status and remaining design effort:

R&D effort: ASIC R&D to continue through 2025

E&D status and outlook: The bulk of the engineering design efforts still required for the readout electronics are centered around the development of RDO and FEB designs needed to support all the detector subsystems. This information is needed to establish baseline costs and better define construction and testing schedules. Project Engineering design for a GTU engineering article can be completed prior to CD2/3. Finally, we expect to procure several FLX155 engineering articles in 2025 to support further timing and communication protocol testing and initial firmware development.

Status of maturity of the subsystem: Electronics and DAQ held a second PDR in June 2024. We expect to hold a third PDR in 2025 on track to an FDR in 2026. There are CD-3B items in

6377 the Electronics for VTRX+ and lpGBT. The FDR was held in June 2024, and will be presented
6378 during the CD-3B review in January 2025.

6379 **Environmental, Safety and Health (ES&H) aspects and Quality Assessment (QA plan-**
6380 **ning:**

6381 **Construction and assembly planning:** Figure 8.162 shows the current project schedule for
6382 DAQ/Computing. It is broken down into four general categories: Design/Procurement, Fabricate
6383 and Delivery, Test and Accept and Installation. Early in the construction phase there is a heavy
6384 focus on building and testing custom hardware (GTU, DAMs, RDOs) in order to facilitate detector
6385 subsystem testing and DAQ firmware/software development. This will take place primarily in
6386 several DAQ/Electronics labs at BNL in the Physics building.

6387 Once IP-6 infrastructure upgrades have been completed (DAQ and Control rooms, Wide Angle
6388 Hall), we can begin the main trunk fiber pulls into the hall and tunnels and install required patch
6389 panels and terminate fibers. At this time we can also start installation of the general IP-6 network
6390 infrastructure in the Hall, DAQ and Control Rooms.

6391 Computing hardware procurement and installation are scheduled in three phases during the course
6392 of construction. Phase I at the beginning of construction will be for a small subset of machines for
6393 development and evaluation. They will be placed in both the DAQ/Electronics development labs
6394 as well as in the SDCC. Phase II will be primarily in the DAQ Room as part of the DAQ subsystem
6395 installations and will provide the opportunity for full chain large scale testing of the DAQ as well as
6396 for detector subsystems as they begin to be installed at IP-6. Finally Phase III will be implemented
6397 at the end of the full ePIC detector installation as we have a better understanding of the required
6398 resources needed for initial Physics operation. This hardware will be installed at both the DAQ
6399 Room and in the SDCC which will define the full Echelon 0 enclave.

6400 **Collaborators and their role, resources and workforce:** The institutions specifically devel-
6401 oping the readout electronics and ASICs are listed under the electronics section. Figure 8.163 lists
6402 the institutions which have expressed interest in participating in the design of various other parts
6403 of the readout chain. Formal agreements committing engineering and technical personnel have not
6404 been officiated.

6405 **8.3.11 Software and Computing**

6406 **Requirements**

6407 **Requirements from physics:** Add text here.

6408 **Requirements from Radiation Hardness:** Add text here.

6409 **Requirements from Data Rates:** Add text here.

6410 **Justification**

6411 **Device concept and technological choice:** Add text here.

6412 **Subsystem description:**

6413 General device description: Add text here.

6414 Sensors: Add text here.

6415 FEE: Add text here.

6416 Other components: Add text here.

6417 **Performance**

6418 **Implementation**

6419 **Services:** Add text here.

6420 **Subsystem mechanics and integration:** Add text here.

6421 **Calibration, alignment and monitoring:** Add text here.

6422 **Status and remaining design effort:**

6423 R&D effort: Add text here.

6424 E&D status and outlook: Add text here.

6425 Other activity needed for the design completion: Add text here.

6426 Status of maturity of the subsystem: Add text here.

6427 **Environmental, Safety and Health (ES&H) aspects and Quality Assessment (QA plan-**
6428 **ning:** Add text here.

6429 **Construction and assembly planning:** Add text here.

6430 **Collaborators and their role, resources and workforce:** Add text here.

6431 **Risks and mitigation strategy:** Add text here.

6432 **Additional Material** Add text here.

6433 **8.4 Detector Integration**

6434 Add text here.

6435 **8.4.1 Installation and Maintenance**

6436 Add text here.

6437 **8.5 Detector Commissioning and Pre-Operations**

6438 Add text here.

Maximum rates		
Pixel (P1)	70 kHz	
2 column (C1)	8 MHz	
Tpix4 (T1)	600 MHz	38 Gb/s
Board (B1)	1500 MHz	96 Gb/s
Layer (L1)	2500 MHz	160 Gb/s
Total integrated rates		
Tagger 1	2 GHz	130 Gb/s
Tagger 2	7 GHz	480 Gb/s
Total	9 GHz	600 Gb/s
Data buffered & filtered: need a hadron in main detect		
Trigger rate: 500 kHz: 99.4% rejection (brem only)		
Data rate (signal): 4 Gb/s		
Data rate (incl BG and rand sample) <20 Gb/s To tape		

Figure 8.132: Maximum and integrated rates for Low- Q^2 trackers

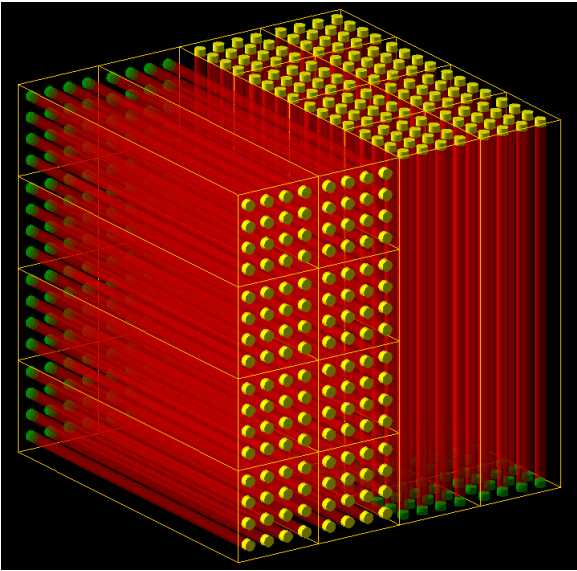


Figure 8.133: Layout of SciFi calorimeter

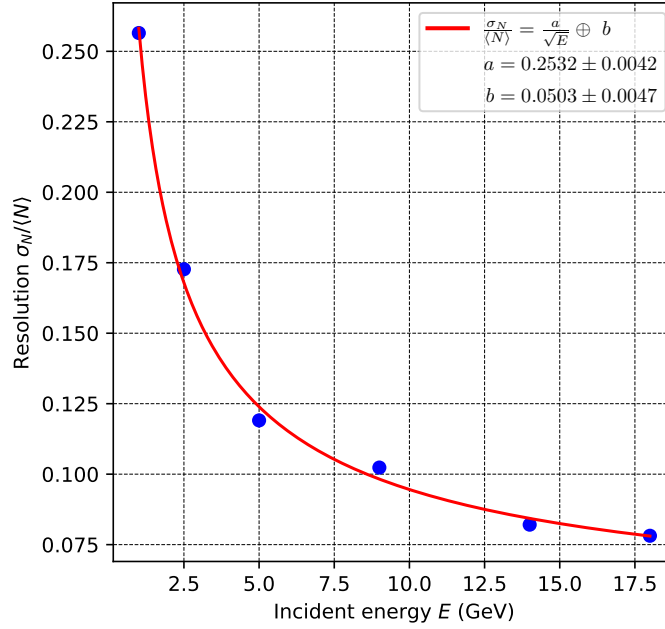


Figure 8.134: Energy resolution for Cherenkov fiber calorimeter

Detector Group	Channels					Det Fiber Down	Det Fiber Up	RDO	Fiber Pair (DAQ)	DAM	Data Volume (RDO) (Gb/s)	Data Volume (To Tape) (Gb/s)
	MAPS	AC-LGAD	SiPM/PMT	MPGD	HRPPD/MCP-PMT							
Tracking (MAPS)	16B					183	5863	183	183	7	15	15
Tracking (MPGD)				164k		160	640	160	160	5	27	5
Calorimeters	500M		100k					510	510	17	70	17
Far Forward		1.5M	10k					80	80	6	36	12
Far Backward	66M	128k	4k					60	82	14	301	16
PID (TOF)		6.1M				500	1364	500	500	14	50	12
PID Cherenkov			318k		143k			1283	1283	32	1275	32
TOTAL	16.6B	7.7M	432k	164k	143k	843	7,867	2,776	2,798	95	1,774	109

Figure 8.135: ePIC DAQ component count summary

Detector System	Channels	ASIC	FEB	RDO	Gb/s (RDO)	Gb/s (Tape)	DAM Boards	Readout Technology	Notes
SI Tracking: Inner Barrel (IB) Outer Barrel (OB) Backward Disks (BE) Forward Disks (FE)	1.88 Pixels 5.08 Pixels 4.78 Pixels 4.78 Pixels	160 495 462 462	592 1870 1744 1744	24 55 52 52	2.36 3.52 4.68 4.68	2.36 3.52 4.68 4.68	1 2 2 2	ITS-3 sensors & ITS-2 staves / w improvements	ASIC corresponds to VTRX+ counts FEB corresponds to detector fiber RDO is off detector fiber aggregator
MPGD tracking: Electron Endcap Hadron Endcap Inner Barrel Outer Barrel	16,384 16,384 32,768 98,304	256 256 512 1536	64 64 128 384	16 16 32 96	2.86 4.01 4.10 15.81	0.58 0.80 0.82 3.16	1 1 1 2	uRWELL / SALSA uRWELL / SALSA MicroMegas / SALSA uRWELL / SALSA	VTRX+ based FEB
Forward Calorimeters: LFHCAL 8k ECAL W/ScFI 16,000 Barrel Calorimeters: HCAL 1,536 ECAL ScFI/PB 5,760 ECAL ASTROPiX 500M pixels Backward Calorimeters: NHCAL 3,256 ECAL (PWO) 2,852	63,280 8k 16,000 1,536 5,760 500M pixels 3,256 2,852	1130 142 500 28 102 500M pixels 58 102	1130 142 500 28 102 58 102	74 9 64 2 4 340 4 13	18.54 17.72 14.75 0.87 11.45 1.25 3.46 2.00	2.47 2.36 7.36 0.12 1.52 1.25 0.47 0.99	2 1 2 1 1 8 1 1	SIPM / CALOROC SIPM / CALOROC SIPM / Discrete SIPM / CALOROC SIPM / CALOROC Astropix SIPM / CALOROC SIPM / Discrete	CALOROC: 56 Ch/CALOROC 16 CALOROC / RDO Discrete: 32 Ch/FEB, 8 FEB/RDO conservative (16 estimate).
Far Forward: 80: Crystal Calorimeter 4 AC-LGAD layer 2 Roman Pots 2 Off Momentum ZDC: Crystal Calorimeter HCAL	135 688,128 524,288 294,912 900 9,216	672 512 288 165	168 128 72 165	1 42 32 11	2.3 12.75 14.53 0.7 2.30 0.22	2.3 2.1 2.1 0.7 4.5 -22	1 1 1 1 1 1	SIPM/APD / Discrete AC-LGAD / EICROC AC-LGAD / EICROC AC-LGAD / EICROC SIPM/APD / Discrete CALOROC	4 layer x 42 module x 4 EICROC x 1024 ch 2 stations x 2 layer x 32 module x 4 EICROC x 1024 ch 2 stations x 2 layer x 18 module x 4 EICROC x 1024 ch
Far Backward: 2 x Low Q Tagger 2 x Low Q Tagger Cal 2 x Lumi PS Calorimeter 2 x Lumi PS tracker Direct Photon Lumi Cal	66M pixels 420 3,360 128k 100	3456 512 1000 18,432 3,632	288 128 250 24	24 1 64 24*	37 - 19 45 200	.3 - 7 2 7	10 1 1 2 1	Timepix4 SIPM / CALOROC SIPM / Discrete AC-LGAD: FCDF or EICROcX SIPM / RAD250	Firmware Trigger to reduce output rate Low Q Calorimeter doesn't run at high luminosity Direct Photon: commercial digitizer, no RDO
PID-TOF: Barrel Endcap	2,359,296 3,719,168	18,432 3,632	288 212	288 212	15.95 33.92	4.79 7.34	8 6	AC-LGAD: FCDF or EICROcX AC-LGAD: EICROC	bTOF 128 ch/ASIC, 64 ASIC/RDO eTOF 1024 pixel/ASIC, up to 28 ASIC/RDO
PID-Cherenkov: dRICH pRICH DIRC	317,952 69,632 73,728	4968 544 576	4968 68 144	1242 17 24	1240 24 11	13.5 12.5 6	30 1 1	SIPM / ALCOR HRPPD / FCDF or EICROcX MCP-PMT / FCDF or EICROcX	Worse case after radiation. Includes 30% timing window. Requires further data volume reduction Firmware trigger

Figure 8.136: ePIC DAQ component counts

Summary of Data Flow

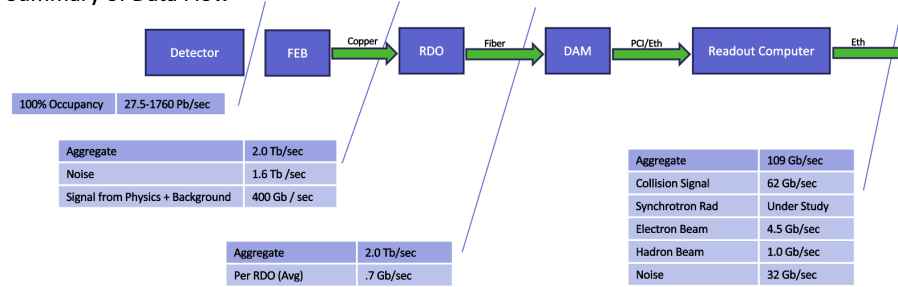


Figure 8.137: Expected worst case data rates contributions for the ePIC detector

Detector	Channel Max Hit Rate (Hz)	Noise To RDO (gbps)	Noise Per RDO (gbps)	Noise To Tape (gbps)	RDO (max) (gbps)	RDO_max / with Noise (gbps)
SiBarrelTracker	4.13E-04	3.25	0.06	3.25	0.00	0.06
SiBarrelVertex	5.22E-03	1.15	0.05	1.15	0.17	0.21
SiEndcapTracker	2.78E-03	6.02	0.06	6.02	0.23	0.29
BackwardMPGDEndcap	2.19E+02	1.74	0.11	0.35	0.42	0.52
ForwardMPGDEndcap	4.44E+02	1.74	0.11	0.35	0.86	0.97
MPGDBarrel	8.67E+01	3.26	0.10	0.65	0.04	0.14
OuterMPGDBarrel	1.29E+01	15.23	0.16	3.05	0.01	0.17
LFHCAL	2.10E+04	10.33	0.14	1.38	1.30	1.44
HcalEndcapPInsert	6.18E+04	1.31	0.15	0.17	2.78	2.93
EcalEndcapP	1.51E+05	0.78	0.01	0.35	2.69	2.70
HCcalEndcapN	7.81E+04	0.53	0.13	0.07	2.64	2.77
EcalEndcapN	8.07E+04	0.14	0.01	0.06	1.06	1.07
HcalBarrel	1.30E+03	0.25	0.13	0.03	0.08	0.21
EcalBarrelImaging	2.92E-02	0.32	0.00	0.32	0.01	0.01
EcalBarrelSciFi	1.52E+03	0.94	0.07	0.13	2.69	2.76
TOFBarrel	1.74E+00	13.59	0.05	4.53	0.01	0.06
TOFEndcap	8.34E-01	32.13	0.15	7.14	0.07	0.22
hpDIRC	2.35E+02	3.22	0.13	1.07	0.00	0.13
pfRICH	4.99E+02	3.05	0.18	1.02	0.00	0.18
dRICH	1.09E+02	1220.94	0.98	6.10	0.00	0.98
B0 Crystal Calorimeter	2.66E+05	0.00	0.00	0.00	0.00	0.00
B0 AC-LGAD	1.72E+01	5.95	0.20	1.32	0.00	0.20
RP	3.31E+01	4.53	0.21	1.01	0.00	0.21
OM	5.93E+00	2.53	0.21	0.56	0.00	0.21
ZDC Crystal Calorimeter	7.81E+04	0.02	0.00	0.02	0.00	0.00
ZDC HCAL	3.39E+01	0.20	0.02	0.20	0.00	0.02
DirectPhoton	2.00E+08	0.00	0.00	0.00	0.00	0.00
LowQ2Tracker	8.76E+00	0.04	0.00	0.04	0.00	0.00
LowQ2Calorimeter	0.00E+00	0.01	0.01	0.01	0.00	0.01
PairSpectrometerTracker	2.44E+02	0.74	0.07	0.25	0.00	0.07
PairSpectrometerCalorimeter	3.26E+04	0.07	0.07	0.07	0.00	0.07
Total		1334.01		40.67		

Figure 8.138: Maximum data volume per RDO with noise estimates.

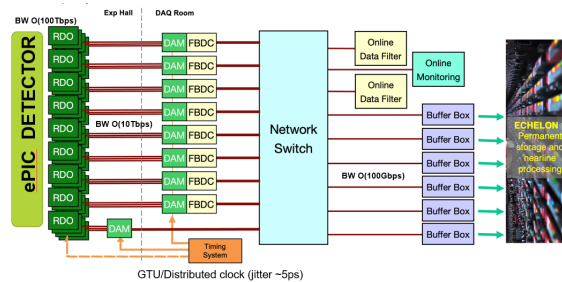


Figure 8.139: Schematic of the ePIC Streaming DAQ

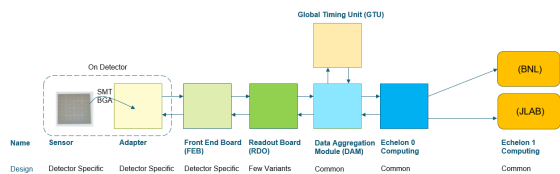


Figure 8.140: Components of the ePIC Streaming DAQ System

Implementation	Detector/Sensor	Key Attributes
Discrete	Calorimeter/SiPM	COTS devices, 14-bit digitization
CALOROC	Calorimeter/SiPM	ASIC, 10-bit digitization
EICROC	AC-LGAD, pixel	ASIC, High-precision timing for Cd < 5 pF
FCFD	AC-LGAD, strip	ASIC, High-precision timing for Cd < 10 pF
ALCOR	dRICH/SiPM	ASIC, uses shutter for 1 p.e. sensitivity
SALSA	MPGD	ASIC, peaking time to 50 ns, includes DSP

Figure 8.141: ePIC Electronics and ASICs summary

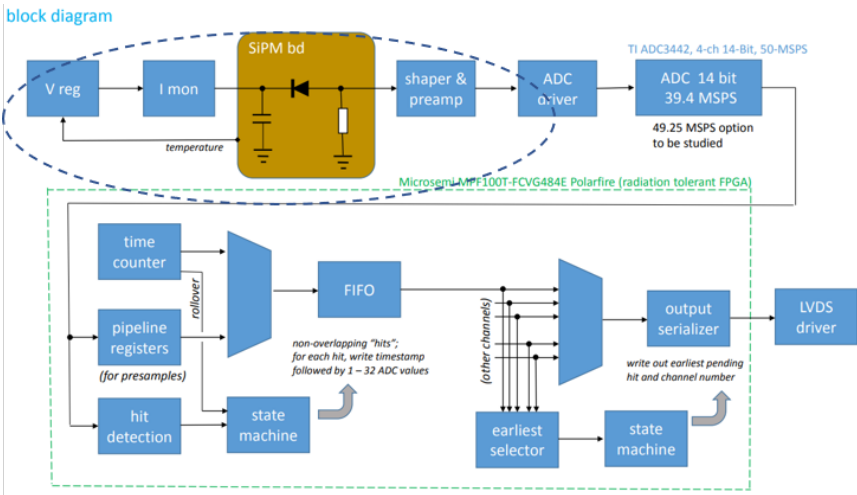


Figure 8.142: Discrete block diagram

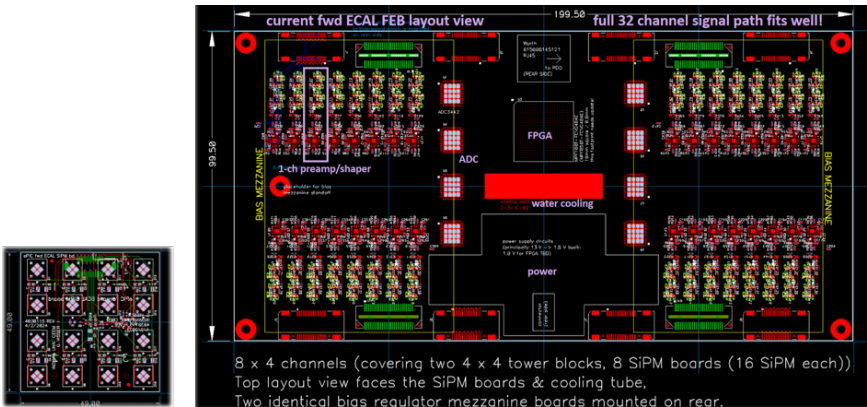


Figure 8.143: Discrete Adapter (left) and digitizer FEB PCBs

Function	Waveform digitizer with COTS devices
Channels	32
Digitizer	Ti ADC 3422
Resolution	14-bit (12-bit also available)
Shaping	80 ns peaking time
FPGA	Microsemi MPF100T-FCVG484E Polarfire (Rad Hard)
Power	DC-DC converter (bPOL12V, bPOL48V, LTC36xx)
Cooling	Liquid
Cabling	CAT6

Figure 8.144: Discrete key specifications

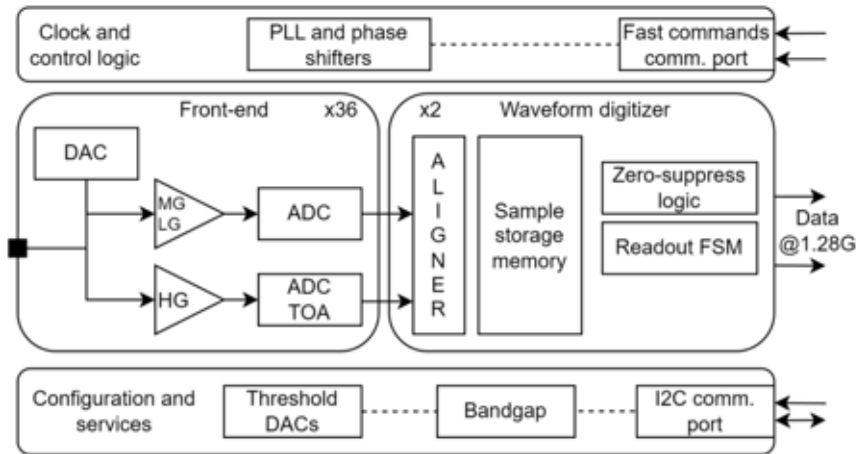


Figure 8.145: CALOROC block diagram

Function	Charge and timing digitization from SiPMs
Tech Node	130 nm CMOS
Channels	64
C _{din}	500 pF – 10 nF
Digitization	Charge: 10-bit ADC, 15-bit TOT; Timing: <500 ps TOT (1 MIP)
Dynamic Range	Up to 12 nC
Clock	39.4 MHz operation from BX 98.5 MHz
Links	1260.8 Mbps @ 39.4 MHz, multiple
Power	10 mW/ch
Package	BGA
Rad Tolerance	Radiation hard

Figure 8.146: CALOROC Key Specifications

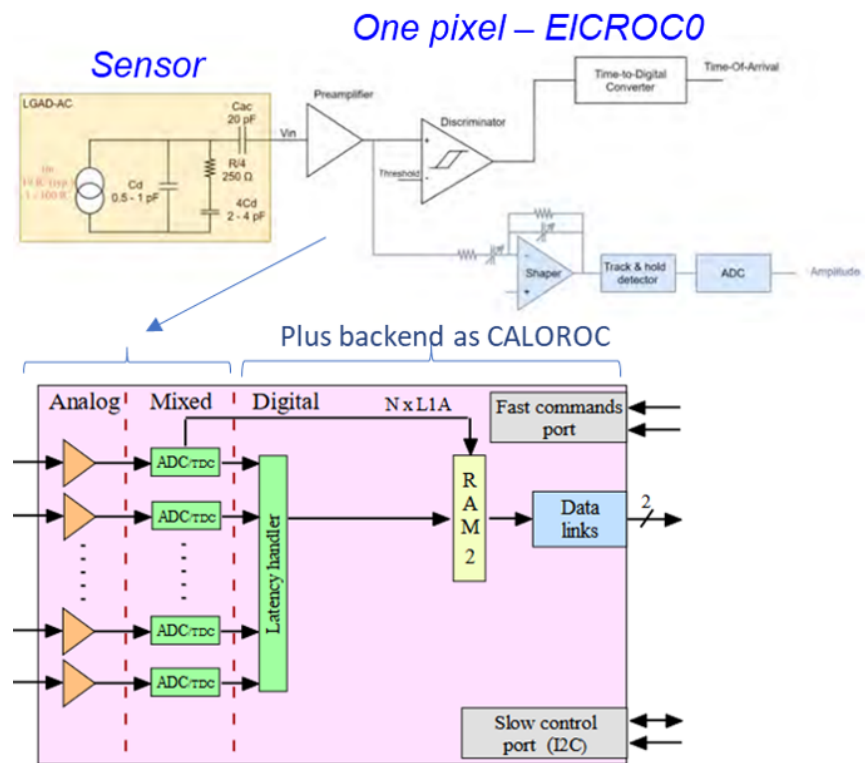


Figure 8.147: EICROC block diagram

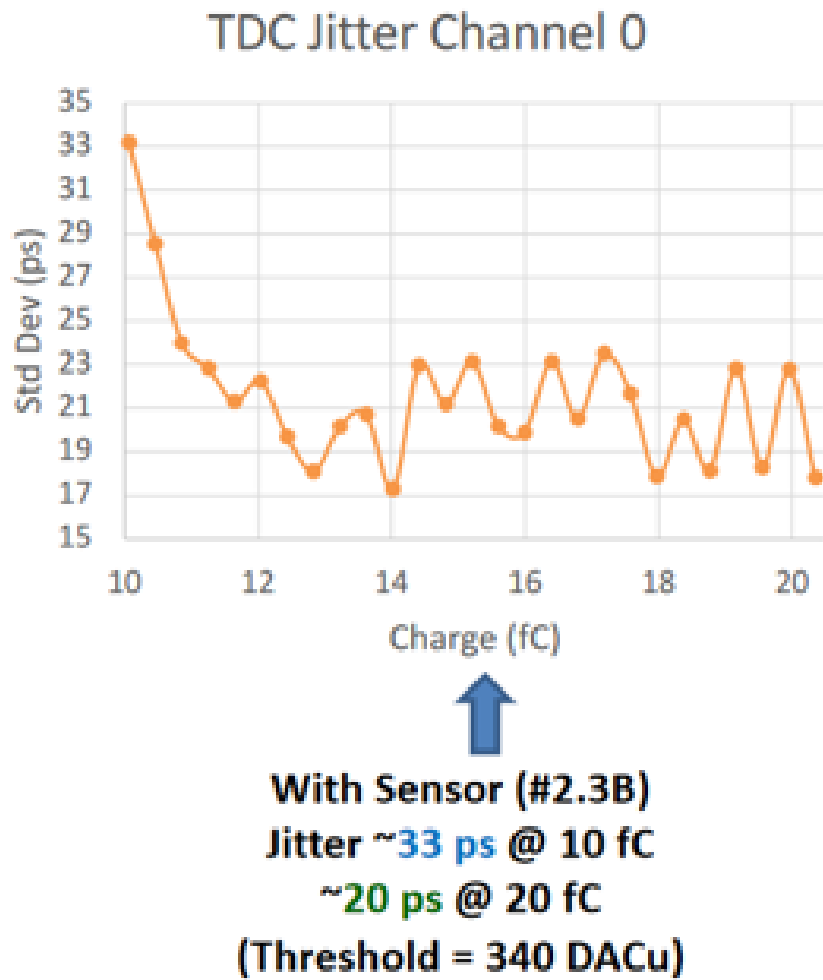


Figure 8.148: EICROC timing performance

Function	Timing digitization from AC-LGAD pixels
Tech Node	130 nm CMOS
Channels	1024 (32x32)
Cdin	1 – 5 pF
Digitization	ADC: 8-bit, TDC: 10b; Timing: 30 ps
Dynamic Range	1 – 50 fC
Clock	39.4 MHz operation from BX 98.5 MHz
Links	1260.8 Mbps @ 39.4 MHz, multiple
Power	<2 mW/ch
Package	Bump + wire bonds
Rad Tolerance	Radiation hard

Figure 8.149: EICROC Key Specifications

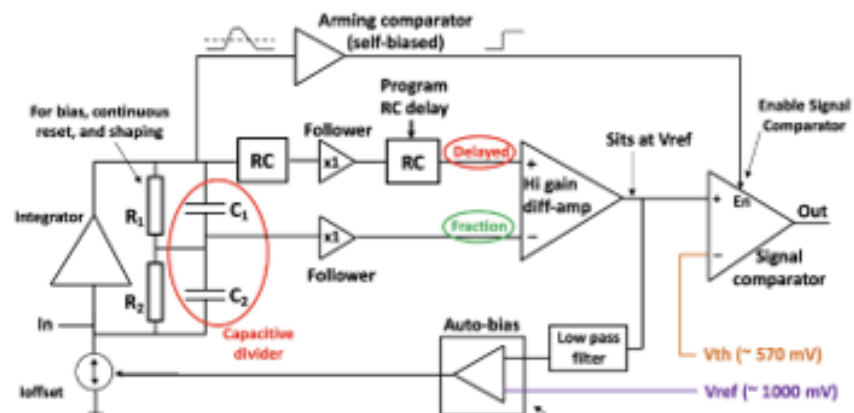


Figure 8.150: FCFD block diagram of the frontend

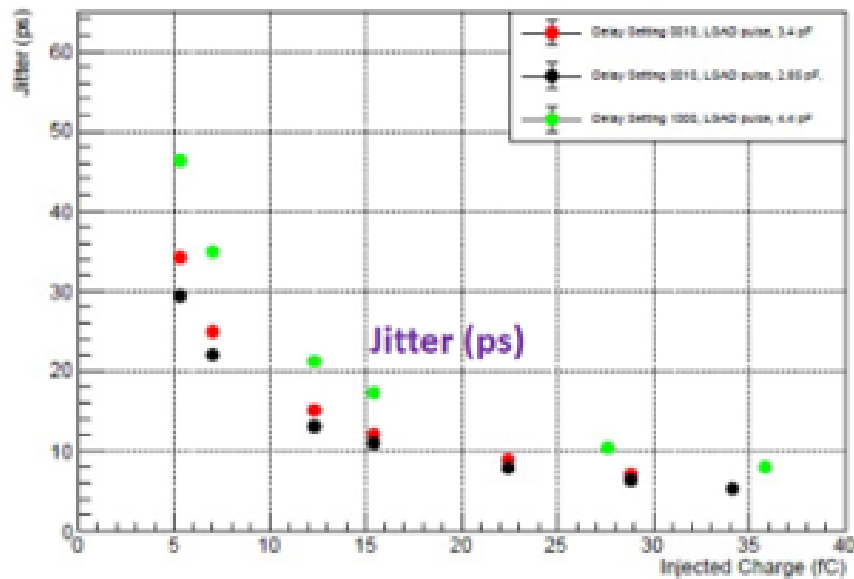


Figure 8.151: FCFD timing performance

Function	Timing digitization from AC-LGAD strips
Tech Node	65 nm CMOS
Channels	128
C _{din}	<15 pF
Digitization	TBD; Timing: 10 - 30 ps
Dynamic Range	5 – 40 fC
Clock	39.4 MHz operation from BX 98.5 MHz
Links	1260.8 Mbps @ 39.4 MHz, multiple
Power	<2 mW/ch
Package	Bump + wire bonds
Rad Tolerance	Radiation hard

Figure 8.152: FCFD Key Specifications

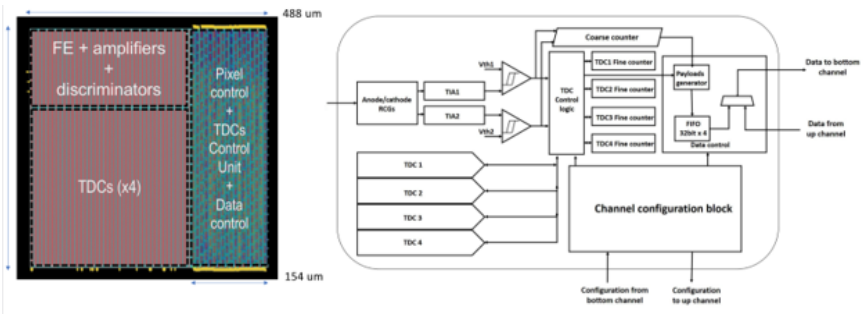


Figure 8.153: ALCOR Si Die (left) and block diagram

Function	Digitization from SiPMs with 1 p.e. sensitivity
Mode	Single-photon tagging or time and charge
Tech Node	110 nm CMOS
Channels	64 (8x8), dual polarity
Cdin	<1 nF
Digitization	25 ps TDCs, TOA + TOT; Timing <100 ps
Shutter	Width: 1 – 2 ns, programmable latency
Input Rate	<5 MHz
Clock	39.4 MHz operation from BX 98.5 MHz
Links	640 Mbps LVDS, SPI configuration
Power	12 mW/ch
Package	BGA
Rad Tolerance	Radiation hard

Figure 8.154: ALCOR Key Specifications

	# Ch	# Ch/ Unit	#ASICs/ Wafer	#Wafers	Node (nm)	Package	Institution
Discrete/COTS	24 k	32	NA	740	COTS	NA	IU
CALOROC	97 k	64	480	5	Digitizers	BGA	OMEGA/IN2P3/IJCL/ORN
EICROC	5.2 M	1024	160	42	130	Wafer Bump	OMEGA/IN2P3/IJCL/CEA- IRFU/AGH
FCFD	2.6 M	128	180	149	65	Wire Bond	FNAL
ALCOR	318 k	64	800	8	110	BGA	INFN
SALSA	202 k	64	500	9	65	BGA	CEA-Saclay/U of Sao Paulo

Figure 8.155: Scope of the electronics and ASICs developments



Figure 8.156: TOF pre-prototype RDO

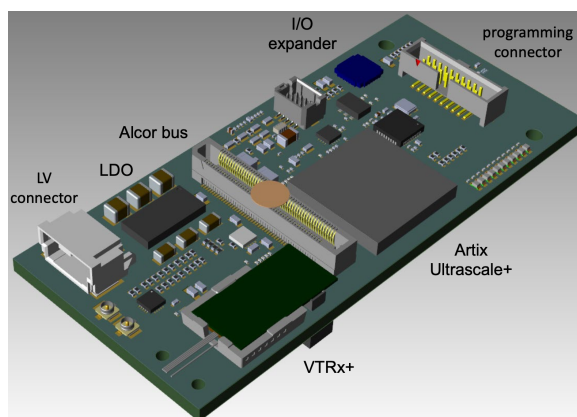


Figure 8.157: 3D model of dRICH RDO

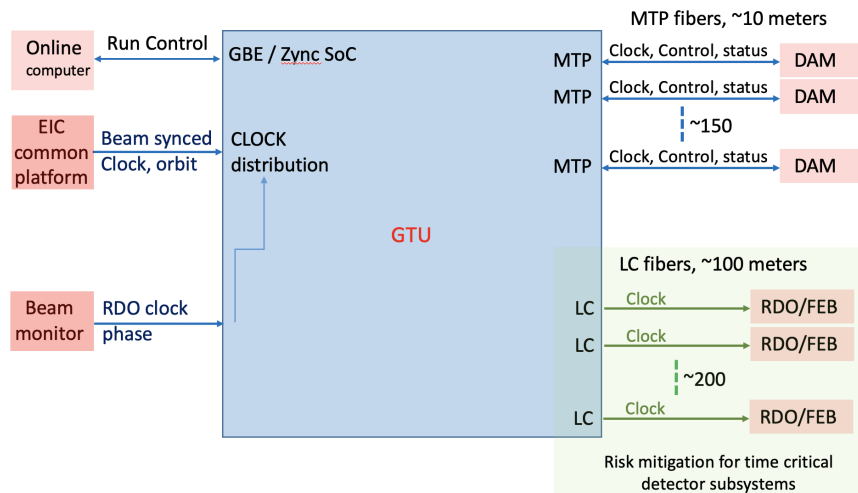


Figure 8.158: Schematic layout based for the GTU

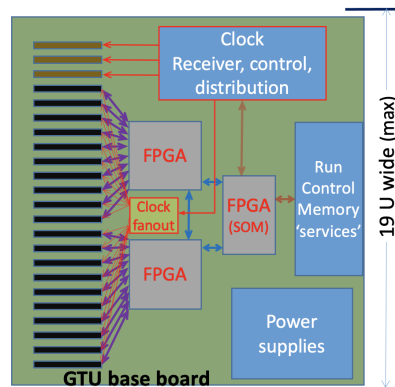
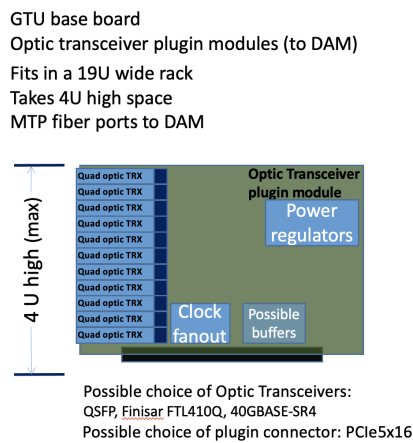


Figure 8.159: Physical concept for the fiber distribution for the GTU

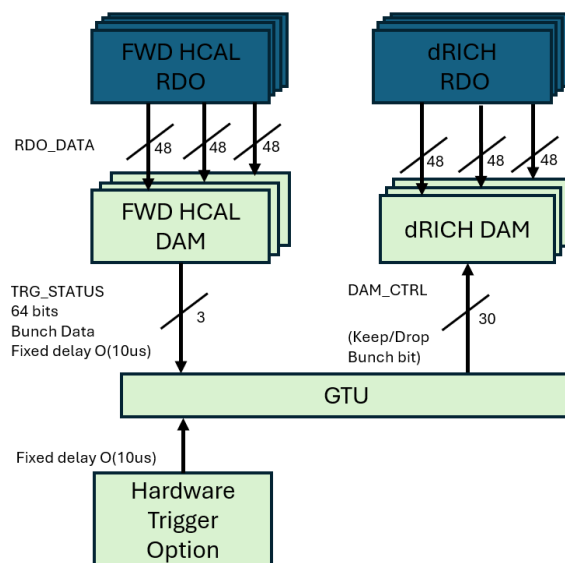


Figure 8.160: Operation of firmware trigger under assumption that the trigger decision for the dRICH depends upon data from fHCAL

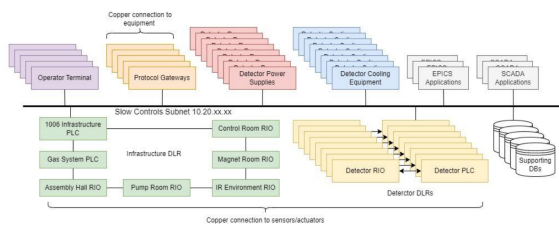


Figure 8.161: Proposed ePIC slow controls network topology



Figure 8.162: DAQ/Computing schedule

Detector System		Channels	SensorTechnology	Readout Technology	Institution
SI Tracking	3 vertex layers	7 m ²	MAPS	ipGBT, VTRX+	STFC, UK, ORNL
	2 sagitta layers	368 pixels	MAPS	ipGBT, VTRX+	STFC, UK, ORNL
	5 backward disks	5,200 MAPS sensors	MAPS	ipGBT, VTRX+	STFC, UK, ORNL
	5 forward disks		MAPS	ipGBT, VTRX+	STFC, UK, ORNL
MPGD Tracking					
	Barrel, e & H Endcaps	202 k	uRWELL, MicroMegas	SALSA	CEA, OMEGA, JLab
Forward Calorimeters					
	LHCAL	63,280	SIPM	CALOROC	ORNL, Debrecen
	HCAL Insert	8 k	SIPM	CALOROC	ORNL, Debrecen
	pECAL W/SciFi	16,000	SIPM	Discrete	IU
Barrel Calorimeters					
	HCAL	7,680	SIPM	CALOROC	ORNL, Debrecen
	ECAL SciFi/Pb	5,760	SIPM	CALOROC	U Regina, ORNL
	ECAL Imaging Si ASTROPiX	500 M pixels	Astropix	Astropix	KIT,NASA (GSFC), ANL
Backward Calorimeters					
	nHCAL	3,256	SIPM	CALOROC	ORNL
	ECAL (PWO)	2,852	SIPM	Discrete	IU, EEMCAL Consortium
Far Forward					
	B0: 3 Crystal Calorimeter	135	SIPM/APD	Discrete	IU, JLab
	B0: 4 AC-LGAD layers	688,128	AC-LGAD Pixel	EICROC	UCLab, OMEGA, BNL, ORNL, Rice
	2 Roman Pots (RP)	524,288	AC-LGAD Pixel	EICROC	UCLab, OMEGA, BNL, ORNL, Rice
	2 Off Momentum (OMD)	294,912	AC-LGAD Pixel	EICROC	UCLab, OMEGA, BNL, ORNL, Rice
	ZDC: Crystal Calorimeter	900	SIPM/APD	Discrete	IU, JLab
	ZDC: HCAL	9,216	SIPM	CALOROC	ORNL, Debrecen, JLab
Far Backward					
	Low Q Tagger 1	33,030,144	Timepix4	Timepix4	U. Glasgow
	Low Q Tagger 2	33,030,144	Timepix4	Timepix4	U. Glasgow
	Low Q Tagger 1+2 Cal	420 (2x210)	SIPM	CALOROC	U. York
	2 Lumi PS Calorimeter	3,360 (2x1680)	SIPM	Discrete	U. York
	2 Lumi PS Tracker	128,000 (2x64,000)	AC-LGAD Strip	FCFD/EICROcX	FNAL, OMEGA, Hiroshima, NTU, ORNL, UIC, UH, Rice, KSU, Tokyo
	Lumi Direct Photon Calorimeter	100	SIPM	Flash250	AGH Krakow, JLab
PID-TOF					
	Barrel bTOF	2,359,296	AC-LGAD Strip	FCFD/EICROcX	FNAL, OMEGA, Hiroshima, NTU, ORNL, UIC, Rice, BNL, KSU, Tokyo
	Hadron Endcap fTOF	3,719,168	AC-LGAD Pixel	EICROC	UCLab, OMEGA, BNL, ORNL, Rice
PID-Cherenkov					
	dRICH	317,952	SIPM	ALCOR, VTRX+	INFN (BO, FE, TO)
	pRICH	69,632	HRPPD	FCFD/EICROcX	BNL, FNAL, JLab
	hpDIRC	73,728	MCP-PMT or HRPPD	FCFD/EICROcX	BNL, FNAL, JLab

Figure 8.163: Electronics and DAQ Resources

References

- 6440 [1] Irene Dutta and Christopher Madrid and Ryan Heller and Shirsendu Nanda and Danush
6441 Shekar and Claudio San Martín and Matías Barria and Artur Apresyan and Zhenyu Ye and
6442 William K. Brooks and Wei Chen and Gabriele D’Amen and Gabriele Giacomini and Alessan-
6443 dro Tricoli and Aram Hayrapetyan and Hakseong Lee and Ohannes Kamer Köseyan and
6444 Sergey Los and Koji Nakamura and Sayuka Kita and Tomoka Imamura and Cristian Peña
6445 and Si Xie, “Results for pixel and strip centimeter-scale AC-LGAD sensors with a 120 GeV
6446 proton beam,” 7 2024.
- 6447 [2] M. Tabata *et al.*, “Silica aerogel radiator for use in the A-RICH system utilized in the Belle II
6448 experiment,” *Nucl. Instrum. Meth. A*, vol. 766, pp. 212–216, 2014.
- 6449 [3] M. Tabata, I. Adachi, H. Kawai, T. Sumiyoshi, and H. Yokogawa, “Hydrophobic silica aerogel
6450 production at kek,” *Nuclear Instruments and Methods in Physics Research Section A: Accelerators,*
6451 *Spectrometers, Detectors and Associated Equipment*, vol. 668, pp. 64–70, 2012.
- 6452 [4] R. Abdul Khalek *et al.*, “Science Requirements and Detector Concepts for the Electron-Ion
6453 Collider: EIC Yellow Report,” *Nucl. Phys. A*, vol. 1026, p. 122447, 2022.
- 6454 [5] “The electron-ion collider user group.”.
- 6455 [6] R. A. Khalek *et al.*, “Science Requirements and Detector Concepts for the Electron-Ion Collider:
6456 EIC Yellow Report,” *Nucl. Instr. and Meth. A*, vol. 1026, p. 122447, 2022.
- 6457 [7] “The epic collaboration website.”.
- 6458 [8] A. Collaboration, “Technical Design report for the ALICE Inner Tracking System 3 - ITS3 ; A
6459 bent wafer-scale monolithic pixel detector,” tech. rep., CERN, Geneva, 2024.
- 6460 [9] lpGBT Design Team, “lpGBT documentation – release,” 2024.
- 6461 [10] J. Troska *et al.*, “The VTRx+, an optical link module for data transmission at HL-LHC,” 2017.
- 6462 [11] “Technical Design Report: A High-Granularity Timing Detector for the ATLAS Phase-II Up-
6463 grade,” tech. rep., CERN, Geneva, 2020.
- 6464 [12] C. Madrid, R. Heller, C. San Martín, S. Nanda, A. Apresyan, W. Brooks, W. Chen, G. Giacomini,
6465 O. Kamer Köseyan, S. Los, C. Peña, R. Rios, A. Tricoli, S. Xie, and Z. Ye, “First survey of
6466 centimeter-scale ac-lgad strip sensors with a 120 gev proton beam,” *Journal of Instrumentation*,
6467 vol. 18, p. P06013, June 2023.
- 6468 [13] C. Bishop, A. Das, J. Ding, M. Gignac, F. Martinez-McKinney, S. Mazza, A. Molnar, N. Nagel,
6469 M. Nizam, J. Ott, H.-W. Sadrozinski, B. Schumm, A. Seiden, T. Shin, A. Summerell, M. Wilder,
6470 and Y. Zhao, “Long-distance signal propagation in ac-lgad,” *Nuclear Instruments and Meth-*
6471 *ods in Physics Research Section A: Accelerators, Spectrometers, Detectors and Associated Equipment*,
6472 vol. 1064, p. 169478, 2024.

- [14] L. Menzio *et al.*, “First test beam measurement of the 4D resolution of an RSD pixel matrix connected to a FAST2 ASIC,” *Nucl. Instrum. Meth. A*, vol. 1065, p. 169526, 2024.
- [15] S. Xie, A. Apresyan, R. Heller, C. Madrid, I. Dutta, A. Hayrapetyan, S. Los, C. Peña, and T. Zimmerman, “Design and performance of the fermilab constant fraction discriminator ASIC,” *Nuclear Instruments and Methods in Physics Research Section A: Accelerators, Spectrometers, Detectors and Associated Equipment*, vol. 1056, p. 168655, 2023.
- [16] C. Chock, K. Flood, L. Macchiarulo, F. Martinez-Mckinney, A. Martinez-Rojas, S. Mazza, I. Mostafanezhad, M. Nizam, J. Ott, R. Perron, E. Ryan, H.-W. Sadrozinski, B. Schumm, A. Seiden, K. Shin, M. Tarka, D. Uehara, M. Wilder, and Y. Zhao, “First test results of the trans-impedance amplifier stage of the ultra-fast hpsoc ASIC,” *Journal of Instrumentation*, vol. 18, p. C02016, feb 2023.
- [17] O. H. W. Siegmund *et al.*, “Advances in microchannel plates and photocathodes for ultraviolet photon counting detectors,” *Society of Photo-Optical Instrumentation Engineers Proceedings*, vol. 81450J.
- [18] C. J. Hamel *et al.*, “LAPPD and HRPPD: Upcoming Upgrades to Incom’s Fast Photosensors,”
- [19] “EICROC ASIC.” https://indico.bnl.gov/event/18539/contributions/73731/attachments/46348/78403/CdLT_EICROC_6mar23.pdf.
- [20] “Organization for Micro-Electronics desiGn and Applications.” <https://portail.polytechnique.edu/omega/>.
- [21] J. Anderson *et al.*, “FELIX: a PCIe based high-throughput approach for interfacing front-end and trigger electronics in the ATLAS Upgrade framework,” *JINST*, vol. 11, no. 12, p. C12023, 2016.
- [22] “Chiba Aerogel Factory Co., Ltd.” <https://www.aerogel-factory.jp/>.
- [23] M. Yonenaga *et al.*, “Performance evaluation of the aerogel RICH counter for the Belle II spectrometer using early beam collision data,” *Prog. Theor. Exp. Phys.*, no. 093H01, 2020.
- [24] S. Agostinelli *et al.*, “GEANT4—a simulation toolkit,” *Nucl. Instrum. Meth. A*, vol. 506, p. 250, 2003.
- [25] “ePIC IRT Package.” <https://github.com/eic/irt/tree/pfrich>.
- [26] R. Brun and F. Rademakers, “ROOT - An Object Oriented Data Analysis Framework, Proceedings AIHENP’96 Workshop, Lausanne,” *Nucl. Inst. & Meth. in Phys. Res. A*, no. 389, pp. 81–86, 1997.
- [27] M. Tabata, I. Adachi, Y. Hatakeyama, H. Kawai, T. Morita, and T. Sumiyoshi, “Large-area silica aerogel for use as cherenkov radiators with high refractive index, developed by supercritical carbon dioxide drying,” *The Journal of Supercritical Fluids*, vol. 110, pp. 183–192, 2016.
- [28] “CAEN A1515BV 16-channel floating ground High Voltage module.” <https://www.caen.it/products/a1515b/>.
- [29] “CAEN SY4527 High Voltage mainframe.” <https://www.caen.it/products/SY4527/>.
- [30] “Wiener Mpod Low Voltage system.” <https://www.wiener-d.com/power-supplies/mpod-lv-hv/>.
- [31] S. K. Sahu *et al.*, “Measurement of Radiation Damage on Silica Aerogel Cherenkov Radiator,” *Nucl. Instrum. Meth. A*, vol. 382, pp. 441–446, 1996.
- [32] R. Abjean, A. Bideau-Mehu, and Y. Guern, “Refractive index of hexafluoroethane (C-2F-6) in the 300-nm to 150-nm wavelength range,” *Nucl. Instrum. Meth. A*, vol. 354, pp. 417–418, 1995.

- [33] C. Piemonte and A. Gola, "Overview on the main parameters and technology of modern Silicon Photomultipliers," *Nucl. Instrum. Meth. A*, vol. 926, pp. 2–15, 2019.
- [34] L. P. Rignanese, P. Antonioli, R. Preghenella, and E. Scapparone, "SiPMs and examples of applications for low light detection in particle and astroparticle physics," *Riv. Nuovo Cim.*, vol. 47, no. 5, pp. 299–349, 2024. [Erratum: *Riv. Nuovo Cim.* 47, (2024)].
- [35] R. Hawkes, A. Lucas, J. Stevick, G. Llosa, S. Marcatili, C. Piemonte, A. Del Guerra, and T. A. Carpenter, "Silicon photomultiplier performance tests in magnetic resonance pulsed fields," in *2007 IEEE Nuclear Science Symposium Conference Record*, vol. 5, pp. 3400–3403, 2007.
- [36] S. España, L. Fraile, J. Herraiz, J. Udías, M. Desco, and J. Vaquero, "Performance evaluation of sipm photodetectors for pet imaging in the presence of magnetic fields," *Nuclear Instruments and Methods in Physics Research Section A: Accelerators, Spectrometers, Detectors and Associated Equipment*, vol. 613, no. 2, pp. 308–316, 2010.
- [37] F. Acerbi *et al.*, "Cryogenic Characterization of FBK HD Near-UV Sensitive SiPMs," *IEEE Trans. Electron. Dev.*, vol. 64, pp. 521–526, 10 2016.
- [38] S. Merzi, F. Acerbi, C. Aicardi, D. Fiore, V. Goiffon, A. G. Gola, O. Marcelot, A. Materne, and O. Saint-Pe, "Radiation Damage on Silicon Photomultipliers from Ionizing and Non-Ionizing Radiation of Low-Earth Orbit Operations," *Sensors*, vol. 24, no. 15, p. 4990, 2024.
- [39] E. Garutti and Y. Musienko, "Radiation damage of SiPMs," *Nucl. Instrum. Meth. A*, vol. 926, pp. 69–84, 2019.
- [40] T. Tsang, T. Rao, S. Stoll, and C. Woody, "Neutron radiation damage and recovery studies of SiPMs," *JINST*, vol. 11, no. 12, p. P12002, 2016.
- [41] R. Preghenella *et al.*, "Study of radiation effects on SiPM for an optical readout system for the EIC dual-radiator RICH," *Nucl. Instrum. Meth. A*, vol. 1056, p. 168578, 2023.
- [42] E. Nappi, "Aerogel and its applications to rich detectors," *Nuclear Physics B - Proceedings Supplements*, vol. 61, no. 3, pp. 270–276, 1998. Proceedings of the Fifth International Conference on Advanced Technology and Particle Physics.
- [43] EU, "Regulation (EU) 2024/573 of the European Parliament and of the Council on fluorinate greenhouse gases," <https://eur-lex.europa.eu/eli/reg/2024/573/oj>, 2024.
- [44] M. Kubantsev, I. Larin, and A. Gasparian, "Performance of the PrimEx electromagnetic calorimeter," *AIP Conf. Proc.*, vol. 867, no. 1, pp. 51–58, 2006.
- [45] T. Horn *et al.*, "Scintillating crystals for the Neutral Particle Spectrometer in Hall C at JLab," *Nucl. Instrum. Meth. A*, vol. 956, p. 163375, 2020.
- [46] A. Asaturyan *et al.*, "Electromagnetic calorimeters based on scintillating lead tungstate crystals for experiments at Jefferson Lab," *Nucl. Instrum. Meth. A*, vol. 1013, p. 165683, 2021.
- [47] F. Ameli *et al.*, "Streaming readout for next generation electron scattering experiments," *Eur. Phys. J. Plus*, vol. 137, no. 8, p. 958, 2022.
- [48] ePIC Collaboration, "Background studies - epic." <https://wiki.bnl.gov/EPIC/index.php?title=Background>, 2023. Accessed: 2024-09-28.
- [49] Y. Suda *et al.*, "Performance evaluation of the high-voltage CMOS active pixel sensor AstroPix for gamma-ray space telescopes," *Nucl. Instrum. Meth. A*, vol. 1068, p. 169762, 2024.
- [50] A. Accardi *et al.*, "Electron Ion Collider: The Next QCD Frontier: Understanding the glue that binds us all," *Eur. Phys. J. A*, vol. 52, no. 9, p. 268, 2016.

- [51] J. K. Adkins *et al.*, “Design of the ECCE Detector for the Electron Ion Collider,” 9 2022.
- [52] J. Adam *et al.*, “ATHENA detector proposal — a totally hermetic electron nucleus apparatus proposed for IP6 at the Electron-Ion Collider,” *JINST*, vol. 17, no. 10, p. P10019, 2022.
- [53] O. D. Tsai *et al.*, “Results of \& on a new construction technique for W/ScFi Calorimeters,” *J. Phys. Conf. Ser.*, vol. 404, p. 012023, 2012.
- [54] C. A. Aidala *et al.*, “Design and Beam Test Results for the sPHENIX Electromagnetic and Hadronic Calorimeter Prototypes,” *IEEE Trans. Nucl. Sci.*, vol. 65, no. 12, pp. 2901–2919, 2018.
- [55] T. Nicholls *et al.*, “Performance of an electromagnetic lead / scintillating fiber calorimeter for the H1 detector,” *Nucl. Instrum. Meth. A*, vol. 374, pp. 149–156, 1996.
- [56] O. D. Tsai *et al.*, “Development of a forward calorimeter system for the STAR experiment,” *J. Phys. Conf. Ser.*, vol. 587, no. 1, p. 012053, 2015.
- [57] F. Aaron *et al.*, “Measurement of the proton structure function $f_1(x, q^2)$ at low x ,” *Physics Letters B*, vol. 665, no. 4, pp. 139–146, 2008.
- [58] R.-D. Appuhn *et al.*, “The h1 lead/scintillating-fibre calorimeter,” *Nuclear Instruments and Methods in Physics Research Section A: Accelerators, Spectrometers, Detectors and Associated Equipment*, vol. 386, no. 2, pp. 397–408, 1997.
- [59] A. White *et al.*, “Design, construction and commissioning of a technological prototype of a highly granular sipm-on-tile scintillator-steel hadronic calorimeter,” *Journal of Instrumentation*, vol. 18, p. P11018, nov 2023.